Design, Control, and Perception of Bionic Legs and Exoskeletons

by

Alejandro Francisco Azocar

A dissertation submitted in partial fulfillment
of the requirements for the degree of
Doctor of Philosophy
(Mechanical Engineering)
in the University of Michigan
2020

Doctoral Committee:

Assistant Professor Elliott J. Rouse, Chair
Associate Professor Robert D. Gregg
Dr. Luke M. Mooney, Dephy, Inc.
Assistant Professor Ramanarayan Vasudevan

Alejandro Francisco Azocar

afazocar@umich.edu

ORCID iD: 0000-0001-8789-1077

Para Aby y Tio Hector. Los quiero mucho.

Acknowledgments

I am eternally grateful for getting to work with Elliott Rouse over the past 5 years. Thank you for guiding me when I needed it and for stepping back when you knew I could handle it, for pushing me when I didn't want to be pushed, for giving me opportunities to lead, for the experience of living in 3 new cities, for letting me vacation all over the world (and present at conferences on the side), for letting me use the faculty coffee maker, and for trusting me to leave for X.

A special thank you to Todd Kuiken, who co-advised me at Northwestern with Elliott. You saw something in a young aerospace engineer eager for a career change, and welcomed me with open arms. You were the first to give me confidence that I could be successful in this field.

Thank you to the rest of my committee members—Luke Mooney, Robert Gregg, and Ramanarayan Vasudevan—for helping me wrap up this dissertation in spite of everything that's going on in the world. Luke, your involvement has been key in much of my work, and I appreciate all the late night and weekend debugging you've helped me do, especially over the last few months. Bobby, you've been an incredible source of support since we met at RehabWeek in London (I still can't believe how much you love fish and chips), and our career conversations have meant a lot to me. Ram, you have given me a newfound appreciation for math and its applications (loved your self-driving cars class), and I hope to grow into a better mathematician throughout my career.

To my past and present labmates in the Neurobionics Lab and the Center for Bionic Medicine: none of this would be possible without you, especially Yves Nazon, Max Shepherd, Kim Ingraham, Ung Hee Lee, Tyler Clites, and Hashim Quraishi. You kept me sane, entertained, and gave me an environment I looked forward to working in every day (and night). Yves, thank you for taking the plunge to move to Michigan with me. You've been there since the beginning, hyping me up, traveling, living together, and have been one the best friends anyone could ever ask for. I want to be like you when I grow up.

Working with the Highlands Team over the last 16 months has been an incredible privilege. Thank you Kathryn Zealand for bringing me on for a 3 month internship, and then for convincing me to stay. Thank you for valuing my opinion, letting me take the lead, and giving me so many opportunities for growth. Working at X has been a culmination of all my Ph.D. experiences, where all the pieces have finally come together. P.S. Thank you for finally getting me into whiskey.

Most importantly, I want to thank the Azocar Lab. We started this journey together, and somehow—even though my work has been in Illinois, Michigan, and California—we're finishing it together in Texas. The last few months have been a lot of work, but y'all have been there supporting me like always: Papi with the tech support, Mami with the wellness support, and Penelope with the work-life balance support. The three of you are the inspiration for everything I've done in my career, and I hope I've made you proud.

I can't end this without thanking Floki. You're the best lil man I could've adopted, and you've been at my side (or on my keyboard) every single late night I've been writing this dissertation.

Table of Contents

Chapter

List of Figures

List of Tables

List of Appendices

List of Acronyms

AFO ankle-foot orthosis

ANOVA analysis of variance

DC direct current

DF dorsiflexion

ER-BLDC exterior-rotor brushless DC

EMF electromotive force

EMG electromyographic

FlexSEA Flexible, Scalable Electronics Architecture

GRF ground reaction force

GUI graphical user interface

HILO human-in-the-loop optimization

IMU inertial measurement unit

JND just noticeable difference

MVC maximum voluntary contraction

NU IRB	Northwestern University Institutional Review Board
OSL	Open Source Leg
PF	plantarflexion
PSD	power spectral density
RFSEA	Reaction-force Series-elastic Actuator
RMSE	root-mean-square error
SEA	series-elastic actuator
SMD	spring-mass-damper
VAF	variance accounted for
WF	Weber fraction
2IFC	two-interval forced-choice

Abstract

Bionic systems—wearable robots designed to replace, augment, or interact with the human body—have the potential to meaningfully impact quality of life; in particular, lower-limb prostheses and exoskeletons can help people walk faster, better, and safer. From a technical standpoint, there is a high barrier-to-entry to conduct research with bionic systems, limiting the quantity of research done; additionally, the constraints introduced by bionic systems often prohibit accurate measurement of the robot's output dynamics, limiting the quality of research done. From a scientific standpoint, we have begun to understand how people regulate lower-limb joint impedance (stiffness and damping), but not how they sense and perceive changes in joint impedance. To address these issues, I first present an open-source bionic leg prosthesis; I describe the design and testing process, and demonstrate patients meeting clinical ambulation goals in a rehabilitation hospital. Second, I develop tools to characterize open-loop impedance control systems and show how to achieve accurate impedance control without a torque feedback signal; additionally, I evaluate the efficiency of multiple bionic systems. Finally, I investigate how well people can perceive changes in the damping properties of a robot, similar to an exoskeleton. With this dissertation, I provide technical and scientific advances aimed at accelerating the field of bionics, with the ultimate goal of enabling meaningful impact with bionic systems.

Chapter 1

Thesis Summary

1.1 Specific Aims

The overall objective of this dissertation is to advance the field of lower-limb bionic systems using both technological and scientific approaches. This is accomplished with hardware development, control system characterization, and human perception experiments. Specifically, this dissertation encompasses the following aims:

1. **Develop a high-performance, open-source bionic leg.**

   Robotic prostheses can improve the quality of life for individuals with amputation, but safe, reliable controls research remains a challenge. Many research groups are developing improved control systems, but do not necessarily have access to a bionic leg for testing and have to spend considerable resources to build their own. In this aim, we developed an open-source bionic leg to lower the barriers-to-entry, facilitate and standardize bionics research, and enable direct comparison of control strategies.

2. **Characterize and improve the performance of novel actuators for bionic systems.**

   Recent bionic systems are being designed with high-torque motors from the drone industry; although they provide many benefits, these motors have not been rigorously characterized for use in robotics. In this aim, we conducted a series of experiments to evaluate and improve the performance of actuators that couple drone motors with low transmission ratios. Specifically, we developed system identification techniques to quantify and improve open-loop impedance control, characterized actuator-drive efficiency, and evaluated open-loop torque control.

3. **Quantify human perception of exoskeleton damping.**

   The mechanical impedance (stiffness and damping) of the leg governs many important aspects of locomotion, including energy storage, transfer, and dissipation between joints; however, little is known about the human ability to sense changes in impedance. In this aim, we investigated how small of a change to exoskeleton damping users can reliably perceive. This aim builds upon my master's thesis, which investigated the ability to sense changes in exoskeleton stiffness.

1.2 Thesis Contributions

Chapter 3 introduces the Open Source Leg (OSL), a simple, portable, scalable, customizable, and economical prosthesis for the research community [1, 2]. The OSL is the first prosthesis to use motors initially developed for the drone industry; we chose these motors for their high torque density, and because they are more electrically and thermally efficient than typical motors, resulting in a prosthesis with performance comparable to—or better than—heavier, more expensive prostheses. The OSL serves as a common hardware platform for evaluation of prosthesis control strategies, reduces redundant effort across researchers, and enables untethered testing outside the laboratory—in the community and at home. The OSL was designed for both new and experienced researchers in the field of bionics, and has already begun to achieve its purpose. As of publication, 9 different research groups are actively using or building the OSL—including labs with years of experience and labs just entering the field—demonstrating its impact in the last 2 years. Besides the Vanderbilt Prosthetic Leg, which has been used by 2 research groups, no other powered transfemoral prosthesis has been tested by multiple researchers. The labs currently using or building the OSL include:

1. **Neurobionics Lab, University of Michigan:** biologically-inspired impedance control
2. **Center for Bionic Medicine, Northwestern University & Shirley Ryan AbilityLab:** machine learning for intent recognition and targeted muscle reinnervation
3. **Locomotor Control Systems Lab, University of Michigan:** phase-based control and adaptive optimization
4. **Hartmut Geyer Lab, Carnegie Mellon University:** neuromuscular model control and online optimization
5. **Exoskeleton and Prosthetic Intelligent Controls Lab, Georgia Institute of Technology:** machine learning for intent recognition
6. **Rombolabs, University of Washington:** deep learning for coordinated movement control
7. **Human Neuromechanics Laboratory, University of Florida:** proportional myoelectric control
8. **Locomotion & Biomechanics Lab, University of Notre Dame:** hybrid volitional control
9. **Neuromechanics and Rehabilitation Technology Group, Imperial College London:** multi-sensor, hybrid model- and signal-based control

Chapter 4 presents the first study to thoroughly characterize and publish open-loop output impedance for drone-style actuators with and without integrated transmissions; we show how characterization can be used to decrease open-loop impedance errors from 42% to 3%. In this chapter, we also build upon previous work from our lab and present the first characterization of end-to-end (bus-to-output) actuator efficiency for these systems; we found that the average positive efficiency of all the actuators tested was 65%. Finally, we outline methods for others to characterize open-loop dynamics for different applications as well.

Chapter 5 completes the first set of studies investigating impedance (stiffness and damping) perception in the lower limb; previous work has been limited to the upper limb only. Specifically, Chapter 5 investigates damping perception, whereas my master's thesis investigated stiffness perception [3–5]. We found that users can detect changes in damping as small as 12%, with best perception at high damping values; this sensory threshold can be implemented on impedance-controlled devices for training or haptic feedback. By keeping impedance changes below the threshold, users can be trained to reach a desired performance level without being disturbed; alternatively, impedance changes above the threshold can be used for haptic feedback—to interact with users and improve their performance. These methods were also extended in a separate study investigating the resolution with which prostheses should be individually optimized [6, 7]. In this study, we found that individuals with below-knee amputations could detect changes in prosthesis stiffness as small as 7% and could consistently tune the prosthesis to their preferred stiffness (14% variation). This high sensitivity suggests prosthetic foot stiffness should be tuned on an individual basis, and with a high degree of precision.

Chapter 2

Introduction to Bionic Systems

Bionic systems—wearable robots designed to replace, augment, or interact with the human body—have the potential to meaningfully impact quality of life. This dissertation is focused on lower-limb prostheses (*i.e.*, mechanical devices that replace missing body segments) and exoskeletons (*i.e.*, mechanical devices that are worn over body segments and augment user performance). Although bionic prostheses[1] and exoskeletons[2] serve different populations and purposes, they share many similarities; bionic systems require control strategies that safely and comfortably interact with users, face similar hardware/software constraints, and must provide enough benefit to justify their weight and cost. When implemented well, bionic systems can have a significant positive impact on their user; however, design and control of these systems is challenging. In this dissertation, I develop tools and experiments aimed at improving and accelerating the field of bionics, with the ultimate goal of enabling meaningful impact with bionic systems.

2.1 Motivation

2.1.1 Prostheses

More than 2 million people in the United States have a limb amputation, with an expected 3.6 million by 2050 [8]. 65% of amputations are at the lower-limb, including above-knee (*i.e.*, trans-

---

[1] Also called bionic legs.

[2] This dissertation does not focus on exoskeletons designed to assist individuals with paralysis, stroke, *etc*.

femoral) and below-knee (*i.e.*, transtibial) amputations. Most individuals with lower-limb amputations wear prostheses that enable them to return to some activities of daily living; unfortunately, despite the benefits that most commercially-available prostheses provide, they have many drawbacks. Individuals with lower-limb amputations walk 13-56% slower, consume 25-65% more energy, and have a 50% chance of falling each year [9–11]. Additionally, many of these individuals develop compensatory gait modifications and favor their intact limb, leading to long term degeneration such as knee/hip osteoarthritis (intact limb) and osteoporosis (residual limb) [12]. The impacts of amputation go beyond the physical, as individuals with amputation are faced with social stigmatization, depression, and unemployment [13–15].

Although other factors—such as age, physical fitness, amputation level, cause of amputation, and socket fit—impact the biomechanical changes outlined above, a major source of these deficits is the passive nature of commercially-available prostheses. Passive prostheses—which have fixed mechanical properties—cannot produce net-positive mechanical energy; in contrast, the muscles in the intact leg contract during walking to produce large amounts of net-positive mechanical energy [16]. For example, the biological ankle generates 0.25 J/kg of positive work during walking, whereas passive ankle prostheses—which typically behave like springs—can store and release, but not generate, energy [17]; to compensate for the missing 18.75 J[3] of positive work, individuals with below-knee amputation increase both hamstring and quadriceps muscle activity during early- and mid-stance [18]. Similarly, the biological knee generates 0.71 J/kg during stair ascent, whereas passive knee prostheses—which typically behave like dampers—can dissipate, but not generate, energy [17]; to compensate, individuals with above-knee amputation typically ascend stairs step-by-step (instead of step-over-step) or using rapid knee and ankle flexion on the intact limb [19, 20]. Powered prostheses—which use motors to generate net-positive mechanical energy—have the potential to restore lost motor function and improve quality of life for individuals with amputation.

---

[3] Assuming a 75 kg subject.

2.1.2 Exoskeletons

Approximately 100 million people in the United States work in physically demanding jobs that require lifting/carrying weight, standing, or walking for extended periods [21, 22]. On average, occupations such as construction, extraction, transportation, and healthcare require 5-7 hours of walking a day while carrying 18-23 kg. A number of passive and powered exoskeletons have been developed for these applications, typically to assist the back muscles [23–27]. Lower-limb exoskeletons have the potential to assist as well, particularly in tasks that require heavy lifting and/or walking. For example, the hip and knee joints are heavily involved in squat lifting and the sit-to-stand transition [28, 29]; during locomotion, lower-limb exoskeletons that reduce the metabolic cost of walking may allow users to walk farther and faster, or carry more weight before getting tired [30, 31]. Additionally, the improvements that exoskeletons provide to physically demanding jobs may also extend to assist the United States' aging population, which currently consists of approximately 100 million people above the age of 50 [32]. Bionic exoskeletons have the potential to improve user performance, reduce injuries, and keep people active as they age.[4]

2.2 Bionic Legs

The age of bionic legs began 15 years ago, at Vanderbilt University and the Massachusetts Institute of Technology [33–36]. Vanderbilt's Center for Intelligent Mechatronics developed the first bionic leg (both knee and ankle joints), using pneumatic actuators tethered to off-board power and computation; since then, the Vanderbilt Prosthetic Leg has undergone multiple iterations to its actuators, transmissions, and structure. Through extensive studies—including running, cycling, uneven terrain, and bilateral amputations—this prosthesis has provided key insights on the complexities of developing a multi-degree-of-freedom bionic leg [37–42]; additionally, until now, this was the only bionic leg used by a second research group, where it showed meaningful clinical impact [43–46]. The Biomechatronics Group at the Massachusetts Institute of Technology devel-

---

[4] Although most of the following sections focus on bionic prostheses, many of the same design philosophies, control approaches, constraints, and limitations apply to exoskeletons as well.

oped the first bionic ankle, using both series and parallel elasticity to provide the biological ankle's dynamics while matching the shape and mass of the missing limb. The MIT Powered Ankle has also been tested extensively, and has shown an 8-14% reduction in metabolic cost, 57% increase in trailing leg mechanical work, 10% decrease in leading leg mechanical work, and 23% increase in self-selected walking speed, relative to a passive prosthesis [47, 48]; additionally, subjects walking with the bionic ankle exhibit similar metabolic energy costs, walking speeds, and biomechanical patterns compared to able-bodied subjects [48]. The MIT Powered Ankle became the first commercialized powered ankle prosthesis, originally as the BiOM Ankle (BionX) and now as the emPOWER Ankle (Ottobock).

The work started by these two research groups inspired many others to develop their own bionic systems (Table 2.1). Early designs used pneumatic actuation, then transitioned to high-speed, low-torque electric motors. To achieve biological speeds and torques, motors have been coupled to

Table 2.1: Overview of prominent bionic prostheses.

	Institution	Primary Transmission	Series Elasticity	Parallel Elasticity	Control	Publication(s)	Notes
Both	Neurobionics Lab, University of Michigan	Belt drive Four-bar linkage	Optional	-	Impedance	[1, 2]	OSL, introduced in this dissertation
	Center for Intelligent Mechatronics, Vanderbilt University	Belt drive Chain	-	Y	Impedance	[37–42]	Has been tested by an individual with double above-knee amputations
	Biomechatronics Group, Massachusetts Institute of Technology	Ball screw	Y	-	Impedance	[49]	The same actuator can be configured as a knee or ankle, without modification
	Locomotor Control Systems Lab, University of Michigan	Planetary gear	-	-	Position Impedance	[50]	Uses a single-stage stepped-planet compound planetary gear
	Hartmut Geyer Lab, Carnegie Mellon University	Harmonic drive	Y	-	Torque	[51]	Developed to test neuromuscular model control
	Advanced Mechanical Bipedal Experimental Robotics Lab, California Institute of Technology	Harmonic drive	-	-	Impedance	[52]	Used to translate controllers from bipedal robots to prostheses
Knee	Biomechatronics Group, Massachusetts Institute of Technology	Ball screw Cable	Y	-	Impedance	[53]	Includes an electromechanical clutch
	Delft University of Technology	Ball screw Four-bar linkage	Y	Y	Impedance	[54, 55]	Series stiffness changes as a function of knee angle
	Bionic Engineering Lab, University of Utah	Lead screw Roller screw	-	-	Torque	[56, 57]	Uses an actively varying transmission
Ankle	Biomechatronics Group, Massachusetts Institute of Technology	Ball screw	Y	Y	Position Torque Impedance	[36, 47, 48]	Commercialized by Ottobock, previously by BionX
	Human Machine Integration Lab, Arizona State University	Lead screw	Y	-	Torque	[58]	Commercialized by SpringActive
	Robotics and Multibody Mechanics Research Group, Vrije Universiteit Brussel	Ball screw Four-bar linkage	-	-	Position Torque	[59]	Uses springs for catapult-like actuation Commercialized by Axiles Bionics
	Bionic Engineering Lab, University of Utah	Roller screw	-	-	Position Torque	[60]	Uses a polycentric design
	Biomechatronics Lab, Stanford University	Bowden cable	Y	-	Torque	[61–65]	Emulator system using off-board motors Commercialized by Humotech

transmissions, springs (in series or parallel), and clutches. Due to the torque-speed regimes of the motors used, transmission ratios have historically been quite high (150-800:1), leading to inefficiencies, audible noise, and control challenges [36, 38, 53, 56, 66–68]. More recent systems—including the OSL introduced in this dissertation—are implementing novel low-speed, high-torque motors, which can be coupled to lower transmission ratios (20-50:1) [1,2,49,50]. There is no standard actuation scheme, as designs have used ball screws, gearboxes, cables, chains, and (occasionally) series or parallel springs. This has led to a wide range of prosthesis performance, particularly in terms of size, weight, complexity, and controllability; all of this variability makes it particularly difficult to compare the benefits and drawbacks of different designs and control systems.

2.3 Control Strategies

Control strategies for bionic systems must assist or augment the user in a safe, comfortable, and seamless manner. In general, control can be divided into three hierarchical levels [69]. At the highest-level, control systems must predict the user's goals or intended motions. The mid-level controller translates the high-level controller's predictions into desired device behavior. Finally, the low-level controller performs traditional motor control strategies to achieve the desired behavior. Reliable performance within and between each of these levels is important for meaningful ambulation with bionic systems.

2.3.1 High-level

The high-level controller—or perception layer—is responsible for estimating the user's intent [69]. In intent recognition approaches, the high-level controller predicts the user's desired activity (*e.g.*, walking) and sends that information to the mid-level controller. To date, the most comprehensive and successful implementation of high-level control—for both prostheses and exoskeletons—was developed at the Center for Bionic Medicine and Northwestern University [43–46, 70]. In this system, the user's present and future state are selected from a set of discrete activities, including:

sitting, standing, level-ground walking, ramp ascent, ramp descent, stair ascent, and stair descent, in addition to transitions between each activity.

To predict a user's activity, researchers have options to record data from the bionic system, the user, and/or the environment. Sensors on the bionic system typically measure mechanical and electrical information, including motor/joint/limb kinematics and (occasionally) kinetics, as well as motor electrical states. Sensors on the user measure similar mechanical information, in addition to electromyographic (EMG) activity from muscles [70,71]. An emerging area of research involves sensing the physical environment around the user, using laser rangefinders and cameras (standard or depth-sensing) [72–75].

Transitions between activities can be accomplished using a combination of heuristics and machine learning. In purely heuristic approaches, finite state machines divide the activities and transitions are based on simple, manually- or analytically-selected sensor thresholds [69]. Machine learning approaches typically use instantaneous or historical sensor data, along with sensor fusion techniques, to predict both the user's current activity and the transition to the next activity. These approaches often use classifiers like Gaussian mixture models, linear discriminant analysis, dynamic Bayesian networks, support vector machines, artificial neural networks, and image-based convolutional neural networks [70, 76–79]. The best performing systems typically result in 1-2% error rates, meaning that the control system makes 1-2 mistakes every 100 steps. Some errors—like incorrectly classifying ramp ascent as level-ground walking—may go unnoticed by the user; however, other errors—like incorrectly classifying stair descent as level-ground walking—may lead to serious injury. As bionic systems transition out of lab settings, high-level control becomes more and more important for safe, intuitive ambulation.

High-level control is the least studied level of bionic control, because in most research settings the experimenter serves as the high-level 'controller'. That is, most research studies only test a few activities at a time, typically independent of each other and in steady state (on treadmills). In these studies, there is no need for a real-time activity recognition system, so the researcher manually sets the activity and instead focuses on developing mid-level controllers.

2.3.2 Mid-level

The mid-level controller—or translation layer—is responsible for generating the appropriate assistance strategy for a given activity [69]. For example, if the user wants to walk on level ground, what should the bionic system actually do to help them? Historically, three main approaches have emerged—position, torque, and impedance control. In position control approaches, the robot enforces a kinematic trajectory that the user must follow. Enforcing a motion on a prosthesis or exoskeleton—particularly when the leg is on the ground—can be uncomfortable and unsafe, potentially leading to high forces on the user and robot; therefore, pure position control is rarely used in bionics, except during the swing phase of walking [47]. Torque control provides an improvement over position control, assisting the user's kinetics while allowing them to determine their own motion; however, accurately measuring torque on a bionic device can be challenging, due to size and weight constraints. Finally, impedance control provides a balance between position and torque control. Controlling mechanical impedance—the instantaneous, dynamic relationship between joint kinematics and kinetics—enables compliant interaction between the user and the robot, and may lead to more natural and capable bionic systems [80–82]. In bionic systems, the inputs to an impedance controller are positions and velocities, and the output is a desired torque; therefore, impedance and torque control are closely linked together. Impedance control is largely inspired by the human body; the neuromuscular system regulates lower-limb impedance to enable energy storage and exchange across joints, and safely transfer disturbances from the ground to the body [82, 83]. Most bionic systems implement a combination of position, torque, and impedance control, and use heuristics, biologically-inspired modeling approaches, or optimization methods to generate assistance profiles that enable safe locomotion.

In conjunction with their high-level control approach, the Center for Bionic Medicine developed a comprehensive set of impedance-based prosthesis control strategies for standing, level-ground walking, ramp ascent, ramp descent, stair ascent, and stair descent [45]. Most of the impedance laws used heuristics; however, studies that estimated the biological impedance of the ankle while walking were also incorporated to provide biologically-inspired control [84]. The impedance parameters were tuned with prosthetists and therapists until a set of clinical goals were met. Although this approach successfully enables clinically-meaningful locomotion across many activities, it is time consuming; the impedance controller had 140 parameters and took 5 hours to tune.

The Locomotor Control Systems Lab at the University of Michigan developed an alternative mid-level control approach that drastically reduces the tuning parameters and time using phase variables and virtual constraints [85–87]. Instead of subdividing the gait cycle into different states (*e.g.*, early stance, late stance, early swing, and late swing), these controllers unified the gait cycle into a continuous user-synchronized sense of phase. Phase variables are unactuated degrees of freedom that monotonically increase/decrease throughout a rhythmic process. For transfemoral prostheses, thigh angle served as the phase variable [88]; for transtibial prostheses, a separate group used shank angle as the phase variable [89]. Recent work combining phase-based virtual constraint control with state machines expanded the capabilities of these systems to include non-rhythmic tasks, including: starting/stopping motion, obstacle avoidance, and kicking a soccer ball [87]. Additionally, by drastically reducing the number of control parameters, this approach provided clinically significant improvements with only 10 minutes of tuning.

Neuromuscular model control, developed at Carnegie Mellon University, generates torque assistance profiles based on a model of the human neuromuscular system [51,90,91]. This model is motivated by the idea that limited control is needed when exploiting the natural dynamics of legged systems, and encodes biological muscle reflex activity to generate joint torques. In simulation, the model successfully reproduced human walking kinematics and kinetics, and was robust to ground disturbances and slopes changes. On a transtibial prosthesis, the neuromuscular model successfully adapted to changes in slope; on a transfemoral prosthesis, limited tests showed that the model reproduces normal walking patterns and effectively responds to some disturbances in early and late swing. Ultimately, the goal of the model is to enable balance recovery on transfemoral prostheses, a currently unsolved challenge.

The Biomechatronics Lab at Stanford University has developed a mid-level control technique for exoskeletons using human-in-the-loop optimization (HILO) [92]. In this approach, the torque profile provided by an exoskeleton is determined by optimizing an objective function related to the user or device; typically, the goal is to reduce the user's metabolic cost of walking. Briefly, user's begin an experimental session walking with predetermined torque assistance profiles (drawn from a multivariate normal distribution of possible profiles) while respiratory measurements estimate the metabolic cost of walking at each condition. After a set number of trials, covariance matrix adaptation—an evolution strategy used to solve optimization problems—is used to identify the best torque profiles, update the distribution of possible profiles, and generate new profiles for further testing; this process continues for multiple generations until convergence. HILO has been used successfully on ankle and hip-knee-ankle exoskeletons to reduce the metabolic cost of walking by 14-40%, relative to not wearing an exoskeleton at all [92–94]. Other groups have also performed HILO with gradient descent and Bayesian optimization methods [95, 96].

2.3.3 Low-level

The low-level controller—or execution layer—is responsible for accurately producing the desired behavior with the actuator [69]. As in classical controls literature, the low-level controller is intended to minimize the error between the desired behavior (coming from the mid-level controller) and the measured behavior (coming from sensor readings) while remaining stable. This can be accomplished using a combination of feedback and feedforward loops. Feedback control requires a measure or estimate of the variable being controlled (*e.g.*, motor/joint angle, motor/joint torque, or motor current), whereas feedforward control requires a model to predict the system's future state based on its current and previous states. Low-level control has been extensively studied in other fields, is fairly well understood, and is not a major area of focus in bionics.

2.4 Remaining Challenges

Despite promising research results, bionic systems—in particular transfemoral prostheses—have yet to make large-scale clinical or commercial impact. Although bionic systems provide a benefit to the user, the improvements do not yet outweigh the increased costs, risks, and added weight. A passive knee or ankle prosthesis that performs well enough for community ambulation costs $10,000-15,000 [97]; in contrast, commercially available powered prostheses—such as the emPOWER Ankle (Ottobock) and the POWER KNEE (Ossur)—cost up to $100,000 each. In some cases, the improvements observed in research settings to do not necessarily translate to the clinic. Early research prototypes of the emPOWER Ankle showed 8-14% reduction in metabolic cost and 23% increase in self-selected walking speed [47, 48]; however, when the commercial version of the prosthesis was tested by a separate group, no differences were found [98]. Additionally, the field has yet to develop a flexible, intuitive control architecture that reliably lets users ambulate without errors. Finally, many bionic are legs still too heavy (6-8 kg) compared to lightweight passive prostheses like the Vari-Flex Foot (Ossur, 0.6 kg) and the Comfort-Brake Knee (Ottobock, 0.7 kg) [51, 52]. There are a number of challenges the field needs to solve to enable meaningful, widespread impact of bionic systems.

2.4.1 Hardware

Mass is perhaps the biggest challenge for both bionic legs and exoskeletons, and many other challenges are further constrained by mass limitations. Unlike passive systems—which are typically built with springs, dampers, and simple structures—bionic systems have the added mass of motors, transmissions, batteries, and electronics. For example, the emPOWER Ankle (2.3 kg) is approximately 4 times heavier than the passive Vari-Flex Foot (0.6 kg). Added mass becomes particularly detrimental at the ankle, as the metabolic cost of walking increases when mass is moved distally (down the leg) [99]. In addition to affecting mass, the geometry of the bionic systems is critical as well. Prostheses that are too tall may not fit some users, especially if they have a long residual limb. Similarly, large exoskeletons may interfere with the user's motion, and the inertia may actually hinder locomotion.

Torque sensing is an often-overlooked challenge in bionics. A measure of joint torque is needed for closed-loop torque and impedance control; unfortunately, measuring torque is a major challenge in bionics, primarily due to mass and size constraints. High-quality torque sensors—with the range, resolution, signal-to-noise ratio, and sampling rates needed for locomotion—are large, heavy, and expensive. Series-elastic actuators (SEAs) offer an alternative to torque sensors by placing a spring between the transmission and the output [100]; measuring the deflection of the spring provides an estimate of the system's torque. Although SEAs provide torque measurement, they also increase mass, size, and design complexity, so only about half of bionic systems use them (Table 2.1).

2.4.2 Controls

Although not always clarified, many groups use open-loop torque and impedance control strategies, due to the difficulties in measuring torque on a wearable device; closed-loop control is typically only implemented with SEAs. Without a measurement of output torque, bionic systems usually use closed-loop *current* control, since motor current is proportional to motor torque; the device's transmission ratio provides the relationship between motor and output torque. Previous systems, which used highly-geared transmissions, typically required complex modeling to account for losses in the transmission [38]; more recent systems, with smaller transmission ratios, are less susceptible to unmodeled transmission dynamics, and are likely to perform better with open-loop control strategies [50]. Regardless, more effort needs to be directed at characterizing and improving open-loop control strategies.

Most high- and mid-level controllers are developed and tested under steady-state conditions (*e.g.*, on treadmills). Although these test conditions provide a valuable foundation for control system development, they do not accurately reflect community ambulation; that is, they do not account for the variability of day-to-day life. Consequently, many research prototypes are not equipped to handle changes in walking speed, sudden starting/stopping of motion, shuffling in place, walking backwards, side-stepping, *etc*.

The challenges in translating control systems from the lab to a more unconstrained environment are compounded by the fact that most researchers focus either on high- or mid-level control; very few groups develop both in tandem. This type of isolated testing means that, the best mid-level control strategies will rarely be tested together, and transitions between them will not be developed, because they are not coupled with a high-level controller. Similarly, the best high-level control strategies may be paired with poor mid-level controllers, resulting in great intent recognition but a poor user experience.

2.4.3 User

Ultimately, these bionic systems are being designed for end users (individuals with an amputation, factory workers, *etc*.); unfortunately, bionics research is focused more on device performance and less on testing and developing with the user in mind. For example, some prosthesis studies are run on able-bodied subjects, instead of users with an amputation [51, 62, 63, 101]. Although it is critical to test bionic systems on able-bodied subjects first, researchers should be wary of applying the results of able-bodied studies to individuals with amputation. Along the same lines, many research groups invest heavily in developing bionic systems, but then only perform a single study with the device. There is a serious lack of continuity and user testing in the field of bionics, which is, in part, preventing the field as a whole from advancing.

There is a gap in our understanding of how exoskeleton users respond to, and perceive, external assistance. Early work on both prostheses and exoskeletons suggests that assistance should be customized to each user, but the exact metrics to customize are unclear [6, 7, 92]. Metabolic cost is a popular metric for exoskeletons, but comfort, preference, and overall experience may provide different results. Developing algorithms that automatically adapt to users' short- and long-term needs, in a way that does not interfere with their gait (physically or perceptually), may help with acceptance of bionic systems.

2.5 Potential Pathways

To address many of the aforementioned challenges, the primary goal of this dissertation is to introduce tools to unify and provide continuity in bionics research. In Chapter 3, I outline the design, control, and implementation of the OSL. The OSL is a powerful hardware platform for biomechanics, controls, and machine learning researchers (among others) to perform a wide range of studies on a common device. The OSL design enables it to be 20% lighter than comparable prostheses, and its low transmission ratio simplifies open-loop control. In Chapter 4, I explore different actuators, both for prostheses and exoskeletons, to understand their open-loop control capabilities and efficiencies; in particular, I show how to characterize and improve upon open-loop impedance control. Finally, in Chapter 5, I explore how users perceive externally-applied actuation, from a system similar to an exoskeleton; specifically, I investigate how well users can detect changes in the damping properties of an external system attached to the lower-limb. It is my hope that with this work, researchers can shift their focus away from designing bionic legs from scratch, and toward developing integrated controllers, understanding the user's experience, and accelerating the adoption of bionic systems outside of academia.

Chapter 3

Design, Control, and Clinical Implementation of an Open-source Bionic Leg

Portions of this chapter appear in:

1. **A F Azocar,** L M Mooney, J F Duval, A M Simon, L J Hargrove, and E J Rouse, “Design and Clinical Implementation of an Open-source Bionic Leg,” *Nature Biomedical Engineering*, accepted, in press.
2. **A F Azocar,** L M Mooney, L J Hargrove, and E J Rouse, “Design and Characterization of an Open-source Robotic Leg Prosthesis,” *Proceedings of the IEEE RAS/EMBS International Conference on Biomedical Robotics and Biomechatronics (BioRob)*, August 2018. Finalist, Best Hardware Demo Finalist, Student Paper Competition

3.1 Abstract

Over one million individuals with amputations live in the United States, many of whom walk slower, use more energy, fall more often, and develop devastating secondary deficits over time. Robotic prostheses hold the promise to address many of these challenges, but safe, reliable control strategies have remained out of reach—that is, a critical gap is the ability to provide appropriate instructions to robotic legs that enable robust ambulation in the real world. Fortunately, there are many researchers studying control strategies, but each group tests their strategies with different

robotic hardware in constrained laboratory settings. This mismatch in prosthesis hardware severely limits comparison of control solutions and, along with the lack of testing in real-world environments, hinders the translation of these promising technologies. To address these challenges, we developed the OSL: a robotic knee-ankle prosthesis that facilitates control, biomechanics, and clinical research. This chapter presents the OSL's design innovations, characterizes its electromechanical performance, and demonstrates clinical implementation with an advanced high-level control strategy. The OSL provides a common hardware platform for scientific and clinical testing, lowers the barrier for prosthetics research, and enables research beyond the laboratory: in settings such as the hospital, community, and home.

3.2 Introduction

Millions of people with lower-limb amputations suffer from a reduced quality of life [8, 15]. With the exception of highly athletic individuals, the majority of these people walk slower, get tired faster, and are less stable than non-amputees [9, 11, 36, 102]. In the intact human body, leg muscles contract during walking to add mechanical energy [16]; however, traditional passive prostheses are not able to provide this energy, and, subsequently, cannot restore the natural functions of muscles lost during an amputation. This makes more demanding activities, such as climbing stairs and ramps, particularly difficult [103]. Additionally, individuals with lower-limb amputations often develop compensatory modifications to their gait, biomechanics, and muscle activation patterns that lead to further complications, such as osteoarthritis, osteoporosis, and back pain [12, 18, 104]. Finally, the resulting mobility challenges can lead to depression, social stigmatization, and unemployment [13–15]. Although passive prostheses provide substantial mobility benefits, their physical, psychological, and social impacts may limit the quality of life for many individuals with amputations.

Several research groups are developing powered knee [53, 54], ankle [47, 58, 59, 105], and knee-ankle [38, 56, 68] (whole-leg) prostheses capable of producing able-bodied kinematics and kinetics that are not possible, or extremely difficult, with passive systems [106–108]. These capabilities are typically achieved using electric motors that add net-positive mechanical energy analogous to the muscles within the leg. For example, powered knee prostheses are capable of recreating early-stance knee flexion and extension—a region of the gait cycle that most passive prostheses cannot reproduce without an increased risk of falls [53, 109, 110]. Additionally, powered ankle prostheses can add energy for powered push-off; in contrast, individuals with passive ankle prostheses often rely on exaggerated hip motions to compensate for the lack of push-off [18]. Powered knee-ankle systems combine the benefits of powered knee and ankle prostheses—and have the potential to further improve quality of life—but introduce the need for more complex, coordinated control strategies. Consequently, results from studies of powered prostheses have often been debated. For example, although some individual experiments show patients walking faster, using less metabolic energy, or exhibiting improved center of pressure progression, there has been discussion of the applicability of these systems in clinical settings or for people with lower activity levels [98]; this is not necessarily a limitation of the prosthesis hardware, but instead a lack of understanding how to best control these devices. Finally, prosthesis emulators are a recently-developed tool for quickly and systematically testing control systems [61, 64, 111]. Emulators utilize off-board motors and Bowden cable tethers, leading to high performance and low prosthesis weight; however, the tether between the motor and prosthesis can limit experiments to a laboratory setting with a treadmill.

There have also been promising advances in the development of safe, natural, and intuitive control approaches. Today's state-of-the-art control architectures typically include three overarching levels of control, each bearing responsibility for certain aspects of successful community ambulation. The control systems must recognize the user's intended movement (*i.e.*, high-level control), translate the intended movement into an appropriate pattern of leg movement and effort (mid-level control), and execute the desired motions with closed-loop control (low-level control) [69]. Errors or failures at any of these levels may lead to falls, injuries, loss of confidence, and reduced community mobility. Fortunately, this is an active area of research, with many groups studying different approaches to the levels of control [51, 85, 112–115]. For example, recently-developed high-level control approaches range from simple thresholds to machine learning techniques that automatically transition between control strategies for different ambulation modes, such as level ground walking, ramp ascent/descent, and stair ascent/descent [38, 46]. Modern mid-level strategies implement impedance-based control, phase-based control, or biologically-inspired neuromuscular models [38, 51, 85, 112]. Finally, low-level control methods use a combination of feedback and feedforward control loops to minimize the error between the measured and desired states of the robot [69]. Overall, control systems for robotic legs are highly sophisticated, and most groups focus on a subset of high-, mid-, or low-level control [69]; although this practice avoids the challenges associated with integrating the three levels of control, it limits the impact of these controllers in real-world settings. Thus, despite promising work, key challenges remain in the development of control strategies that are safe, robust, and intuitive.

Although talented researchers around the world are investigating the best ways to control robotic prostheses, development of prosthetic hardware requires substantial investments of time and resources before research can begin. Even after research is complete, differences in design, performance, and limitations hinder the ability to compare the merits of different control systems. For example, robotic prostheses today vary widely in size, weight, transmission type, controllability, and degrees of freedom; additionally, many research prostheses must be tethered to a power supply—preventing researchers from testing in more challenging and realistic environments. Finally, since most research prostheses are prototypes, they are typically only tested in a few studies by the original designers, and can be difficult for other researchers to use. Commercially-available emulator systems help address many of these issues. Although they are powerful, versatile, and enable quick exploration of novel control systems, they do not have the portability or potential clinical relevance of a self-contained prosthetic leg. The lack of a low-cost, high-performance, and accessible powered prosthetic leg technology has hindered progress in the field, and ultimately, the quality of life of individuals with lower-limb amputations.

To facilitate the study and fair comparison of control approaches, lower the barrier to performing controls research, and prevent duplication of effort, we have created the Open Source

Leg (OSL): a unique robotic knee-ankle prosthesis system developed for open-source adoption (Fig. 3.1, Appendices A and B). The OSL includes novel hardware, actuation, sensing, low-level control software, and software libraries to communicate with researcher-specific mid- and high-level control systems. In this chapter, we present the design, technical characteristics, and performance of the OSL. We provide a detailed description of the design process, mechatronics implementation, and characterize multiple control architectures. We also highlight two novel design components: integration of high-torque motors and a customizable series-elastic actuator. Finally, we demonstrate patients successfully walking with the OSL across level ground, ramps, and stairs in a hospital setting, with all control parameters provided for reference for future researchers.

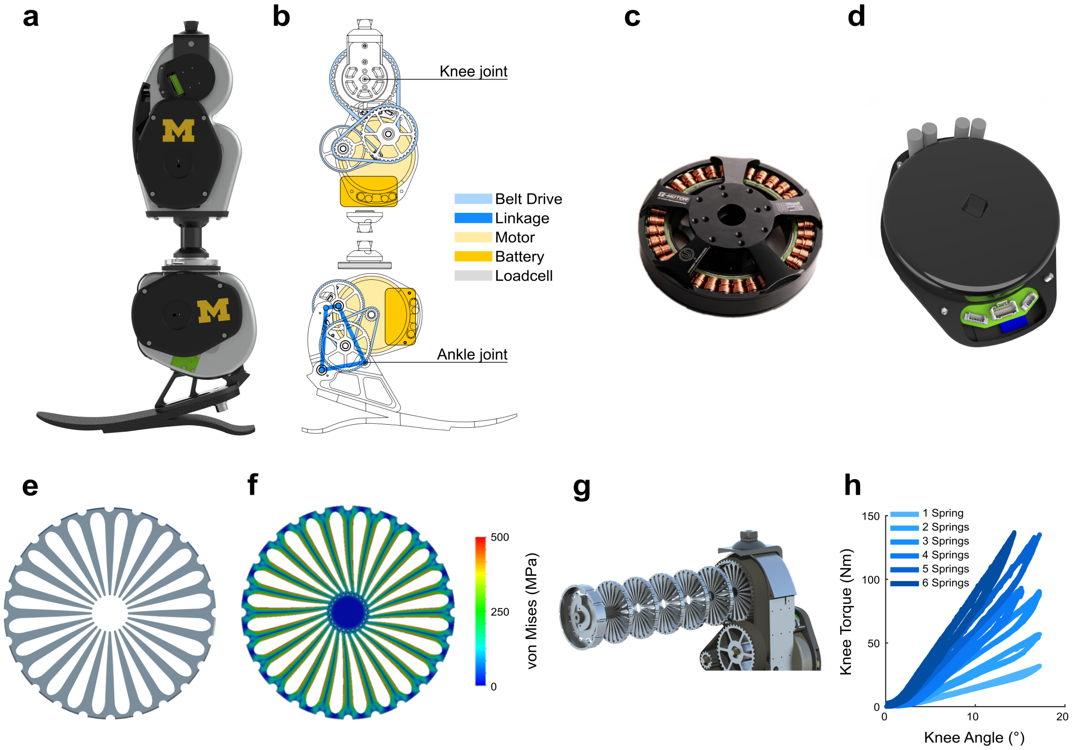

Figure 3.1: The Open Source Leg (OSL) and its novel design components. **a,** Rendering of the OSL. **b,** Schematic of the OSL highlighting the transmission, electronics, and load cell. **c,** Output view of the electric motor used in the OSL. **d,** Output view of the motor integrated with the open-source motor controller and embedded system. **e,** Side view of a single spring disk. **f,** Finite element analysis of a spring disk being deflected by the gear-shaped internal shaft. Colors represent the von Mises stress. **g,** Exploded view of six springs stacked inside the knee output pulley. **h,** Torque-angle relationship of the knee with 1-6 springs stacked inside. Each spring has a stiffness of approximately 100 Nm/rad.

Table 3.1: Hardware model information.

Item	Model	Company	Location
Motor	U8-16	T-motor	Nanchang, Jiangxi, China
Batteries	25087X2	Venom Power	Rathdrum, ID, USA
Temperature Sensor	MCP9700A	Microchip Technology Inc.	Chandler, AZ, USA
IMU	MPU-9250	InvenSense	San Jose, CA, USA
Motor Encoder	AS5047P	ams AG	Premstaetten, Austria
Joint Encoder	AK7452	Asahi Kasei Microdevices Corporation	Tokyo, Japan
Load Sensor	M3564F	Sunrise Instruments	Nanning, China
Single-board Computer	Raspberry Pi 3	Raspberry Pi Foundation	Cambridge, UK
Embedded Microcontroller	DM3730	Texas Instruments	Dallas, TX, USA

3.3 Methods

3.3.1 Design

3.3.1.1 Overview

The OSL incorporates a number of design innovations to facilitate adoption and improve performance. For example, we used a low-cost electric motor from the drone industry (Fig. 3.1, Table 3.1); since drone motors cannot rely on transmissions to increase torque output (due to the added mass), they produce 2-10 times more torque than the motors typically implemented in prosthetic legs. The motor's increased torque density allows us to implement transmission ratios 2-5 times lower than comparable prostheses (Table 3.2). Transmissions amplify the torque produced by the motors, and higher ratios will require more stages; transmissions generally have an efficiency of 70-98% per stage, depending on transmission type [116]. Additionally, the inertia reflected onto the motor increases with the square of transmission ratio. Therefore, low transmission ratios are important in prostheses because they improve efficiency, electrical power demands, size, and bandwidth, ultimately impacting mass, battery size, controllability, and other factors [116, 117].

Table 3.2: OSL specifications with comparison to other prostheses and the human body.

		OSL	MIT	Vanderbilt	Utah	Human[h]
Mass (g)	Knee	2160-2330[a]	2700	2700[e]	1680	2616[i]
	Ankle	1740	2000	2300	1045[f]	1959[j]
Height (mm)	Knee	240	285	-	290	314[i]
	Ankle	213	220	210	120	171[j]
Range of Motion (°)	Knee	120	120	120	120	90
	Ankle	30	45	65	55	60
Transmission Ratio	Knee	49	143	176	0-375	-
	Ankle	58 ± 16[b]	170	116	50-800	-
Series Elasticity (Nm/rad)	Knee	∼100-600	240	-	-	-
	Ankle	-[c]	1688[e]	-	-	-
Peak Torque, Continuous (Nm)	Knee	50[d]	40	-	39[e]	-
	Ankle	59 ± 16[d]	-	-	-	-
Peak Torque, Instantaneous (Nm)	Knee	150[c]	120	85	125	90
	Ankle	178 ± 49[d]	125	150	125	105
Peak Speed (rad/s)	Knee	5.2	-	-	-	6.8
	Ankle	5.6	-	-	-	5.4
Position Bandwidth (Hz)	Knee	10-20	-	-	7[g]	2[k]
	Ankle	10-20	-	-	-	4[k]
Torque Constant (Nm/A)	Knee	0.14	0.028	0.028	0.014	-
	Ankle	0.14	0.060	0.053	0.014	-
Motor Constant (Nm/W$^{1/2}$)	Knee	0.182	0.044	0.044	0.023	-
	Ankle	0.182	0.057	0.096	0.043	-
Bus Voltage (V)	Knee	36	24	24	24	-
	Ankle	36	24	24	24	-

- Not applicable/available

[a] Knee mass varies with SEA configuration

[b] See Fig. 3.6 for ankle transmission ratio profile

[c] The ankle does not have an explicit series elastic element; however, the carbon fiber foot provides some of the benefits of series elasticity without the added size, complexity, or closed-loop torque control

[d] Estimated with torque constant, transmission ratio, continuous (10 A) and instantaneous (30 A) motor current, and 90% efficiency at each transmission stage (73% overall efficiency)

[e] Estimated

[f] Does not include batteries or electronics

[g] 10° amplitude

[h] Assuming a 75 kg, 1.7 m tall subject walking on level ground or ascending/descending stairs

[i] Assuming 75% shank mass and height

[j] Assuming 25% shank plus foot mass and height

[k] Defined as the frequency range over which 70% of the total signal power is captured

We designed the OSL through a multi-step design process which involved modeling human joint biomechanics, transmission kinematics, mechatronics (including motor electrical and thermal limitations), and the structural housing (Fig. 3.2, Appendix A). This was an iterative design process with the overall goal of achieving able-bodied kinematics/kinetics while meeting the desired design principles, minimizing prosthesis mass/volume, and satisfying mechatronic constraints.

3.3.1.2 Biomechanics

We began the design of the OSL by extracting the kinematic (*e.g.*, angle, angular velocity, and angular acceleration) and kinetic (torque) trajectories of the knee and ankle joints from the literature. The data we used included walking at slow, self-selected, and fast speeds, in addition to stair ascent/descent, for 75 kg and 100 kg subjects [17].

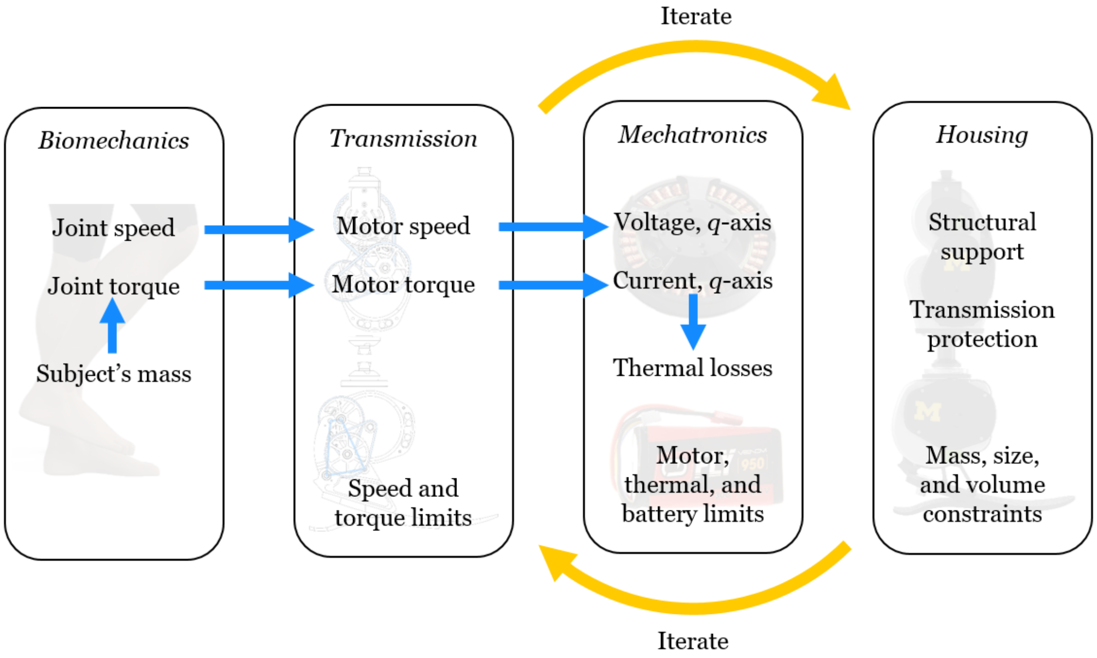

Figure 3.2: Overview of the OSL design process. Able-bodied kinematics and kinetics provide load requirements, which are transmitted into motor kinematic (voltage) and kinetic (current) requirements. The final transmission, battery, and housing designs resulted from iterating to meet speed, torque, electrical, thermal, mass, and size constraints.

3.3.1.3 Transmission

We simulated the transmission and motor requirements for each of the knee and ankle prostheses by incorporating the governing equations of SEAs and direct current (DC) motors, and using the extracted biomechanical joint angles (θ_l) and torques (τ_l) as the desired load requirements [53,118]. The motor mechanical requirements for a given ambulation mode are:

$$\theta_m = (\theta_l + \frac{\tau_l}{k_s})N \tag{3.1}$$

$$\tau_m = J_m\ddot{\theta}_m + \frac{\tau_l}{\eta N} \tag{3.2}$$

where θ_m, τ_m, and J_m are motor angle, torque, and inertia, respectively; and are transmission ratio and efficiency (assumed = 0.9 in each stage), respectively; and is the stiffness of the series elastic element. Using Eqs. 3.1 and 3.2, we simulated a range of transmission ratios and stiffness values (including infinite stiffness for the rigid configuration) for each of the ambulation modes; these simulations helped determine the range of acceptable transmission ratios and series elastic elements (Fig. 3.3). Based on these simulations, we selected target transmission ratios of 49:1 and 40:1-100:1 for the knee and ankle, respectively.

Timing belts serve as the primary torque transmission mechanism in the OSL; specifically, we chose the recently-developed PowerGrip GT3 (Stock Drive Products / Sterling Instrument, Hicksville, NY, USA) belts because they provide longer belt life, increased load-carrying capacity, and quieter operation relative to other available belts [119]. Our overall goal when selecting belt/pulley configurations was to minimize the volume of each stage while resisting tooth jump. Tooth jump typically occurs with high torques or low belt tensioning, and is highly dependent on transmission geometry (*i.e.*, tooth profile, number of teeth of each pulley, number of teeth engaged, pulley center-to-center distance, and belt width); however, there is little data available addressing the relationship between transmission geometry and the torque that endangers tooth jump. Based on the manufacturer's documentation, we calculated conservative estimates of tooth jump torque

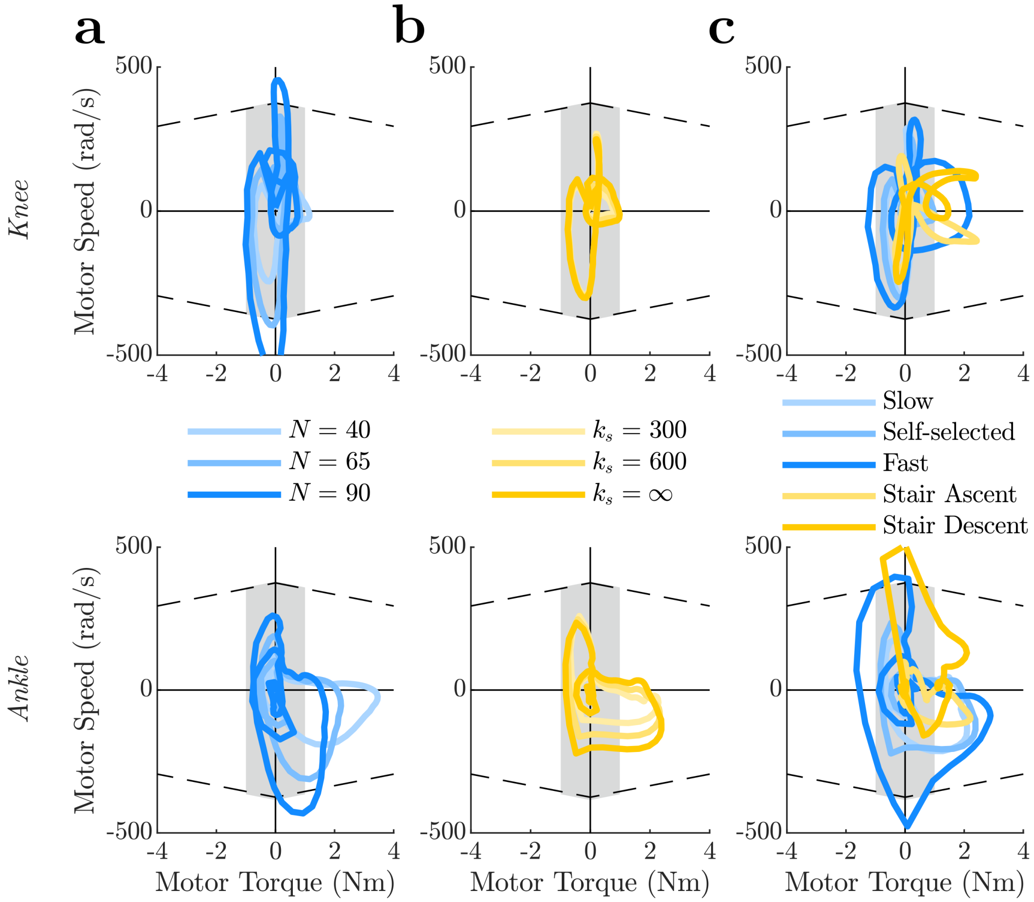

Figure 3.3: Simulated motor speed-torque curves for the knee and ankle prostheses. a, Transmission ratio simulation in a rigid configuration for self-selected walking. **b,** SEA simulation with the OSL transmission ratios for self-selected walking. **c,** Ambulation mode simulation in a rigid configuration using the OSL transmission ratios. Shaded area denotes the continuous operating region.

(per mm belt width) for 2, 3, and 5 mm pitch GT3 belts to be approximately 0.19, 0.66, and 2.4 Nm/mm, respectively [119]; we used these torques to specify the minimum acceptable belt width for each transmission stage. To select the final belt drive geometries, we performed an iterative design process, investigating overall transmission volume, number of belt stages, pitch of each belt stage, width of each stage, number of teeth engaged, ease of assembly, and availability of belt lengths and widths; this process resulted in a 2 mm pitch stage followed by two 5 mm stages in the knee, and two 3 mm stages in the ankle (Table 3.3). These belt drives were simulated to ensure that the torques at each stage would not lead to tooth jump during ambulation (Fig. 3.4). The pul-

Table 3.3: Transmission stage specifications.

		Knee			Ankle		
		Stage 1	Stage 2	Stage 3	Stage 1	Stage 2	Stage 3
Belt Drive	Pitch (mm)	2	5	5	3	3	-
	Input Pulley Teeth	16	14	14	17	17	-
	Output Pulley Teeth	80	40	48	60	60	-
	Transmission Ratio	5.00	2.86	3.43	3.53	3.53	-
	Belt Teeth	92	50	60	72	72	-
	Belt Width (mm)	30	15	45	9	21	-
Linkage	Crank Length (mm)	-	-	-	-	-	2
	Coupler Length (mm)	-	-	-	-	-	10
	Rocker Length (mm)	-	-	-	-	-	7
	Frame Length (mm)	-	-	-	-	-	10
	Transmission Ratio	-	-	-	-	-	3.44-8.75
	Range of Motion (°)	-	-	-	-	-	30.54

leys were machined from either 7075-T6 Aluminum or 17-4 PH stainless steel using subtractive manufacturing, and the belts were purchased directly from the manufacturer.

In addition to a two-stage belt drive, the ankle prosthesis incorporates a four-bar linkage mechanism for torque transmission. We included the four-bar linkage instead of a third belt stage to reduce the overall size of the prosthesis and directly couple motion of the linkage to motion of the ankle joint and foot. To design the linkage, we began by simulating the range of motion and transmission ratio of more than 3000 linkage configurations. The simulation varied the lengths of the individual links, through integer values between 1 and 10 units, and constrained the range of motion to a minimum of 20° angular distance between links to avoid singularities (Fig. 3.5). Using these simulations, we explored a subset of linkage configurations while iterating through different belt drive options, and selected the mechanism that provided the best combination of range of motion, transmission ratio, and size (Fig. 3.5, Table 3.3). Increasing the range of motion of the linkage requires increasing the transmission ratio and size of the belt drive; we chose to limit the range of motion to 30° to reduce the overall size of the prosthesis. Unlike the knee, which has a constant transmission ratio, the addition of the four-bar linkage resulted in a kinematically-varying transmission ratio for the ankle (Fig. 3.6).

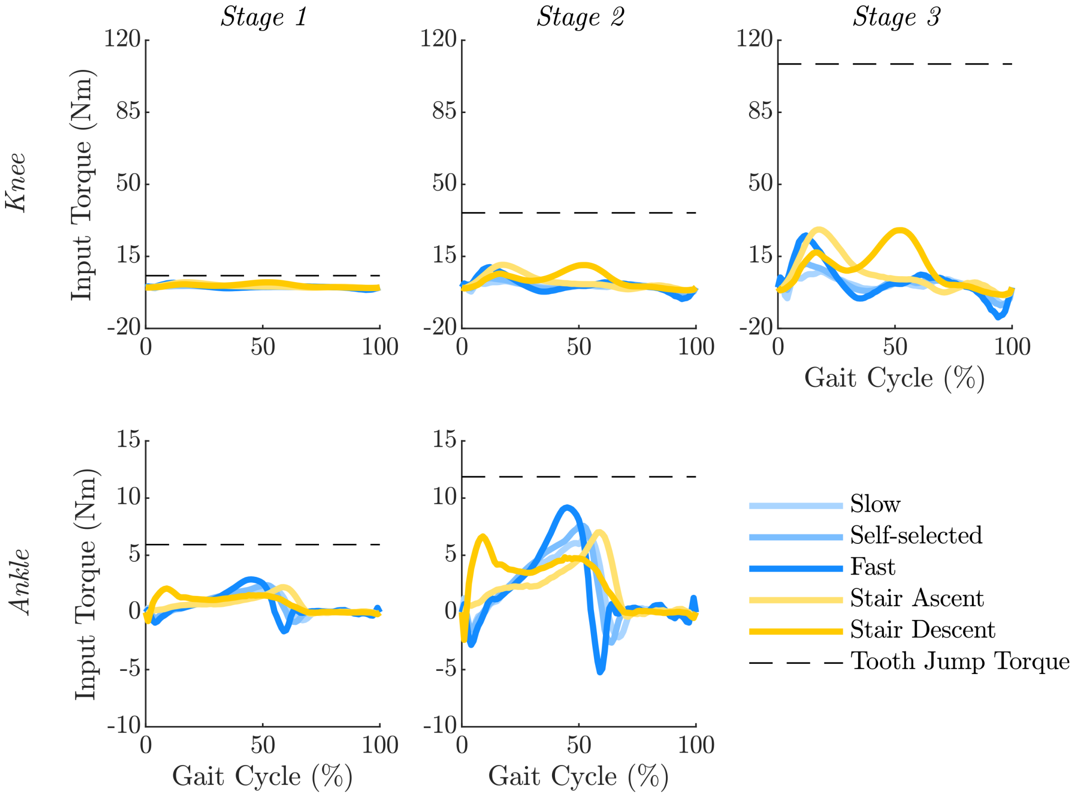

Figure 3.4: Simulated belt drive torques for the knee and ankle prostheses. The expected torques applied to the input pulleys of the belt drive stages are below the tooth jump torque across all the simulated ambulation modes.

3.3.1.4 Series Elasticity

The OSL also incorporates selectable series elasticity: the knee functions either as a SEA—and allows for modification of the series stiffness—or as a rigid actuator (Fig. 3.1) [100]. Selectable series elasticity allows researchers to use the SEA for energy storage/return, shock tolerance, and torque control, whereas the rigid actuator is simpler, lighter, and requires motor current to estimate torque. Depending on the desired magnitude of the series stiffness element, up to six torsional springs disks—each with a stiffness and mass of 97 ± 20 Nm/rad and 23 g, respectively—can be stacked inside the knee's transmission, resulting in a compact SEA without any added volume (Fig. 3.1).

Each spring disk is 4.3 mm thick and contains 24 radially cantilevered beams, with a maximum

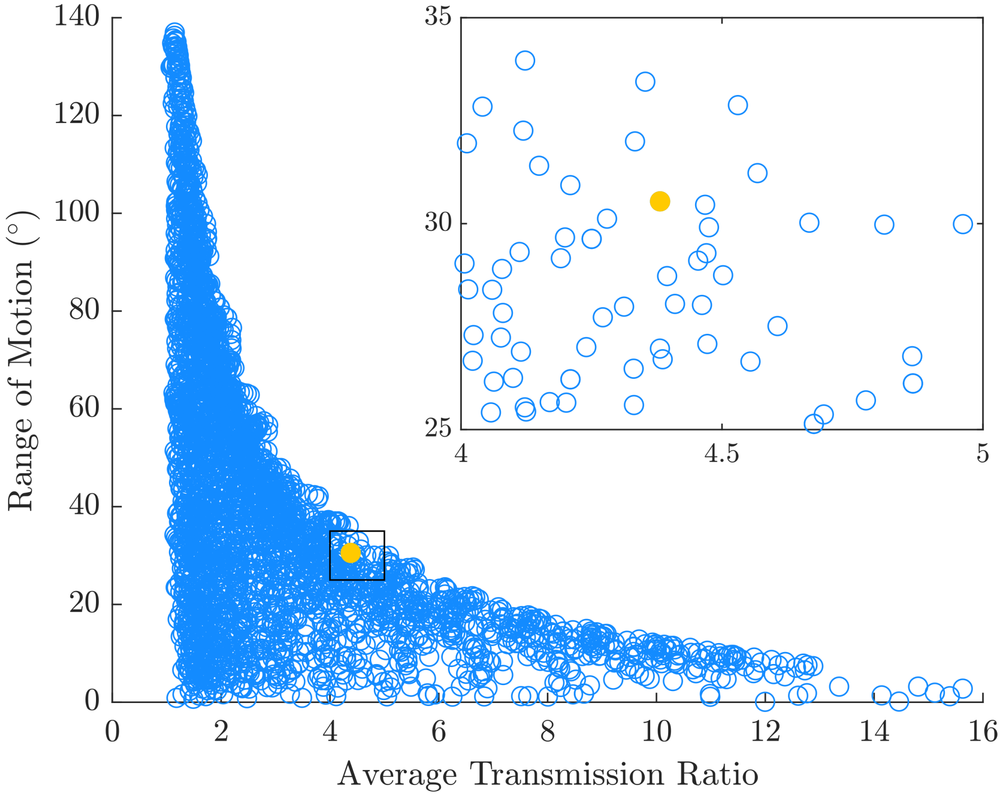

Figure 3.5: Simulated range of motion and transmission ratio for various linkage configurations. Design of the linkage required a trade-off between ankle range of motion and transmission ratio. Filled yellow circle denotes the linkage implemented in the ankle prosthesis.

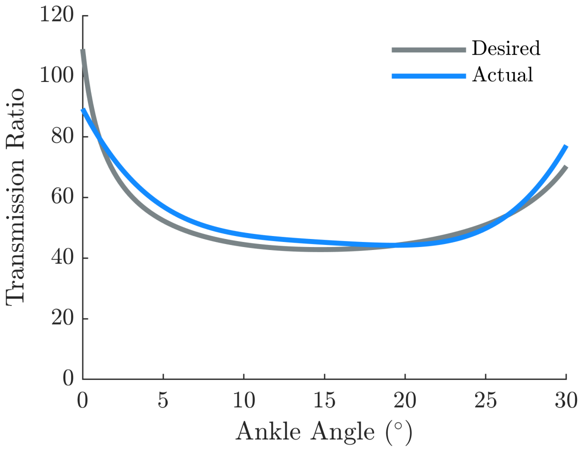

Figure 3.6: Ankle transmission ratio throughout the range of motion.

deflection of 15°. At maximum deflection, the peak von Mises stress in the spring is approximately 250 MPa (half of 7075-T6 Aluminum's yield strength). Torque measurement range increases with series stiffness; depending on the number of springs used, the measurable torque range is 25-150 Nm. In contrast, torque measurement accuracy decreases with series stiffness; based on the joint encoder's resolution (0.02°), torque measurement resolution is 0.04-0.22 Nm, depending on the number of springs used.

3.3.1.5 Mechatronics

Given the mechanical requirements in Eqs. 3.1 and 3.2, the brushed DC electromechanical model was used to determine the electrical demands:

$$i_m = \frac{\tau_m}{k_t} \tag{3.3}$$

$$v_m = i_m R_m + k_b \dot{\theta}_m + L_m \frac{di_m}{dt} \tag{3.4}$$

where i_m, v_m, R_m, and L_m are motor current, voltage, phase resistance, and phase inductance, respectively; k_t is the torque constant; and k_b is the back-electromotive force (EMF) constant (equivalent to the magnitude of k_t in SI units). The current and voltage represent the q-axis current and voltage of field oriented control, which enables a convenient analogue of the brushed electromechanical model. Using Eqs. 3.3 and 3.4, we simulated various motor-battery combinations. Ultimately, the current and voltage demands (which are driven by the mechanical requirements) determined the overall mechanical design, power supply, and motor selection.

We considered multiple motors for the OSL, including the 30 mm EC-4pole motor used in the MIT and Vanderbilt knee prostheses (model: 305015, Maxon Motor, Sachseln, Switzerland) and a high-torque, exterior rotor motor (model: U8-16, T-motor, Nanchang, Jiangxi, China) that has shown promising results in other areas of robotics [38, 53, 105, 117, 120, 121]. The T-motor's motor constant k_m—which describes the motor's ability to convert electrical energy to mechanical energy—is approximately 6 times higher than the EC-4pole's motor constant (Table 3.2); that is, the EC-4pole motor loses approximately 36 times more power than the T-motor for a given motor torque (Fig. 3.7). However, since the EC-4pole motors are often coupled with larger transmission ratios, they do not have to produce the same amount of torque as the T-motor. Therefore, we simulated the T-motor with the OSL knee's transmission ratio and the EC-4pole motor with the MIT and Vanderbilt knees' transmission ratios to estimate the motors' electrical power losses within a prosthesis. After accounting for transmission ratio, the EC-4pole motor loses approximately 3-4 times more power to heat for a given knee torque, when compared to the T-motor (Fig. 3.7).

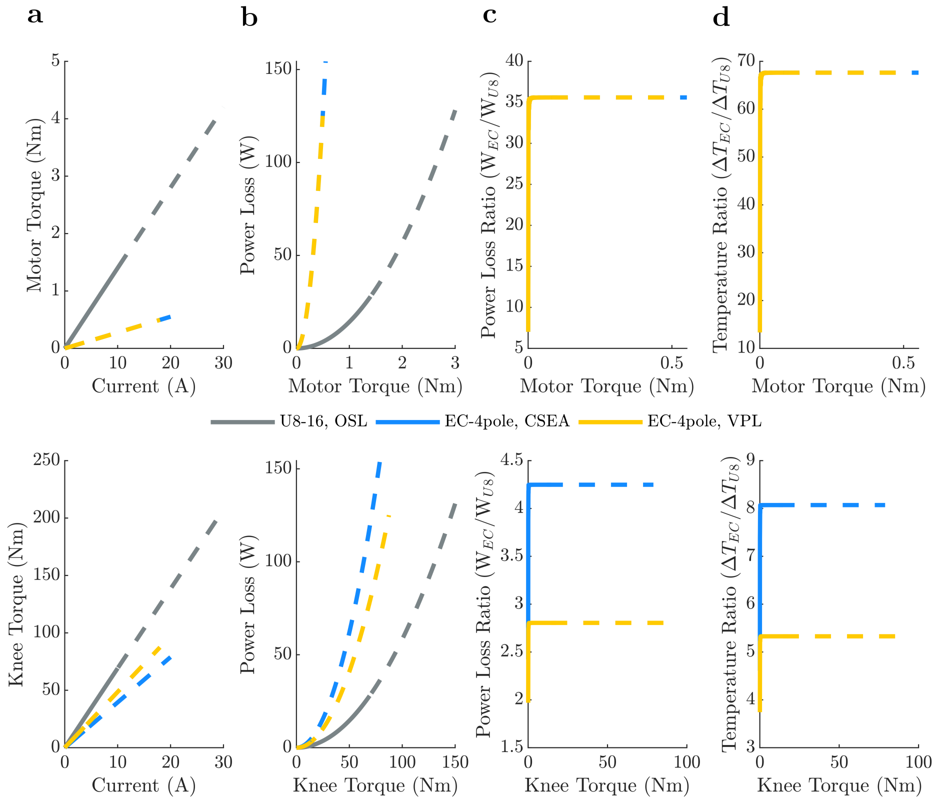

Figure 3.7: Motor and prosthesis efficiency comparison. Comparison of the (top) T-motor and Maxon motor used in the MIT Clutchable Series-Elastic Actuator (CSEA) and Vanderbilt Powered Leg (VPL), and of the (bottom) motors coupled to the transmission ratio used in their respective prostheses [38, 53]. **a,** Torque-current relationship in the continuous (solid) and peak (dashed) current regions. **b,** Electrical power loss (i^2R) as a function of torque, assuming zero angular velocity. **c,** Ratio of the EC-4pole motor's power loss to the U8-16 motor's power loss. **d,** Ratio of the EC-4pole motor's temperature increase to the U8-16 motor's temperature increase.

3.3.1.6 Housing

The OSL housing features a clamshell-style design, in which two halves are fastened together to enclose the prosthesis components (Fig. 3.1). The clamshell housings—machined from 7075-T6 Aluminum—serve multiple purposes: they simplify the assembly process, reduce pinch points, locate the shafts for the timing belt pulleys, and provide structural support for the OSL. The housings incorporate a system to properly tension the belt stages; appropriate belt tensioning ensures that the transmission achieves maximum torque capacity and prevents tooth jump under load. The housings also include mechanical hard stops to ensure that the OSL remains within a biomechanically-appropriate range of motion. All moving transmission components—except for the knee's proximal pyramid and the ankle's foot—are completely contained within the housing, preventing user injury and protecting the transmission from dirt and debris during testing in outdoor environments. The motors mount to the outside of the housings, allowing for convenient assembly, removal, and troubleshooting. Finally, the housings include space for batteries and electronics, creating a self-contained, portable prosthesis.

3.3.1.7 Embedded System

The OSL's embedded system integrates the motor with a commercial version of the Flexible, Scalable Electronics Architecture (FlexSEA)—an open-source motor controller—in a compact, reliable platform [122,123] (Fig. 3.1). The embedded system implements low-level motor control and field oriented control commutation; closes the feedback loops in the position, velocity, current, and impedance controllers; and facilitates communication between the motor controller and external computers/sensors, using most common communication protocols.

To control overall prosthesis behavior, researchers provide control commands (*e.g.*, desired position, desired current, controller gains, *etc.*) using their preferred hardware system (*e.g.*, microcontroller, laptop computer) and an open-source Python or MATLAB interface (Fig. 3.8). A graphical user interface (GUI) is also available to quickly test the system, tune controllers, and display and save sensor data.

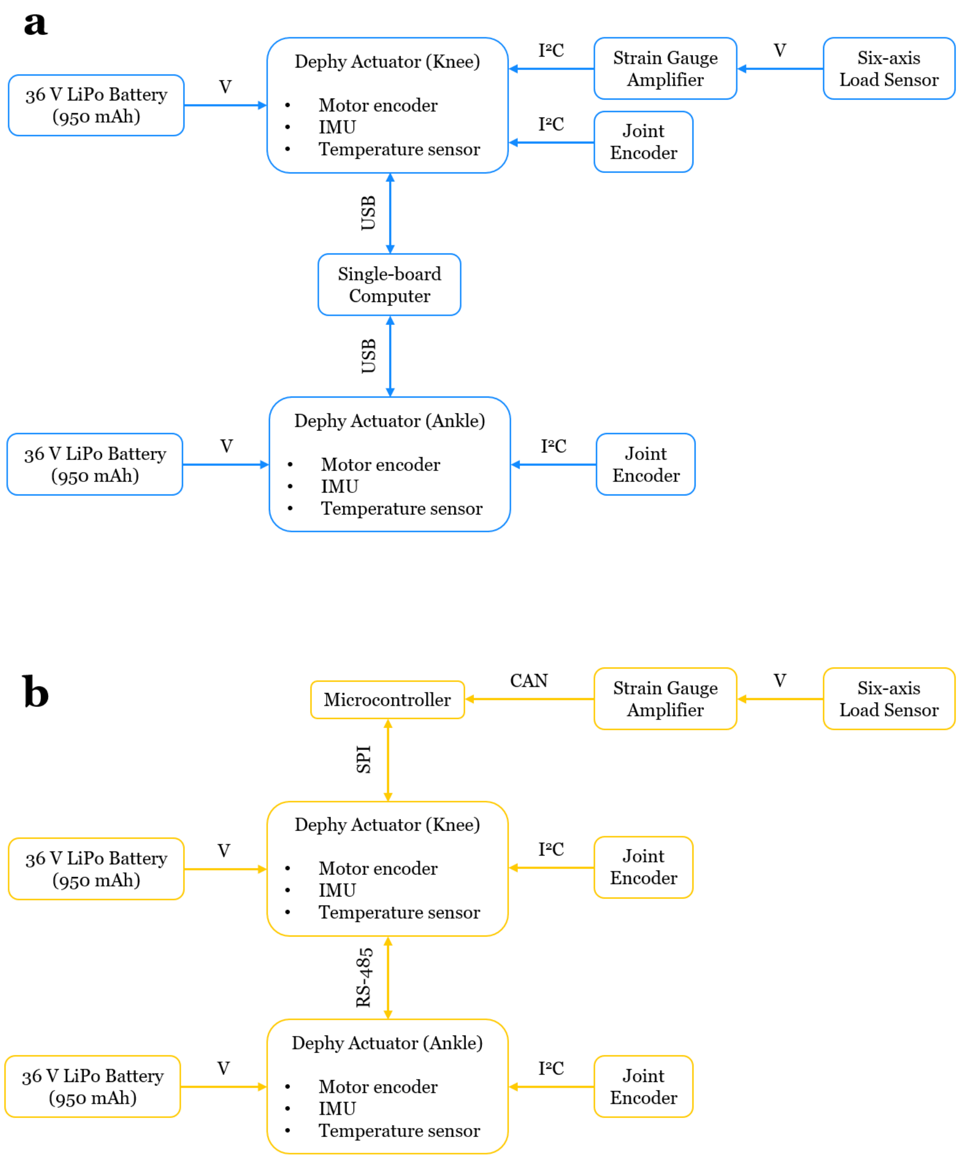

Figure 3.8: Two possible embedded system configurations. High-level overview of electronics, sensors, and power supplies, along with the type of communication between components. **a,** The actuators are connected in parallel with a single-board computer (Raspberry Pi) via USB; this configuration was used for the benchtop testing, with a single motor. This is the recommended configuration because it does not require knowledge of specialized communication protocols; instead, the embedded system handles the I^{2}C and USB communications for the user. **b,** The actuators are connected in series with a microcontroller, and the load sensor communicates with the microcontroller via Controller Area Network (CAN) bus; this configuration was used for the clinical testing.

The OSL includes the following sensors: winding and bus electrical states, temperature, nine-axis inertial measurement unit (IMU), a 14-bit motor encoder, and a 14-bit joint encoder (Table 3.1). An optional six-axis load cell can also be mounted to either the knee's distal or the ankle's proximal pyramid adaptor (Fig. 3.1). Finally, the embedded system includes a number of features to improve safety and reduce user error, including: over- and under-voltage protection, over-current protection with programmable and physical fuses, and electrostatic discharge protection on the inputs and outputs.

3.3.2 Benchtop Testing

We performed several benchtop tests to quantify the OSL's performance in both the time and frequency domains. We characterized closed-loop position and current controller performance, open-loop torque controller performance, and tested the thermal response of the motor given a constant current input. In these tests, and the dissertation as a whole, we report the q-axis current, which is analogous to the DC current in the standard brushed electromechanical model [124].

A testing rig mechanically grounded the knee and ankle—and provided a reaction torque—during the current control tests; during the position control tests, the joints were free to rotate (Fig. 3.9). For these benchtop tests, we used a single-board computer (Table 3.1) to send the desired current and position trajectories (via USB at approximately 750 Hz) to the Dephy actuator, which subsequently performed low-level feedback control (Fig. 3.8). We tested the knee and ankle separately, and did not test with series elasticity.

We quantified the OSL's ability to track desired position and current commands by conducting step response tests (Fig. 3.10). We commanded motor encoder steps corresponding to 5°, 10°, and 15° steps at the joint, starting from the midpoint of the range of motion; we also commanded current steps of 2 A, 4 A, and 6 A (peak phase current), corresponding to 0.8 A, 1.5 A, and 2.3 A of q-axis current, respectively. We performed 5 trials for each condition.

To quantify the range of frequencies in which the OSL can track position and current commands, we performed frequency response tests (Fig. 3.10). The position trajectories were Gaussian

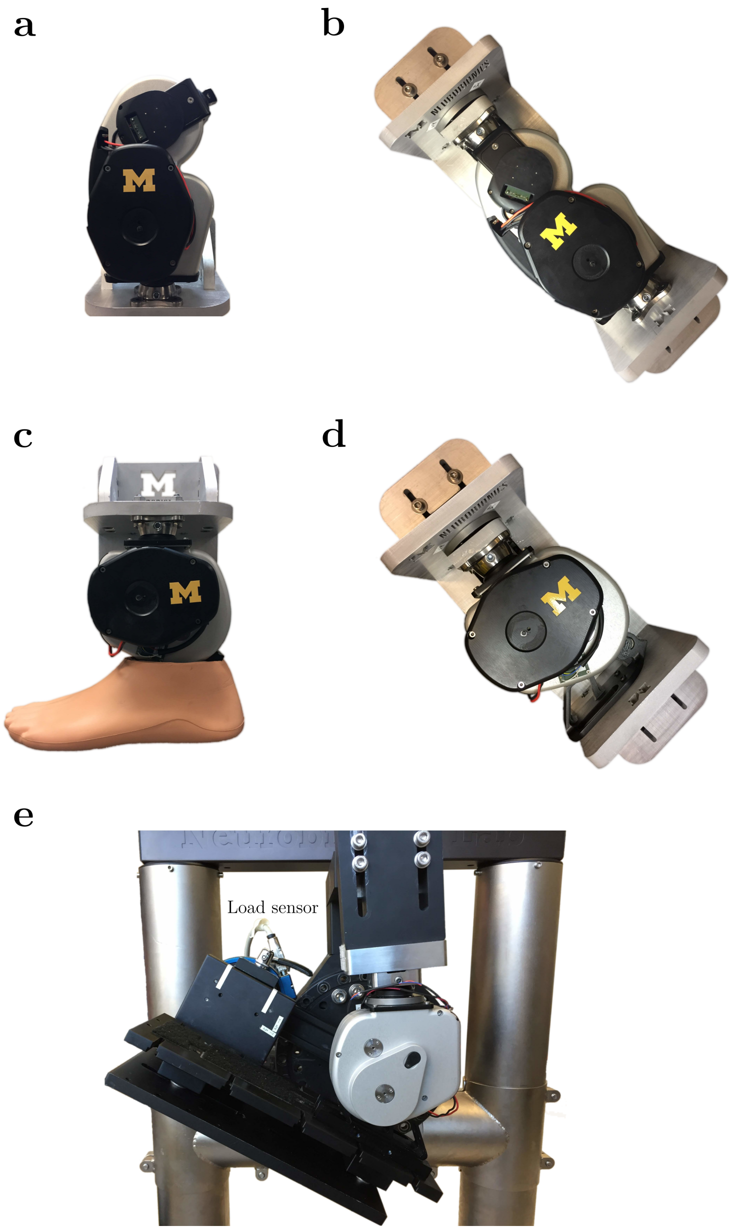

Figure 3.9: Benchtop testing setup. a, Knee closed-loop position controller testing; knee joint is free to rotate. **b,** Knee closed-loop current controller and thermal response testing. **c,** Ankle closed-loop position controller testing; ankle joint is free to rotate. **d,** Ankle closed-loop current controller testing. **e,** Ankle open-loop torque controller testing. The dynamometer either locked (static trials) or rotated (dynamic trials) the ankle joint while the prosthesis commanded open-loop torque values. The external load sensor was used to measure output torque.

white noise signals—3rd order, 40 Hz low-pass filtered—scaled to ± 5°, 10°, and 15° amplitudes, and centered at the midpoint of the range of motion; the current trajectories were also Gaussian

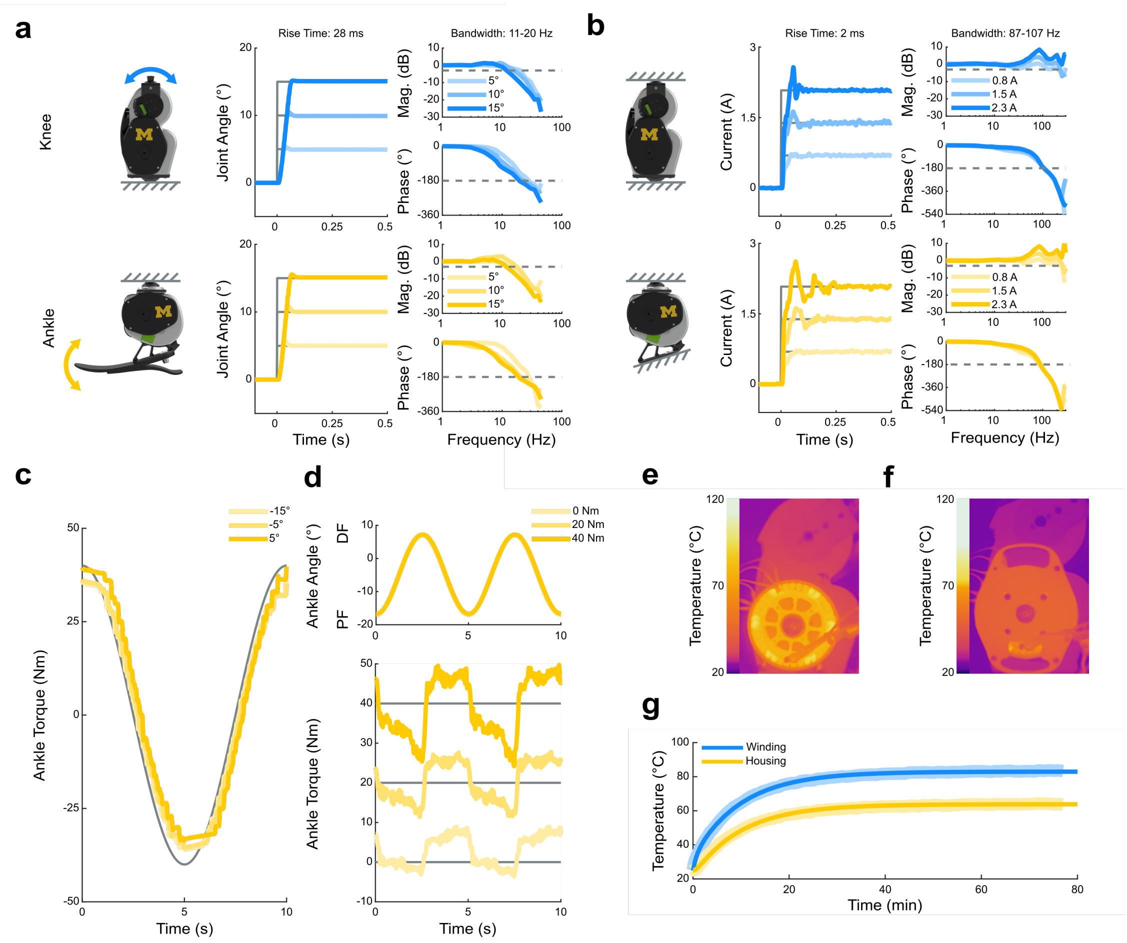

Figure 3.10: Electromechanical and thermal benchtop testing. a, Test setup, step response, and frequency response for the closed-loop position control system. The output of each joint was free to rotate for these tests. The dashed lines represents the thresholds used to calculate bandwidth. **b,** Test setup, step response, and frequency response for the closed-loop current control system. The output of each joint was locked in place for these tests. **c,** Open-loop torque tracking of a sinusoidal torque trajectory while the ankle prosthesis was mechanically grounded. **d,** Open-loop torque tracking of a constant torque trajectory while the ankle prosthesis was sinusoidally rotated through its range of motion. **e,** Thermal image of the knee prosthesis, without the embedded system mounting plate, after providing the motor with a constant current of 8 A for 70 minutes. The windings reach a steady-state temperature of 92 °C. **f,** Thermal image of the knee prosthesis, with the mounting plate, after providing the motor with a constant current of 8 A for 70 minutes. The windings reach a steady-state temperature of 83 °C. **g,** Simulated (bold) and experimental (shaded) thermal response of the motor to a constant current of 8 A. Series elasticity was not included in these tests.

white noise signals—3rd order, 200 Hz low-pass filtered—scaled to ± 0.8 A, 1.5 A, and 2.3 A amplitudes, and centered at 0 A. The position trials lasted for 15 s whereas the current trials lasted for 60 s. We conducted 5 trials for each condition and constructed Bode plots using Blackman-Tukey spectral analysis, where the auto-spectrum and cross-spectrum are divided in the frequency domain [125]. Using the Bode plots, we calculated bandwidth as the frequency in which the magnitude crossed -3 dB.

We estimated the ankle's open-loop torque controller in both static and dynamic conditions by rigidly mounting the ankle prosthesis to the Neurobionics Lab Rotary Dynamometer (Fig. 3.9). The dynamometer includes a frame-mounted motor (model: BSM90N-3150AF, Baldor, Fort Smith, AR, USA) and a six-axis load cell (model: 45E15A4, JR3, Inc., Woodland, CA, USA). In the static condition, the dynamometer locked the ankle at angles of -15°, -5°, and 5°, where negative values correspond to plantarflexion (PF) and positive values correspond to dorsiflexion (DF); the ankle prosthesis—without torque feedback—tracked a ±40 Nm, 0.1 Hz sinusoidal torque trajectory. In the dynamic condition, the dynamometer rotated the ankle through a 24°, 0.2 Hz sinusoidal angle trajectory; while being rotated, the ankle prosthesis—without torque feedback—tracked constant torque values between 0-40 Nm. Each trial lasted 10 s, and we conducted 3 trials in each condition.

To test the thermal behavior of the OSL we supplied the motor with a constant current of 8 A (6.5 A q-axis current) across two winding leads for 70 minutes using a power supply (model: 1688B, B&K Precision Corp., Yorba Linda, CA, USA), and measured the resulting change in winding and housing temperature using a thermal imaging camera (model: ONE Pro LT, FLIR Systems, Inc., Wilsonville, OR, USA). The T-motor is delta wound, meaning when current is supplied between two leads, one phase has twice the current of the other two phases (Fig. 3.10). Consequently, we estimated winding temperature as the weighted average of the more and less powered windings. We subsequently modeled the thermal dynamics of the motor by simulating the equivalent electrical circuit (Fig. 3.11) in Simulink [56, 126]. In this model, temperature and heat flow are analogous to voltage and current, respectively; heat flow is equivalent to the thermal power lost (P_{loss}) through the electrical resistance of the motor, which is a function of temperature:

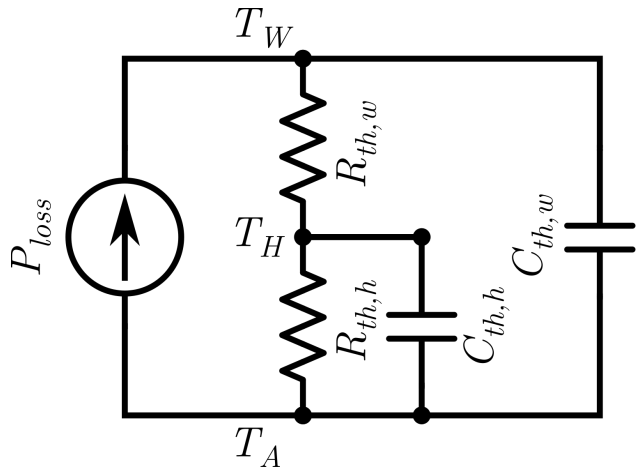

Figure 3.11: Equivalent electrical circuit used to model the thermal dynamics of the motor. We used the measured temperature data to calculate the motor's thermal resistances and capacitances.

$$P_{loss} = i_m^2 R_m = i_m^2 R_{m,A}(1 + \alpha_{Cu}(T_w - T_A)) \tag{3.5}$$

where $R_{m,A}$ is the motor electrical resistance at ambient (room) temperature, α_{Cu} is copper's temperature coefficient of resistance, and T_w and T_A are winding and ambient temperature, respectively. We used the measured temperature data to calculate the motor's optimal thermal parameters: winding-housing thermal resistance and capacitance ($R_{th,w}$ and $C_{th,w}$), as well as housing-ambient thermal resistance and capacitance ($R_{th,h}$ and $C_{th,h}$).

Although we did not use series elasticity in the benchtop and amputee experiments, we did characterize the stiffness of the elastic elements when included inside the knee output pulley (Fig. 3.1). We mounted the knee onto a six-axis load sensor (model: 45E15A4, JR3, Inc., Woodland, CA, USA) and manually rotated the knee from 0° to 15° and back. We performed 5 trials each for the following configurations: 0, 1, 2, 3, 4, 5, and 6 springs. We also locked the input shaft to ensure that the knee's rotation was due to spring deflection instead of belt drive motion.

3.3.3 Clinical Testing

To test the OSL's capability to restore gait, and demonstrate real-time impedance control on the hardware platform, we used a previously-developed control approach [45]. We implemented locomotion controllers for standing, level-ground walking, ramp ascent, ramp descent, stair ascent, and stair descent using impedance control; the impedance parameters for each ambulation mode regulated the current to the knee and ankle motors based on the desired torque [127]. The desired motor current was determined by converting the desired joint torque τ_j, into motor current:

$$\tau_j = -k_j(\theta_j - \theta_{0j}) - b_j\dot{\theta}_j \tag{3.6}$$

where j corresponds to the knee or ankle joint, θ is joint angle (positive values represent knee extension and ankle DF), and $\dot{\theta}$ is joint angular velocity. The three tunable impedance parameters for each joint were virtual stiffness k, virtual equilibrium angle θ_0, and virtual damping coefficient b (Fig. 3.12). The desired joint torque was converted to desired motor torque using the transmission ratio, and desired motor current was calculated using equation 3.3.

Within our tuning process, a finite state-machine divided all gait activities (except for standing) into four sub-phases: early-to-mid stance, late stance, swing flexion, and swing extension; simple logic based on mechanical sensors within the prosthesis (*e.g.*, joint encoders, load sensor, *etc.*) enabled progression through the state-machine. The standing mode controller only used two states; the first was relatively stiff to support the weight of the body when the prosthesis was in contact with the ground, and the second allowed the leg to swing freely when it was not in contact with the ground.

For 60% of the states (across all ambulation modes), we held impedance parameters at tuned, but constant values; for the remaining 40% of the states, we modulated the impedance parameters according to one of the following control laws: (1) basing impedance parameters on values from the previous state; (2) mimicking biological joint responses (*i.e.*, modifying joint impedance as a function of ankle angle); (3) modifying joint impedance as a function of knee angle; or allowing

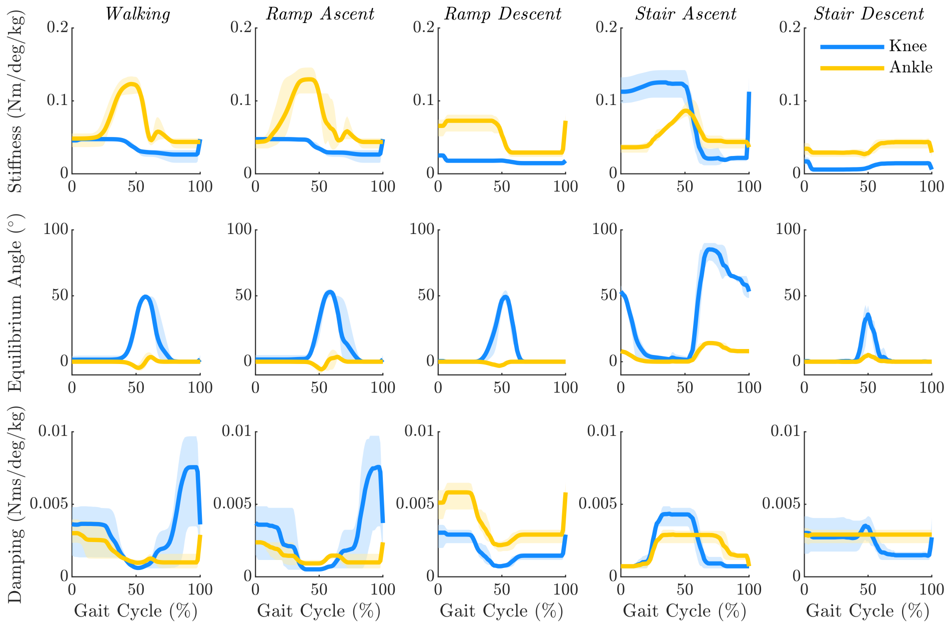

Figure 3.12: Tuned impedance parameters across five ambulation modes. Mean (bold) and range (shaded) of virtual stiffness, equilibrium angle, and damping coefficient profiles for 3 subjects, tuned for level ground, ramp ascent/descent, and stair ascent/descent.

users to control the rate of power generation/dissipation (*i.e.*, modifying joint impedance as a function of (4) decreasing or (5) increasing prosthesis load). We discuss each of these approaches in detail in our previous work [45]; these control strategies were used to reduce the number of independent parameters required to tune the prosthesis and improve transitions between different types of activities. This control scheme created an overall system response that allowed each subject to walk safely, comfortably, and confidently. For these clinical tests, we used an embedded microcontroller (Table 3.1) to perform high-level control (at approximately 40 Hz) and send the desired current trajectories to the embedded system, which subsequently performed low-level feedback control; the microcontroller and embedded system communicated via SPI (Fig. 3.8).

During the first visit, a certified prosthetist fitted and aligned the OSL to each subject, ensuring suspension, comfort, and stability on the leg during standing. Next, subjects walked within a set of parallel bars while we tuned the impedance parameters for level-ground walking. Subjects subsequently ambulated up/down stairs, and up/down ramps while we tuned the impedance parameters

Table 3.4: Clinical ambulation goals and their performance metrics.

Goal	Metric	Walking	Ramp Ascent	Ramp Descent	Stair Ascent	Stair Descent
Controlled weight acceptance	Knee extended at heel strike (°)	0.3 [-0.9][a]	0.1 [33.7]	1.1 [8.9]	29.0 [50.1]	2.6 [2.3]
	Ankle early stance PF (°)	8.2 [3.8]	5.9 [0]	8.1 [3.3]	13.0 [15.2]	-
Ambulation at desired speed	Ankle push-off time (%)	61.3 [64.0]	62.3 [66.0]	60.7 [66.0]	60.7 [64.0]	74.0 [74.0]
	Ankle push-off torque (Nm/kg)	1.2 [1.3]	1.5 [1.3]	1.0 [1.3]	0.3 [1.4]	0.3 [1.2]
	Knee swing extension time (%)	67.7 [72.0]	70.0 [77.0]	57.3 [69.0]	84.7 [81.0]	52.3 [63.0]
Appropriate amount of swing clearance	Knee swing flexion (°)	52.5 [55.0]	53.7 [61.7]	63.3 [71.8]	71.9 [92.5]	70.5 [88.3]
	Ankle swing DF (°)	12.0 [22.6]	12.6 [25.2]	1.9 [6.9]	10.1 [33.6]	-
Minimal upper limb support	Peak vertical GRF (%)	116.4 [114.2]	119.7 [111.5]	111.5 [133.4]	109.8 [107.4]	85.4 [126.2]
Reciprocal gait pattern	Visual inspection	-	Yes	Yes	Yes	Yes

- Not applicable/available
a Able-bodied data in brackets

using a combination of visual inspection and feedback from the prosthetist, a physical therapist, and the subjects (Fig. 3.12); tuning continued until a set of clinical ambulation goals—including appropriate weight acceptance, plantarflexion, knee power, swing clearance, step length, walking speed, and minimal upper extremity support (Table 3.4)—were met, and the prosthetist, therapist, and subjects were satisfied with the OSL's performance [45]. This visit lasted approximately 2-3 hours.

During the second visit, subjects performed a series of ambulation circuits that included all of the following activities: standing, walking, stair ascent, stair descent, ramp ascent, and ramp descent, as described in prior work [46, 71]. The circuit included seamless transitions between activities, achieved using a mobile phone that communicated with the embedded controller [44]. Seamless transitions within the experiment included: standing to walking, walking to standing, walking/standing to stairs, stairs to walking/standing, walking to ramps, and ramps to walking. We instructed subjects to ambulate at a comfortable speed and recorded data using the OSL's on-board sensors. This visit also lasted approximately 2-3 hours.

3.4 Results

3.4.1 Design

In addition to this chapter, we have developed a companion website (`www.opensourceleg.com`) with detailed, step-by-step guides to order parts, videos to build and test the hardware, and code to begin walking with the OSL using a preliminary control system (see Discussion for more details).

To ensure that the OSL is accessible by researchers from diverse backgrounds (*e.g.*, controls, biomechanics, clinical, *etc.*), we abided by the following design principles:

1. *Simple*: the OSL can be assembled, controlled, and maintained with moderate ‘hands-on’ skills. To this end, we reduced the number of components and suppliers; the vast majority of parts are machined from a single supplier, without dependencies on other precision machine components or mechanisms (Appendix A).
2. *Portable*: the OSL weighs less than the biological counterpart, and each joint has on-board batteries, sensing, and control, facilitating research outside of the laboratory.
3. *Scalable*: the knee and ankle joints can operate independently, enabling research with both above- and below-knee amputees.
4. *Customizable*: the OSL includes several design and control features that can be customized, depending on the specific requirements of the researcher, including the knee’s series elastic element, foot type, and inclusion of a load cell, among other options.
5. *Economical*: the OSL costs approximately \$10,000-\$30,000 in prototype quantities, depending on degrees of freedom and sensing options, given today’s manufacturing and material costs. In contrast, commercially available powered prostheses—such as the Ottobock emPOWER Ankle and the Ossur POWER KNEE—cost up to \$100,000 each, without access to control modifications.

The intent of our design was to provide the highest performance, while facilitating ease-of-use, as well as reducing mass and cost. We implemented brushless electric motors from the drone industry because their efficiency and torque density permitted lower transmission ratios, enabling the use of timing belt drive transmissions, instead of more expensive or complex alternatives that can have substantial product lead times and cost (*e.g.*, harmonic drives, roller screw transmissions) (Fig. 3.1). Additionally, the OSL takes advantage of an open-source motor controller and embedded system, allowing researchers to focus on mid- and high-level control strategies, rather than developing low-level controllers and communication protocols. The OSL actuators have built-in position, current, and impedance controllers, along with an IMU, and a motor encoder. Together with Python and Matlab interfaces, the actuators allow researchers to quickly begin control investigations with the OSL.

Portability and scalability are important characteristics enabling the OSL to be tested in various environments and by users with different levels of amputation. The OSL's low mass and compact power supply enable research beyond typical lab-based treadmill tests. The OSL is shorter than the 4th percentile and lighter than the 16th percentile male shank and foot [16, 128]. The housings completely encompass the transmissions, batteries, and most of the electronics, reducing the risk of contamination or injury. Finally, the knee and ankle have independent embedded control hardware and batteries, allowing researchers to work with either the entire leg or a single joint. The portability and scalability of the OSL provide the capability to investigate control strategies with both above- and below-knee amputees in indoor and outdoor environments.

Customization options enable the OSL to be suited to the individual uses of each researcher. The knee functions either as a SEA or rigid actuator, and the stiffness of the series elasticity can be selected by the researcher using custom 100 Nm/rad spring disks (Fig. 3.1). The springs fit inside of the belt drive's output pulley; therefore, the SEA configuration does not change the OSL's volume. Although the ankle does not include a specific series elastic element, it can integrate with either a compliant commercial foot or a rigid flat foot. The ankle has a maximum range of motion of 30°. In the default OSL configuration, this corresponds to 20° of PF and 10° of DF.

By redesigning one component in the ankle, the amount of PF and DF can be modified, within the 30° range; for example, we have also made a version with 15° PF and 15° DF. The ability to change the ankle's operating region provides researchers with additional customization based on their specific needs. In addition to hardware customization, researchers have multiple options for high-level control implementation. For example, we used two different embedded computers (Raspberry Pi 3 vs. Texas Instruments DM3730) and communication protocols (USB vs. SPI) to control the motors in the benchtop and clinical tests (Fig. 3.8, Fig. 3.8). The OSL also functions with other high-level control schemes (*e.g.*, MATLAB/Simulink, Robot Operating System, *etc.*) and external sensors (*e.g.*, EMG, additional IMUs, *etc.*).

3.4.2 Benchtop Testing

To facilitate the success of future researchers who may use the OSL, we completed electromechanical and thermal performance testing using a benchtop setup. We tested low-level closed-loop position and current control, open-loop torque control, and also tracked the OSL's temperature increase during 70 minutes of continuous operation. Motor current is often used in prostheses to estimate output torque, and the current controller's performance is critical for open-loop torque and impedance control. The knee joint's series elasticity was not included in these tests; that is, the knee operated as a rigid actuator.

We characterized the performance of the two primary closed-loop controllers (position and current control) on the OSL. A step response test was used to quantify the OSL's ability to track changes in desired position and current reference values; frequency response tests estimated the bandwidth—the range of input frequencies that the OSL can track with high fidelity—of the low-level position and current controllers. The position and current controllers exhibit fast and accurate step responses, with bandwidths of 10.7-20.2 Hz and 86.8-107.4 Hz, respectively (Fig. 3.10, Table 3.2). Although we did not quantify torque bandwidth, we expect it to be much lower than the current control bandwidth, due to the dynamics of the transmission. Further results on the closed-loop controller performance can be found in our previous work [1].

Measuring torque is challenging in wearable robots because torque sensors with sufficient capacity can be large and heavy. Many groups instead use motor current as a substitute for output torque, resulting in an open-loop torque controller [38,45]. We quantified open-loop torque control performance using the ankle prosthesis; that is, these tests were accomplished without torque feedback. In the static condition, the ankle tracked a ±40 Nm sinusoidal torque trajectory while locked in placed (Fig. 3.10). In the dynamic condition, the ankle was sinusoidally rotated through most of its range of motion (16° PF to 8° DF) while tracking constant torques of 0, 20, and 40 Nm (Fig. 3.10). The root-mean-square error (RMSE) for torque tracking across the static and dynamic trials ranged from 4.4-7.4 Nm.

The heat generated by an electric motor ultimately limits the torque it can generate, and how long it will operate safely. Therefore, we quantified the thermal response and developed a thermal model of the motor and OSL to a current step input of 8 A (Fig. 3.10). Starting from an ambient temperature of 25 °C, the motor windings reached a steady-state temperature of 92°C; after adding an additional housing (mounting plate for the embedded system), the windings and housing reached steady-state temperatures of 83 °C and 64 °C, respectively. That is, the embedded system—which behaves as a heatsink—improved the thermal response by 16%. Using this data, we developed a thermal simulation, which predicts that the motor can operate at its continuous (10 A) and peak (30 A) current limits—corresponding to approximately 50 Nm and 150 Nm of joint torque (Table 3.2)—for 513 s and 17 s, respectively, before reaching potentially unsafe temperatures (set at 125 °C).

3.4.3 Clinical Testing

The OSL was tested clinically to highlight its kinematic and kinetic capabilities in a real-world setting, demonstrate patients successfully ambulating with it, and provide biomechanical and control data to serve as a benchmark for future researchers. We conducted clinical testing with three individuals with unilateral transfemoral (above-knee) amputations (Table 3.5, Fig. 3.13, Appendix B) who did not have prior experience with the OSL, but did have prior experience ambulating with

Table 3.5: Subject characteristics.

Subject	Gender	Age (years)	Time Post-amputation (years)	Etiology	Weight (kg)	Height (m)	Mobility Level	Prescribed Knee Prosthesis
TF1	F	51	29	Traumatic	61.7	1.65	K3	Rheo
TF2	M	33	2	Sarcoma	63.1	1.77	K3	Genium
TF3	M	70	44	Traumatic	86.2	1.75	K3	C-Leg

other powered leg prostheses [38]. We implemented an impedance-based control system to enable different locomotion activities within a rehabilitation hospital [45]. Each subject provided written informed consent, approved by the Northwestern University Institutional Review Board.

Figure 3.13: Subjects with a transfemoral amputation ambulating with the OSL.

During ambulation, the OSL produced the desired joint torques (based on motor current); the RMSE between desired and actual current ranged from 0.5-2.9 A per step, with peak currents ranging from 5-25 A. The subjects successfully ambulated through a circuit that included level ground walking, ramp ascent/descent, and stair ascent/descent (Fig. 3.14). We quantified clinical success with a set of clinically relevant ambulation goals, developed by a physical therapist [45]; these goals were evaluated using the timing and magnitude of different kinematic and kinetic variables, along with visual inspection (Table 3.4). During level ground and ramp ambulation, the OSL achieved heel strike with an extended knee (0.5 ± 0.7°) and exhibited 7.4 ± 2.0° of controlled PF during early stance. The timings of push-off and knee extension were within 3.0 ± 2.7% and 6.0 ± 6.2% of able-bodied timing, respectively; additionally, the PF torque at push-off was 92.0 ± 23.4% of able-bodied torque. To enable swing clearance, the OSL produced 85.6 ± 7.8% of able-bodied knee flexion and 14.3 ± 10.1° of DF. Across all ambulation modes, the peak vertical ground reaction force (GRF) on the prosthetic side was 92.5 ± 17.2% of able-bodied GRF. Finally, subjects successfully ascended and descended stars with a reciprocal gait pattern. Subjectively, subjects noted during ambulation that the leg felt supportive, responsive, and smooth.

3.5 Discussion

This study describes the design, implementation, and characterization of an open-source robotic knee-ankle prosthesis, and demonstrates control with three subjects with transfemoral amputations successfully ambulating with the leg on level ground, ramps, and stairs. The OSL is intended to be a simple, portable, scalable, customizable, and economical hardware platform for development and evaluation of control systems, both in and out of the laboratory (Fig. 3.1, Appendices A and B). Through the OSL, we hope to reduce the amount of time and resources needed to pursue prosthetics research, enable fair comparison between different control systems, and provide a long-term, multi-study hardware platform to accelerate progress in the field of powered prosthetic legs.

3.5.1 Facilitating Controls Research

To simplify usage and accelerate adoption of the OSL, we developed a companion website: `www.opensourceleg.com`, a powerful resource we hope will be a standard for open-source robotic hardware dissemination. The website includes solid model files, a bill of materials, links to sup-

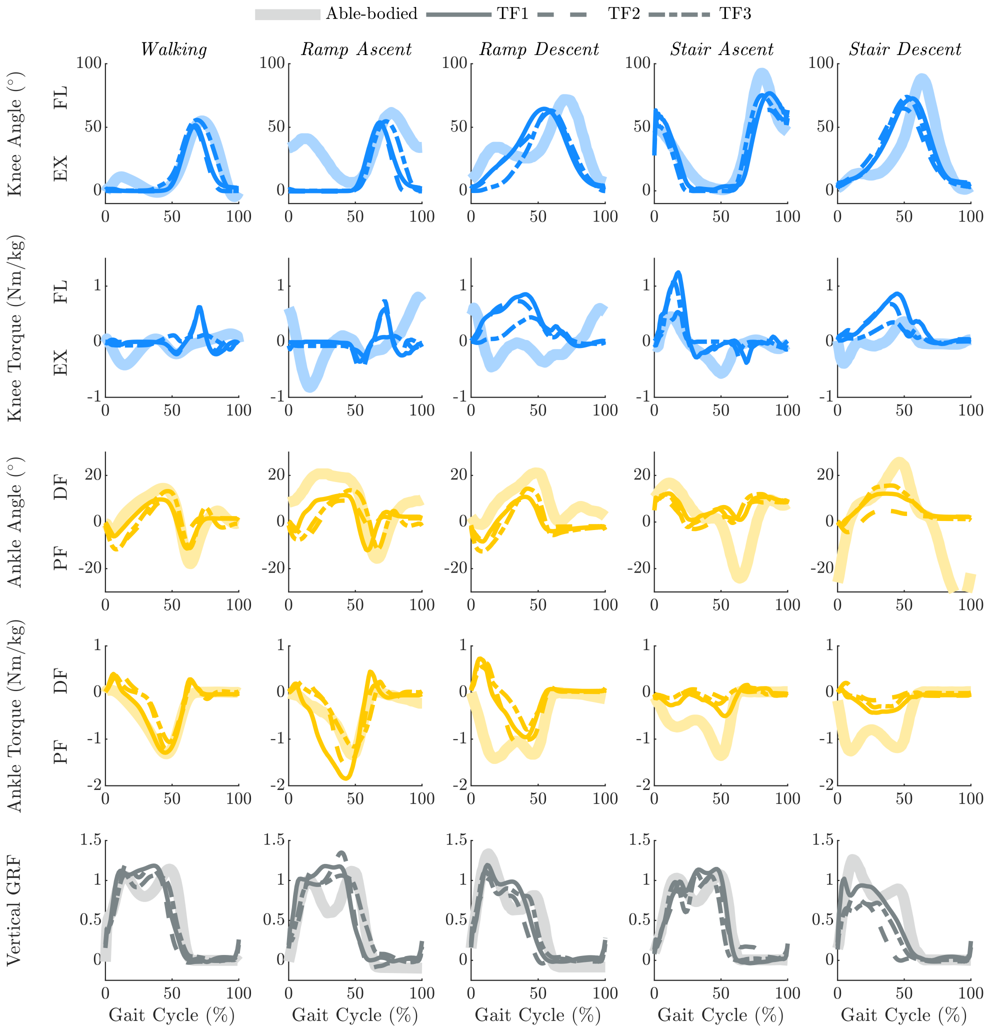

Figure 3.14: OSL kinematics and kinetics across five ambulation modes. Mean user and able-bodied joint angles, moments, and vertical GRFs for level ground, ramp ascent/descent, and stair ascent/descent. Joint torques are normalized by subject mass and GRF is normalized by subject weight.

pliers, control system code, instructional guides, videos on assembly/disassembly, and any other relevant information to improve the usability of the OSL. The content on the website provides the necessary documentation and videos to guide new users through the steps required to 1) purchase the required machined and off-the-shelf components, 2) assemble/disassemble the OSL, 3) connect and communicate with external sensors, 4) perform benchtop controller experiments, and 5) begin walking on level-ground with a simple impedance controller. Furthermore, we have developed an online forum to allow researchers to post questions, results, or independently developed modifications. Together, these tools will help researchers use the OSL and encourage a more collaborative community focused on transforming amputee quality of life.

One of the greatest challenges to performing research with powered prostheses is developing reliable and robust mechatronic and embedded systems. We included embedded electronic systems that automatically implement sensing, motor commutation, low-level control, communication with other devices, and safety protocols. By providing a built-in embedded system with the OSL, we are enabling researchers to focus on clinical testing and development of higher level control strategies instead of low-level embedded systems engineering and mechatronics. As an open-source tool, the OSL is also capable of integrating with other sensors and peripheral systems. For example, some users may be interested in adding EMG (to measure muscle activity), force-sensitive resistors (pressure on the residual limb), or cameras (environment classification) to the OSL; others may be interested in providing real-time stimulation and sensory feedback directly to the user [115]. Although we do not currently use these systems with the OSL, they can be integrated quickly if they are compatible with Python or MATLAB, using the open-source embedded system; more advanced systems may require further expertise. Researchers are encouraged to share their sensor systems and solutions on the OSL website, to help accelerate other groups.

Through this chapter, we are also providing a baseline dataset for future controls research. This dataset includes prosthetic leg kinematics and kinetics for level-ground walking, ramp ascent/descent, and stair ascent/descent, along with the impedance control parameters used. These data may serve as a starting point for researchers to test a clinically meaningful controller, or as a comparison point for novel control systems. Importantly, since this dataset encompasses multiple ambulation modes, it will enable testing in unstructured, uncontrolled environments much faster. The data will be hosted on the project's website (`www.opensourceleg.com`).

3.5.2 Design Benchmarks and Limitations

Prosthesis mass and size play a critical role in the success of these systems. Heavy prostheses require higher metabolic expenditure from the user [99]; this effect increases as the mass moves distally (*i.e.*, towards the ankle). Additionally, as the build height of a prosthesis increases, fewer users can wear the leg; that is, if the prosthesis is too long, it will not fit below the residual limb. Therefore, it is critical to design lightweight and short prostheses. The OSL (4000 g) is lighter than most comparable prostheses (Table 3.2). The minimum build height of the OSL (450 mm) is also comparable to the build height of other prostheses. Finally, the OSL is lighter and shorter than the foot and shank of a 75 kg, 1.7m tall adult (Table 3.2).

A limitation of the OSL is the ankle joint's range of motion (Table 3.2). During most ambulation tasks, the biological ankle remains within 10º of DF and 20º of PF, as in the OSL; however, some subjects require a range of motion of 45-60º during stair descent [17,129]. Many other prosthetic ankles have a range of motion of 45-65º. The OSL ankle's 30º range of motion is limited by the kinematics of the four-bar linkage, and could be improved by decreasing the ankle's transmission ratio or using a different transmission design (Fig. 3.5). However, amputees with passive prostheses can typically only achieve 10-15º during stair descent [130]; therefore, although the OSL ankle does not achieve the full biological range of motion, it provides a substantial improvement over passive prostheses. The OSL knee's range of motion is equal to other prostheses (120º), and is much higher than needed for typical ambulation tasks (70-90º) (Table 3.2).

Transmission ratios determine prosthesis size, electrical demands, efficiency, performance, and other factors. Using the high-torque drone motors, we reduced transmission ratios to 2-5 times lower than comparable prostheses (Table 3.2). The combination of high-torque motors and low transmission ratios enables the OSL to produce peak torques similar to other systems, while demonstrating higher bandwidth. For example, the OSL's position bandwidth is approximately 5 times higher than the bandwidth of the biological knee or ankle; that is, the OSL is capable of recreating the human kinematics and kinetics (Table 3.2). The motors on the OSL have an overall winding-ambient thermal resistance of 3.9 K/W, compared to the 7.6 K/W thermal resistance of motors used in other prostheses [38, 53]. In addition to being 3-4 times more electrically efficient than these prostheses, the OSL's motors produce 5-8 times less heat at steady-state, for a given joint torque (*i.e.*, after accounting for their respective transmission ratios) (Fig. 3.7).

The OSL is capable of locomotion for extended periods using the recommended batteries (36 V/950 mAh). During level ground walking, the knee and ankle operate with an average power consumption of 9.3 W and 11.2 W, respectively, and the electronics operate at approximately 1-2 W. Given the energy in the batteries (34.2 Wh), a user could walk continuously for approximately 2.8 hours, 13.1 km, or 8,750 strides (*i.e.*, 17,500 total steps) on a single charge, assuming consistent power consumption, a walking speed of 1.3 m/s, and cadence of 104 steps/min14. The batteries lasted for the entire duration of our experiments (three hours). On average, lower-limb amputees walk approximately 6,000 steps/day, and healthy able-bodied adults are considered active if they walk at least 10,000 steps/day [131, 132]. Therefore, the OSL batteries have sufficient capacity for lab sessions and, potentially, daily ambulation.

3.5.3 Clinical Testing

All subjects in this study successfully ambulated on level ground, ramps, and stairs using the OSL, with all control parameter trajectories provided for reference (Figs. 3.12, 3.13, 3.14, Appendix B). While walking on level ground and ramps, subjects achieved plantarflexion during early stance, controlled dorsiflexion during mid-stance, and powered push-off in late stance. Subjects successfully descended ramps and stairs with a reciprocal gait pattern by taking advantage of stance-phase knee flexion; during stair ascent with a reciprocal gait, subjects relied primarily on knee extension to propel themselves up and forward.

Across most ambulation modes, joint angle and torque trajectories followed similar timing and amplitude patterns to able-bodied data [17, 129, 133]; however, there are notable differences. For example, subjects did not demonstrate early-stance knee flexion during level ground walking (Fig. 3.14). At heel contact, transfemoral amputees often pull back with their hip extensors to lock their prescribed, passive knee prosthesis into knee extension to prevent buckling and injury from falling;

due to this habit, the subjects overrode the impedance controller's natural dynamics in favor of an extended knee joint. Additionally, subjects relied primarily on the knee to ambulate up and down stairs; the ankle provided little torque and only rotated through approximately 30% of its range of motion.

It is important to note that the OSL is capable of producing early-stance knee flexion and ankle power across all ambulation modes; however, the subjects exhibited compensatory movement based on their daily ambulation strategies with a passive prosthesis. We can overcome these compensatory motions through training (not shown), or by tuning the controller to recreate able-bodied kinematics and kinetics, but that was not the goal of this demonstration. We chose to not train the patients to overcome their compensatory strategies because they needed to return to their daily-use prosthesis after the experiment; we had concerns that such training on the OSL might lead to a fall when they returned to their daily-use device, which did require compensatory strategies. Instead, we tuned the OSL to meet a set of clinical ambulation goals (Table 3.4). Overall, our implementation succeeded in performing similarly to walking with the Vanderbilt Powered Leg using a similar impedance controller [45].

3.6 Summary

In this chapter, we present the design and mechanical, electrical, and thermal evaluation of an open-source robotic knee-ankle prosthesis, and demonstrate subjects utilizing the prosthesis across a range of activities, while providing controller parameters for reference. Future work includes advancement of the embedded systems, implementing the SEA for closed-loop torque control, and development of bio-inspired impedance control policies [84, 134]. We will also produce an open-source version of our high-level controller that runs on a desktop or mobile device, providing researchers with a simple method of manually/automatically switching between ambulation modes and testing in non-steady-state conditions.

Chapter 4

Characterizing Open-loop Control and Efficiency in Wearable Robots

4.1 Abstract

Traditionally, bionic legs and exoskeletons were designed with low-torque, high-speed motors and high transmission ratios; however, recent designs have begun to incorporate high-torque, low-speed, exterior-rotor motors and lower transmission ratios. These motors recently emerged from the drone industry and have the potential to improve the performance—and impact—of wearable and mobile robots. Due to these motors' relative novelty in the field of robotics, there is insufficient characterization of their performance, particularly when coupled to a transmission. In this study, we conducted a series of experiments to quantify and improve the performance of actuators that use high-torque motors and low transmission ratios, including the motor used in the OSL and two actuators being developed for a knee exoskeleton. First, we developed system identification techniques to characterize the output impedance (*i.e.*, stiffness and damping) of these actuators operating in open-loop impedance control; open-loop impedance control is common in bionic systems because measurement of output torque—which is needed for feedback—requires large and heavy sensors or springs. Second, we characterized the actuator-drive efficiency of these devices across various power regimes, and during both positive and negative work. Understanding how efficiency changes across current-voltage conditions informs us how to most efficiently operate these actuators in a wearable robot. Finally, we tested open-loop torque control and characterized

the mechanical efficiency of the actuator transmissions. With these characterization experiments, we can compensate for transmission losses and render more accurate open-loop control. This work motivates the need, and provides a framework, for more thorough characterization of output dynamics in robotic systems with open-loop control strategies.

4.2 Introduction

Wearable robotic leg systems—like bionic exoskeletons and prostheses—have the potential to augment, assist, or restore gait in users. As tools used in ambulation, they should be lightweight, efficient, and portable, providing torque in a safe and comfortable manner. Traditionally, these bionic systems were designed with high-speed, low-torque motors coupled to highly-geared transmissions. Prosthesis transmission ratios have spanned 150-800:1 (Table 3.2) [36,38,53,56,66–68]; similarly, exoskeleton and orthosis transmission ratios have spanned 64-400:1, with higher ratios used to assist patients with paralysis, stroke, and other impairments [30,135–140]. Although many of these devices have successfully assisted users, they have several drawbacks; typically, highly-geared systems are inefficient, complex, large, heavy, loud, and difficult to backdrive.

The drone industry recently expanded motor technology with high-torque, low-speed motors that do not require transmissions (*i.e.*, direct-drive); these exterior-rotor brushless DC (ER-BLDC) motors are useful in autonomous aerial vehicles because they are lighter, quieter, and more efficient than motors with high transmission ratios. Wearable robotic systems and aerial vehicles face similar constraints, so recent bionic systems have begun to incorporate ER-BLDCs with transmission ratios spanning 7-50:1 [1, 2, 49, 50, 141, 142]. Unfortunately, the rapid development and adoption of ER-BLDC motors has not been accompanied with rigorous electromechanical characterization and testing, in part, due to the challenges controlling these motors [122–124]. Recently, our research group performed the first in-depth characterization of these types of motors, which are being used in multiple bionic legs [1, 2, 49, 124]; however, the effects of transmissions on ER-BLDC performance—specifically on efficiency—are not well understood.

A major challenge in wearable robotics—in which ER-BLDC systems may help—is implementing open-loop control. Closed-loop torque and impedance control systems require a torque signal to close the feedback loop; however, torque sensors are generally too large and heavy to include in a wearable robot. Alternatively, some designs incorporate SEAs, which can estimate output torque via a spring's deflection [36, 53, 135, 140]; however, SEAs also add size, mass, and complexity, leading many groups to adopt open-loop impedance control strategies. This is typically achieved with closed-loop control around motor *current*; motor torque is estimated from motor current using the torque constant (k_t) and output torque is subsequently measured using a model of the transmission. In some cases, analysis and characterization is used to build high-fidelity models of the transmission dynamics to estimate output torque [38]; however, most groups simply multiply motor torque by the transmission ratio (and occasionally an efficiency term) to estimate output torque [1, 2, 45]. The low transmission ratios associated with ER-BLDC motors—which use simpler and more efficient transmissions—may enable reliable open-loop impedance control; however, open-loop impedance control has not been investigated in ER-BLDCs.

In this study, we performed a series of experiments to characterize ER-BLDC motors coupled to low transmission ratios, including those currently being used in both prostheses and exoskeletons [1, 2]. We tested a direct-drive ER-BLDC motor, and the same motor coupled to 6:1 and 9:1 planetary gear transmissions. First, we developed a system-identification process to estimate the output impedance rendered by open-loop impedance controllers, and used the estimates to improve the performance of the open-loop impedance controllers. Second, we expanded upon our group's previous work characterizing direct-drive ER-BLDCs [124]; we empirically determined the actuator-drive efficiency—the ability to convert bus (battery) power to mechanical power, and vice versa—for these systems across a range of torque-speed regimes. Finally, we performed open-loop torque step response tests and characterized the transmission efficiency—the ability to convert motor torque to output torque through a transmission—of these actuators in static conditions. Our work highlights the need to characterize the output dynamics of actuators using open-loop control, investigate the efficiencies of wearable robotic systems (particularly in the relevant torque-speed regimes), demonstrates the effects of transmission losses, and proposes system identification methods for accurate characterization of robotic systems under dynamic conditions.

4.3 Methods

4.3.1 Overview

We used two of the same class of high-torque exterior rotor motors—each with a torque constant (k_t) of 0.15 N·m/A—across all experiments (models: U8/U8 Lite KV100, T-motor, Nanchang, Jiangxi, China). These motors were originally developed for drones, and have gained popularity in other areas of robotics [105, 117, 120, 121]; however, since they are relatively new, these motors lack systematic characterization of their specifications and control capabilities [1, 2, 124].

In Experiment 1, we characterized the open-loop output impedance of the standalone U8 motor (direct-drive), along with the U8 Lite motor coupled to 6:1 (model: AK80-6) and 9:1 (model: A80-9) planetary gear transmissions (Table 4.1). These geared actuators were designed for lightweight, mobile robots, and are being considered in a new knee exoskeleton. In Experiment 2, we characterized the actuator-drive efficiency across a variety of power regimes on all these systems. Finally, in Experiment 3, we performed step responses with open-loop torque control and subsequently characterized the transmission efficiencies to estimate transmission losses.

Across all experiments, the actuators were controlled by the FlexSEA, a motor driver and embedded system developed for wearable robotic applications [122, 123]. FlexSEA implements Field Oriented Control commutation for the 21 pole pairs and can operate under closed-loop position, voltage, or current control. FlexSEA also operates under open-loop impedance control (Fig. 4.1);

Table 4.1: Summary of actuators used in each experiment.

Actuator	Transmission Type	Transmission Ratio	Application
U8 KV100	Direct-drive	1:1	Prosthesis
AK80-6	Planetary	6:1	Exoskeleton
A80-9	Planetary	9:1	Exoskeleton

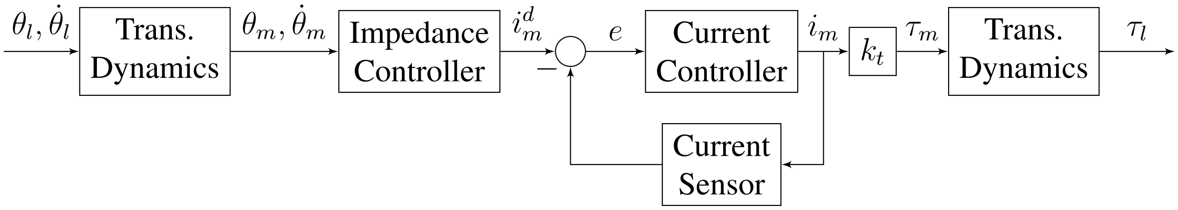

Figure 4.1: Block diagram for the impedance controller. The open-loop impedance controller takes in motor kinematics ($\theta_m, \dot{\theta}_m$)—which are affected by output kinematics ($\theta_l, \dot{\theta}_l$) and the transmission dynamics—and outputs a desired motor current for the closed-loop current controller. Motor current results in motor torque (τ_m), and ultimately in unmeasured output torque (τ_l).

the output of the impedance controller is a desired motor current (i_m^d)—corresponding to a desired motor torque (τ_m)—which subsequently becomes the input to the closed-loop current controller. This is open-loop control because there is no measurement of the actuator's output torque (τ_l) to close the control loop. The impedance and position controllers operate at 1 kHz whereas the current controller operates at 10 kHz. We used a single-board computer (model: Raspberry Pi 3, Raspberry Pi Foundation, Cambridge, UK) to sample data and send the desired control commands—via USB at 250-300 Hz—to the FlexSEA drivers, which subsequently performed low-level control.

4.3.2 Experiment 1: Open-loop Impedance Control

We estimated the actuators' output impedance using a benchtop setup that rigidly coupled two actuators to a torque sensor, such that they rotated together (Fig. 4.2). The direct-drive actuators were tested with a ±5 N·m torque sensor (model: TRS605, FUTEK Advanced Sensor Technology, Inc., Irvine, CA, USA) whereas the geared actuators were tested with a ±50 N·m torque sensor (model: TRS600, FUTEK Advanced Sensor Technology, Inc., Irvine, CA, USA). The driving actuators provided position (angular) perturbations to identify the output stiffness and damping properties of the driven actuators, which operated in open-loop impedance control. In this experiment, each actuator was powered by a separate 36 V battery.

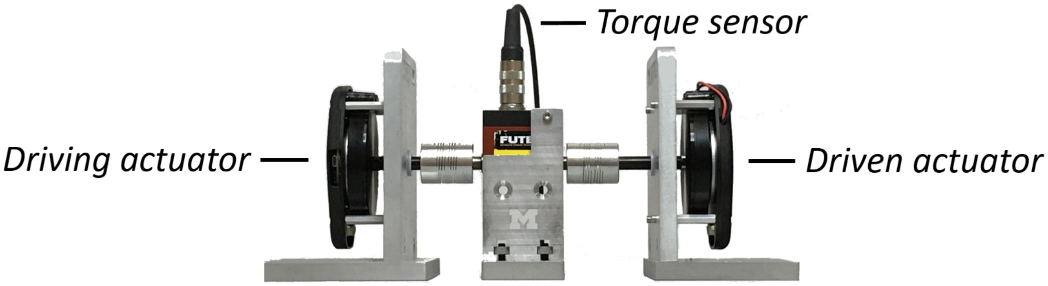

Figure 4.2: Example setup for the actuator characterization experiments. Across Experiments 1 and 2, the driving and driven actuators were rigidly coupled with a torque sensor. In Experiment 1, the driving actuator provided position perturbations while the driven actuator operated in impedance control. In Experiment 2, the driving actuator typically operated in voltage control while the driven actuator operated in current control. In Experiment 3, the driving actuator produced open-loop torque step commands and the driven actuator was replaced with a mechanical ground.

4.3.2.1 Experiment 1A: Direct-drive Impedance

To estimate the U8 motor's output impedance, the driving motor provided Gaussian white noise perturbations—3rd order, 25 Hz low-pass filtered—scaled to ±60° amplitudes while the driven motor commanded desired stiffness (k_d) and damping (b_d) values from: $\{0, 1.5, 3, 4.5, 6\}x10^{-3}$ N·m/deg and $\{0, 1, 2, 3, 4\}x10^{-4}$ N·m·s/deg, respectively. We conducted five 30-second trials for each condition (125 total trials).

4.3.2.2 Experiment 1B: Exoskeleton Actuator Impedance

To estimate the geared actuators' output impedance, the driving actuator provided Gaussian white noise perturbations—3rd order, 20 Hz low-pass filtered—scaled to ±10° amplitude while the driven actuator commanded the same k_d and b_d values from Experiment 1A. When amplified through the actuators' transmissions—that is, multiplied by N^2—these impedance values result in desired output stiffness and damping values of approximately 0-0.5 N·m/deg and 0-0.03 N·m·s/deg, respectively (assuming no losses in the transmission). These output impedance values cover the range of values typically used in lower-limb exoskeletons [31, 84, 134, 143–151]. We conducted five 60-second trials for each condition (125 total trials per actuator).

4.3.2.3 Analysis

Before performing system identification, we verified data quality through the power spectral density (PSD) of the input and output signals, as well as the input-output cross-correlation and coherence. We subsequently performed non-parametric system identification using Blackman-Tukey spectral analysis [125]; we divided the input-output cross-spectrum by the input auto-spectrum in the frequency domain and used a Hann window with a frequency resolution of 0.002 Hz. This spectral analysis resulted in a non-parametric transfer function, $G_{SPA}(s)$, which is represented by a Bode plot describing the frequency response of each impedance controller condition (Fig. 4.3). However, to meaningfully describe the physical system, we sought a parametric transfer function:

$$G(s) = \frac{T(s)}{\Theta(s)} = Is^2 + bs + k \tag{4.1}$$

where T is torque, Θ is angle, I is inertia, b is damping, and k is stiffness (Fig. 4.3). To obtain physical estimates of stiffness and damping, we implemented an optimization routine (using MATLAB's fmincon function) to minimize the difference between the frequency responses of $G_{SPA}(s)$ and $G(s)$, using the cost function:

$$J = \sum_{\omega=1}^{\omega_r} \Big[W_M \big| \, |G_{SPA}(j\omega)| - |G(j\omega)| \, \big| + W_\phi \big| \angle G_{SPA}(j\omega) - \angle G(j\omega) \big| \Big] \tag{4.2}$$

where ω is frequency, ω_r is the frequency range for optimization (ranging from 13 - 25 Hz depending on the experiment), W_M is a gain on the absolute difference between the magnitudes of the transfer functions, and W_ϕ is a gain on the absolute difference between the phases of the transfer functions. We manually tuned W_M and W_ϕ to 0.9 and 0.1, respectively.

We verified the quality of the optimized parameters using variance accounted for (VAF):

$$\text{VAF} = 100 \left(1 - \frac{\sum_{t=0}^{t_f} \big(\tau(t) - \tau_e(t)\big)^2}{\sum_{t=0}^{t_f} \tau(t)^2} \right) \tag{4.3}$$

where, t is time, t_f is length of each trial, τ is measured torque, and τ_e is the estimated torque that

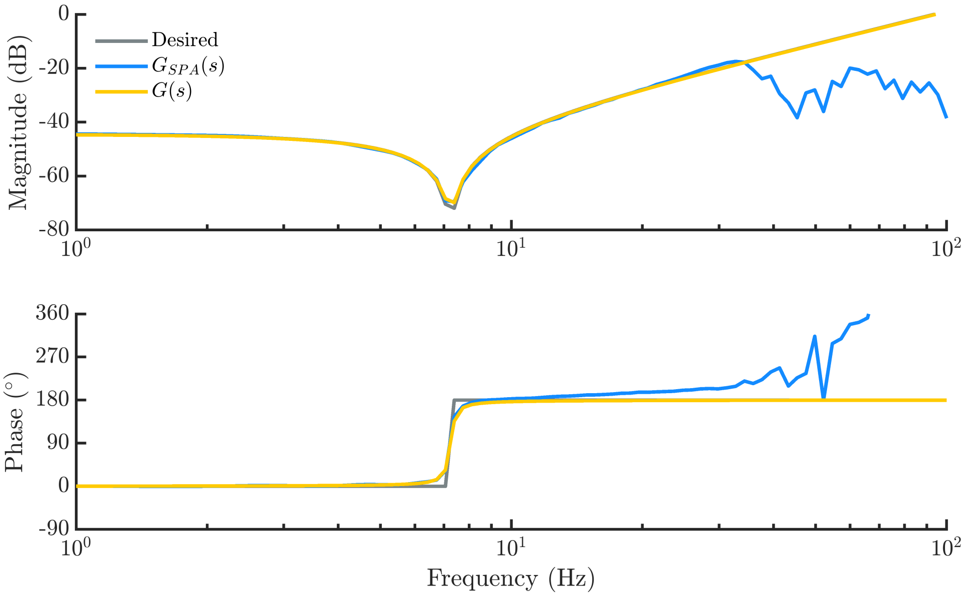

Figure 4.3: Representative Bode plots resulting from system identification. Bode plots correspond to the desired system (given by k_d and b_d), the non-parametric transfer function ($G_{SPA}(s)$), and the optimized parametric transfer function ($G(s)$).

would be produced by the optimized impedance parameters subject to same angular displacements, velocities, and accelerations (filtered) from each trial:

$$\tau_e(t) = I\ddot{\theta}(t) + b\dot{\theta}(t) + k\theta(t) \tag{4.4}$$

We completed this analysis procedure for each trial in all experiments.

In Experiment 1A, the input signal was motor angle, measured by the motor's 14-bit encoder (model: AS5047P, ams AG, Premstaetten, Austria); the output signal was motor torque, measured by the torque sensor. The primary outcome of Experiment 1A was motor stiffness (k_m) and damping (b_m). In Experiment 1B, the input signal was actuator angle, measured by the motor's encoder, then multiplied by the actuator's transmission ratio; the output signal was actuator torque, measured by the torque sensor. The primary outcome of Experiment 1B was actuator stiffness (k_a) and damping (b_a).

Statistical testing included an analysis of variance (ANOVA) with k_d and b_d as fixed factors;

ANOVAs for dependent variables k_m and b_m (Experiment 1A), or k_a and b_a (Experiment 1B) were performed independently. Two-sample t-tests with Bonferroni corrections were used for individual comparisons when necessary. All statistical tests assumed significance at $\alpha = 0.05$.

4.3.3 Experiment 2: Actuator-drive Efficiency

Actuator-drive efficiency—the ability to convert bus (battery) power to mechanical power—is critical in wearable robotics applications; actuator-drive efficiency varies with the current-voltage (torque-speed) regime of operation, so understanding an actuator's regions of high and low efficiency helps ensure that it operates at the best conditions possible. This experiment builds upon previous work estimating the efficiency of the standalone U8 motor [124].

We estimated the actuators' efficiency using a benchtop setup similar to Experiment 1 (Fig. 4.2). The driving actuators operated in positive power while the driven actuators operated in negative power; this was accomplished by operating one motor in voltage control and the other in current control, both in steady-state. In contrast to Experiment 1, both actuators were powered by a common 36 V battery (instead of separate batteries for each).

We performed tests across a wide range of power regimes (current-voltage conditions). The voltage-controlled motor operated at commanded open-loop voltages, v_m^c, between 0 and 39.2 V (2.4 V intervals); the current-controlled motor operated at desired closed-loop currents, i_m^c, between 0 and 19.8 A (0.8 A intervals). We tested all combinations of motor voltage and current satisfying:

$$v_m^c + 3i_m^c \leq 62 \tag{4.5}$$

ensuring that the current sensor on board the actuator did not saturate.

For all actuators, we conducted a single trial at each of 379 voltage-current combinations; each trial resulted in 2 measurements of efficiency (driving and driven, 758 total efficiency estimates per actuator). Trials consisted of three consecutive half-second conditions: (1) ramp up from zero to

v_m^c and i_m^c, (2) hold v_m^c and i_m^c, and (3) ramp down from v_m^c and i_m^c to zero. Only the steady-state condition was used for the efficiency calculation. We selected the ramps and trial length to allow the actuators to safely reach steady-state while limiting the rise in winding temperature.

4.3.3.1 Analysis

We calculated the efficiency of the driving actuator—the actuator rotating in the same direction of the measured torque—as:

$$\eta^+ = \frac{\tau_a \dot{\theta}_a}{i_b^+ v_b^+} \tag{4.6}$$

where η^+ is driving efficiency, τ_a is actuator torque, $\dot{\theta}_a$ is actuator velocity, i_b^+ is bus current, and v_b^+ is bus voltage. The denominator and numerator in Eq. 4.6 represent the input electrical power coming from the battery and the generated mechanical power, respectively.

We calculated the efficiency of the driven actuator—the actuator rotating in the opposite direction of the measured torque—as:

$$\eta^- = \frac{i_b^- v_b^-}{\tau_a \dot{\theta}_a} \tag{4.7}$$

where η^- is driven efficiency, i_b^- is bus current, and v_b^- is bus voltage. The denominator and numerator in Eq. 4.7 represent the input mechanical coming from the driving actuator and the generated electrical power, respectively.

For the efficiency calculations, Eqs. 4.6 and 4.7 where averaged over the steady-state period. We considered trials with an average output angular velocity below 0.1 rad/s to be in a stall condition, and excluded them from analysis.

Statistical testing included two-sample t-tests, with Bonferroni corrections used for individual comparisons when necessary. All statistical tests assumed significance at α = 0.05.

4.3.4 Experiment 3: Open-loop Torque Control

In the final experiment, we quantified the geared actuators' ability to track desired torque commands with open-loop torque control. Using the current controller, we commanded current step responses corresponding to 1-9 N·m (6:1 actuator) and 1-12 N·m (9:1 actuator) of output torque (1 N·m intervals), assuming 100% transmission efficiency; therefore, the actuators were using motor current—not output torque—as the feedback signal. In addition to quantifying the torque step response, we estimated each actuators' transmission efficiency—the transmission's ability to convert motor torque to output torque. We estimated transmission efficiency as the ratio of steady-state torque measured by the load sensor to desired output torque. The experimental setup was similar to Experiments 1 and 2, except only one actuator was used, and it was mechanically grounded via the torque sensor (Fig. 4.2). We performed 10 trials for each condition, 5 in each direction.

4.4 Results

4.4.1 Open-loop Impedance Control

Across all actuators, output stiffness and damping varied significantly with respect to their desired values ($p < 0.001$). Output stiffness did not vary significantly with respect to desired damping ($p \geq 0.077$), but output damping varied significantly with respect to desired stiffness ($p \leq 0.027$).

For the direct-drive motor, the output stiffness and damping values were 5.0 ± 7.8% ($p < 0.001$) and 2.4 ± 6.4% ($p < 0.001$) higher than desired, respectively (92.3 ± 8.7% VAF, Fig. 4.4). For the 6:1 planetary actuator, the output stiffness and damping values were 26.2 ± 11.5% ($p < 0.001$) and 0.6 ± 9.5% ($p = 0.529$) lower than desired, respectively (87.2 ± 11.4% VAF, Fig. 4.4). For the 9:1 planetary actuator, the output stiffness and damping values were 42.0 ± 16.5% ($p < 0.001$) lower and 4.3 ± 11.5% ($p < 0.001$) higher than desired, respectively (86.0 ± 9.8% VAF, Fig. 4.4). As seen in Fig. 4.4, all the actuators had strong linear relationships between desired and output impedance parameters ($r \geq 0.95$). Across all stiffness and damping conditions, the estimated

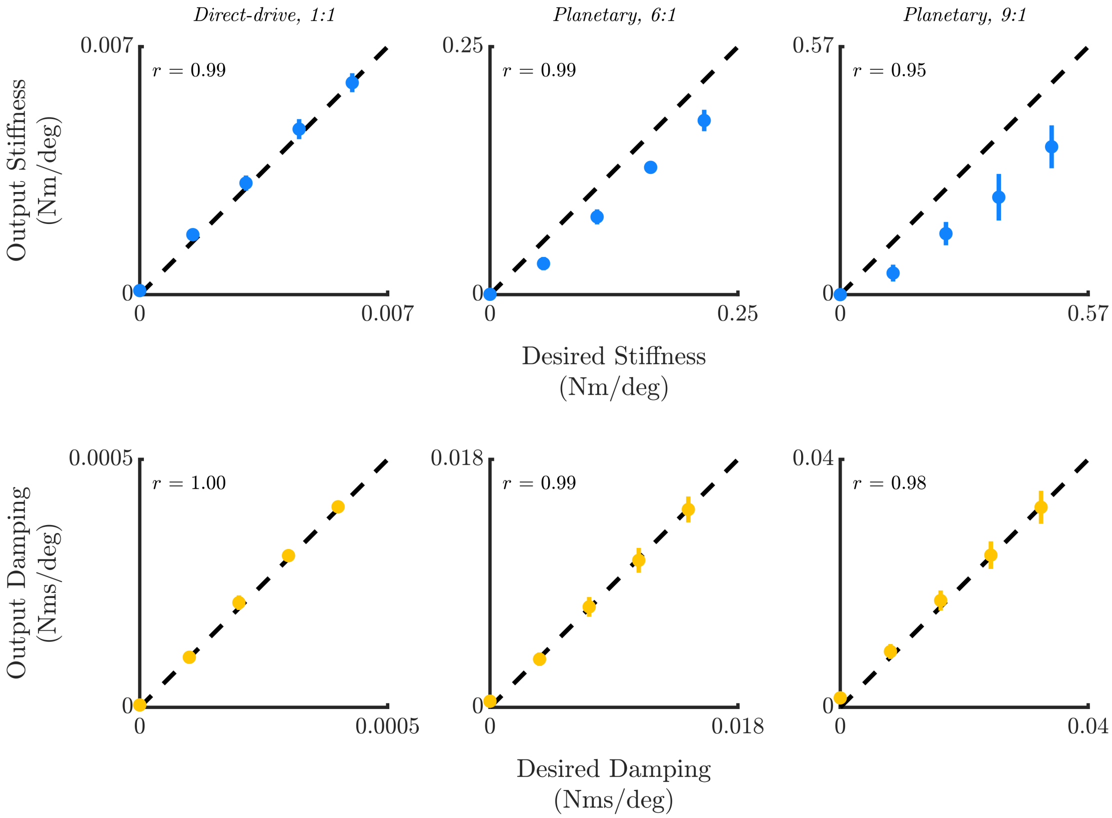

Figure 4.4: Comparison of the desired and estimated impedance parameters across all actuators. Dashed line denotes the ideal relationship between output and commanded impedance. Error bars denote standard deviation. From left to right: 1:1 direct-drive motor, 6:1 planetary actuator, 9:1 planetary actuator.

inertia for the 1:1, 6:1, and 9:1 actuators was 0.003, 0.139, and 0.325 g·m^2/deg, respectively.

In Experiment 1A, the frequency content of the input (position) and output (torque) signals remained below 30 Hz for all impedance gains; additionally, the input and output signals were correlated, with peak cross-correlation at zero lag. The input-output coherence was approximately 1 at 0-30 Hz, then decreased at higher frequencies; therefore, we used a frequency range of 1-25 Hz for the optimization. In Experiment 1B, the frequency content of the input (position) and output (torque) signals remained below 20 Hz for all impedance gains; additionally, the input and output signals were correlated. The input-output coherence was approximately 1 at 0-15 Hz, then decreased at higher frequencies; therefore, we used a frequency range of 1-13 Hz for the optimization.

4.4.2 Actuator-drive Efficiency

We calculated bus-output efficiency across a range of power regimes, with similar results across actuators (Table 4.2, Fig. 4.5). Bus electrical powers regimes ranged from -295-487 W, whereas actuator mechanical power regimes ranged from -380-380 W.

All actuators always had positive efficiency when driving, and a mix of positive and negative efficiency when driven. Comparing across actuators (columns in Table 4.2), the driving efficiency of the direct-drive actuator was higher than that of the geared actuators ($p \leq 0.021$), but the driving efficiencies of the geared actuators were not different from each other ($p = 0.260$); none of the driven efficiencies significantly differed across any actuators ($p \geq 0.226$). Comparing within actuators (rows in Table 4.2), the efficiency magnitudes of the driving and driven actuators were different for the direct-drive actuator ($p < 0.001$) but not for the geared actuators ($p \geq 0.100$). In general, the actuators had highest efficiency at high voltages/velocities and medium currents/torques; the actuators had lowest efficiency at low voltages/velocities and high current/torques, particularly when being driven (Fig. 4.5). The average positive efficiency across all conditions was 65%.

Across all tests, the voltage-controlled actuator was typically driving (Fig. 4.6). The voltage-controlled actuator was driving in 83% of trials whereas the current-controlled actuator was driving in 14% of trials; the actuators were stalled (neither driving) in 3% of trials. The number of stall trials increased with transmission ratio (6, 10, and 15 trials for the 1:1, 6:1, and 9:1 actuators, respectively; Fig. 4.6).

Table 4.2: Summary of bus-output efficiency across different power regimes.

Efficiency	Direct-drive 1:1	Planetary 6:1	Planetary 9:1
Driving (%)	70 ± 17	65 ± 15	64 ± 16
Driven[a,b] (%)	60 ± 22	63 ± 23	61 ± 23
Positive (%)	66 ± 20	64 ± 19	64 ± 19
Negative[b] (%)	-49 ± 27	-53 ± 25	-44 ± 21

[a] Magnitude of both positive and negative efficiencies

[b] Excludes efficiencies below -100%

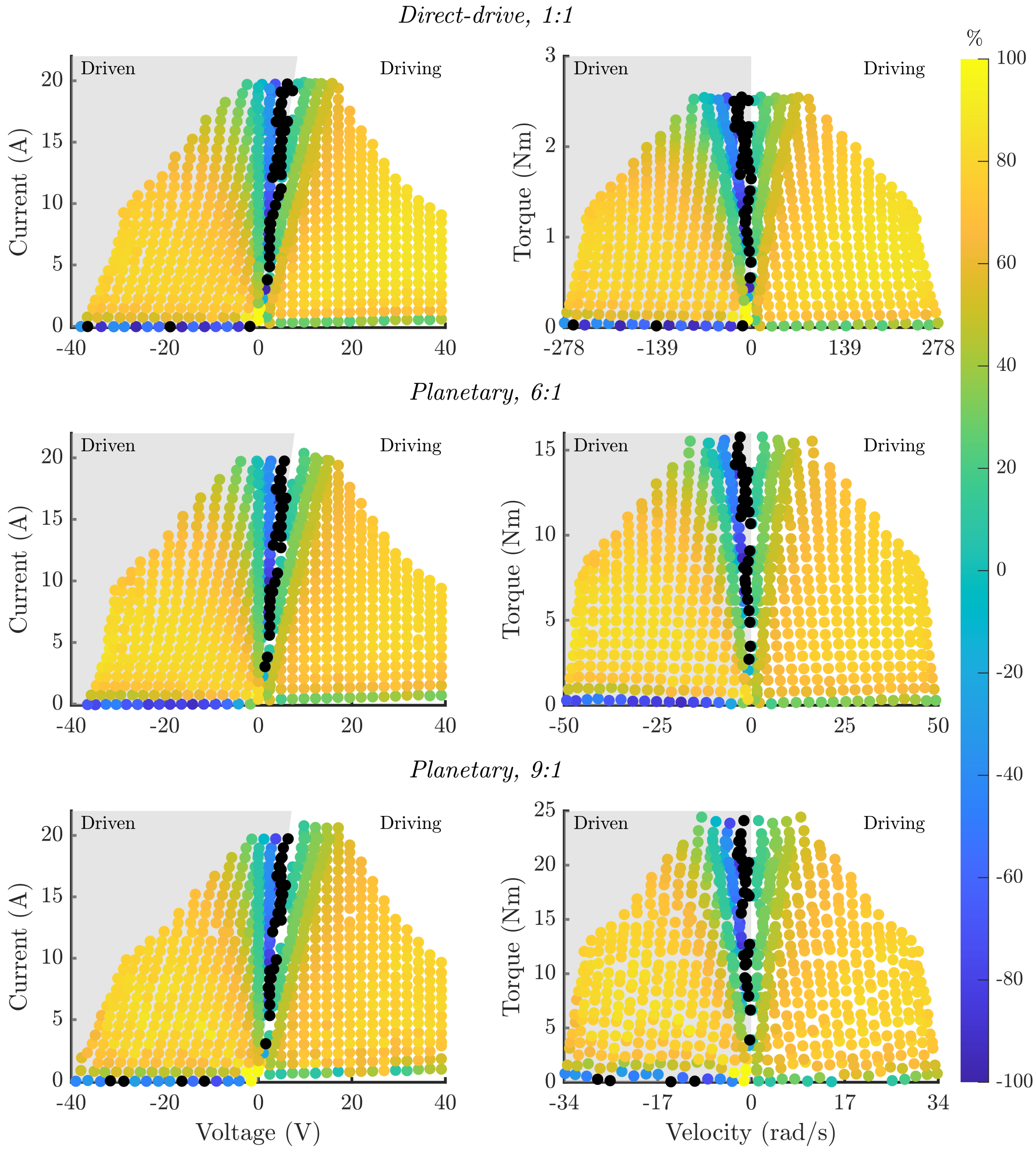

Figure 4.5: Actuator-drive efficiency of the geared U8 Lite actuators. Total efficiencies for the U8 actuators across different current-voltage (left) and output torque-speed (right) conditions. Positive efficiencies (yellow and green regions) correspond to bus electrical power input and mechanical power output; negative efficiencies (blue regions) correspond to mechanical power input and bus electrical power output. Efficiencies below -100% are shown in black. From top to bottom: 1:1 direct-drive motor, 6:1 planetary actuator, 9:1 planetary actuator. The shaded area corresponds to the driven actuator.

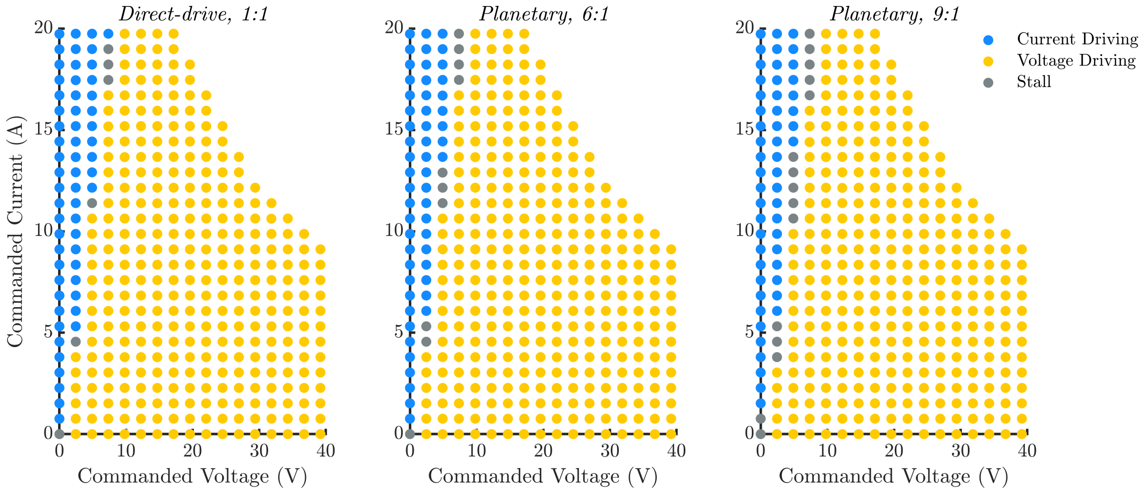

Figure 4.6: Current-voltage conditions resulting in the driving actuator being either current- or voltage-controlled. Stall conditions, with angular velocities below 0.1 rad/s, had neither actuator driving. From left to right: 1:1 direct-drive motor, 6:1 planetary actuator, 9:1 planetary actuator.

4.4.3 Open-loop Torque Control

The actuators tested in this study exhibited fast and accurate open-loop torque step responses (Fig. 4.7). Across all actuators, the open-loop rise time, maximum overshoot, and steady state error were 13 ± 4 ms, 41 ± 17%, and 2 ± 9%, respectively. The estimated mechanical efficiency for the 6:1 and 9:1 planetary actuators was 98 ± 6% and 98 ± 10%, respectively; both efficiencies were significantly less than 100% ($p \leq 0.019$).

4.5 Discussion

In this study, we empirically characterized the performance of four ER-BLDC actuators controlled with FlexSEA; we specifically chose actuation systems that are being developed for bionic systems, like the OSL and the Reaction-force Series-elastic Actuator (RFSEA) Leg [1,2,49]. We also developed a method to characterize the output impedance rendered by these systems operating under open-loop control; building upon previous work, we quantified actuator-drive efficiency across a range of power regimes [124]; Finally, we characterized open-loop torque control performance

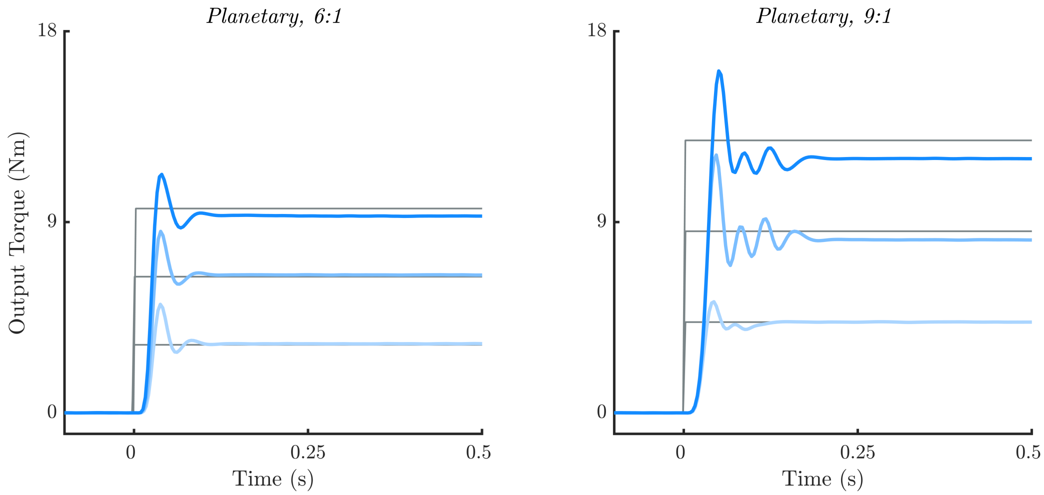

Figure 4.7: Representative step responses with the open-loop torque controller.

and transmission efficiency for these systems under static conditions.

4.5.1 Open-loop Impedance Control

The direct-drive motor rendered accurate open-loop impedance (stiffness and damping) values, within 5% of the desired values; however, as transmissions were added, the ability to accurately render desired impedance values decreased, particularly with stiffness (Fig. 4.4). The rendered output stiffness values were 26% and 42% lower than desired for the 6:1 and 9:1 transmissions, respectively. These losses can be attributed, in part, to the backlash and friction in the transmissions. The transmission losses are in contrast to Experiments 2 and 3, in which we observed 2-8% loss. In Experiments 2 and 3, all tests and analyses were performed in steady-state conditions (*i.e.*, zero acceleration); in contrast, the impedance characterization required non-steady state conditions with high-frequency changes in actuator direction and high accelerations. As a result, backlash and additional friction were introduced by the transmission when the actuator changed direction.

The impedance controller can be improved in various ways. One option is to add an encoder to the output and perform open-loop impedance control around the output instead of the motor. This is still open-loop impedance control because there is no measure of output torque; however, directly measuring output kinematics will reduce the effects of backlash and other transmission dynamics. Another option is to introduce a torque feedback signal, either with a torque sensor or SEA. Knowledge of both the output kinematics and kinetics will enable fully closed-loop impedance control, but may introduce significant size, mass, and complexity to a wearable bionic system.

We can use the impedance characterization to improve open-loop impedance control in these systems—which do not have an output encoder nor a torque sensor (Fig. 4.8). Using Fig. 4.4, we developed a model that applies a correction factor to the commanded stiffness; that is, for a desired output stiffness, the actuator should command the desired stiffness multiplied by a correction factor. The stiffness correction factors for the 6:1 and 9:1 actuators are 1.3 and 1.6, respectively. We repeated Experiment 1 with these correction factors to improve open-loop impedance control. Using the model, the stiffness error for the 6:1 and 9:1 actuators decreased from 26.2% to 0.1%

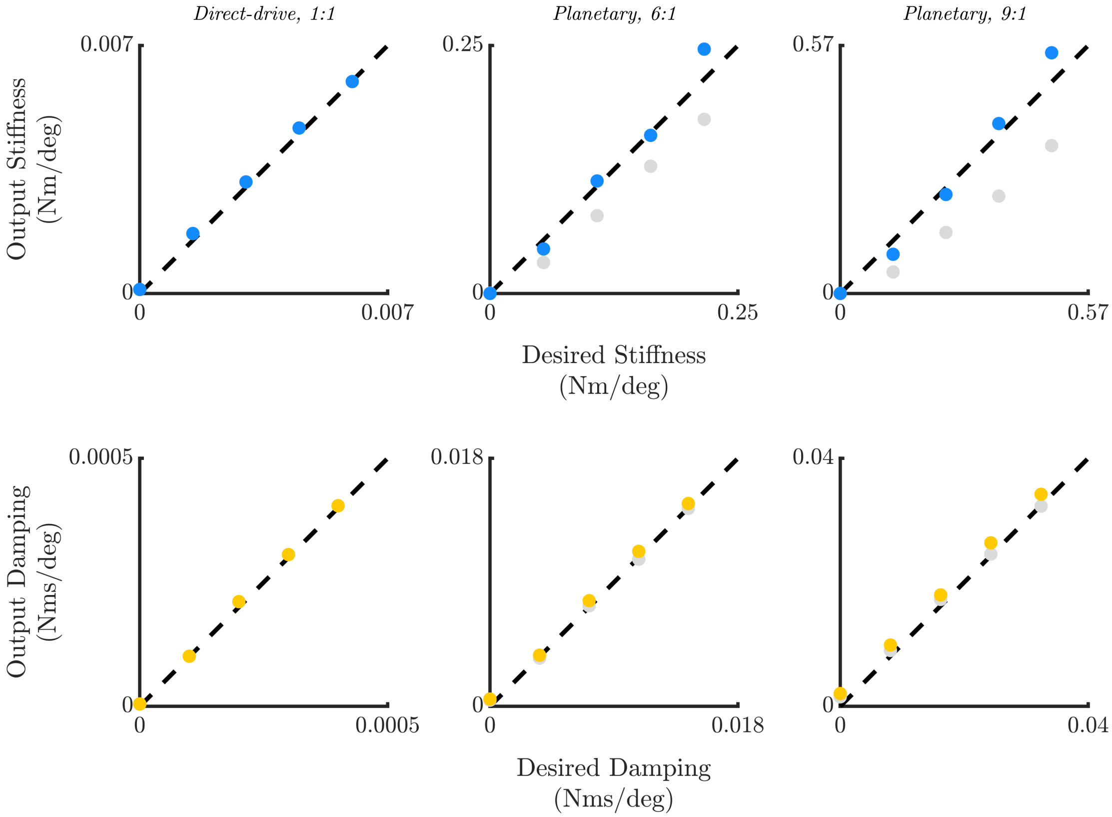

Figure 4.8: Improving open-loop impedance control with a stiffness correction factor. Original data in gray and corrected data in blue (stiffness) and yellow (damping). Dashed line denotes the ideal relationship between output and commanded impedance. From left to right: 1:1 direct-drive motor, 6:1 planetary actuator, 9:1 planetary actuator.

and from 42.0% to 2.9%, respectively (Fig. 4.8). This characterization enables accurate impedance control, despite the lack of a torque feedback signal.

4.5.2 Actuator-drive Efficiency

Throughout most of the power regimes tested, the actuators exhibited an average positive efficiency of 65% (Fig. 4.5). When driving, the geared actuators were 8% less efficient than the direct-drive actuator (Table 4.2). This loss is greater than the 2% losses seen in Experiment 3; the discrepancy is likely due to additional viscous losses in Experiment 2, since Experiment 3 was performed in static conditions. The primary source of inefficiency in these systems was the thermal power lost through the winding resistance ($P_{loss} = i_m^2 R_m$). In general, efficiencies were lowest at low voltages and high currents. Both the voltage- and current-controlled actuators drove the system during different conditions, although the current-controlled actuator only drove at high current, low voltage conditions (Fig. 4.6).

To further understand the physics underlying the efficiency results, we can revisit the brushed DC electromechanical model (Eq. 3.4). Removing the inductance term—due to the steady-state nature of this experiment—the driving and driven motor voltages can be described by:

$$v_m^+ = i_m^+ R_m + k_b \dot{\theta}_m \tag{4.8}$$

$$v_m^- = i_m^- R_m - k_b \dot{\theta}_m \tag{4.9}$$

where v_m^+, v_m^-, i_m^+, and i_m^- are driving motor voltage, driven motor voltage, driving motor current, and driven motor current, respectively. The angular velocities have opposite signs in Eqs. 4.8 and 4.9 because the motors were placed face-to-face.

The driving actuator—typically the voltage-controlled actuator—always exhibited positive efficiencies (Table 4.2, Fig. 4.5). In these conditions, the output mechanical power was less than the input bus power due to losses in the motor driver and motor windings; additionally, both the mechanical output and bus were in positive power, and the driving actuator always discharged the battery.

The driven actuator—typically the current-controlled actuator—exhibited a combination of positive and negative efficiencies (Table 4.2, Fig. 4.5). In conditions with positive efficiency below 100%, the output bus power was less than the input mechanical power; in these conditions, both the mechanical input and bus were in negative power, and the driven actuator charged the battery. In conditions with negative efficiency, the input mechanical power was negative but the bus power was positive; therefore, the driven actuator discharged the battery during negative efficiencies. The discharge occurred because the thermal power lost through the winding resistance was greater than the mechanical power input, requiring positive power from the bus. Alternatively, this phenomenon can be explained using Eq. 4.9; theoretically, negative efficiencies occurred when the motor current was greater than the current induced when the motor voltage is zero:

$$i_m^- > \frac{k_b \dot{\theta}_m}{R_m} \tag{4.10}$$

where $\frac{k_b \dot{\theta}_m}{R_m}$ is the maximum induced current when the motor leads are shorted at a given velocity. Experimentally, the driven motor current satisfied Eq. 4.10 during most negative efficiency conditions (Fig. 4.9).

The driving and driven actuators exhibit asymmetry in the electrical domain, as seen by the right-slanted lean to the driven actuator (Fig. 4.5). In each experiment, the two actuators were mechanically coupled, therefore they had equivalent torques and velocity magnitudes; additionally, the two actuators produced approximately equivalent currents, with a magnitude difference of 0.82 ± 0.29 A across all trials. However, the voltage magnitudes for the two motors typically did not match. That is, for two actuators producing equal torque, velocity, and current magnitudes, their corresponding voltages were different (Fig. 4.10). For most conditions, the voltage difference was positive; however, when the current-controlled motor was driving the system, the difference became negative (Fig. 4.10). This voltage difference can be explained by subtracting Eq. 4.9 from Eq. 4.8:

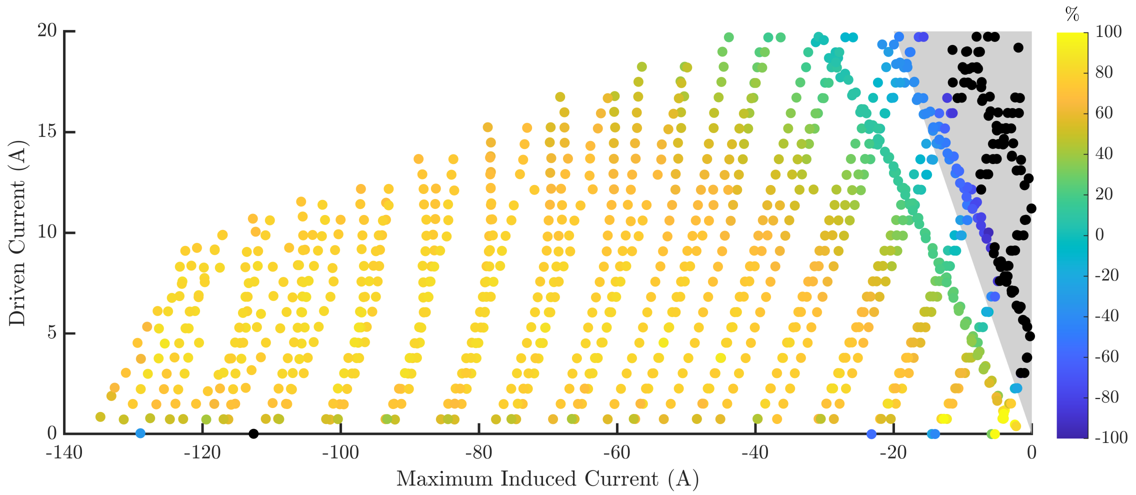

Figure 4.9: Driven actuator produces negative efficiency when the motor current is greater than the maximum induced current. The shaded area corresponds to Eq. 4.10. Positive efficiencies are shown in yellow and green, negative efficiencies in blue, and efficiencies below -100% in black. Data are shown for all actuators tested.

$$v_m^+ - v_m^- = 2k_b\dot{\theta}_m \tag{4.11}$$

which explains that, theoretically, the voltage difference between the driving and driven motors was twice the back-EMF voltage (*i.e.*, the sum of both motors' back-EMF voltage). Experimentally, the voltage difference between the two actuators satisfied Eq. 4.11 (Fig. 4.10). If we had commanded negative currents and voltages, the electrical domain efficiency plots would be mirrored about the y-axis (Fig. 4.5); that is, there would instead be a left-slanted lean to the driven actuator.

4.5.2.1 Implications in Wearable Robotics

This characterization provides insight into the efficiency of robotic prostheses and exoskeletons. The power regimes required for different joints and activities vary based on motor and transmission ratio; to extract the most benefit from the added mass of the robot, bionic devices should operate within each motor's most efficient region. In our previous work, three patients with above-knee amputations walked with the OSL—which uses the U8 KV100 motor tested here (Table 4.1)—on level ground, up/down ramps, and up/down stairs (Fig. 3.14) [2]. Across these activities, the knee

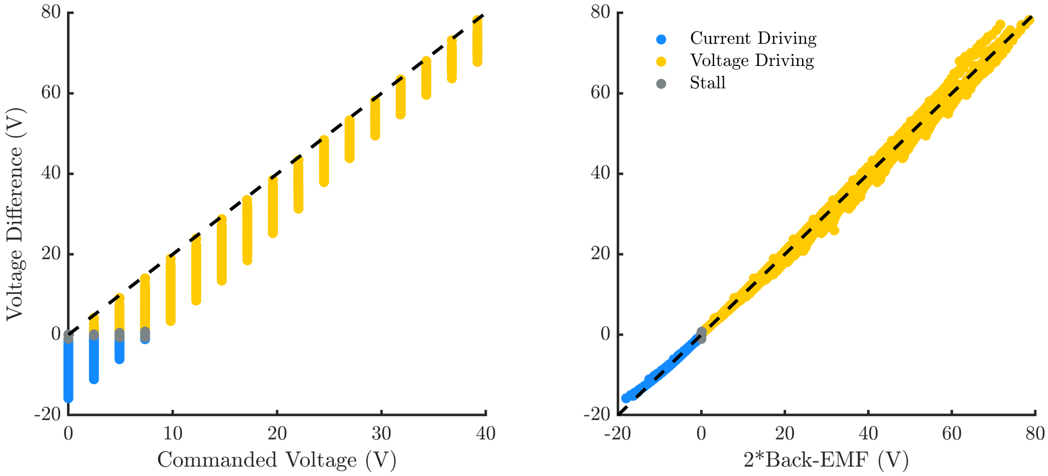

Figure 4.10: The coupled actuators did not produce voltages of equal magnitudes. (Left) The voltage difference between the two actuators varied, resulting in different voltage magnitudes for each; the dashed line (left) corresponds to the voltage difference if both motors produced equal, but opposite voltages. (Right) The voltage difference can be attributed to the back-EMF of both actuators; the dashed line (right) corresponds to Eq. 4.11. Data are shown for all actuators tested.

motor operated at 0-33 V and 0-5 A while the ankle motor operated at 0-18 V and 0-7 A. Using the efficiency characterization (Fig. 4.5), we estimate that the positive efficiencies for the OSL's operating regions are 54 ± 24%; compared to the direct-drive actuator's positive efficiency, this suggests that—during ambulation with the OSL—the actuator operates at approximately 82% of its average efficiency.

4.5.3 Limitations, Recommendations, and Future Work

It is important to note that the results of this study are limited to actuators using the U8 KV100 motors and FlexSEA. Although, we expect similar open-loop performance and efficiency results with motors of similar topology and design, we recommend that other researchers fully characterize their actuators, especially when using a different embedded system. Experiments 1 and 2 are demanding on both the actuator and embedded system, and should be performed carefully.

Although our results with the direct-drive motor are in line with previous characterization experiments, there are some differences [124]. Previously, the torque constant of the U8 motor was estimated to be 0.14 N·m/A; however, Experiment 3 resulted in a torque constant of 0.15 N·m/A. Additionally, previous efficiency testing found an average positive efficiency of 56%, as opposed to the 66% from Experiment 2 (Table 4.2); specifically, in previous testing, the driven motor was less efficient at high currents. Both the previous and present work used the same motor; however, the hardware and software on the embedded system have been upgraded since the original testing. This highlights the need to characterize systems, especially when major hardware or software changes are made. The methods presented here provide a framework for evaluating robotic systems.

During pilot testing for Experiment 1, we found that perturbation amplitude and low-level feedback gains did not affect the rendered impedance values; however, low-level feedforward gains in the current controller did impact the rendered impedance, and should be tuned appropriately. Additionally, the perturbation signal cut-off frequency did not affect impedance estimates as long as it was high enough to capture the expected dynamics of the rendered system (*i.e.*, constant magnitude at low frequencies, break point, and positive slope at high frequencies; Fig. 4.3).

Experiment 2 involves high power regimes that are typically not reached during normal operation, and winding temperature should be monitored to prevent overheating; additionally, the actuators should use a common battery, otherwise the driven motor may overcharge and damage its battery.

Future work involves characterization of the OSL's impedance controller. The transmission on the OSL is larger (approximately 50:1) and more complex than those tested here. The knee has a three-stage belt drive whereas the ankle has a two-stage belt drive coupled to a four-bar linkage; therefore the OSL is more susceptible to transmission losses, backlash, and nonlinearities due to the belt dynamics. Fortunately, the OSL has output encoders to measure joint angle. These encoders can be used to control output impedance directly—instead of indirectly through motor impedance—and reduce errors introduced by the transmission.

4.6 Summary

In this study we characterized open-loop impedance control, actuator-drive efficiency, open-loop torque control, and transmission mechanical efficiency for various actuators used in wearable robotic systems. We found that all actuators had a positive actuator-drive efficiency of 65%. We also found that transmission losses increased as the experiments became more dynamic. In static conditions, the transmissions are 98% efficient and the transmission ratios are low enough for accurate open-loop control. In non-steady state conditions, where the effects of backlash and friction are more prevalent, open-loop control is less accurate; however, by characterizing these losses across a range of frequencies and impedance values, we can successfully account for the losses and improve open-loop control.

Chapter 5

Damping Perception During Active Ankle and Knee Movement

Portions of this chapter appear in:

1. **A F Azocar,** A L Shorter, and E J Rouse, “Damping Perception During Active Ankle and Knee Movement,” *IEEE Transactions on Neural Systems and Rehabilitation Engineering*, 2019.
2. **A F Azocar,** A L Shorter, and E J Rouse, “Perception of Mechanical Impedance During Active Ankle and Knee Movement,” *Proceedings of the IEEE International Conference on Engineering in Medicine and Biology (EMBC)*, July 2018.

   2nd Place, Student Paper Competition

5.1 Abstract

The mechanical impedance of the leg governs many important aspects of locomotion, including energy storage, transfer, and dissipation between joints. These mechanical properties, including stiffness and damping, have been recently quantified at the ankle joint during walking. However, little is known about the human ability to sense changes in impedance. Here, we investigate the ability to detect small changes in damping coefficients when interacting with a mechanical system coupled to the ankle or knee joint. Using a psychophysical experiment (adaptive, weighted

staircase method) and an admittance-controlled dynamometer, we determined the 75% minimum detectable change by tasking subjects to compare the damping values of different virtual spring-mass-damper systems. The Weber fraction for damping coefficient ranged from 12% to 31%, with similar performance across the ankle and knee. Damping perception performance was similar to previous stiffness perception results, suggesting that both the stiffness and damping of the environment are important for the human sensorimotor system, and motivating further investigation on the role of damping in biomechanics, motor control, and wearable robotic technologies.

5.2 Introduction

Throughout the gait cycle, agonist-antagonist muscles activate in a well-coordinated pattern to facilitate balance, forward propulsion, and support of the body's center of mass [152]. As the agonist-antagonist muscles of the leg contract and relax, changes occur in the stiffness and damping properties of the leg joints. The joints' time-varying stiffness and damping properties, along with limb inertia, are often collectively known as joint mechanical impedance [80]. Together, these properties describe the joints' instantaneous response to a perturbation, and are often modeled as a rotational spring-mass-damper (SMD) system. Fundamentally, joint impedance governs how energy is stored, exchanged, and dissipated during locomotion, and as a result, has important implications in basic sensorimotor control of gait, and potentially the development of better, more biomimetic assistive technologies [3, 82, 83].

Recently, researchers have begun quantifying ankle impedance during locomotion [84, 134, 143, 144, 153]; however, there is limited knowledge of the relationship between impedance and the sensorimotor system, particularly regarding human perception of impedance. To estimate joint impedance, researchers apply mechanical perturbations during gait, and use system identification techniques to quantify the stiffness, damping, and inertia properties governing the torque response. Rouse *et al.* and Lee and Hogan estimated ankle impedance during the early- and mid-stance phases of gait, as well as during swing, respectively [84, 143, 144]. Most recently, Shorter and

Rouse investigated ankle impedance during the terminal stance phase of walking [134]. Throughout the gait cycle, stiffness increases linearly during early and mid-stance and decreases quickly during terminal stance to the values reported in swing. Additionally, damping increases in preparation for toe-off. These studies provide new insight describing joint dynamics during gait, but the broader implications of these data in sensorimotor control are not fully understood [16].

The sensorimotor control system likely relies on the ability to sense small changes in the environment. In the context of leg joints, sensing these changes can be important for stability, balance, and safety during locomotion [154]. In our previous work, we quantified the human ability to perceive changes in stiffness when interacting with a mechanical device at the ankle or knee [3]. This study found that stiffness perception at the lower limb is comparable to—or better than—stiffness perception at the upper limb, and supported the importance of stiffness with respect to sensorimotor control and human motor performance. However, the ability to perceive changes in damping coefficient—another component of mechanical impedance—has not been studied.

Understanding the link between mechanical impedance and perception in the lower extremity may facilitate new design, control, and prescription strategies for wearable robotic systems, such as exoskeletons and prostheses [3, 7, 84]. Mechanical impedance is the basis for the development of various robotic exoskeletons and gait trainers [135, 145, 155–157]; impedance control promotes a compliant interaction between the human and machine and is becoming increasingly prevalent in wearable robotics [81]. Quantifying the human ability to detect changes in impedance provides insight into accuracy requirements and the potential for impedance-based feedback via wearable robotic systems [3]. For example, we recently characterized the ability of individuals with transtibial amputation to perceive changes in the stiffness of their prosthesis while walking [7]. We found that during locomotion, the ability to consistently select a preferred prosthesis stiffness depended largely on the ability to correctly discriminate changes in stiffness. Furthermore, we concluded that the stiffness of a prosthetic foot should be specified on an individual basis—which is not part of current clinical practice—using robotic prescription tools, and that more appropriate mechanical characterization of ankle-foot prostheses may be needed.

The human ability to sense small changes in stimuli is commonly analyzed via psychophysical studies. Psychophysical research has provided insight into the mechanisms underlying human proprioception. For example, perception of joint velocity is regulated by primary muscle spindle receptors, whereas the perception of force primarily depends on centrally generated commands [158]. Perception of joint impedance involves the incorporation of different perceptive modalities [159]; for example, damping perception requires both velocity and force information. The incorporation of different types of sensory information, such as velocity and force, reduces sensory resolution; this is evident with previous work showing that, at the elbow joint, humans can discriminate smaller changes in velocity and torque compared to damping coefficient [158]. There are numerous investigations on both upper- and lower-limb perception of kinematic and kinetic variables, and a few on impedance (*i.e.*, stiffness or damping) perception at the upper-limb; however, there is limited knowledge regarding lower-limb impedance perception.

In this investigation, we sought to quantify the human ability to sense small changes in external (environment) damping coefficients at the ankle and knee joints. Specifically, we studied how well humans can perceive changes in damping coefficients applied by an external mechanical device (as opposed to changes in the intrinsic damping coefficient of the biological joints themselves). This study expands on our previous stiffness perception studies [3]. We quantified human perception via the 75% just noticeable difference (JND) and corresponding Weber fraction (WF). The JND is the minimum detectable change for a particular stimulus, and the WF represents the JND as a fraction of the original stimulus [160]. Our results show that, at high damping values, subjects can sense changes in damping coefficient of at least 12% at the ankle and 13% at the knee; at low damping values, subjects can detect changes of at least 25% at the ankle and 31% at the knee. Therefore, people are unlikely to detect changes in the damping coefficients of wearable robots if they remain below these thresholds. This work facilitates a foundation for understanding how humans perceive changes in externally-applied joint impedance. Understanding the ability to perceive changes in lower-limb impedance provides new insight into the sensorimotor system's use of impedance and can inform the development of impedance-based wearable robotic technologies.

5.3 Methods

5.3.1 Experiment

5.3.1.1 Apparatus

The Neurobionics Lab Rotary Dynamometer, a custom dynamometer, rendered the dynamics of a virtual rotational SMD system (Fig. 5.1). A brushless gearmotor (model: BSM90N-3150AF, Baldor, Fort Smith, AR, USA) coupled to a six-axis load cell (model: 45E15A4, JR3, Inc., Woodland, CA, USA) was mounted on a custom frame and adjustable chair (model: 835-000, Biodex Medical Systems, Shirley, NY, USA). An admittance controller rendered the desired SMD dynamics, with an input of net torque and an output of motor angle (corresponding to the angle of the joint):

$$\frac{\Theta(s)}{T(s)} = \frac{1}{Is^2 + bs + k} \tag{5.1}$$

where s denotes the Laplace domain, $\Theta(s)$ is the motor angle, $T(s)$ is torque, I is inertia, b is damping, and k is stiffness [161]. Damping was selected by the psychophysical protocol; inertia and stiffness terms were also included. The motor's encoder (0.036° resolution) monitored joint angles, which were limited to a biomechanically safe range of motion via software and mechanical stops. The system's feedback control loops operated at 2500 Hz and sampled data at 833 Hz.

We monitored subject fatigue throughout the experiment using surface electrodes (model: Bagnoli, Delsys, Boston, MA, USA) to record the EMG activity of the muscles. We recorded from the lateral gastrocnemius and tibialis anterior muscles in the ankle experiment, and the rectus femoris, vastus lateralis, biceps femoris, and semitendinosus muscles in the knee experiment. EMG signal processing included a band-pass filter (20 to 300 Hz), full-wave rectification, and a second-order, low-pass Butterworth filter (2.5 Hz cutoff).

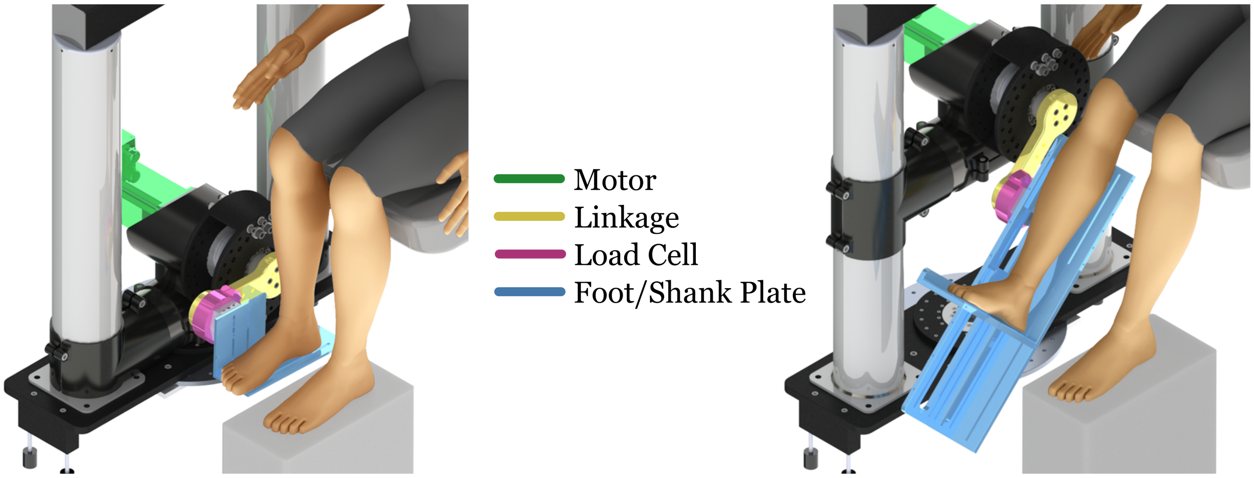

Figure 5.1: Dynamometer arrangement for the ankle (left) and knee (right) experiment. Straps on the foot and shank secured the right leg to the metal plate, and padding behind the heel prevented discomfort (not shown).

5.3.1.2 Ankle Experimental Setup

This study comprised of fourteen healthy, able-bodied subjects (7 female, 7 male; age 24.6 ± 3.5 years; mass 73.6 ± 18.1 kg; mean ± standard deviation), with no history of neurological impairment or ankle injury. Subjects gave written informed consent, which was approved by the Northwestern University Institutional Review Board (NU IRB).

Subjects sat in the dynamometer chair and placed their right foot on a plate, which was mounted rigidly to the gearmotor output shaft. A concentric laser guided the alignment of the ankle's center of rotation to the motor's rotation axis. The chair was adjusted for each subject such that the resting ankle angle was approximately 0° of flexion, and the knee angle was maintained at 90° of flexion. Straps over the toes and ankle secured the subject's foot to the foot plate, and separate straps secured the thigh to prevent movement of the upper leg. During the experiment, subjects could voluntarily rotate their ankle (and the motor) within a limited range of motion of approximately 51°.

5.3.1.3 Knee Experimental Setup

Fourteen healthy, able-bodied subjects (7 female, 7 male; age 24.6 ± 2.5 years; mass 74.0 ± 15.5 kg), distinct from the ankle experiment, were recruited for this study. Subjects gave written informed consent to take part in this study, which was also approved by the NU IRB. They had no history of neurological impairment or knee injury.

Subjects sat in the chair and placed their right leg on a plate, which was rigidly mounted to the gearmotor output shaft. The concentric laser also guided alignment of the approximate knee center of rotation to the motor rotation axis. The resting knee angle was set to approximately 60° of flexion, whereas the ankle angle was maintained at 0° of flexion, such that the foot was perpendicular to the shank. Subjects could voluntarily rotate their knee (and the motor) within a maximum range of motion of approximately 63°. The leg was secured to the leg plate with straps over the toes and shank, and the thigh was secured to the chair.

5.3.1.4 Protocol

In our previous work, we modified the stiffness of the SMD system while keeping damping and inertia constant [3]; in this work, we modified the damping of the SMD system while keeping stiffness and inertia constant.

Subjects wore a blindfold and noise-reducing headphones to diminish distractions and prevent the use of external cues. We implemented a two-interval forced-choice (2IFC) paradigm [162]; in each trial, the motor rendered two SMD systems with which the subjects sequentially interacted. One of the rendered SMD systems included a reference damping value, whereas the other included a comparison damping value. Subjects interacted with the rendered mechanical system through voluntary joint extension and flexion. Subjects had eight seconds to interact with each SMD system, after which they stated which system was perceived to have higher damping, or resistance to movement. A length of eight seconds was chosen during pilot testing because it maintained the experiment duration short while providing subjects with enough time to explore the system dynamics; additionally, this length was consistent with our previous methods [3]. Subjects were not permitted to answer ‘equal damping’; therefore, trials with equal damping values were automatically incorrect. Audible tones notified the subjects at the start and end of trials, as well as at the transition from the first to second SMD systems.

The reference damping values tested were 2.5, 6.25, and 10 N·m·s/rad for both experiments. We selected these damping values based on hardware constraints, human joint damping during locomotion, and damping coefficients currently used in the design and control of wearable robotic systems, including exoskeletons and prostheses [38, 45, 84, 134, 143–145, 150, 151]. We attempted to minimize the contributions of inertia and stiffness by setting the admittance controller’s inertia and stiffness parameters as low as possible. Safety requirements built into the dynamometer resulted in inertia and stiffness terms of 0.3 kg·m^2 and 10 N·m/rad, respectively.

We implemented an adaptive, weighted up-down method that converged to the JND (75% performance point) with a base step size, Δ, of 0.25 N·m·s/rad [163]. The first comparison damping value in a staircase—the entire series of trials corresponding to a reference damping value—was 5Δ away from the reference. After a correct response, the following comparison damping value in the staircase moved Δ closer to the reference; after an incorrect response, the following comparison value in the staircase moved 3Δ farther from the reference. Therefore, the experiment became more challenging as subjects performed better, and vice versa. Each staircase lasted for eight runs—series of damping changes in the same (increasing/decreasing) direction (Fig. 5.2); however, the number of trials in an individual staircase varied depending on the subjects’ performance [164].

To prevent subjects from adapting to the experiment, the six staircases, corresponding to the three reference damping values approached from above and below, were randomly interleaved [164]. The type of damping value presented first in each trial (reference or comparison), was also randomized. An example of one staircase with a low approach to the 10 N·m·s/rad reference value can be seen in Fig. 5.2.

Before participating in the psychophysical protocol, subjects experienced familiarization and practice trials. During the familiarization period, subjects interacted with the SMD system as the damping coefficient changed from 1 to 11 N·m·s/rad in 2.5 N·m·s/rad increments. Subjects

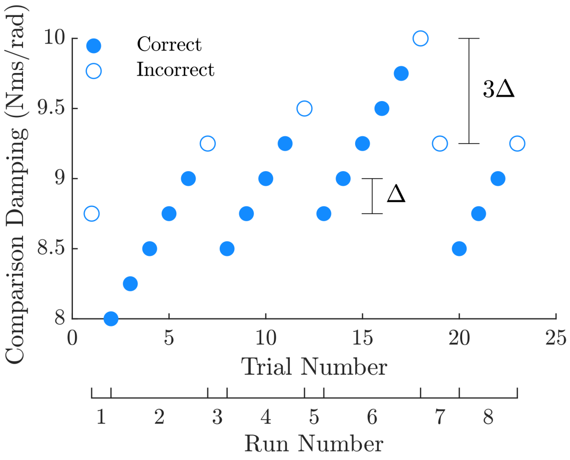

Figure 5.2: Example subject responses for a single staircase while approaching the reference damping value (10 N·m·s/rad) from below. Each trial required subjects to interact with the motor configured to both the reference and comparison damping values. Each run contains the set of consecutive trials that changed in the same (increasing/decreasing) direction.

also practiced five trials of the adaptive psychophysical protocol; feedback on their answers was provided after each practice trial, but not during the remainder of the experiment.

5.3.2 Analysis

We calculated the 75% JND by taking the mean of the comparison damping values from all trials in the last six runs of each staircase; subsequently, we calculated the WF by normalizing the JND by the corresponding reference damping value [162, 163]. Specifically, the WF in this study describes the percent change in damping coefficient that subjects can perceive with 75% accuracy. The ability to perceive smaller changes in damping coefficient indicates better perception; therefore, high performance corresponds to low JND and WF values.

As muscles fatigue, EMG amplitude increases due to the increased motor unit recruitment required to sustain a constant torque; in fact, the EMG amplitude-to-torque ratio ($R_{EMG-\tau}$) has been shown to double after fatigue is induced [165]. Consequently, we monitored fatigue by comparing the EMG amplitude-to-torque ratios produced during maximum voluntary contraction (MVC) before ($R_{EMG-\tau,pre}$) and after ($R_{EMG-\tau,post}$) the experiment. We calculated the ratios by measuring the maximum EMG amplitude produced by each muscle while subjects performed MVCs, and divided the amplitude by the maximum torque of the MVC.

We also calculated the torque contributions of individual impedance parameters to understand how subjects interacted with the dynamics of the SMD systems. We estimated the torque contributions of stiffness, damping, and inertia (τ_k, τ_b, and τ_I, respectively) by multiplying the stiffness, damping, and inertia values from the experiment with the motor's position (relative to neutral), velocity, and acceleration (10 Hz, third-order low-pass filtered) trajectories, respectively. Finally, we calculated the percent contribution of each impedance parameter as:

$$\tau_{\%,p} = 100 \frac{\mid \tau_p \mid}{\mid \tau_k \mid + \mid \tau_b \mid + \mid \tau_I \mid} \tag{5.2}$$

where p corresponds to each impedance parameter. To verify that the torque contributions of the parameters were accurate, we calculated the net torque due to the contributions and compared it to the measured load cell torque.

Throughout the psychophysics literature, a variety of experimental procedures are utilized, which converge to the WF at different points, including 71%, 75%, and 84% performance [160]. To fairly compare our results to WFs from previous investigations, we extrapolated the literature WFs to the 75% performance point. Assuming that perception is a normally-distributed process, the underlying psychometric function—which describes perception across a range of performance points—becomes a linear function of WF and z-score [160]. Therefore, we can extrapolate the literature WFs to the 75% point by calculating the z-scores of the performance points ($z_{0.71}$ = 0.5534, $z_{0.75}$ = 0.6745, $z_{0.84}$ = 0.9945) from previous studies and fitting a line between the origin and the literature WFs. Specifically, the WF at the desired performance point, WFd, is related to the WF at the comparison performance point, WFc, by:

$$WF_d = \frac{z_d}{z_c} WF_c \tag{5.3}$$

where z_d and z_c are the z-scores of the desired (75%) and comparison (71% or 84%) literature performance points, respectively. This relationship has been experimentally shown in a separate set of psychophysical studies [166].

The primary statistical test used was an ANOVA with fixed factors: reference damping coefficient (2.5, 6.25, and 10 N·m·s/rad) and joint (ankle or knee); subjects were treated as a random factor. Separate analyses were completed for dependent variables JND and WF. Two-sample t-tests, with Bonferroni corrections applied when necessary, were implemented for individual comparisons with previous studies. All statistical tests were performed with a significance level of α = 0.05.

5.4 Results

We characterized the minimum detectable change in externally-applied damping coefficients by tasking subjects to interact with a rendered rotational SMD system while participating in an adaptive staircase protocol. The experiment converged to the JND (and WF)—the point in which subjects correctly detected a change in damping coefficient 75% of the time.

JND varied significantly with respect to damping coefficient ($F_{2,167}$ = 36.9, p $<$ 0.001) but not joint ($F_{1,167}$ = 2.7, $p = 0.106$). The JNDs from both approach directions were combined into a single JND at each reference damping level [160]. Except for the knee JNDs at 2.5 and 6.25 N·m·s/rad (p = 0.169), all JND values were significantly different from each other ($p \leq$ 0.005) within each joint. Based on theory and literature data, we assumed and fit a linear relationship between JND and reference damping level:

$$JND_a = 0.076b_r + 0.408 \tag{5.4}$$

$$JND_k = 0.070b_r + 0.558 \tag{5.5}$$

where b_r is reference damping level, JND_a is ankle JND, and JND_k is knee JND (Fig. 5.3) [160].

The regression coefficients in Eqs. 5.4 and 5.5 were all significant ($p < 0.001$).

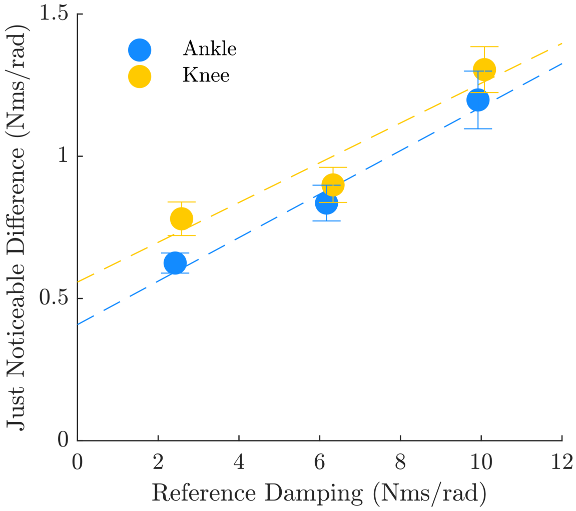

Figure 5.3: JND increases with reference damping level and is not significantly different across joints. Error bars denote standard error of the mean; data are offset for clarity.

WF varied significantly with respect to damping coefficient ($F_{2,167}$ = 85.6, $p < 0.001$) but not joint ($F_{1,167}$ = 3.7, $p = 0.058$). Based on theory and literature data, we assumed and fit a reciprocal relationship between WF and reference damping level:

$$WF_a = 0.069 + 0.448/b_r \tag{5.6}$$

$$WF_k = 0.056 + 0.633/b_r \tag{5.7}$$

where WF_a is ankle WF and WF_k is knee WF (Fig. 5.4) [160]. The regression coefficients in Eqs. 5.6 and 5.7 were all significant ($p \leq 0.002$). The staircases converged in 19 and 18 trials (114 and 108 total trials) for the ankle and knee experiment, respectively.

Subjects explored the SMD system by voluntarily extending and flexing their joint. Subjects self-selected the specific strategies used for exploring the dynamics of the system and comparing damping values. Subjects' maximum extension (ankle DF) velocity, maximum flexion (ankle PF) velocity, maximum extension torque, and maximum flexion torque varied significantly with damp-

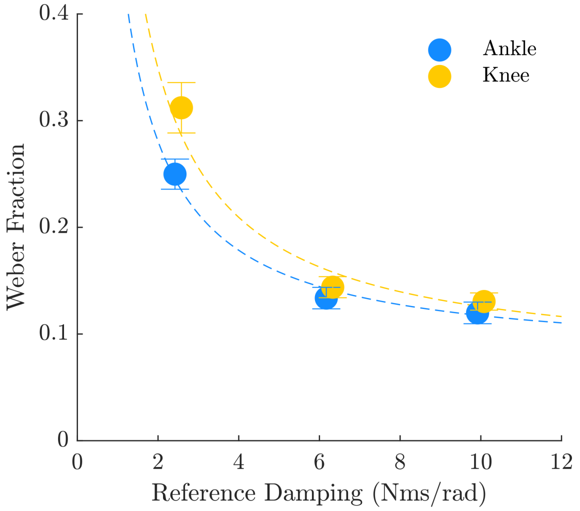

Figure 5.4: WF decreases with reference damping level and is not significantly different across joints. Error bars denote standard error of the mean; data are offset for clarity.

ing coefficient in each trial ($p < 0.001$); however, these correlations were poor to moderate, as indicated by the correlation coefficient, r. Maximum ankle DF and PF velocity decreased with increasing damping coefficient (r_{DF} = -0.41, r_{PF} = -0.46); maximum knee extension and flexion velocity also decreased with damping coefficient (r_{EXT} = -0.32, r_{FLX} = -0.32). Slight positive correlations between subjects' maximum torques and damping coefficient were found; r ranged from 0.24 to 0.40 (Fig. 5.5). The maximum DF and PF torques produced were 49.9 ± 23.4 and 89.2 ± 57.3 N·m, respectively; the maximum knee extension and flexion torques were 124.1 ± 38.7 and 82.9 ± 28.6 N·m, respectively. Motor dynamics were primarily explored via ankle PF (68.6%) and knee flexion (70.8%).

Table 5.1 shows the $R_{EMG-\tau,post}$ to $R_{EMG-\tau,pre}$ ratios for each muscle; a value near 1 indicates that $R_{EMG-\tau}$ remained approximately constant. Across subjects and muscles, $R_{EMG-\tau}$ was not significantly different before and after the experiment ($p \geq 0.525$); that is, motor unit recruitment remained consistent throughout the experiment [165]. Only one subject showed a ratio greater than two in either experiment, occurring in the gastrocnemius and biceps femoris for the ankle and knee experiment, respectively. Muscle fatigue can significantly degrade perception performance, which did not happen in this study [167]. Therefore, we determined that fatigue did not affect subjects'

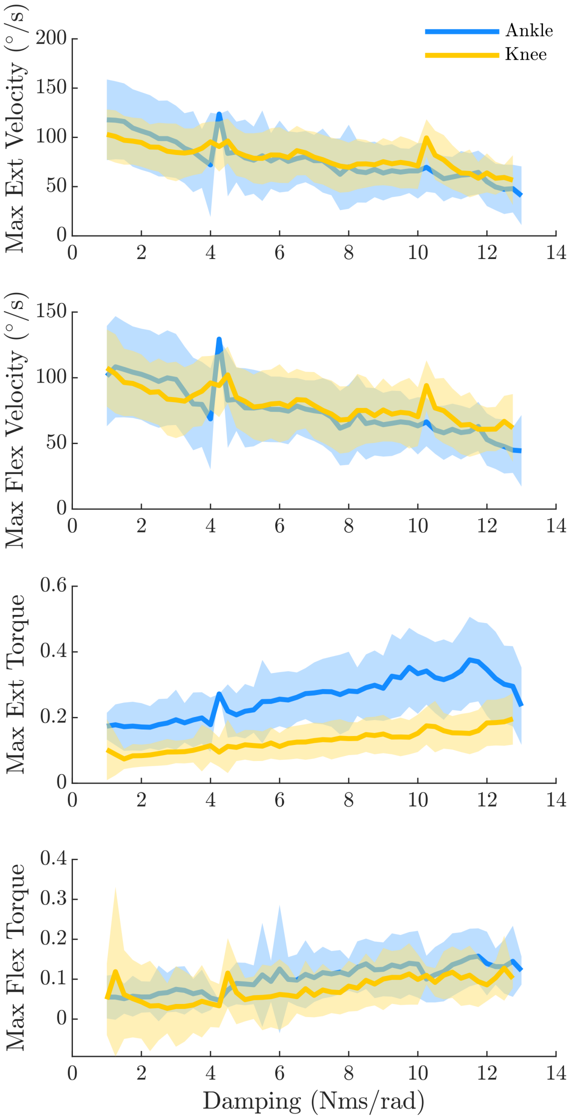

Figure 5.5: Maximum velocities decrease whereas maximum torques increase with damping coefficient. Translucent areas denote standard deviation. Torques are normalized by each subjects' maximum voluntary contraction. The standard deviation at 4.25 N·m·s/rad for the ankle experiment is undefined because only one trial occurred at this damping value.

ability to perceive changes in damping coefficient and included the data in our analysis.

The damping component of impedance contributed most of the torque in the SMD system for damping values of 6.25 and 10 N·m·s/rad (Table 5.2). At the lowest damping value, the combined

Table 5.1: EMG amplitude-to-torque ratio across subjects.

Muscle	$R_{EMG-\tau,post}/R_{EMG-\tau,pre}$
Gastrocnemius	1.2 ± 0.6
Tibialis Anterior	0.9 ± 0.1
Rectus Femoris	1.0 ± 0.3
Vastus Lateralis	1.0 ± 0.1
Biceps Femoris	1.1 ± 0.6
Semitendinosus	1.1 ± 0.3

Table 5.2: Torque contributions by each impedance parameter for each experiment.

	Reference Damping (N·m·s/rad)	Inertia	Damping	Stiffness
Ankle	2.5	31.2 ± 6.3%	38.4 ± 5.2%	30.5 ± 8.7%
	6.25	19.4 ± 5.5%	56.5 ± 5.0%	24.1 ± 7.5%
	10	13.9 ± 4.0%	64.5 ± 5.2%	21.6 ± 7.0%
Knee	2.5	25.9 ± 5.4%	38.6 ± 5.2%	35.4 ± 8.2%
	6.25	17.5 ± 4.3%	54.9 ± 6.2%	27.7 ± 7.9%
	10	13.4 ± 3.9%	63.8 ± 5.4%	22.8 ± 7.1%

contribution of stiffness and inertia was greater than the damping coefficient's contribution; however, damping coefficient was the largest individual contributor to SMD torque across all conditions. The net torque estimated from the individual torque contributions agreed to within 7.8-26.3% of the measured load cell torque, with better agreement as damping increased.

5.5 Discussion

We recently quantified lower-limb stiffness perception; however, lower-limb damping perception is unknown. Quantifying damping perception provides insight into the interaction between the damping properties of the environment (*e.g.*, the ground, or an exoskeleton) and the human sensorimotor system. Thus, this investigation sought to quantify the human ability to sense small changes in externally-applied damping coefficients at the ankle and knee joints using a psychophysical experiment and an admittance-controlled dynamometer. The results of this study provide insight into the role of damping in biomechanics, sensorimotor control, and wearable robotic technologies.

5.5.1 Damping Perception

We calculated the WF for damping coefficient to be 12-25% and 13-31% at the ankle and knee, respectively; furthermore, Eqs. 5.4 to 5.7 can be used to estimate the JND and WF at damping values not tested in this study. These equations are supported by Weber's law, which states that the JND is a constant fraction of the reference stimulus, except at extremely low values [160]; specifically, JND increases with damping coefficient whereas WF exhibits a reciprocal relationship with damping coefficient and approaches a constant WF as damping increases. Equations 5.4 and 5.5 contain an offset, which represents sensory noise in the nervous system that dominates at low damping values [160]. In the absence of noise, the WF would be constant across all damping levels. The WF at high reference values—where the effects of sensory noise are reduced and WF becomes constant—represents the limit of perception, or 'peak' perception; for this reason, many studies summarize perception using the value that the WF approaches [158–160, 168–171]. The peak WF demonstrates that—at high damping values—humans can detect changes in damping coefficient of at least 12.0% at the ankle and 13.1% at the knee (Fig. 5.6).

In our previous work, subjects were able to—at high stiffness values—perceive changes in stiffness of 11.6% and 13.4% at the ankle and knee, respectively [3]. Therefore, stiffness and damping perception are not significantly different at the ankle or knee ($p \geq 0.836$). The similarity in results was unexpected since a previous group found that, in the upper limb, stiffness perception was 32% better than damping perception [158, 159]. The ability to perceive lower-limb damping coefficient and stiffness with similar accuracy suggests that both of these components are important for the human sensorimotor system. Specifically, information about the damping or viscous properties of an environment or wearable robotic system may be as necessary as information about its compliance. Many lower-limb experiments and wearable robots have primarily focused on the effects of stiffness on locomotion. Our results motivate further study into the effects of damping coefficient on locomotion and other dynamic tasks.

Impedance-based psychophysical results have been incorporated in pursuit-tracking tasks at the elbow joint [174, 175]. Both the stiffness and damping properties of a manipulandum affect

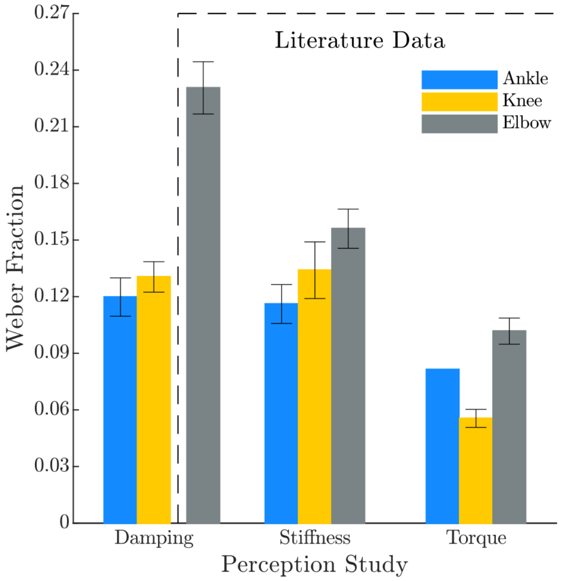

Figure 5.6: Lower-limb damping perception is comparable to lower-limb stiffness perception and better than upper-limb damping perception, at peak stimulus levels. Additionally, impedance perception is worse than torque perception across all joints. Error bars denote standard error of the mean. Ankle and knee stiffness data taken from [3]; elbow, ankle torque, and knee torque data extrapolated from [158, 159, 172, 173].

the performance of a human operator. Tracking speed improves as the stiffness of a manipulandum increases, but degrades with increased damping; tracking accuracy degrades with increasing manipulandum stiffness, but is not affected by damping. Similar studies may be used to optimize user performance when interacting with a lower-limb manipulandum (*e.g.*, an exoskeleton or prosthesis).

The reported damping perception thresholds are restricted to the damping coefficient range tested in this study (Fig. 5.5), which overlaps with the ranges used in wearable robotic devices [38, 45, 145, 150, 151]. For damping coefficients beyond this range, perception can be estimated using Eqs. 5.6 and 5.7. Future studies should characterize how impedance perception is affected by changes in multiple impedance components (stiffness and damping simultaneously), muscle activation, fatigue, footedness, and joint position, in addition to investigating how impedance perception changes in different subject populations. In particular, the effects of muscle fatigue on impedance perception should be investigated, as exoskeleton users may experience fatigue during extended operation. Furthermore, due to hardware limitations, impedance perception at the hip was not quantified; hip impedance perception should also be studied to apply these results to whole-leg exoskeletons.

5.5.2 Application in Wearable Robotics

These perception results can be integrated into the design, control, and prescription of wearable robotic systems [7]. If a robot interacting with the ankle or knee varies its damping characteristics by less than the threshold—which varies with damping level—the human operator is unlikely to sense the changes (see Section 5.5.5). This has implications for the precision needed in the development of exoskeletons, prostheses, and other wearable robots [3]. For example, individuals with neurological disorders—such as stroke or cerebral palsy—often wear an ankle-foot orthosis (AFO); however, the optimal mechanical and dynamical properties of an AFO are unknown, and should likely be tuned on an individual basis [176]. Researchers and clinicians may explore and tune the impedance properties of a robotic AFO without disturbing the patient if the changes remain below the sensory threshold [145, 151].

Additionally, haptic feedback incorporating these results may improve human-machine interaction. Psychophysical experiments inform the appropriate amount of force feedback needed with an upper-limb exoskeleton [177]. Furthermore, stiffness feedback improves performance while operating a haptic gas pedal [178]. Although the use of damping feedback at the lower-limb is relatively unexplored, haptic interfaces often use damping and impedance as a form of feedback [179, 180]. There exists a possibility of integrating impedance feedback with exoskeletons; in these applications, users will likely be able to perceive the feedback if the damping coefficient changes by more than the perception threshold.

5.5.3 Comparison to Elbow and Torque Perception

Elbow perception of torque, stiffness, and damping coefficient, in addition to ankle and knee perception of torque, have been studied by different research groups [158, 159, 166, 172, 173]. An important difference in experimental design is that many of these studies tested perception via matching tasks, which calculate the WF at the point in which subjects would correctly detect a change 84% of the time, instead of the 2IFC procedure used in this work; other studies tested perception at the 71% performance point. To fairly compare these values, Eq. 5.3 was used to extrapolate the peak WFs from previous investigations to the 75% point (Fig. 5.6). This extrapolation method is valid assuming that perception is a Gaussian process, and has been shown to hold experimentally [160, 166]. Furthermore, we recently characterized the psychometric function (*i.e.*, quantified the WF across all performance points) for stiffness perception using a prosthetic ankle [7]. Using data from that study, our extrapolation method estimated the 75% WF from the 84% WF to within 0.005. Therefore, we concluded that extrapolation using Eq. 5.3 was appropriate.

We found that humans can detect smaller changes in damping coefficient at the lower limb than at the upper limb; the difference between both lower-limb WFs and elbow WF was significant ($p <$ 0.001). Better damping perception at the lower limb may suggest that the activities typically performed by the legs (*e.g.*, walking) rely on the viscous properties of the environment more than those typically performed by the arms (*e.g.*, manipulation); however, a more systematic study focused on comparing upper- and lower-limb activities and their damping properties is needed. Furthermore, damping coefficient WF is higher than torque WF ($p \leq$ 0.006), as expected. Recent work suggesting that muscle spindles in passive muscles code for force and the time-derivative of force, instead of length and velocity, supports the improved performance in torque perception [181]. The importance of impedance (stiffness and damping) in sensorimotor control and motor performance is supported by the human ability to sense small changes in these properties [158]. Further studies are needed to completely comprehend how the body regulates and senses its impedance during dynamic tasks.

5.5.4 Strategies

Damping perception was likely informed by the subjects' joint torques and velocities [158]. Subjects produced higher torques but moved slower as damping coefficient increased (Fig. 5.5); however, the precise manner in which kinetics and kinematics individually contribute to damping perception is still unclear. Additionally, the standard deviation of maximum torques produced by subjects—particularly in the ankle experiment—is quite large (Fig. 5.5), suggesting that subjects used a wide range of effort to interact with the system. More specific studies—that isolate the effects of kinematics and kinetics to characterize how the nervous system combines these cues—are needed to understand the mechanisms underlying impedance perception fully [182, 183].

This investigation focused on the ability to sense small changes in damping coefficient. Therefore, the admittance controller's inertia and stiffness were constant across all trials, leading to a constant natural frequency and varying damping ratio. This work facilitates a foundation for our understanding of lower-limb damping perception; additional studies will seek to understand the effects that changes in torque, velocity, stiffness, and inertia have on damping perception.

5.5.5 Limitations

In our previous stiffness perception study, stiffness accounted for approximately 62% to 82% of the SMD dynamics. In this damping perception study, damping accounted for 38% to 64% of the dynamics (Table 5.2). Stiffness is typically the largest torque source during walking [84]; however, for this experiment, we sought to increase the contributions of damping, to ensure that subjects were primarily interacting with a viscous system. Damping coefficient was the largest contributor to the SMD torque, but stiffness and inertia contributed comparably at the lowest damping level. Due to practical limitations in the dynamometer control system, stiffness and inertia contributed between 13% and 35% of the net torque. However, damping coefficient was the only parameter that changed throughout the experiment—stiffness and inertia were constant across all trials. Thus we concluded that subjects indeed perceived changes in damping.

We were only able to test a limited range of damping coefficients. Reference damping values above 10 N·m·s/rad created substantial resistive torque, requiring considerable effort from the subjects, and making the experiment too strenuous to complete. Adding reference damping values above 10 N·m·s/rad would improve the regressions and likely converge to a constant WF. However, even with the limited range of damping coefficients tested, the trends in Fig. 5.4 suggest that the constant WFs at higher damping values would likely be similar to the peak WFs we measured.

This work provides insight into how much an ankle or knee robot's damping characteristics may change while remaining unnoticed by the human operator. However, it is unclear how changes of such magnitude impact gait dynamics, even if subjects do not perceive the changes. The effects of changing the mechanical behavior of a robotic device interacting with the human body must be carefully studied to ensure safety, particularly during dynamics tasks. Future research on impedance-based assistive devices should investigate how variable impedance affects gait and perception.

The high amount of concentration required by subjects made damping perception challenging; therefore, subjects used a blindfold and noise-reducing headphones to minimize distractions. Additionally, changes to intrinsic joint impedance may alter perception of externally-applied joint impedance during locomotion [84, 134, 143, 144]. Understanding the relationship between intrinsic impedance modulation and external impedance perception is challenging because it requires perturbation-based system identification techniques in conjunction with psychophysical studies. Furthermore, during gait, vestibular sensations contribute to the perception of changing dynamics [7]. In summary, the threshold for damping perception is likely different during locomotion due to reduced concentration, varying intrinsic properties, and the addition of vestibular sensations. However, understanding the effects of nonstationary biomechanical conditions on damping perception requires further study.

In these experiments, straps were used to secure the foot/shank to the metal plates, and padding was added to prevent discomfort, particularly at the heel. The straps and padding provide an additional source of sensory information; however, previous studies have shown that cutaneous information has little to no effect on the perception of displacement and stiffness at the knee and fingers, respectively [184, 185]. Therefore, we concluded that the straps and padding did not affect damping perception.

5.6 Summary

This work examined the human ability to perceive small changes in damping coefficients when interacting with a mechanical system at the ankle or knee joint. We estimated damping perception by implementing an adaptive staircase method with a dynamometer that rendered a virtual rotational spring-mass-damper system. The ability to perceive changes in damping coefficient was similar to that of stiffness, suggesting that both impedance parameters are essential for sensorimotor control of the lower extremities. These results offer insight and motivate further investigation on the role of damping coefficient in biomechanics, motor control, and wearable robotic technologies.

Chapter 6

Concluding Remarks

6.1 Contributions

In this dissertation, I present both technical and scientific contributions for the advancement of lower-limb bionic systems. The first contribution of this thesis was the development and dissemination of the OSL. We designed the OSL with performance comparable to—or better than—existing legs, tested it in a clinical setting, and have enabled 8 other research groups to use it. For some of these groups, this is their first time using a bionic leg; for others, they are replacing their previous bionic legs with the OSL. The second contribution was developing the tools to rigorously characterize open-loop control impedance control systems, along with evaluating the efficiency of multiple bionic systems across power regimes; we also show how to achieve accurate impedance control without the need for a torque feedback signal. Finally, we developed and executed the first set of studies investigating perception of lower-limb impedance, with respect to external devices such as exoskeletons. In addition to deepening our understanding of the role of impedance in the human body, this work provides guidance on how to develop impedance-based assistance or haptic feedback with bionic systems.

6.2 Next Steps for the Open-source Leg

In its current state, the OSL provides clinically meaningful performance for individuals with amputation; to improve its capabilities as a research device, where more precise output dynamics may be needed, a number of studies should be performed. First, as an extension of Chapter 4, the open-loop controller should be characterized; this will require a separate system, similar to the Neurobionics Rotary Dynamometer, to apply perturbations to the knee and ankle joints. Second, the dynamics of the belt drive under different tension levels, independent of control system, should also be characterized; this can likely be accomplished using perturbation-based methods similar to the impedance characterization. Characterizing the belt drives will enable better modeling of the transmission dynamics, which could improve open-loop impedance control further. Finally, the SEA on the knee should be integrated with the control system to enable closed-loop impedance and torque control.

Once the OSL's impedance controller has been fully developed, the OSL can be used as a test-bench for new biologically-inspired control strategies. Our group, along with others, quantified the impedance of the human ankle during walking, providing biological stiffness and damping profiles that can be used in a control system [84, 134, 143]. To understand the potential benefits of impedance control, particularly with respect to external perturbations (*e.g.*, uneven terrain), we recommend an experiment that rigorously compares the performance of biologically-inspired position, torque, and impedance controllers on biomechanics, metabolic cost, and user satisfaction.

As previously mentioned, many research groups are developing high-performing mid-level control strategies, but they have never been directly compared. The OSL provides an opportunity to begin these comparisons. The first three external labs to use the OSL—the Center for Bionic Medicine (clinically-based control), Locomotor Control Systems Lab (phase-based control), and the Hartmut Geyer Lab (neuromuscular model control)—have developed promising control strategies in the past [45, 51, 87]. These controllers should be tested and compared directly in a study investigating their performance across ambulation modes, both in structured (ambulation circuit or treadmill) and unstructured settings. Performing direct comparisons on vastly different control strategies will allow us to determine the strengths and weakness of each approach, eventually leading to better strategies overall. On a similar note, once research labs begin to publish results with the OSL, I recommend completing a review that synthesizes all the different approaches and results, and makes new recommendations for control strategies.

6.3 Next Steps for Bionics

While developing the OSL, we observed a lack of rigorous characterization and incomplete specifications reported when designing bionic systems, with the exception of a few research groups [49,50,56,61]. Lack of transparency, and perhaps lack of characterization, makes comparing controls results across different systems even more challenging. We recommend designers of bionic legs and exoskeletons characterize and clearly state—at a minimum—the specifications shown in Table 6.1.

As seen in the OSL and other recently developed bionic systems, high-torque motors with low transmission ratios provide many benefits over low-torque motors with high transmission ratios [49, 50, 141, 142]. We recommend using ER-BLDC motors because, in addition to being more compact, efficient (electrical power loss and temperature), and easier to backdrive, these systems are more straightforward for implementing open-loop control strategies; however, because these motors are relatively new, they require even more characterization than the more established motors used historically (*e.g.*, maxon motors).

Bionics research has focused on design and controls research, but rigorous user-focused research is needed as well; in fact, gaining a better understanding of the user's perspective may

Table 6.1: Minimum specifications to report for bionic systems.

Physical	Performance
Mass	Peak torque[b]
Build height	Peak speed
Range of motion	Position bandwidth[c]
Transmission ratio	Closed-loop torque bandwidth[a,c]
Series stiffness[a]	Open-loop torque control[a]
Parallel stiffness[a]	Open-loop impedance control[a]

[a] If applicable
[b] Continuous and instantaneous
[c] Including the corresponding magnitude

provide the most practical impact in the future. The damping perception study presented here provides a foundation for understanding how users interact with exoskeletons, but there are still many unanswered questions. For example, how well can users perceive change in stiffness and damping at each joint while walking? While going up and down stairs or ramps? How does this change with a rigid (higher stiffness) or soft (lower stiffness) interface? Can an exoskeleton change its impedance-based assistance over time as the user's needs change, without the user noticing? Understanding the relationship between control and the user experience will be critical for both short- and long-term satisfaction with exoskeletons.

Appendix A

Open-source Leg: Mechanical Drawings

The drawings in this appendix correspond to the initial release of the OSL, which was used in Chapter 3. The latest drawings are available on `www.opensourceleg.com`.

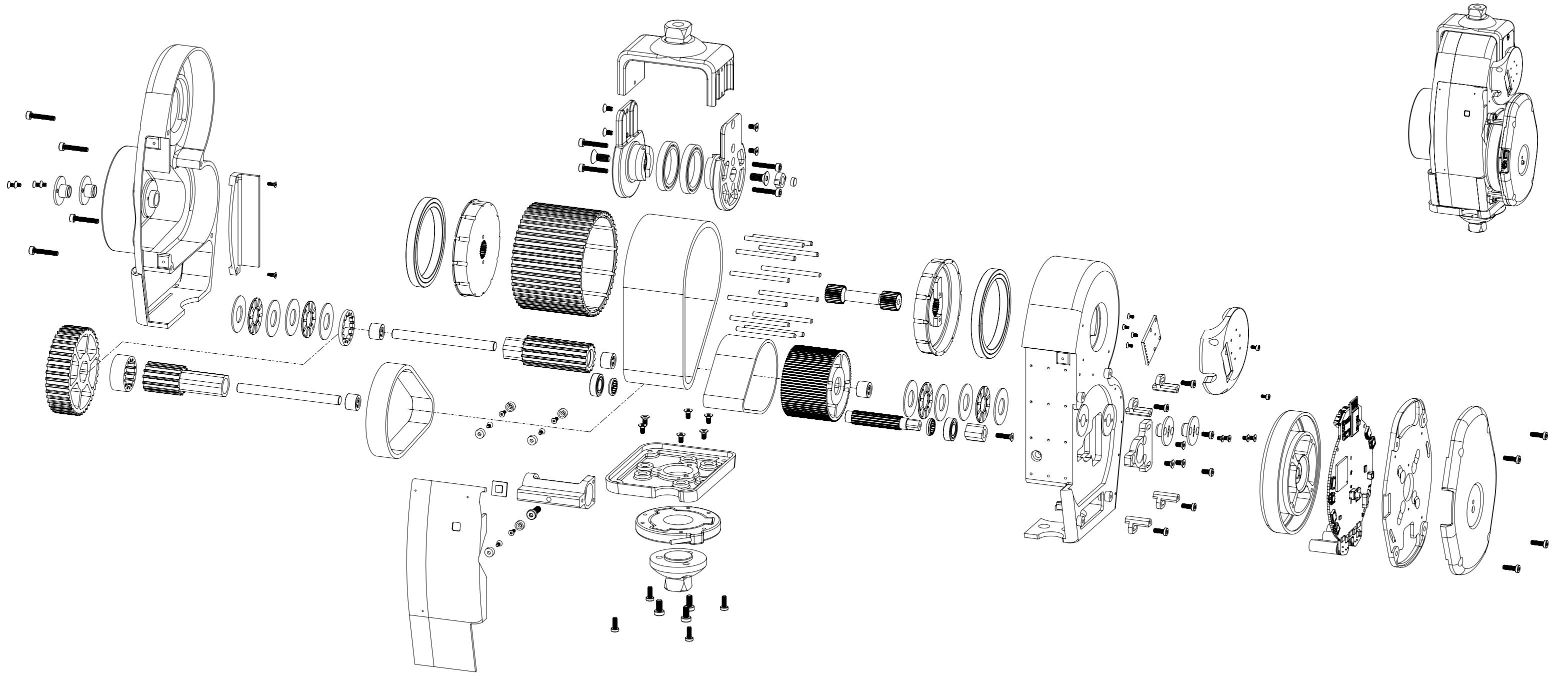

Figure A.1: OSL knee exploded view.

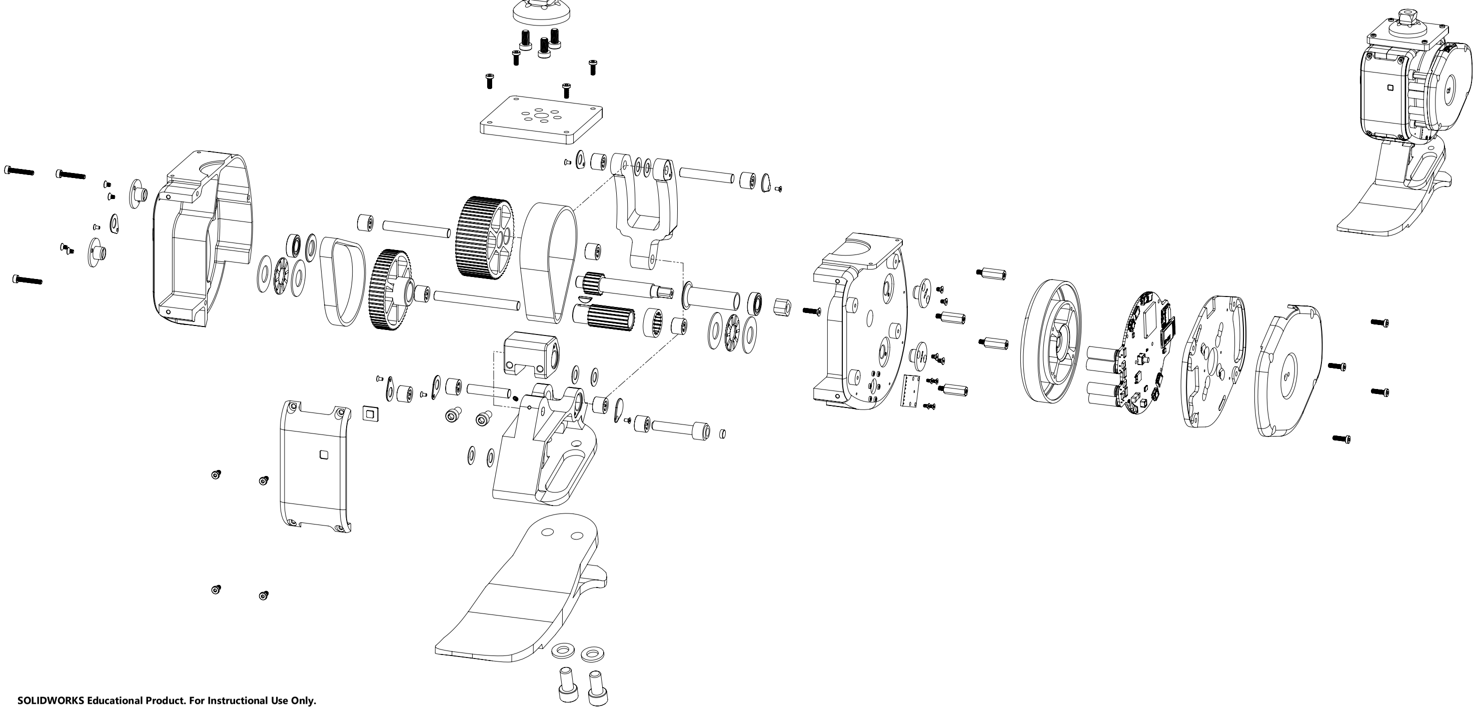

Figure A.2: OSL ankle exploded view.

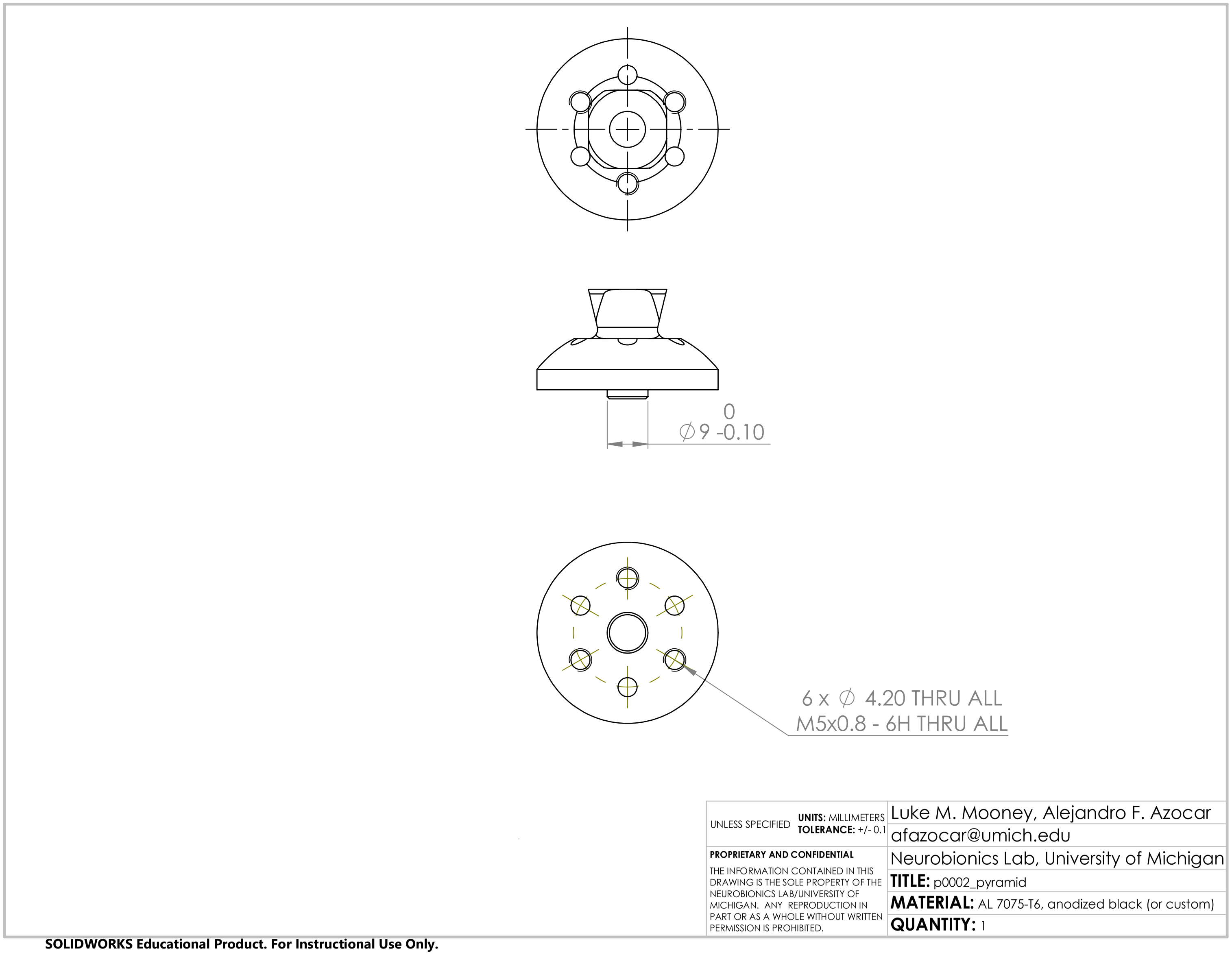

UNLESS SPECIFIED **UNITS:** MILLIMETERS **TOLERANCE:** +/- 0.1

Luke M. Mooney, Alejandro F. Azocar
afazocar@umich.edu
Neurobionics Lab, University of Michigan

PROPRIETARY AND CONFIDENTIAL

THE INFORMATION CONTAINED IN THIS DRAWING IS THE SOLE PROPERTY OF THE NEUROBIONICS LAB/UNIVERSITY OF MICHIGAN. ANY REPRODUCTION IN PART OR AS A WHOLE WITHOUT WRITTEN PERMISSION IS PROHIBITED.

TITLE: p0002_pyramid
MATERIAL: AL 7075-T6, anodized black (or custom)
QUANTITY: 1

Figure A.3: OSL pyramid connector, compatible with M3564F loadcell.

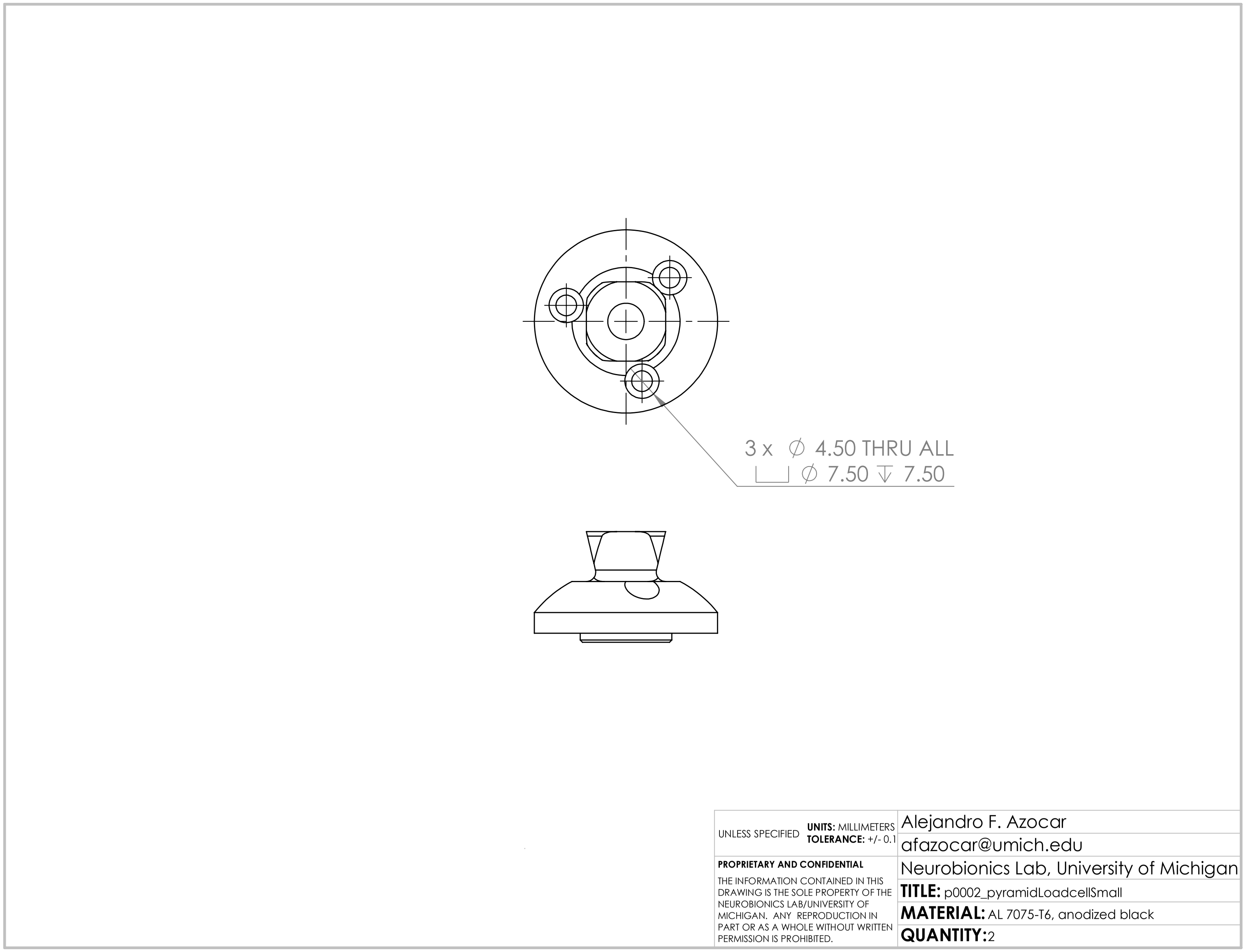

Figure A.4: OSL pyramid connector, compatible with M3554E loadcell.

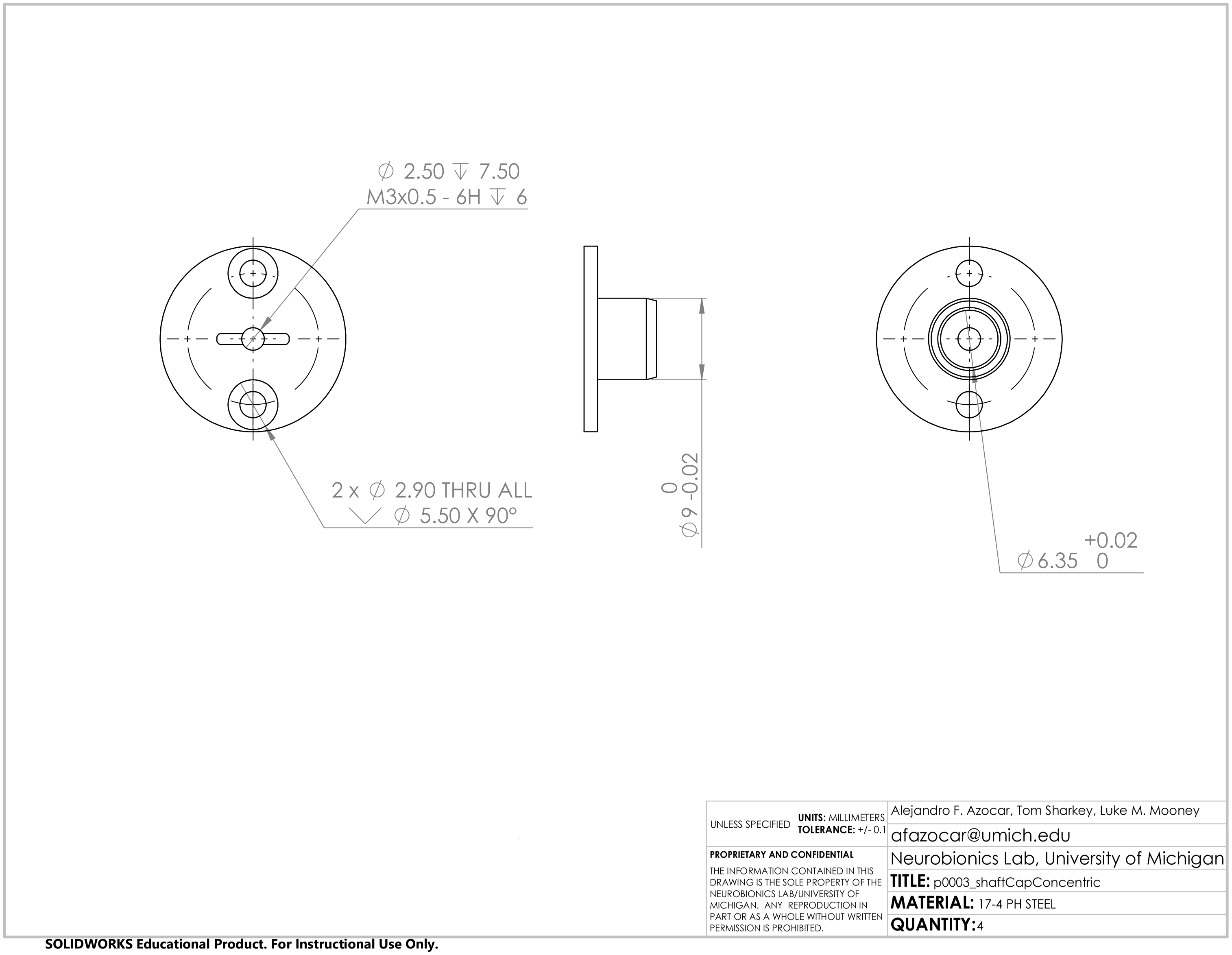

Figure A.5: OSL shaft cap, concentric.

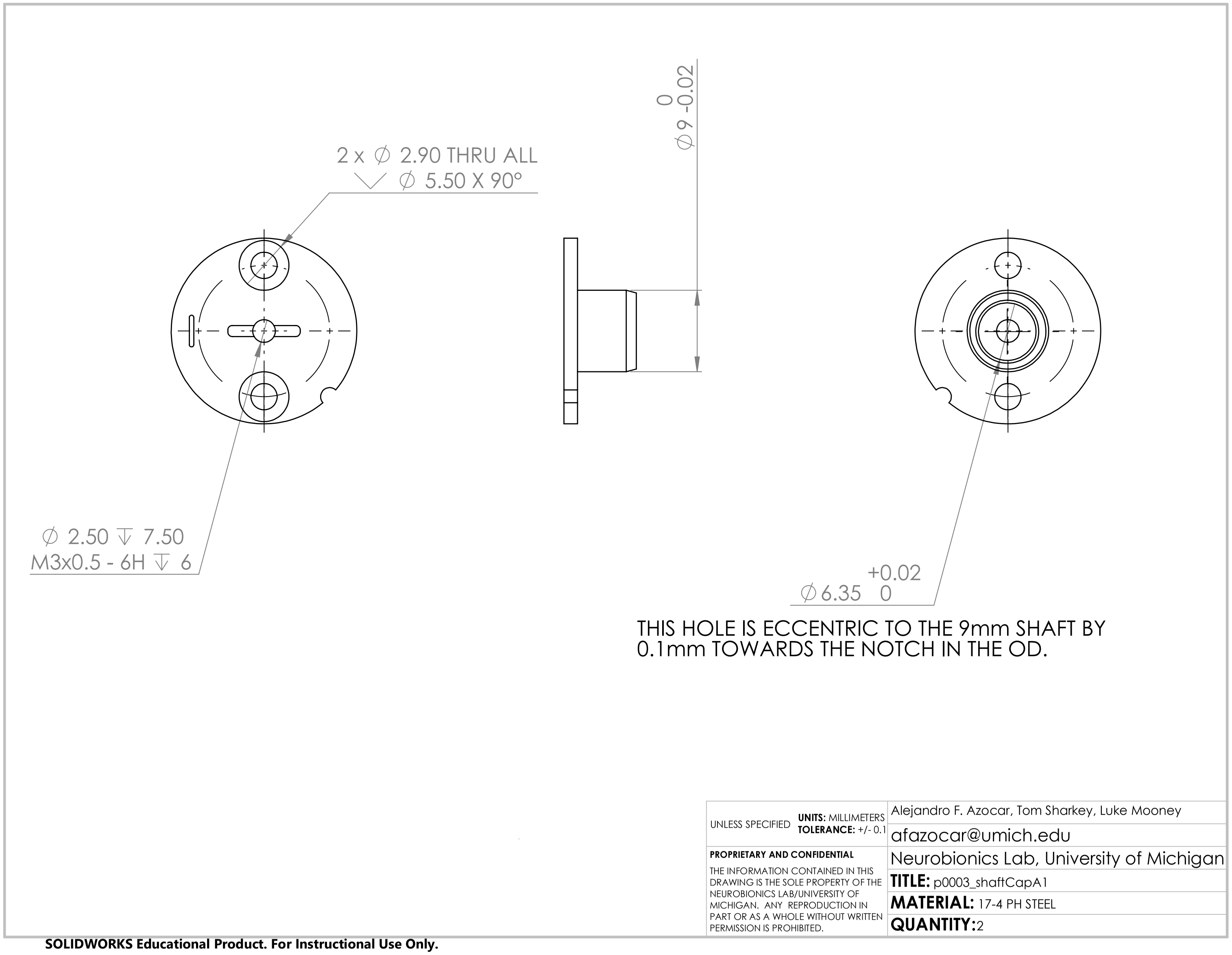

Figure A.6: OSL shaft cap, 0.1 mm offset (side A).

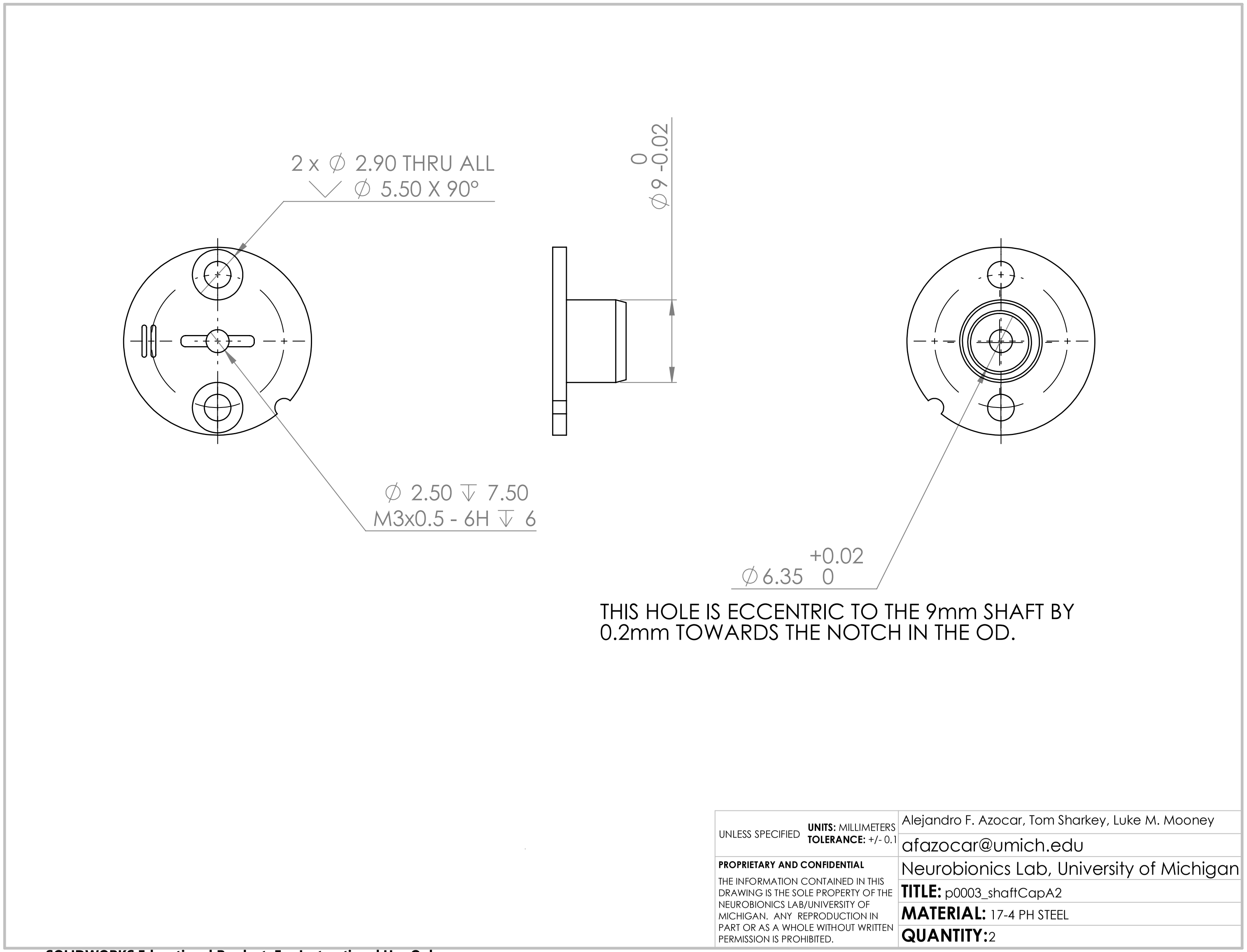

THIS HOLE IS ECCENTRIC TO THE 9mm SHAFT BY 0.2mm TOWARDS THE NOTCH IN THE OD.

UNLESS SPECIFIED **UNITS:** MILLIMETERS **TOLERANCE:** +/- 0.1

PROPRIETARY AND CONFIDENTIAL
THE INFORMATION CONTAINED IN THIS DRAWING IS THE SOLE PROPERTY OF THE NEUROBIONICS LAB/UNIVERSITY OF MICHIGAN. ANY REPRODUCTION IN PART OR AS A WHOLE WITHOUT WRITTEN PERMISSION IS PROHIBITED.

Alejandro F. Azocar, Tom Sharkey, Luke M. Mooney
afazocar@umich.edu
Neurobionics Lab, University of Michigan
TITLE: p0003_shaftCapA2
MATERIAL: 17-4 PH STEEL
QUANTITY:2

Figure A.7: OSL shaft cap, 0.2 mm offset (side A).

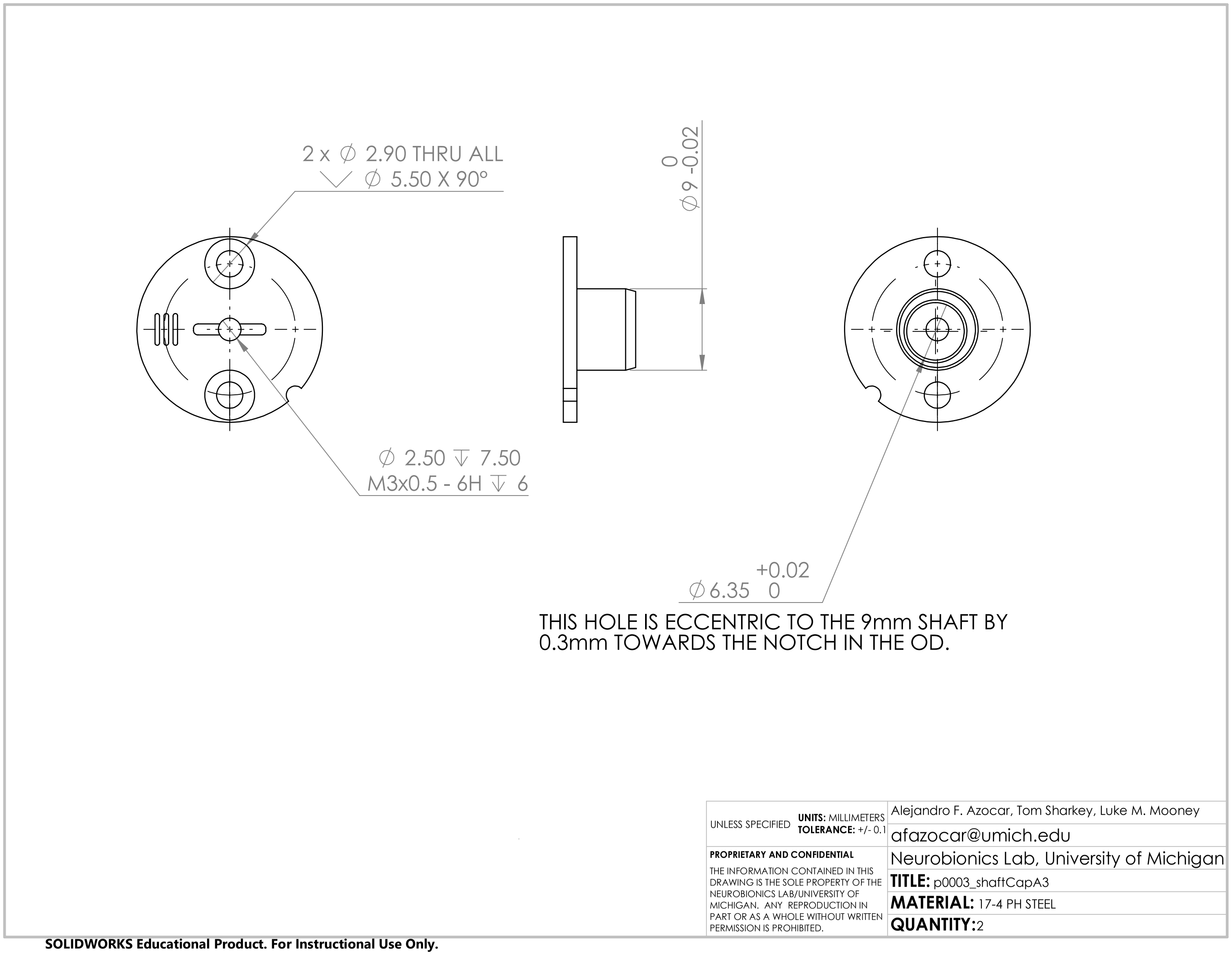

Figure A.8: OSL shaft cap, 0.3 mm offset (side A).

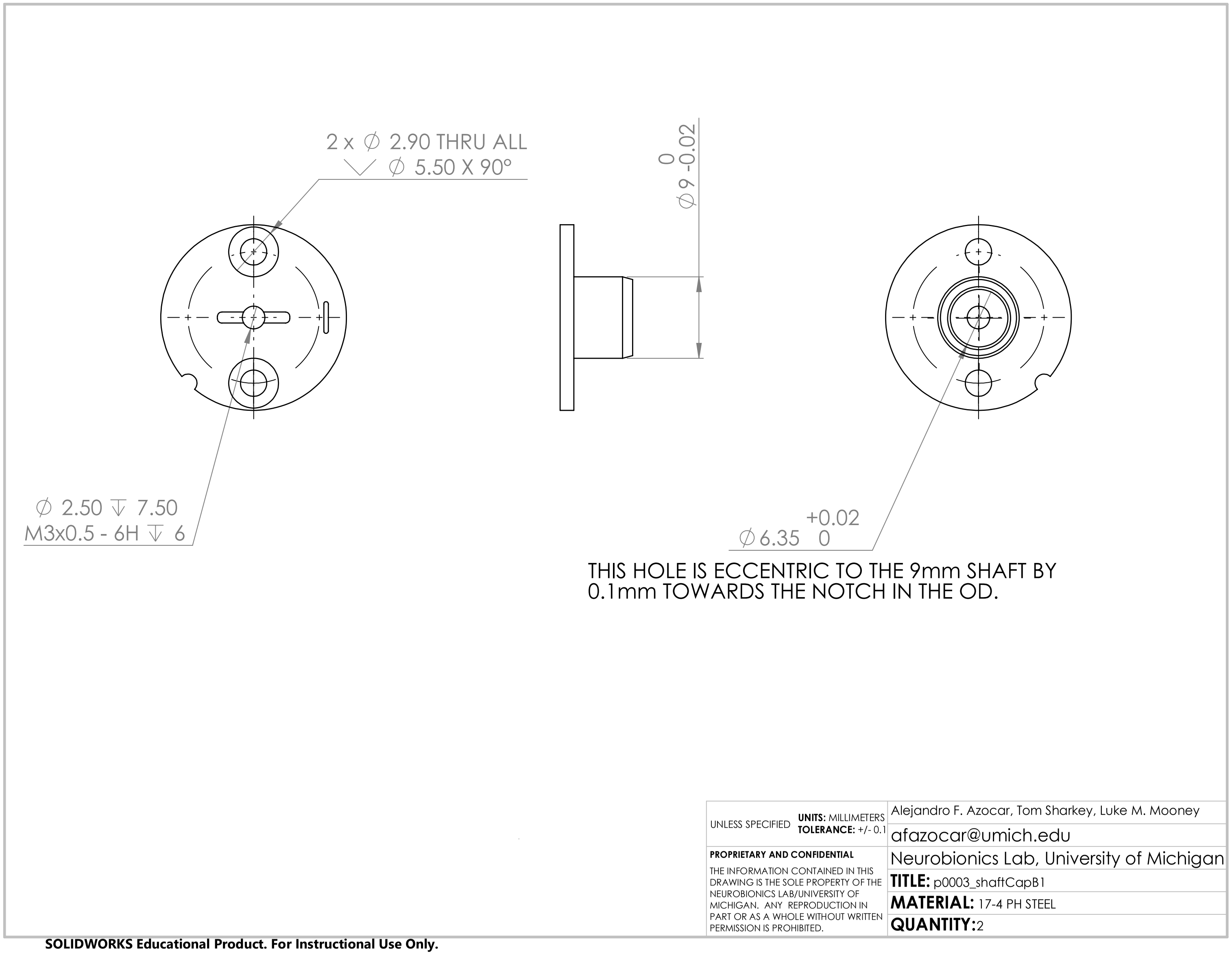

THIS HOLE IS ECCENTRIC TO THE 9mm SHAFT BY 0.1mm TOWARDS THE NOTCH IN THE OD.

UNLESS SPECIFIED **UNITS:** MILLIMETERS **TOLERANCE:** +/- 0.1

PROPRIETARY AND CONFIDENTIAL

THE INFORMATION CONTAINED IN THIS DRAWING IS THE SOLE PROPERTY OF THE NEUROBIONICS LAB/UNIVERSITY OF MICHIGAN. ANY REPRODUCTION IN PART OR AS A WHOLE WITHOUT WRITTEN PERMISSION IS PROHIBITED.

Alejandro F. Azocar, Tom Sharkey, Luke M. Mooney
afazocar@umich.edu
Neurobionics Lab, University of Michigan
TITLE: p0003_shaftCapB1
MATERIAL: 17-4 PH STEEL
QUANTITY:2

Figure A.9: OSL shaft cap, 0.1 mm offset (side B).

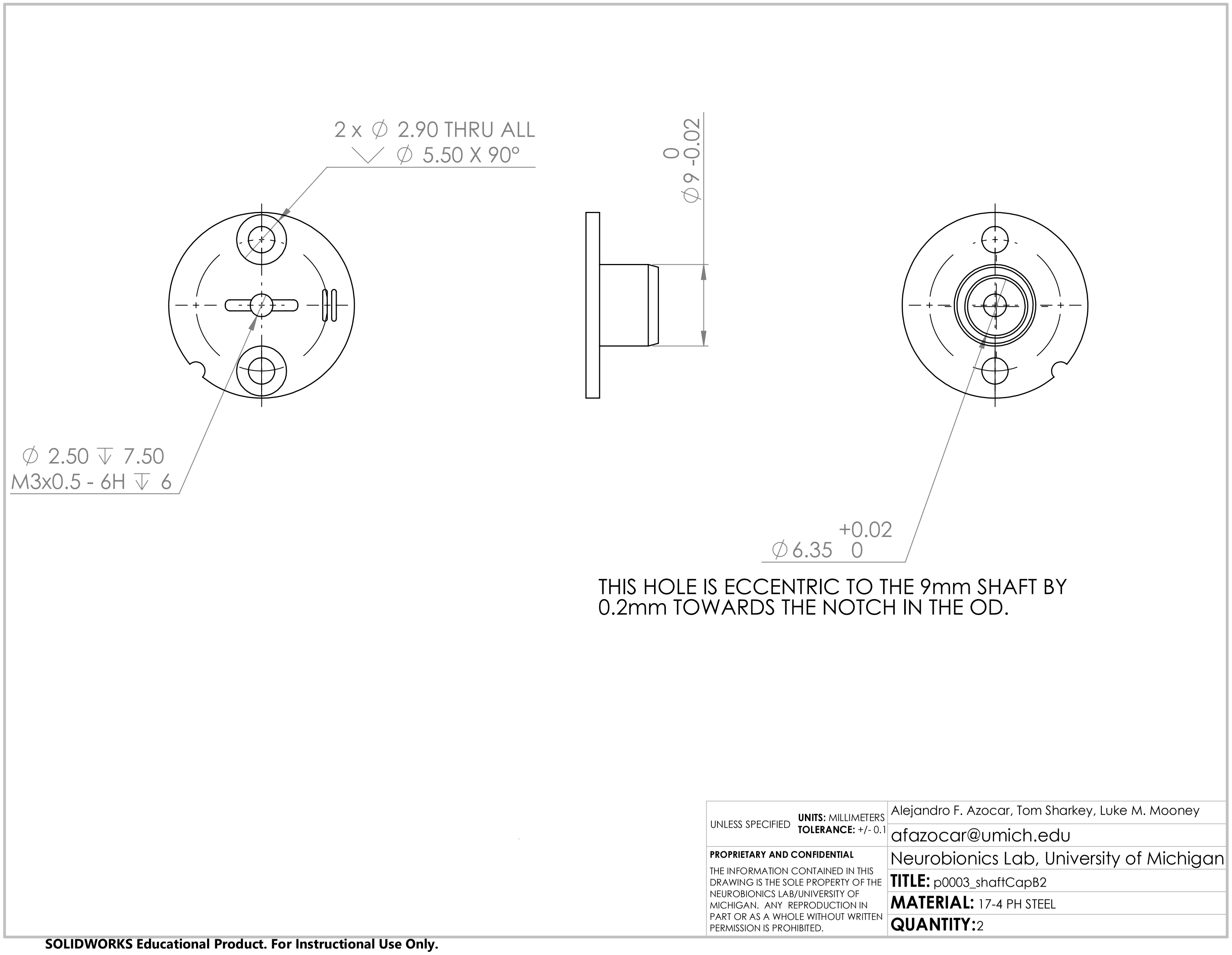

Figure A.10: OSL shaft cap, 0.2 mm offset (side B).

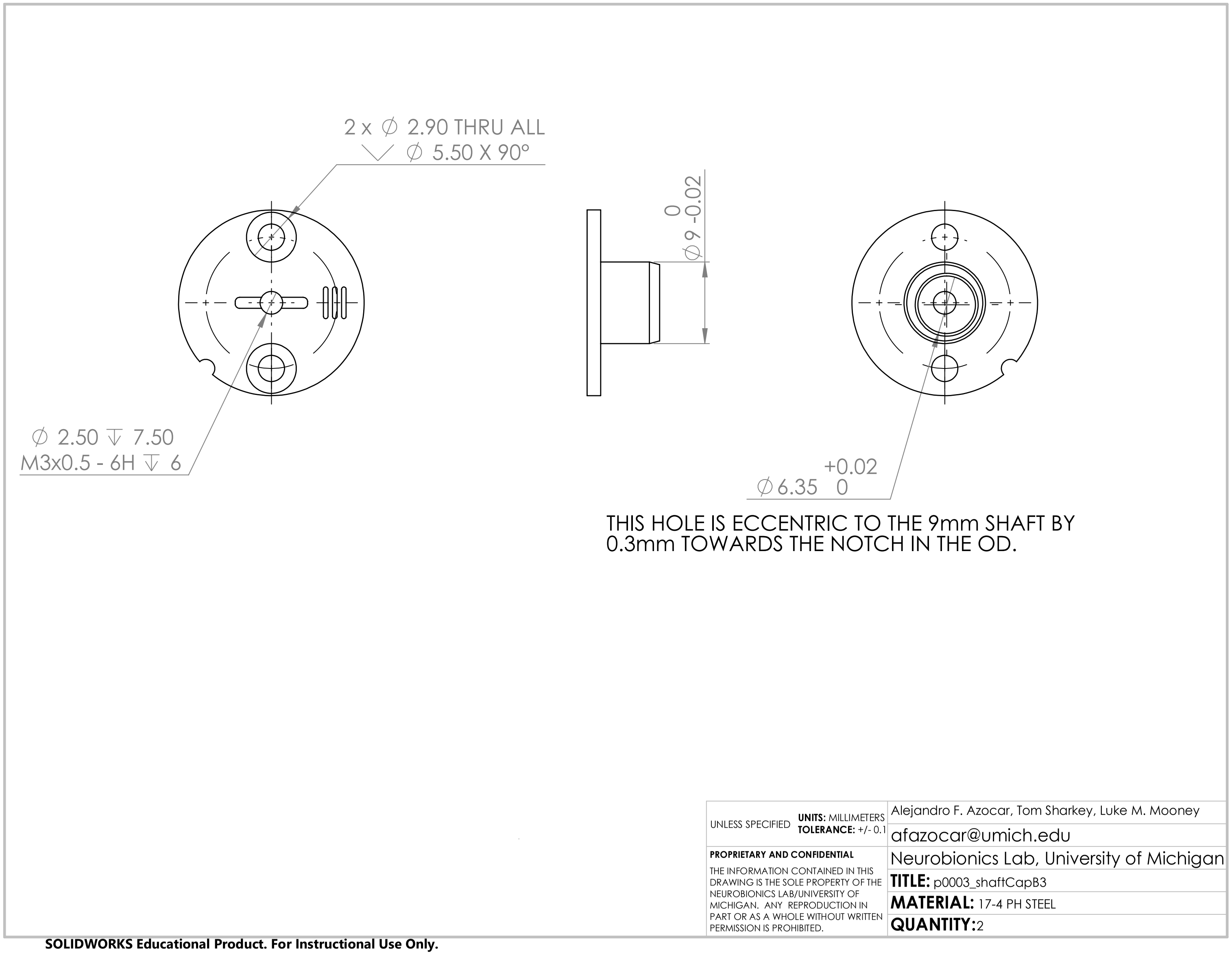

Figure A.11: OSL shaft cap, 0.3 mm offset (side B).

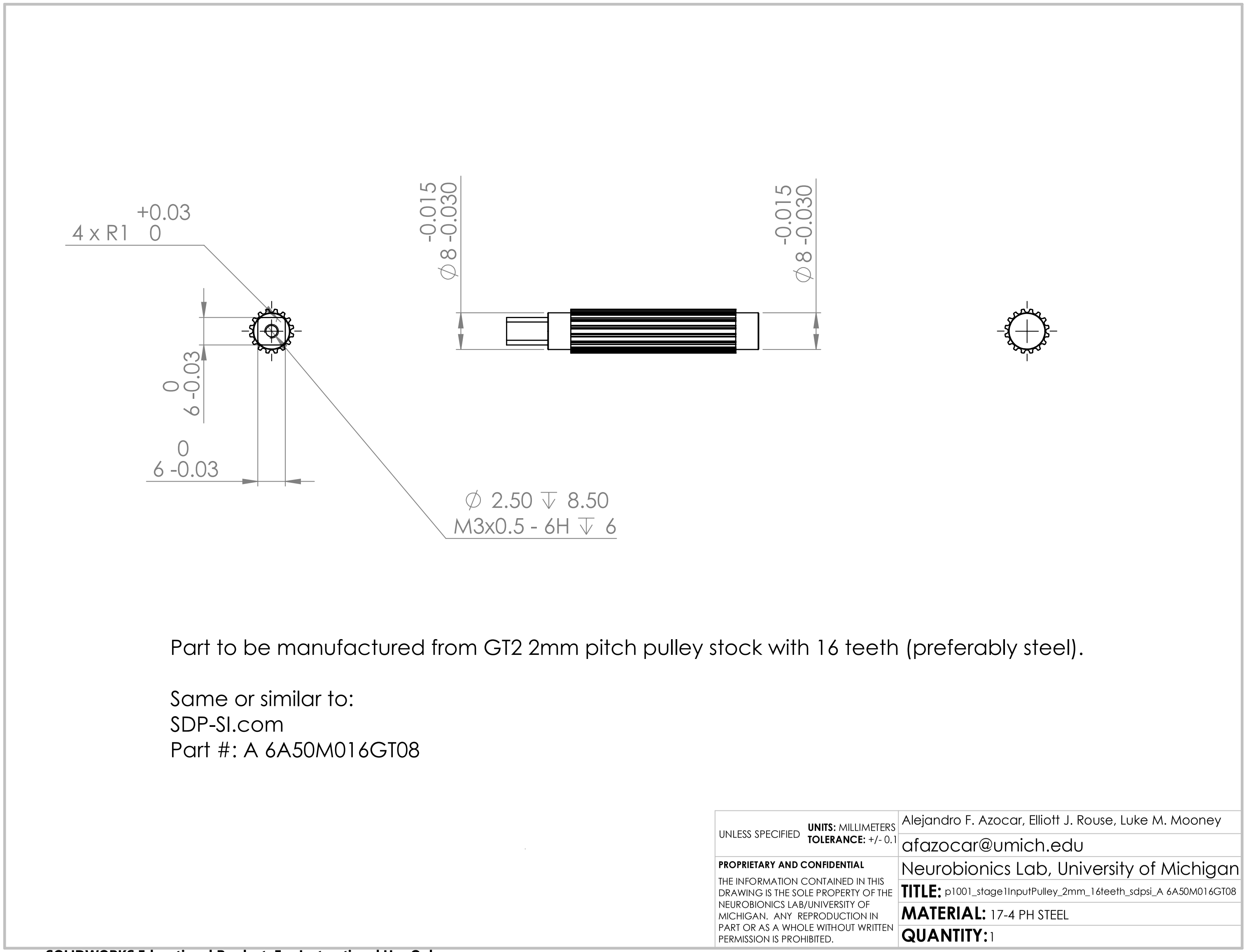

Part to be manufactured from GT2 2mm pitch pulley stock with 16 teeth (preferably steel).

Same or similar to:
SDP-SI.com
Part #: A 6A50M016GT08

UNLESS SPECIFIED **UNITS:** MILLIMETERS **TOLERANCE:** +/- 0.1	Alejandro F. Azocar, Elliott J. Rouse, Luke M. Mooney afazocar@umich.edu
PROPRIETARY AND CONFIDENTIAL THE INFORMATION CONTAINED IN THIS DRAWING IS THE SOLE PROPERTY OF THE NEUROBIONICS LAB/UNIVERSITY OF MICHIGAN. ANY REPRODUCTION IN PART OR AS A WHOLE WITHOUT WRITTEN PERMISSION IS PROHIBITED.	Neurobionics Lab, University of Michigan **TITLE:** p1001_stage1InputPulley_2mm_16teeth_sdpsi_A 6A50M016GT08 **MATERIAL:** 17-4 PH STEEL **QUANTITY:** 1

Figure A.12: OSL knee stage 1 input pulley.

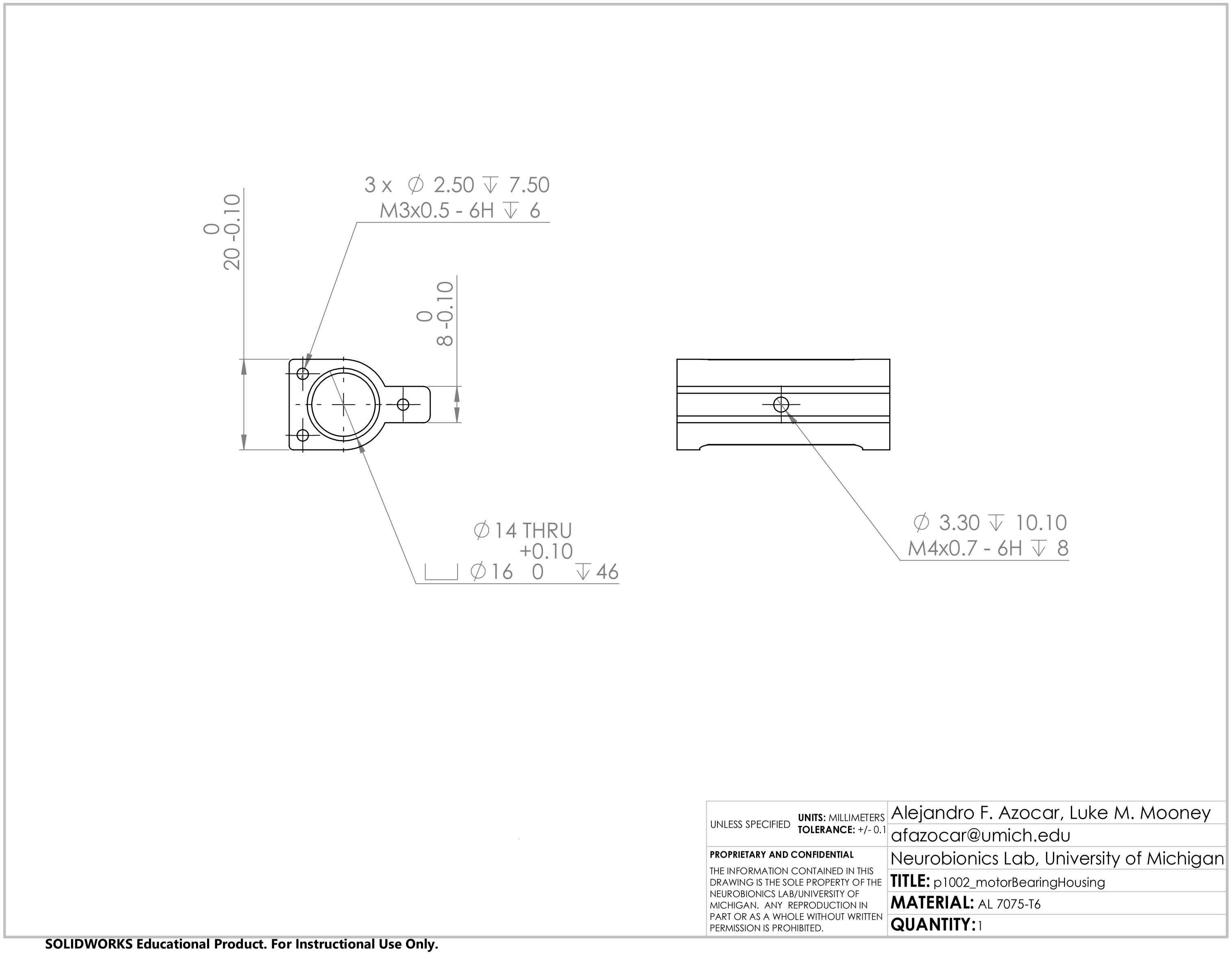

Figure A.13: OSL knee motor bearing housing.

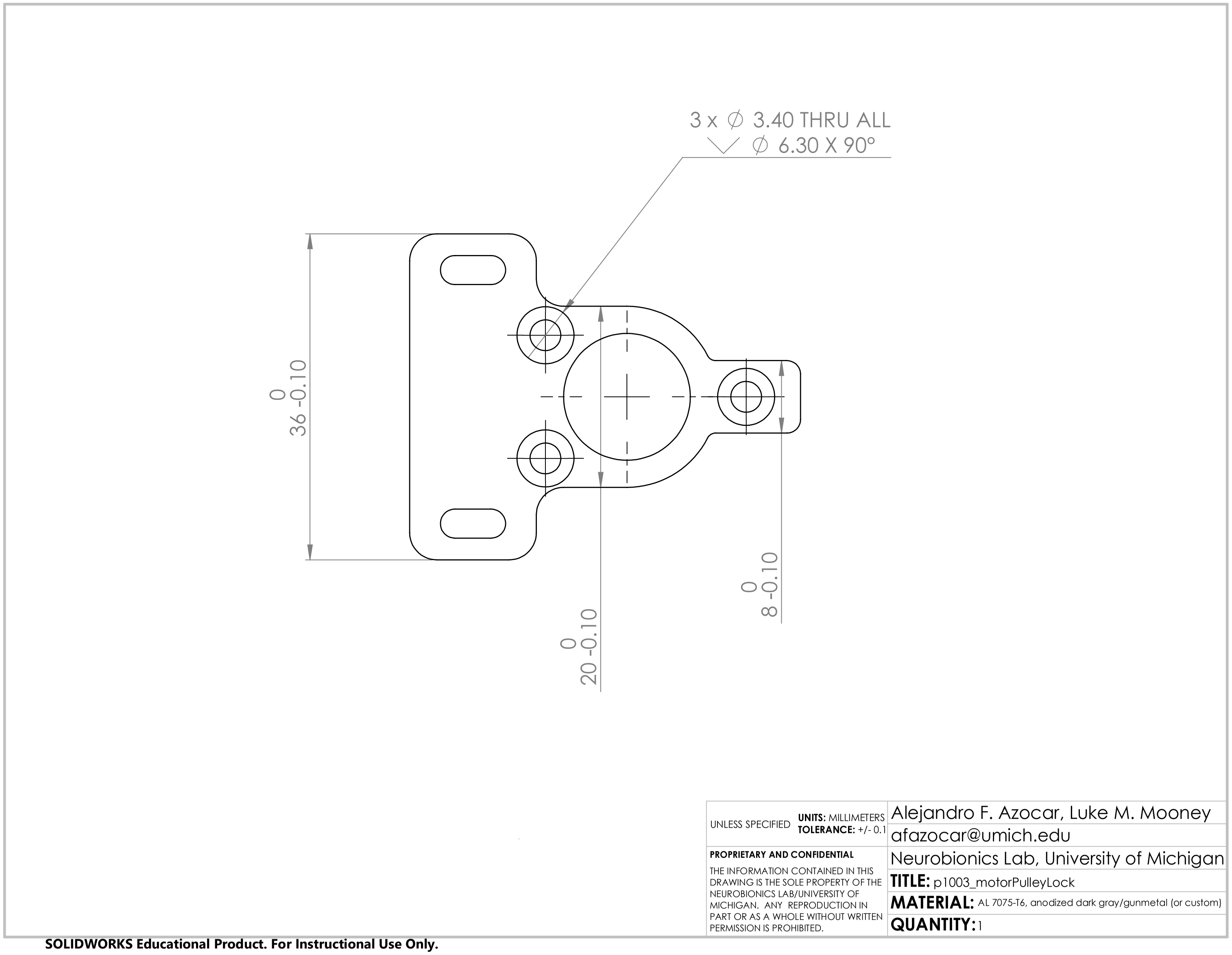

UNLESS SPECIFIED **UNITS:** MILLIMETERS
TOLERANCE: +/- 0.1

PROPRIETARY AND CONFIDENTIAL
THE INFORMATION CONTAINED IN THIS DRAWING IS THE SOLE PROPERTY OF THE NEUROBIONICS LAB/UNIVERSITY OF MICHIGAN. ANY REPRODUCTION IN PART OR AS A WHOLE WITHOUT WRITTEN PERMISSION IS PROHIBITED.

Alejandro F. Azocar, Luke M. Mooney
afazocar@umich.edu
Neurobionics Lab, University of Michigan
TITLE: p1003_motorPulleyLock
MATERIAL: AL 7075-T6, anodized dark gray/gunmetal (or custom)
QUANTITY: 1

Figure A.14: OSL knee motor pulley lock.

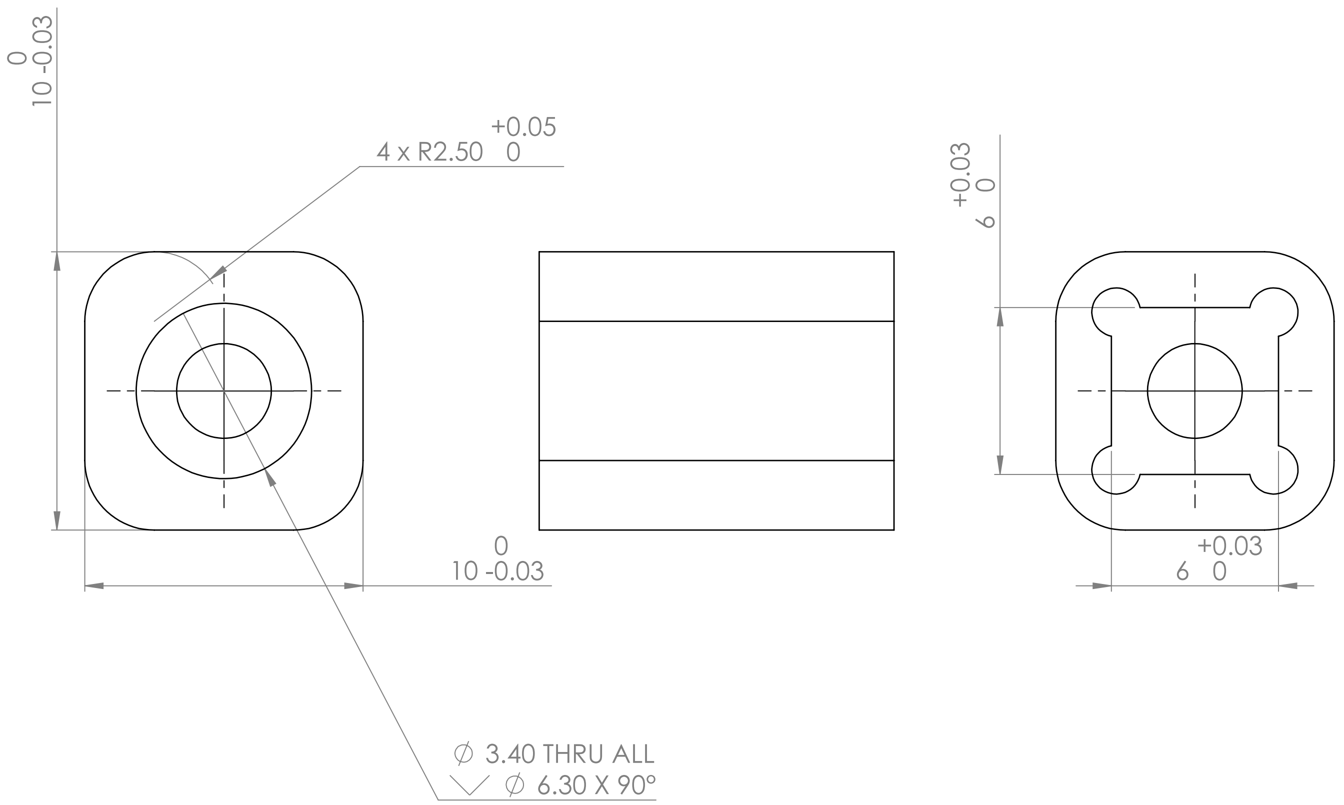

UNLESS SPECIFIED **UNITS:** MILLIMETERS **TOLERANCE:** +/- 0.1	Alejandro F. Azocar afazocar@umich.edu
PROPRIETARY AND CONFIDENTIAL THE INFORMATION CONTAINED IN THIS DRAWING IS THE SOLE PROPERTY OF THE NEUROBIONICS LAB/UNIVERSITY OF MICHIGAN. ANY REPRODUCTION IN PART OR AS A WHOLE WITHOUT WRITTEN PERMISSION IS PROHIBITED.	Neurobionics Lab, University of Michigan **TITLE:** p1004_motorCouplingKnee **MATERIAL:** AL 7075-T6 **QUANTITY:**2

SOLIDWORKS Educational Product. For Instructional Use Only.

Figure A.15: OSL knee motor coupling.

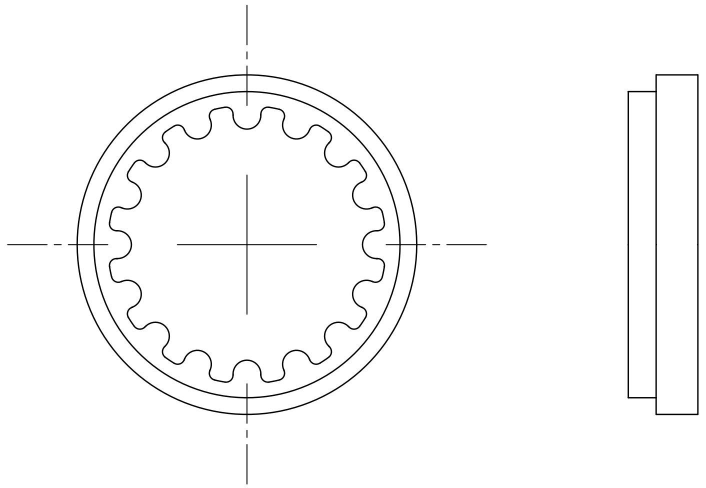

UNLESS SPECIFIED **UNITS:** MILLIMETERS **TOLERANCE:** +/- 0.1	Luke M. Mooney, Alejandro F. Azocar afazocar@umich.edu
PROPRIETARY AND CONFIDENTIAL THE INFORMATION CONTAINED IN THIS DRAWING IS THE SOLE PROPERTY OF THE NEUROBIONICS LAB/UNIVERSITY OF MICHIGAN. ANY REPRODUCTION IN PART OR AS A WHOLE WITHOUT WRITTEN PERMISSION IS PROHIBITED.	Neurobionics Lab, University of Michigan **TITLE:** p1005_pulleyFlange_stage1Input **MATERIAL:** ABS, black **QUANTITY:**4

Figure A.16: OSL knee stage 1 input pulley flange.

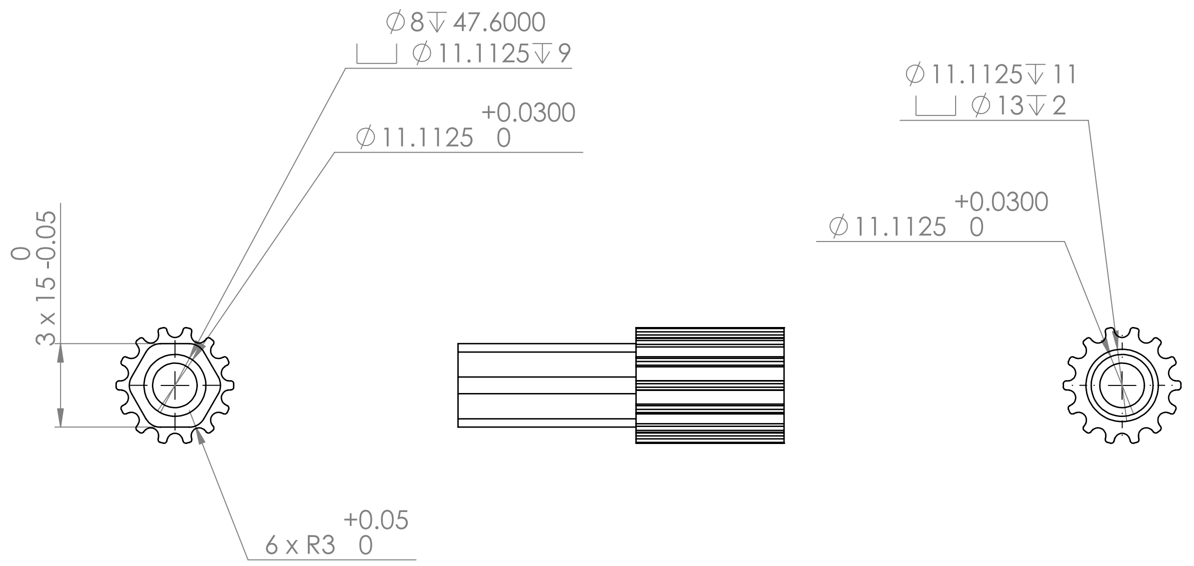

Part to be manufactured from GT2 5mm pitch aluminum pulley stock with 14 teeth.

Same or similar to:
SDP-SI.com
Part #: A 6A54M014GT18

Note: p1006 and p1007 may slide relative to each other, but should not rotate relative to each other.

UNLESS SPECIFIED **UNITS:** MILLIMETERS **TOLERANCE:** +/- 0.1

PROPRIETARY AND CONFIDENTIAL
THE INFORMATION CONTAINED IN THIS DRAWING IS THE SOLE PROPERTY OF THE NEUROBIONICS LAB/UNIVERSITY OF MICHIGAN. ANY REPRODUCTION IN PART OR AS A WHOLE WITHOUT WRITTEN PERMISSION IS PROHIBITED.

Luke M. Mooney, Alejandro F. Azocar
afazocar@umich.edu
Neurobionics Lab, University of Michigan
TITLE: p1006_stage2InputPulley_5mm_14teeth_sdpsi_A 6A54M014GT18
MATERIAL: AL 7075-T6
QUANTITY: 1

Figure A.17: OSL knee stage 2 input pulley.

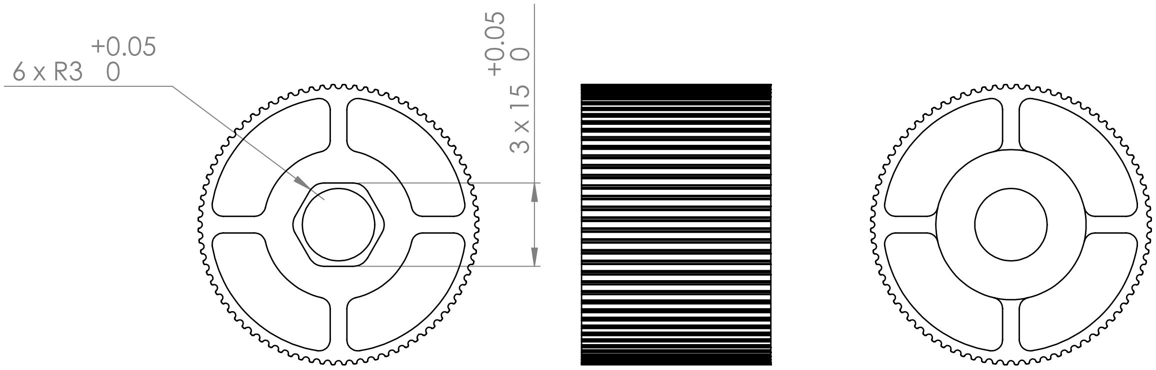

Part to be manufactured from GT2 2mm pitch aluminum pulley stock with 80 teeth.

Same or similar to:
SDP-SI.com
Part #: A 6A50M080GT20

Note: p1006 and p1007 may slide relative to each other, but should not rotate relative to each other.

UNLESS SPECIFIED **UNITS:** MILLIMETERS **TOLERANCE:** +/- 0.1	Luke M. Mooney, Alejandro F. Azocar afazocar@umich.edu
PROPRIETARY AND CONFIDENTIAL THE INFORMATION CONTAINED IN THIS DRAWING IS THE SOLE PROPERTY OF THE NEUROBIONICS LAB/UNIVERSITY OF MICHIGAN. ANY REPRODUCTION IN PART OR AS A WHOLE WITHOUT WRITTEN PERMISSION IS PROHIBITED.	Neurobionics Lab, University of Michigan **TITLE:** p1007_stage1OutputPulley_2mm_80teeth_sdpsi_A 6A50M080GT20 **MATERIAL:** AL 7075-T6 **QUANTITY:** 1

Figure A.18: OSL knee stage 1 output pulley.

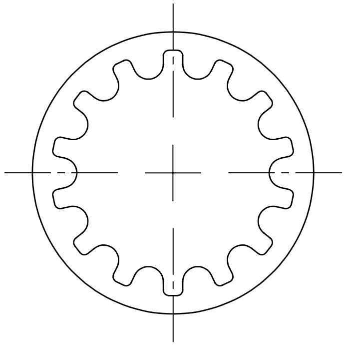

UNLESS SPECIFIED **UNITS:** MILLIMETERS **TOLERANCE:** +/- 0.1

Luke M. Mooney, Alejandro F. Azocar
afazocar@umich.edu
Neurobionics Lab, University of Michigan

TITLE: p1008_pulleyFlange_stage2Input
MATERIAL: ABS, black
QUANTITY:2

Figure A.19: OSL knee stage 2 input pulley flange.

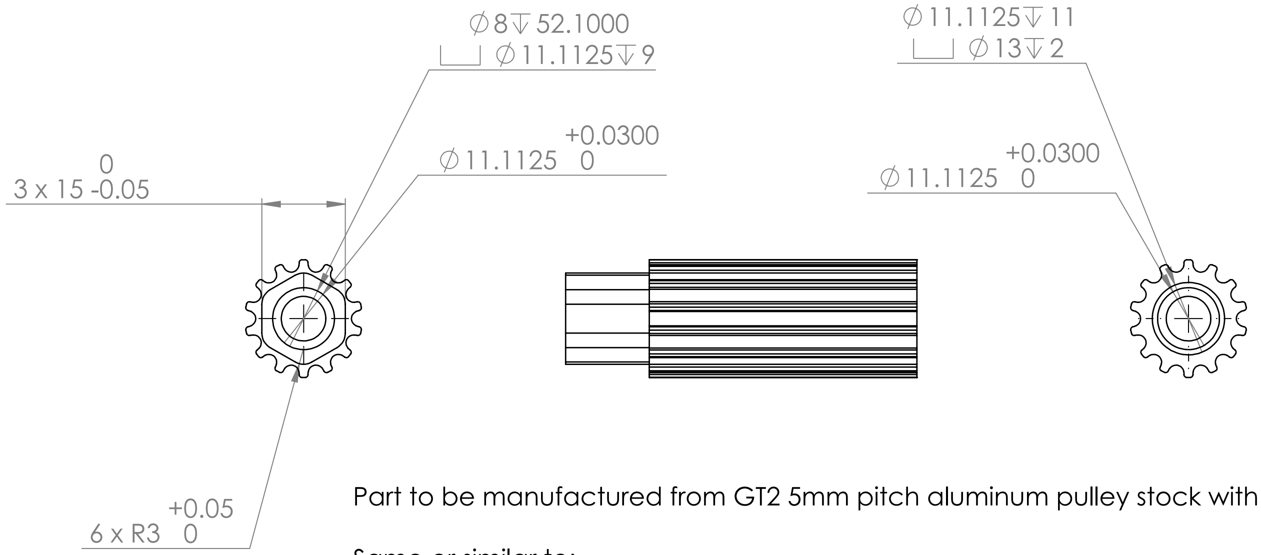

Part to be manufactured from GT2 5mm pitch aluminum pulley stock with 14 teeth.

Same or similar to:
SDP-SI.com
Part #: A 6A54M014GT18

Note: p1009 and p1010 may slide relative to each other, but should not rotate relative to each other.

UNLESS SPECIFIED **UNITS:** MILLIMETERS **TOLERANCE:** +/- 0.1

Luke M. Mooney, Alejandro F. Azocar
afazocar@umich.edu
Neurobionics Lab, University of Michigan

PROPRIETARY AND CONFIDENTIAL
THE INFORMATION CONTAINED IN THIS DRAWING IS THE SOLE PROPERTY OF THE NEUROBIONICS LAB/UNIVERSITY OF MICHIGAN. ANY REPRODUCTION IN PART OR AS A WHOLE WITHOUT WRITTEN PERMISSION IS PROHIBITED.

TITLE: p1009_stage3InputPulley_5mm_14teeth_sdpsi_A 6A54M014GT18
MATERIAL: AL 7075-T6
QUANTITY: 1

Figure A.20: OSL knee stage 3 input pulley.

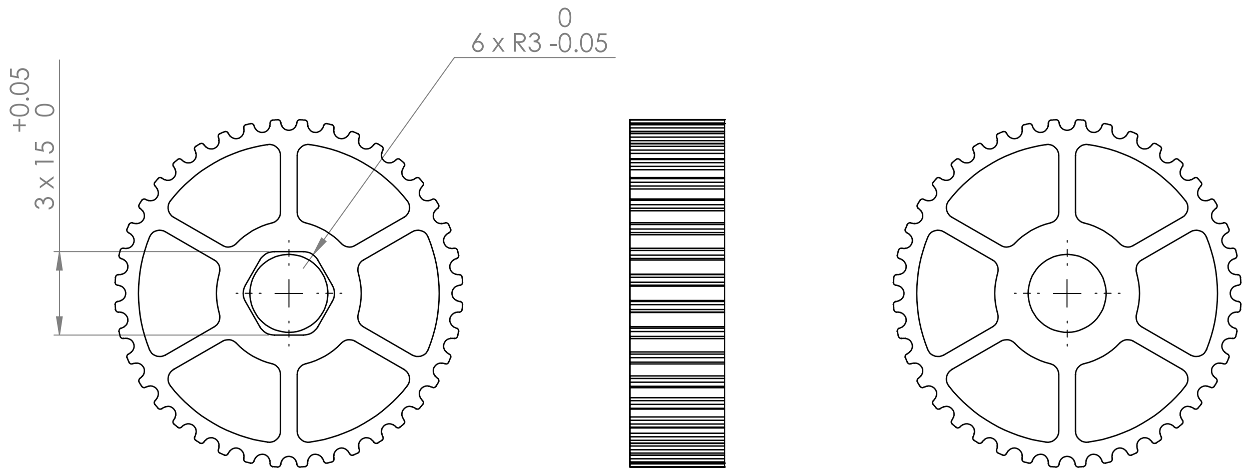

Part to be manufactured from GT2 5mm pitch aluminum pulley stock with 40 teeth.

Same or similar to:
SDP-SI.com
Part #: A 6A54M040GT20

Note: p1009 and p1010 may slide relative to each other, but should not rotate relative to each other.

UNLESS SPECIFIED **UNITS:** MILLIMETERS **TOLERANCE:** +/- 0.1	Luke M. Mooney, Alejandro F. Azocar afazocar@umich.edu
PROPRIETARY AND CONFIDENTIAL THE INFORMATION CONTAINED IN THIS DRAWING IS THE SOLE PROPERTY OF THE NEUROBIONICS LAB/UNIVERSITY OF MICHIGAN. ANY REPRODUCTION IN PART OR AS A WHOLE WITHOUT WRITTEN PERMISSION IS PROHIBITED.	Neurobionics Lab, University of Michigan **TITLE:** p1010_stage2OutputPulley_5mm_40teeth_sdpsi_A 6A54M040GT20 **MATERIAL:** AL 7075-T6 **QUANTITY:** 1

Figure A.21: OSL knee stage 2 output pulley.

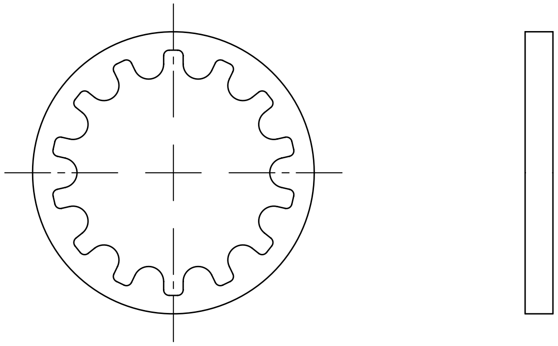

UNLESS SPECIFIED **UNITS:** MILLIMETERS **TOLERANCE:** +/- 0.1	Luke M. Mooney, Alejandro F. Azocar afazocar@umich.edu
PROPRIETARY AND CONFIDENTIAL THE INFORMATION CONTAINED IN THIS DRAWING IS THE SOLE PROPERTY OF THE NEUROBIONICS LAB/UNIVERSITY OF MICHIGAN. ANY REPRODUCTION IN PART OR AS A WHOLE WITHOUT WRITTEN PERMISSION IS PROHIBITED.	Neurobionics Lab, University of Michigan **TITLE:** p1011_pulleyFlange_stage3Input **MATERIAL:** ABS, black **QUANTITY:**2

Figure A.22: OSL knee stage 3 input pulley flange.

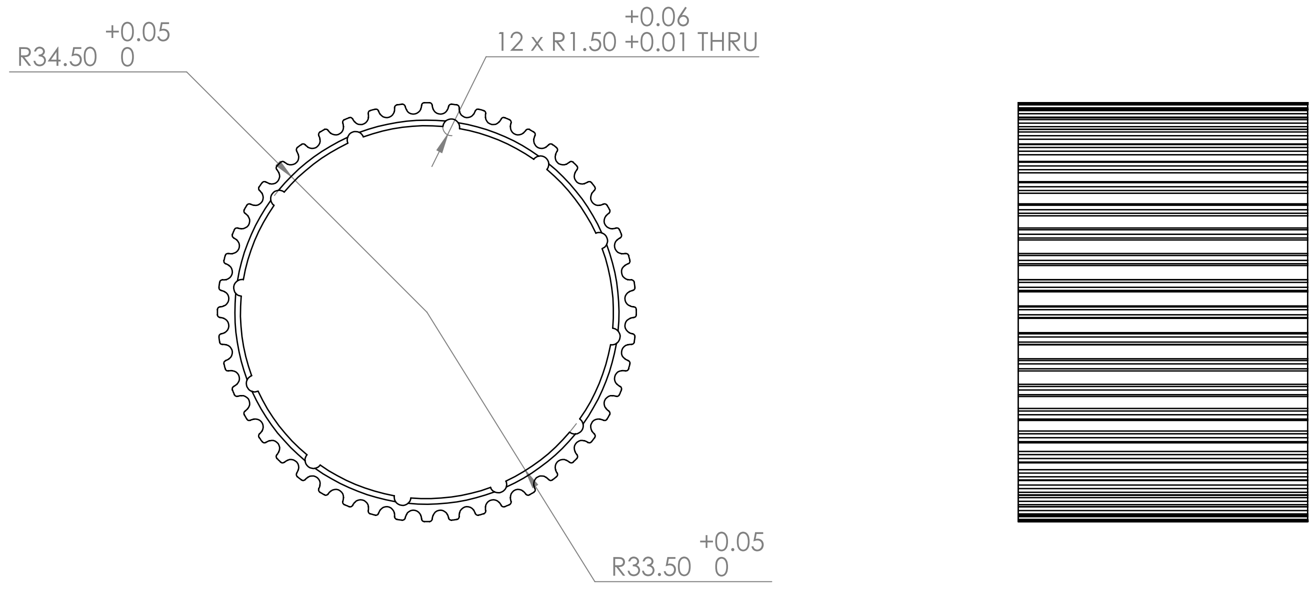

UNLESS SPECIFIED **UNITS:** MILLIMETERS **TOLERANCE:** +/- 0.1	Luke M. Mooney, Alejandro F. Azocar afazocar@umich.edu
PROPRIETARY AND CONFIDENTIAL THE INFORMATION CONTAINED IN THIS DRAWING IS THE SOLE PROPERTY OF THE NEUROBIONICS LAB/UNIVERSITY OF MICHIGAN. ANY REPRODUCTION IN PART OR AS A WHOLE WITHOUT WRITTEN PERMISSION IS PROHIBITED.	Neurobionics Lab, University of Michigan **TITLE:** p1012_stage3OutputPulley_5mm_48teeth_sdpsi_A 6A54M048GT20 **MATERIAL:** AL 7075-T6 **QUANTITY:** 1

Figure A.23: OSL knee stage 3 output pulley.

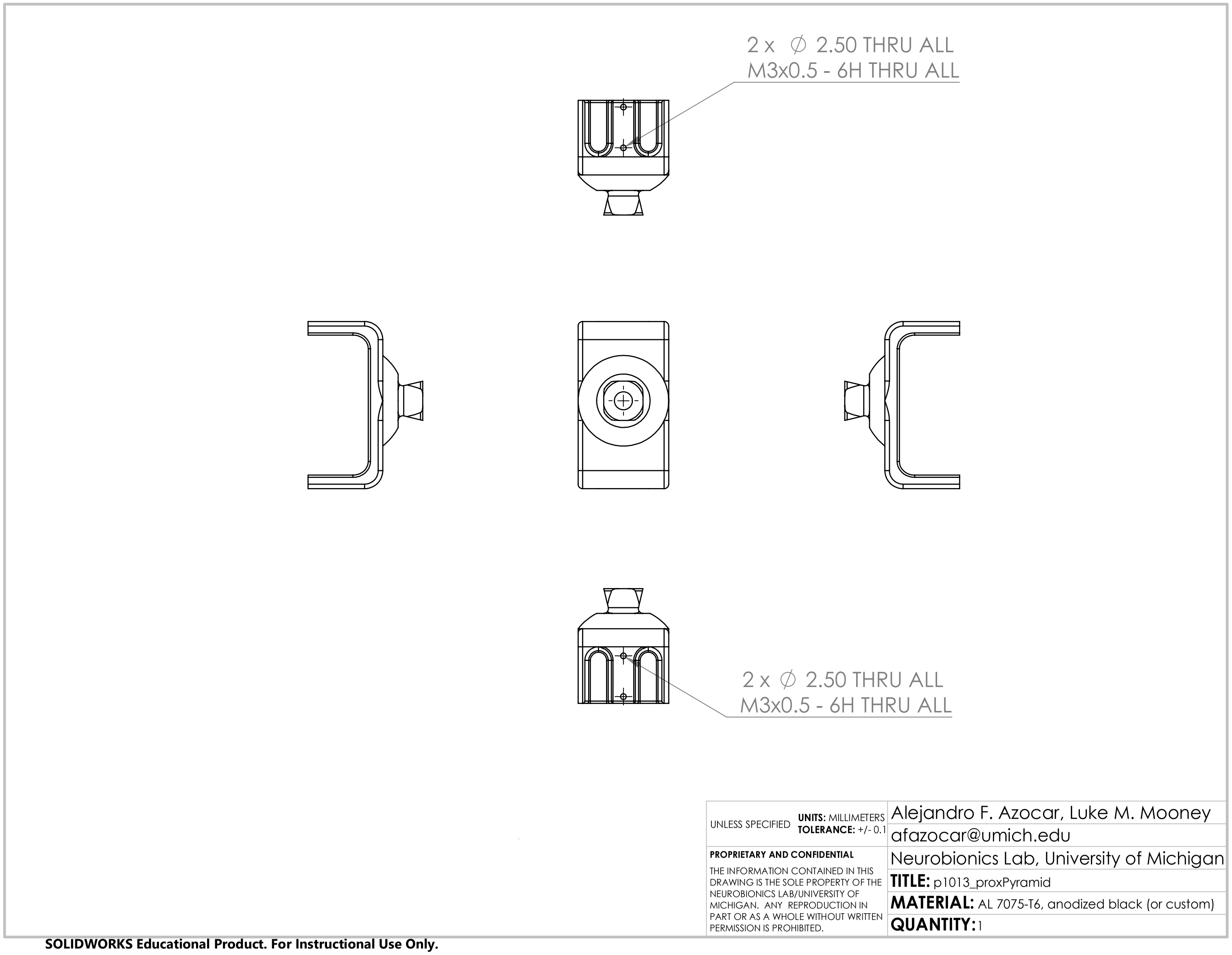

UNLESS SPECIFIED **UNITS:** MILLIMETERS **TOLERANCE:** +/- 0.1

PROPRIETARY AND CONFIDENTIAL

THE INFORMATION CONTAINED IN THIS DRAWING IS THE SOLE PROPERTY OF THE NEUROBIONICS LAB/UNIVERSITY OF MICHIGAN. ANY REPRODUCTION IN PART OR AS A WHOLE WITHOUT WRITTEN PERMISSION IS PROHIBITED.

Alejandro F. Azocar, Luke M. Mooney
afazocar@umich.edu
Neurobionics Lab, University of Michigan
TITLE: p1013_proxPyramid
MATERIAL: AL 7075-T6, anodized black (or custom)
QUANTITY: 1

Figure A.24: OSL knee proximal pyramid.

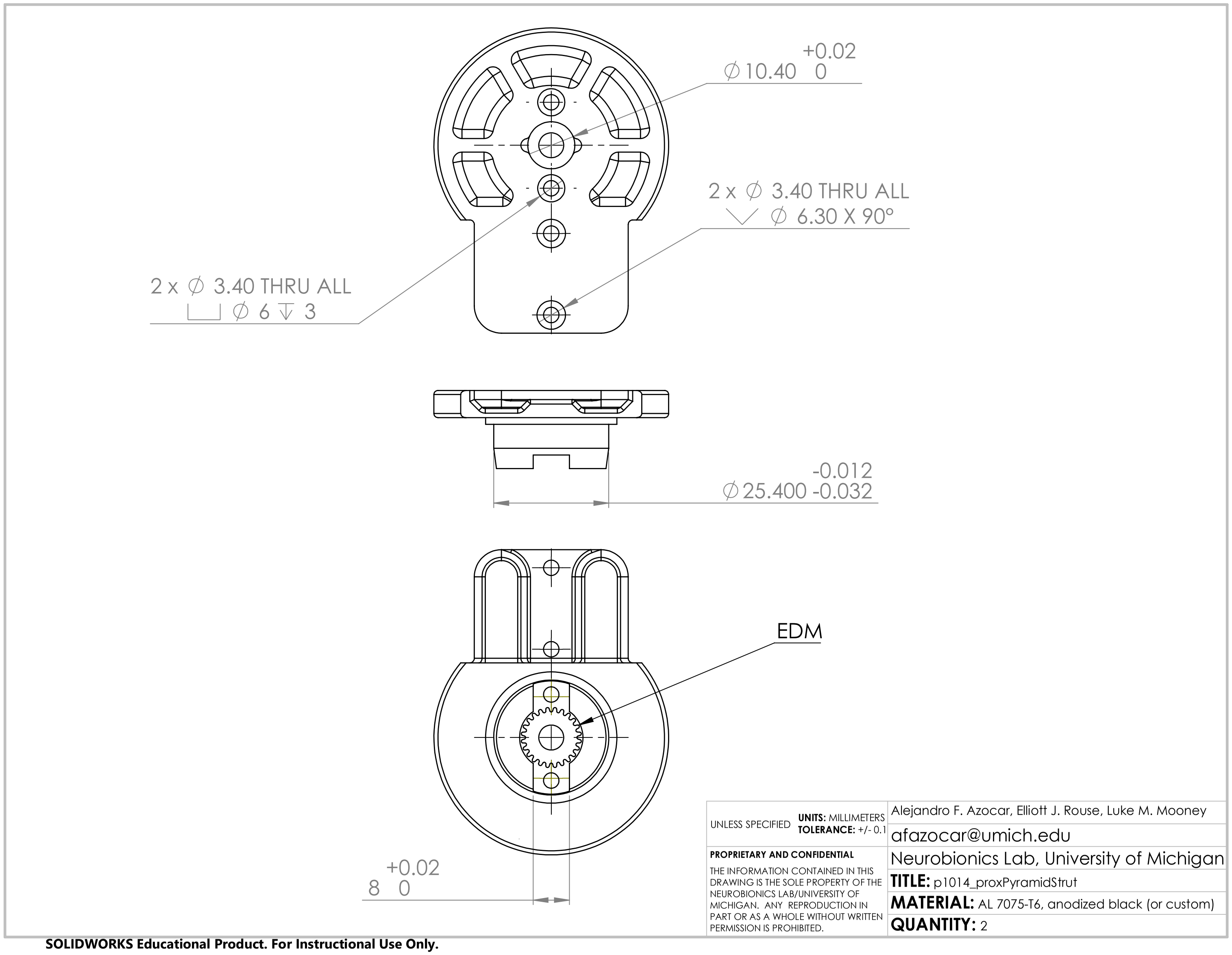

Figure A.25: OSL knee proximal pyramid strut.

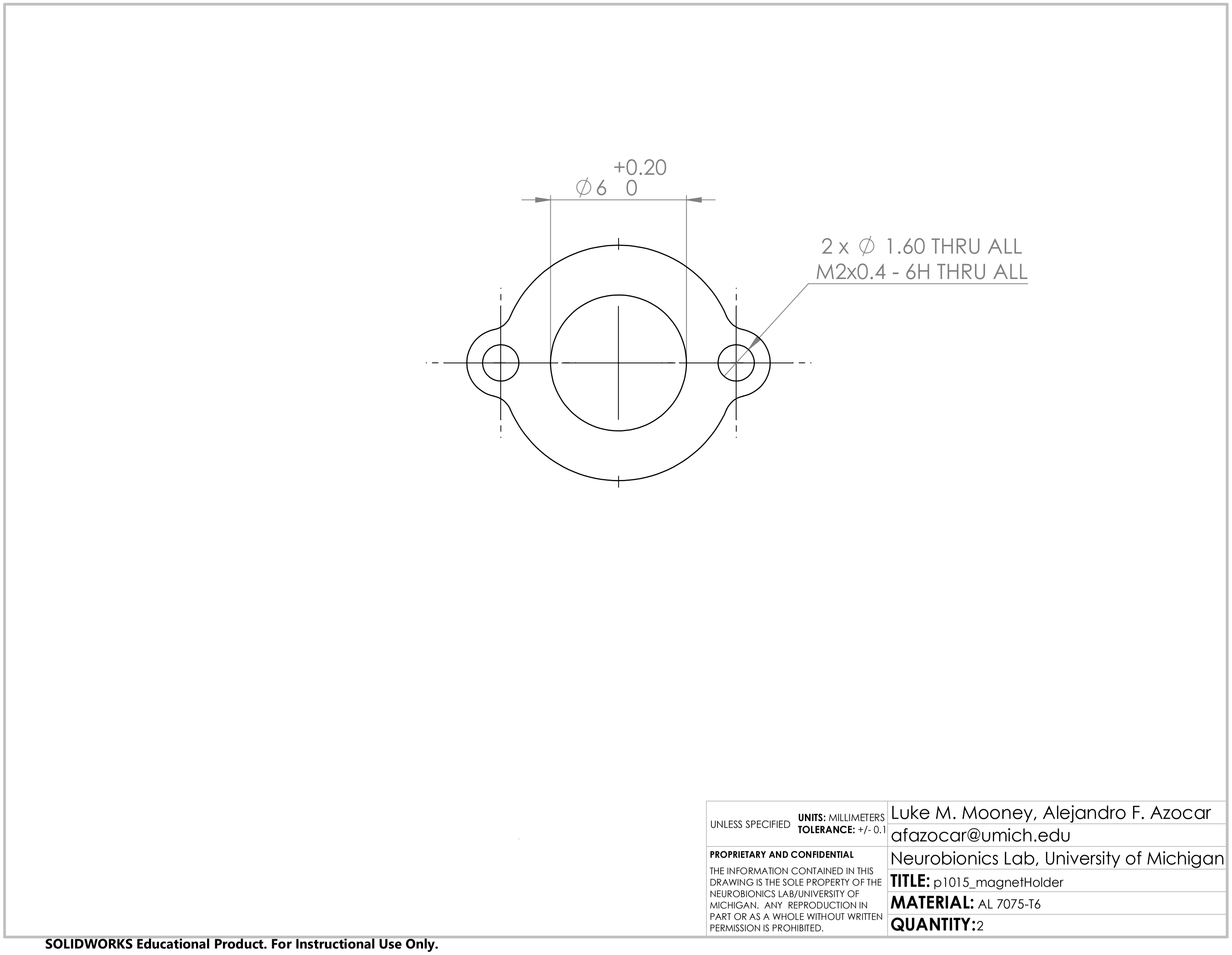

Figure A.26: OSL knee encoder magnet holder.

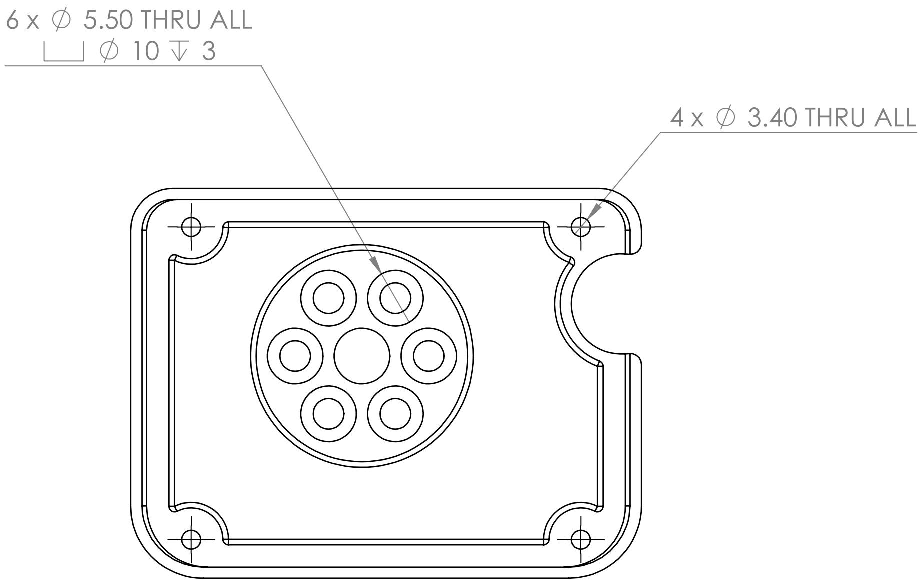

UNLESS SPECIFIED **UNITS:** MILLIMETERS **TOLERANCE:** +/- 0.1	Alejandro F. Azocar, Luke M. Mooney afazocar@umich.edu
PROPRIETARY AND CONFIDENTIAL THE INFORMATION CONTAINED IN THIS DRAWING IS THE SOLE PROPERTY OF THE NEUROBIONICS LAB/UNIVERSITY OF MICHIGAN. ANY REPRODUCTION IN PART OR AS A WHOLE WITHOUT WRITTEN PERMISSION IS PROHIBITED.	Neurobionics Lab, University of Michigan **TITLE:** p1016_distalBase **MATERIAL:** AL 7075-T6, anodized black (or custom) **QUANTITY:** 1

Figure A.27: OSL knee distal base.

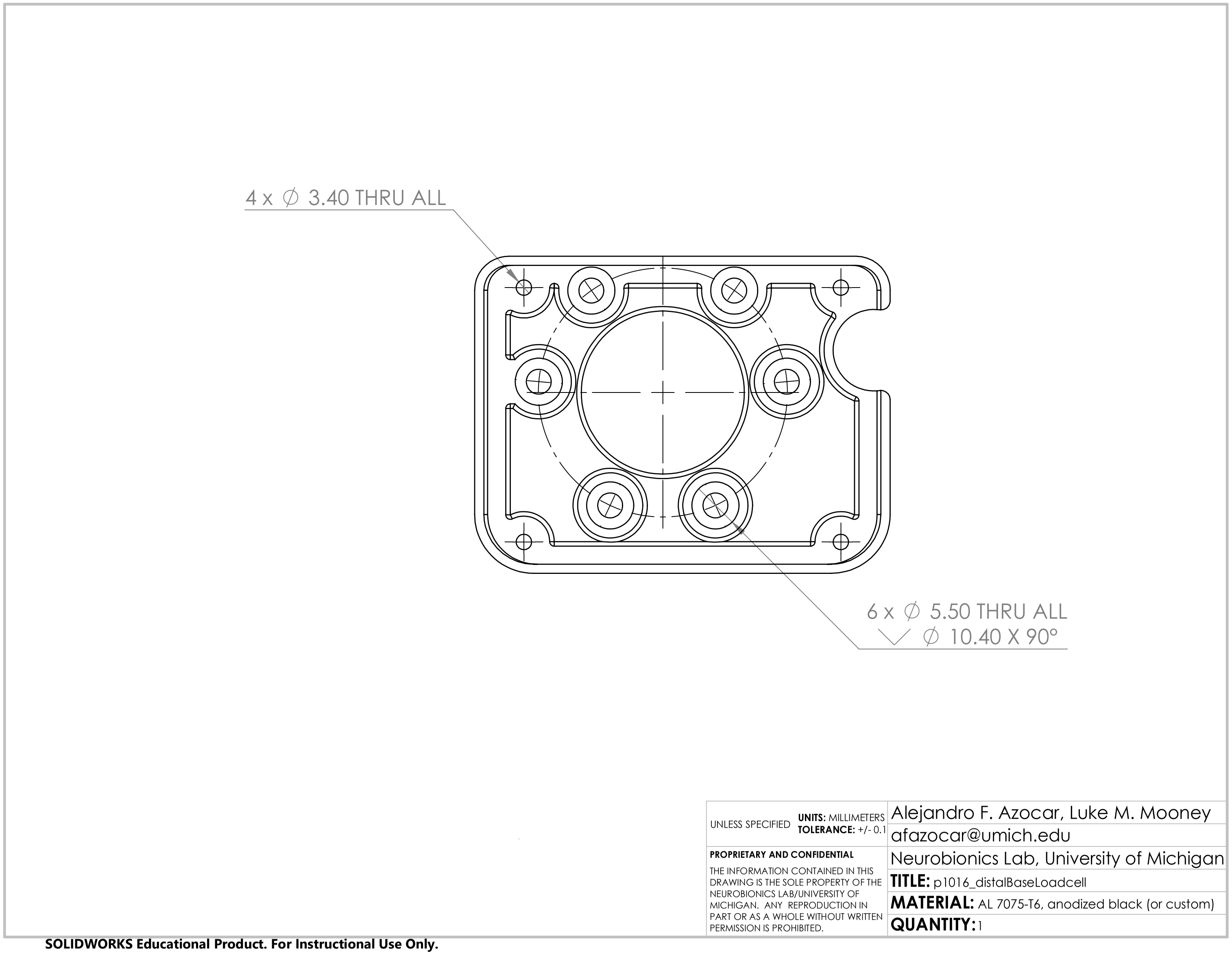

Figure A.28: OSL knee distal base, compatible with M3564F loadcell.

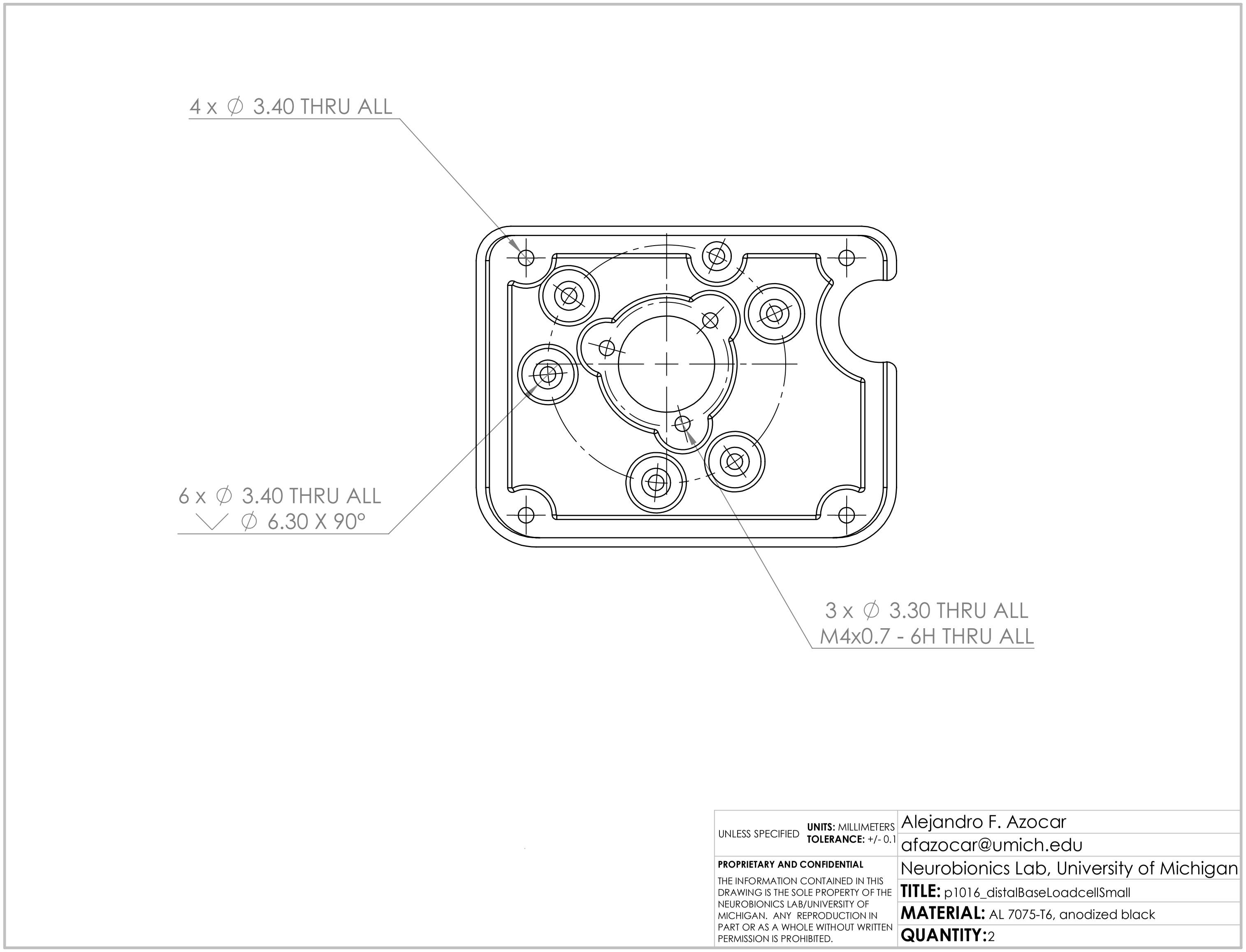

Figure A.29: OSL knee distal base, compatible with M3554E loadcell.

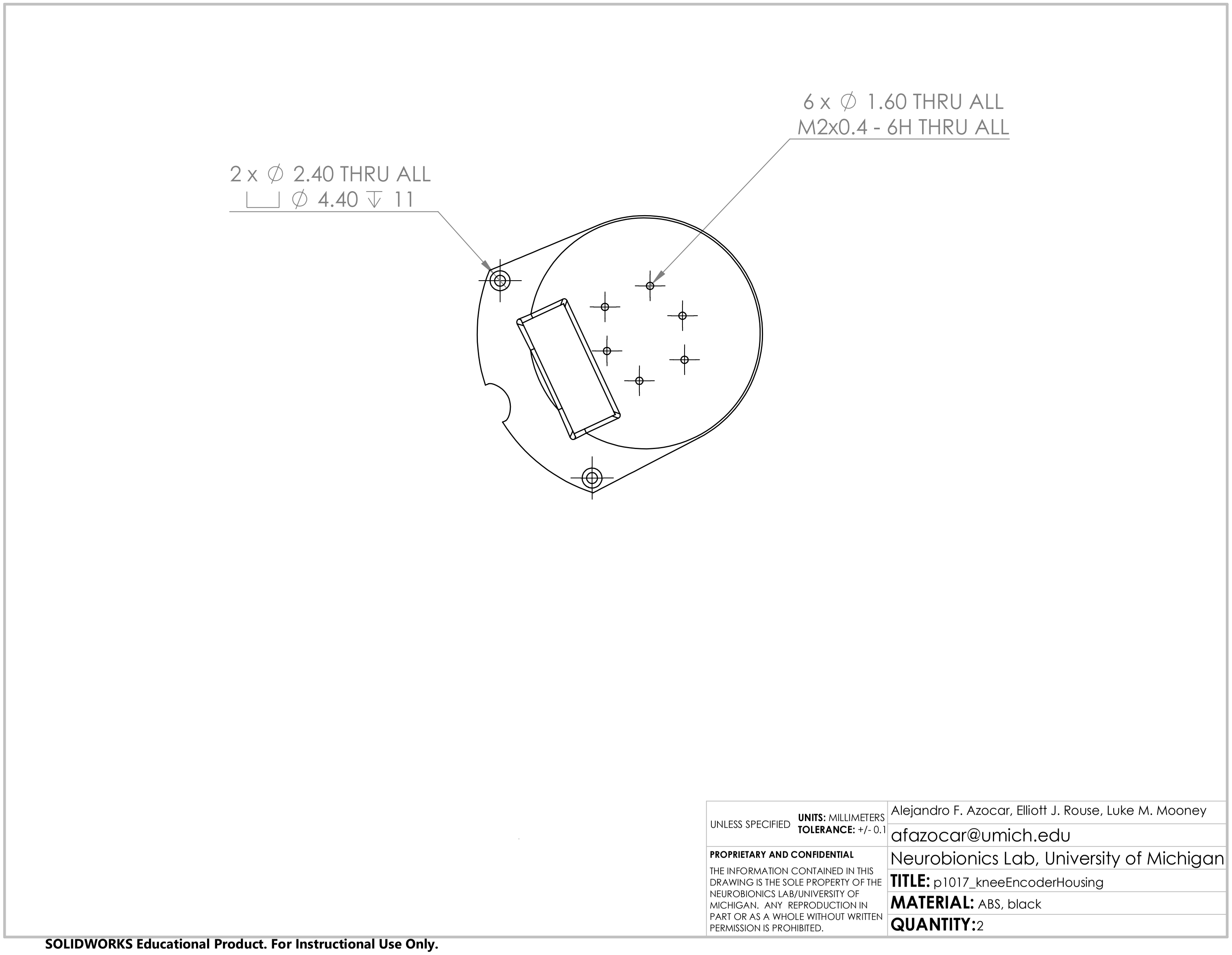

UNLESS SPECIFIED **UNITS:** MILLIMETERS
TOLERANCE: +/- 0.1

PROPRIETARY AND CONFIDENTIAL

THE INFORMATION CONTAINED IN THIS DRAWING IS THE SOLE PROPERTY OF THE NEUROBIONICS LAB/UNIVERSITY OF MICHIGAN. ANY REPRODUCTION IN PART OR AS A WHOLE WITHOUT WRITTEN PERMISSION IS PROHIBITED.

Alejandro F. Azocar, Elliott J. Rouse, Luke M. Mooney
afazocar@umich.edu
Neurobionics Lab, University of Michigan
TITLE: p1017_kneeEncoderHousing
MATERIAL: ABS, black
QUANTITY:2

Figure A.30: OSL knee encoder housing.

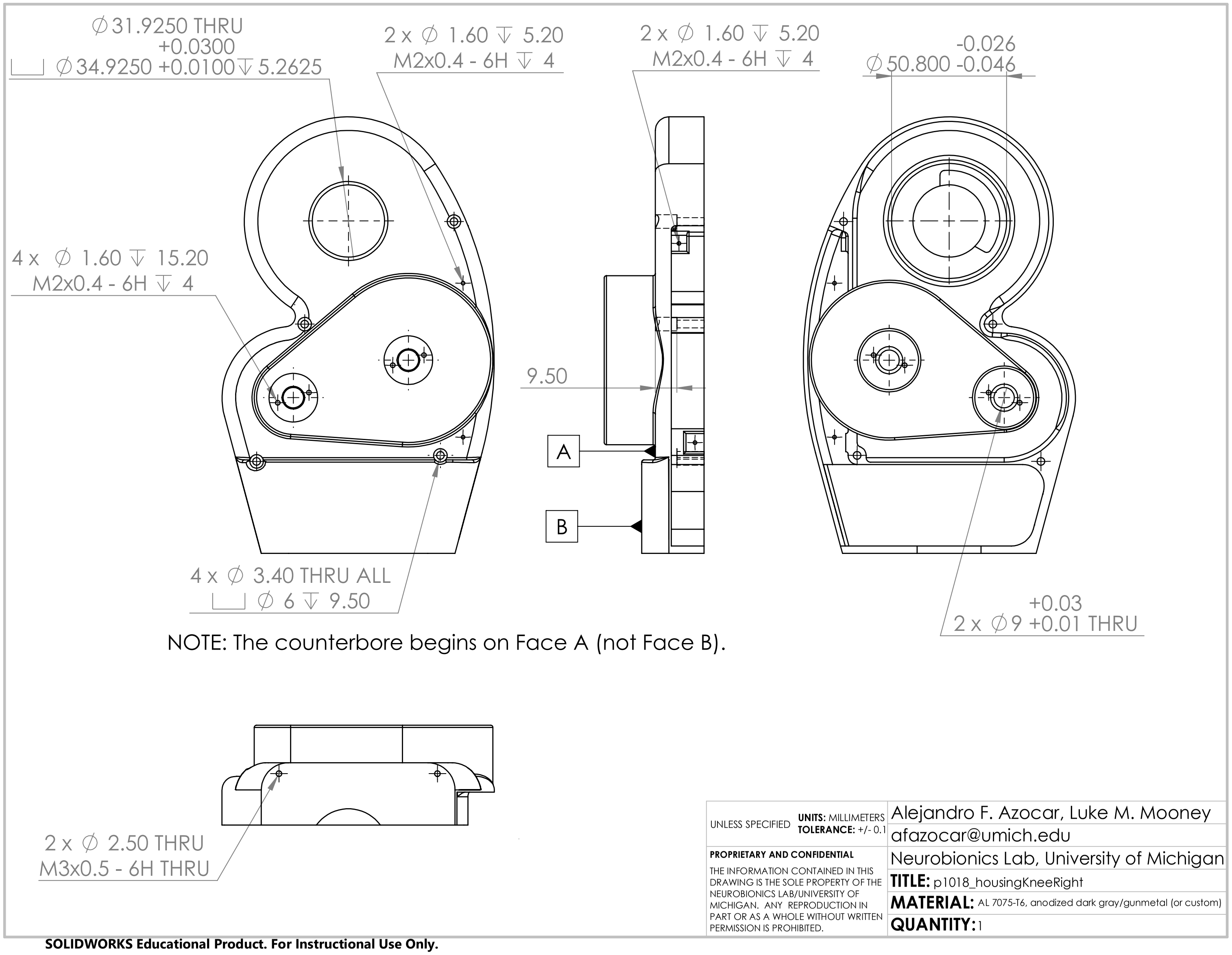

Figure A.31: OSL knee housing, right side.

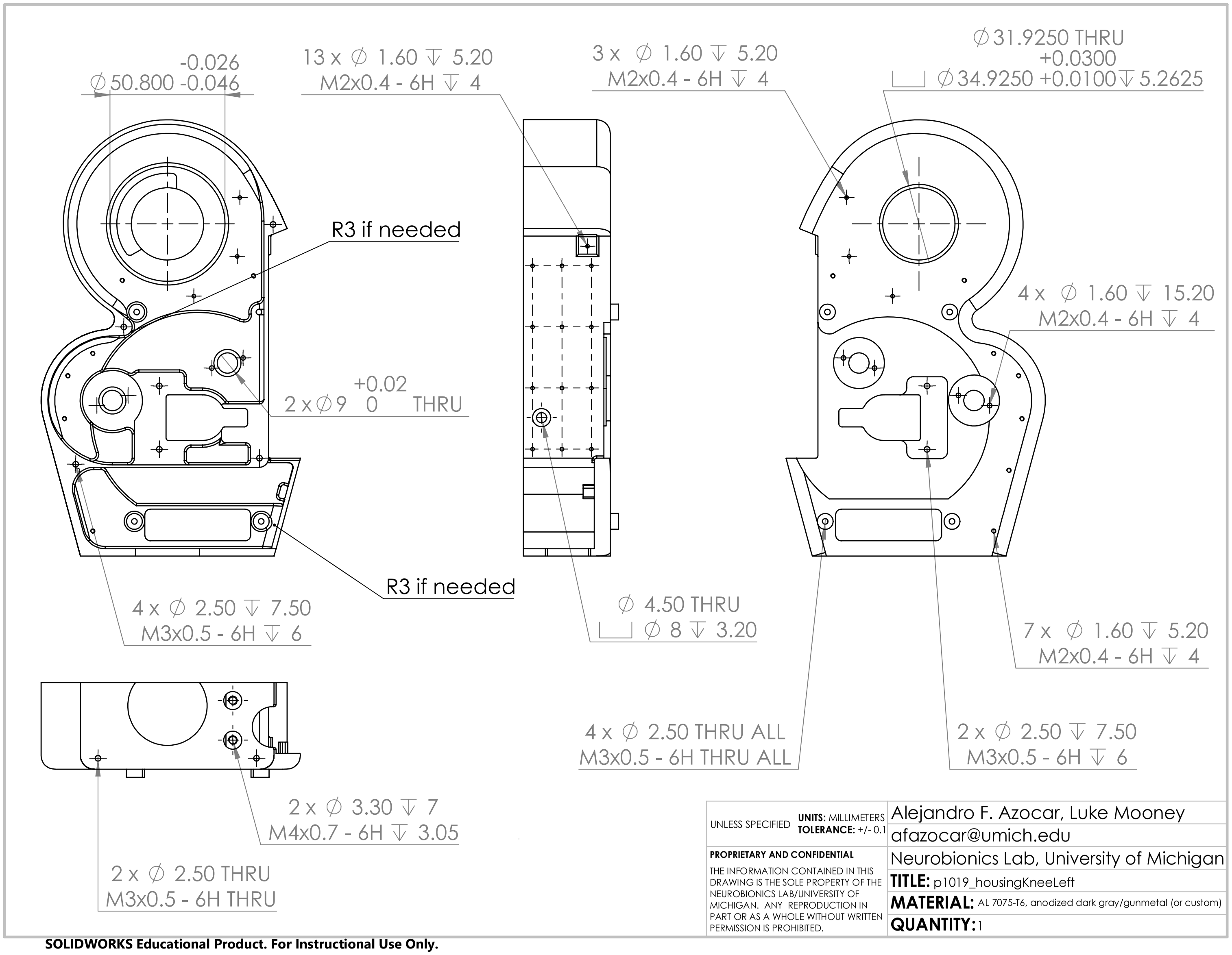

Figure A.32: OSL knee housing, left side.

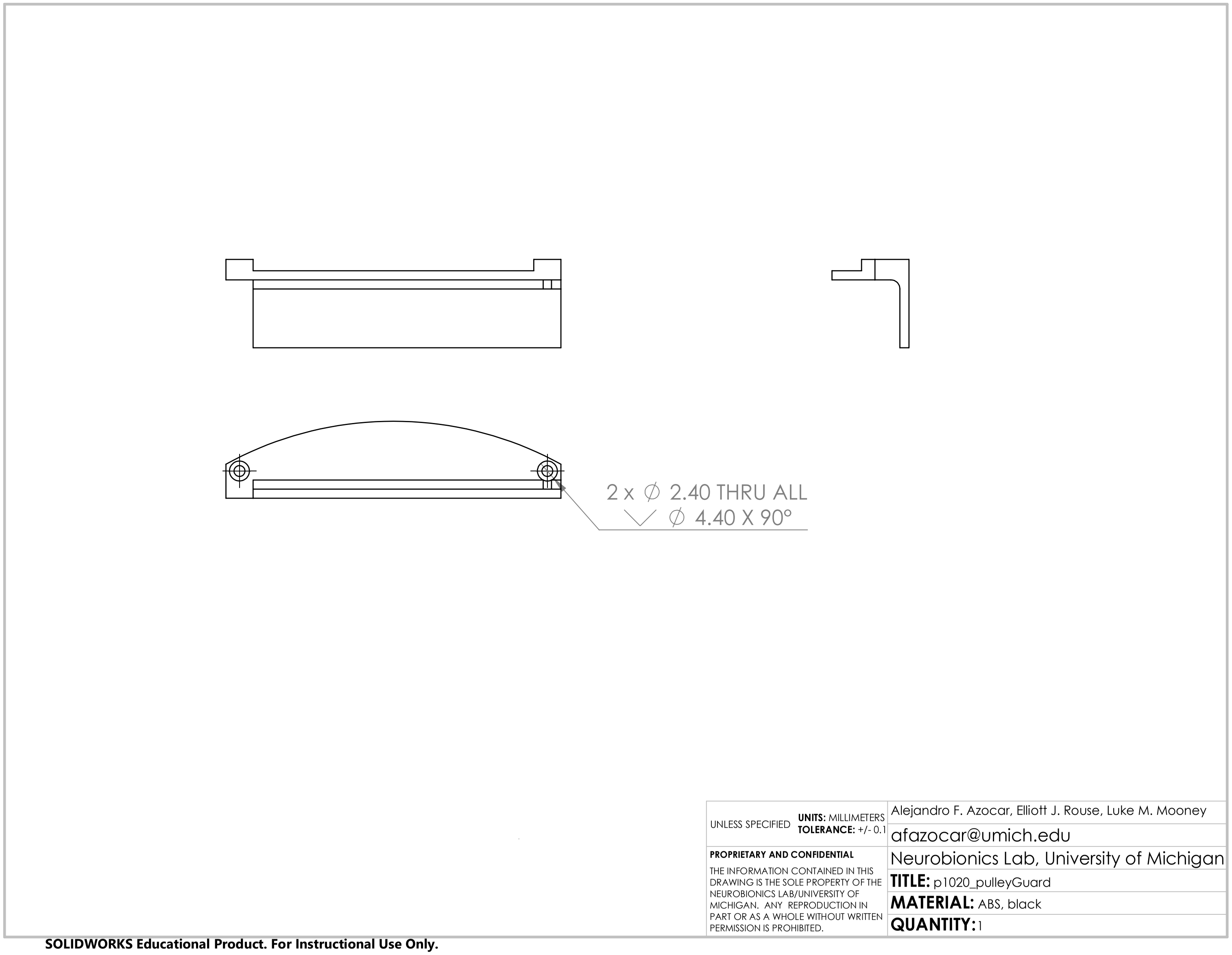

UNLESS SPECIFIED **UNITS:** MILLIMETERS **TOLERANCE:** +/- 0.1

Alejandro F. Azocar, Elliott J. Rouse, Luke M. Mooney

afazocar@umich.edu

Neurobionics Lab, University of Michigan

PROPRIETARY AND CONFIDENTIAL

THE INFORMATION CONTAINED IN THIS DRAWING IS THE SOLE PROPERTY OF THE NEUROBIONICS LAB/UNIVERSITY OF MICHIGAN. ANY REPRODUCTION IN PART OR AS A WHOLE WITHOUT WRITTEN PERMISSION IS PROHIBITED.

TITLE: p1020_pulleyGuard

MATERIAL: ABS, black

QUANTITY: 1

Figure A.33: OSL knee pulley guard.

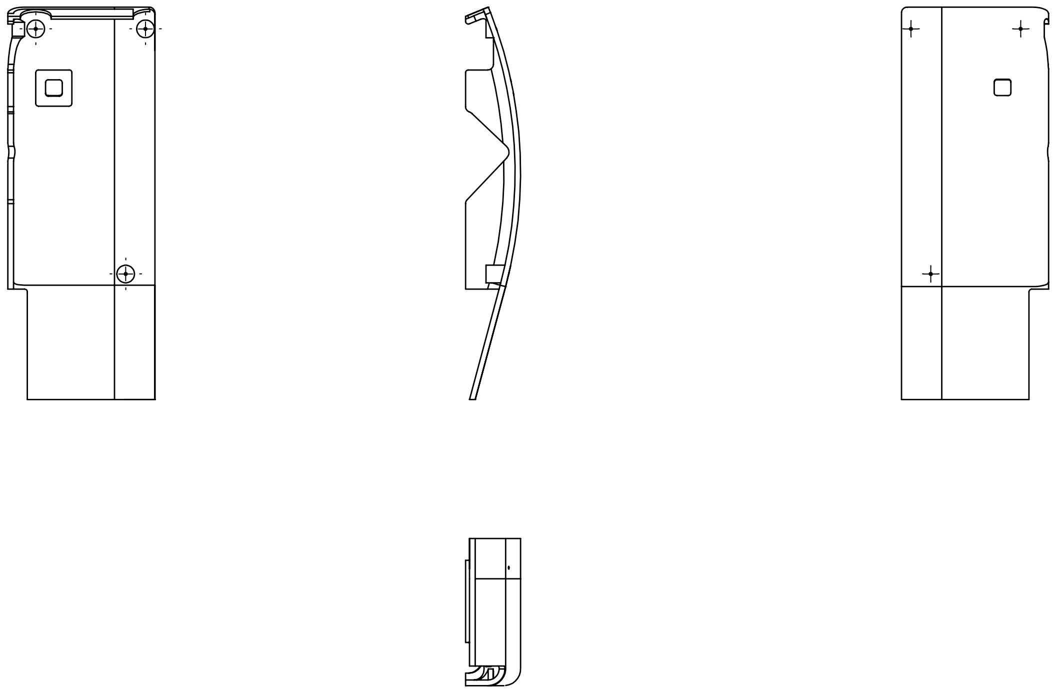

UNLESS SPECIFIED **UNITS:** MILLIMETERS **TOLERANCE:** +/- 0.1	Alejandro F. Azocar, Elliott J. Rouse, Luke M. Mooney
	afazocar@umich.edu
PROPRIETARY AND CONFIDENTIAL	Neurobionics Lab, University of Michigan
THE INFORMATION CONTAINED IN THIS DRAWING IS THE SOLE PROPERTY OF THE NEUROBIONICS LAB/UNIVERSITY OF MICHIGAN. ANY REPRODUCTION IN PART OR AS A WHOLE WITHOUT WRITTEN PERMISSION IS PROHIBITED.	**TITLE:** p1021_electronicsCoverKnee **MATERIAL:** ABS, black **QUANTITY:** 1

Figure A.34: OSL knee electronics cover.

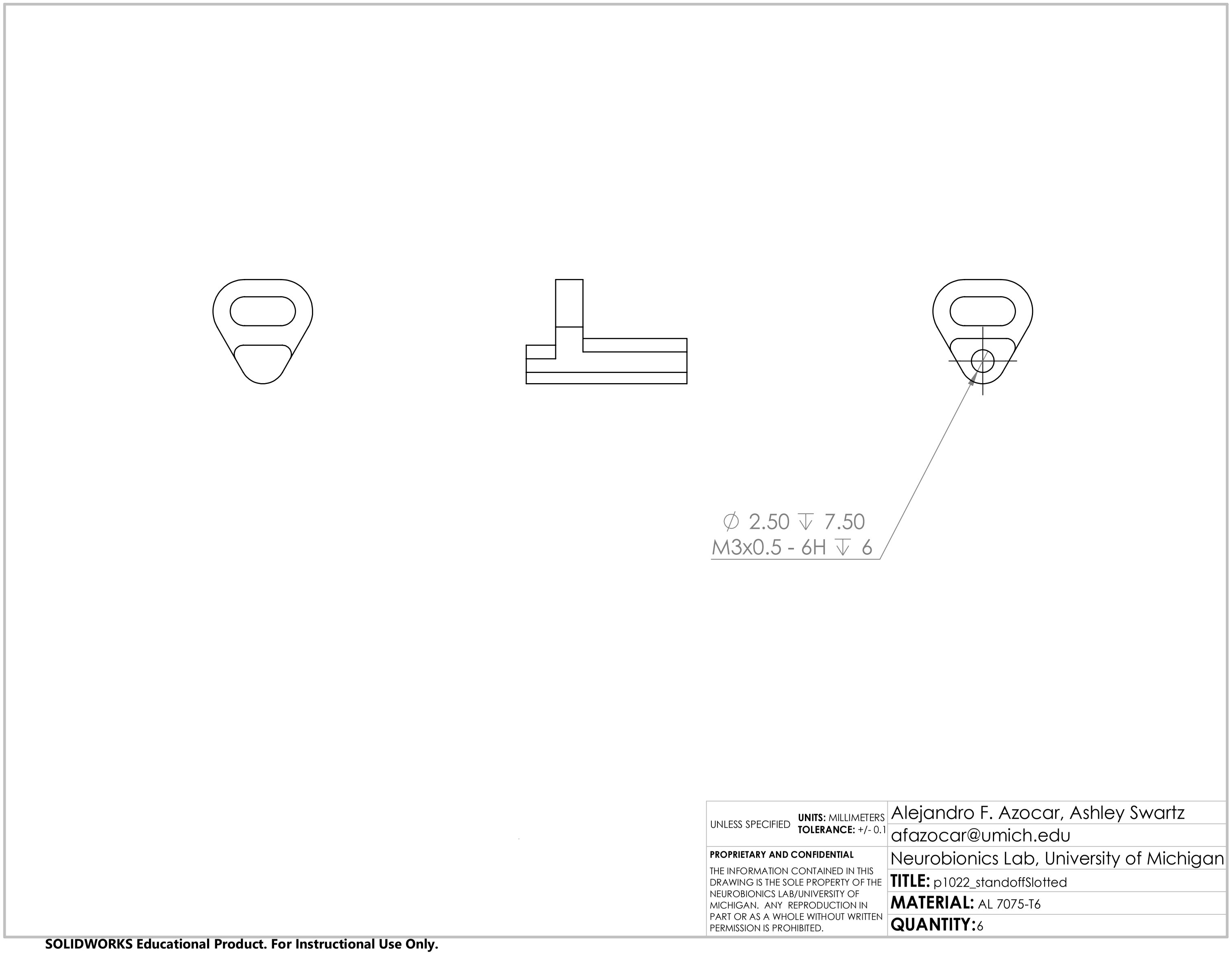

UNLESS SPECIFIED **UNITS:** MILLIMETERS **TOLERANCE:** +/- 0.1

PROPRIETARY AND CONFIDENTIAL

THE INFORMATION CONTAINED IN THIS DRAWING IS THE SOLE PROPERTY OF THE NEUROBIONICS LAB/UNIVERSITY OF MICHIGAN. ANY REPRODUCTION IN PART OR AS A WHOLE WITHOUT WRITTEN PERMISSION IS PROHIBITED.

Alejandro F. Azocar, Ashley Swartz
afazocar@umich.edu
Neurobionics Lab, University of Michigan
TITLE: p1022_standoffSlotted
MATERIAL: AL 7075-T6
QUANTITY: 6

Figure A.35: OSL knee motor standoff.

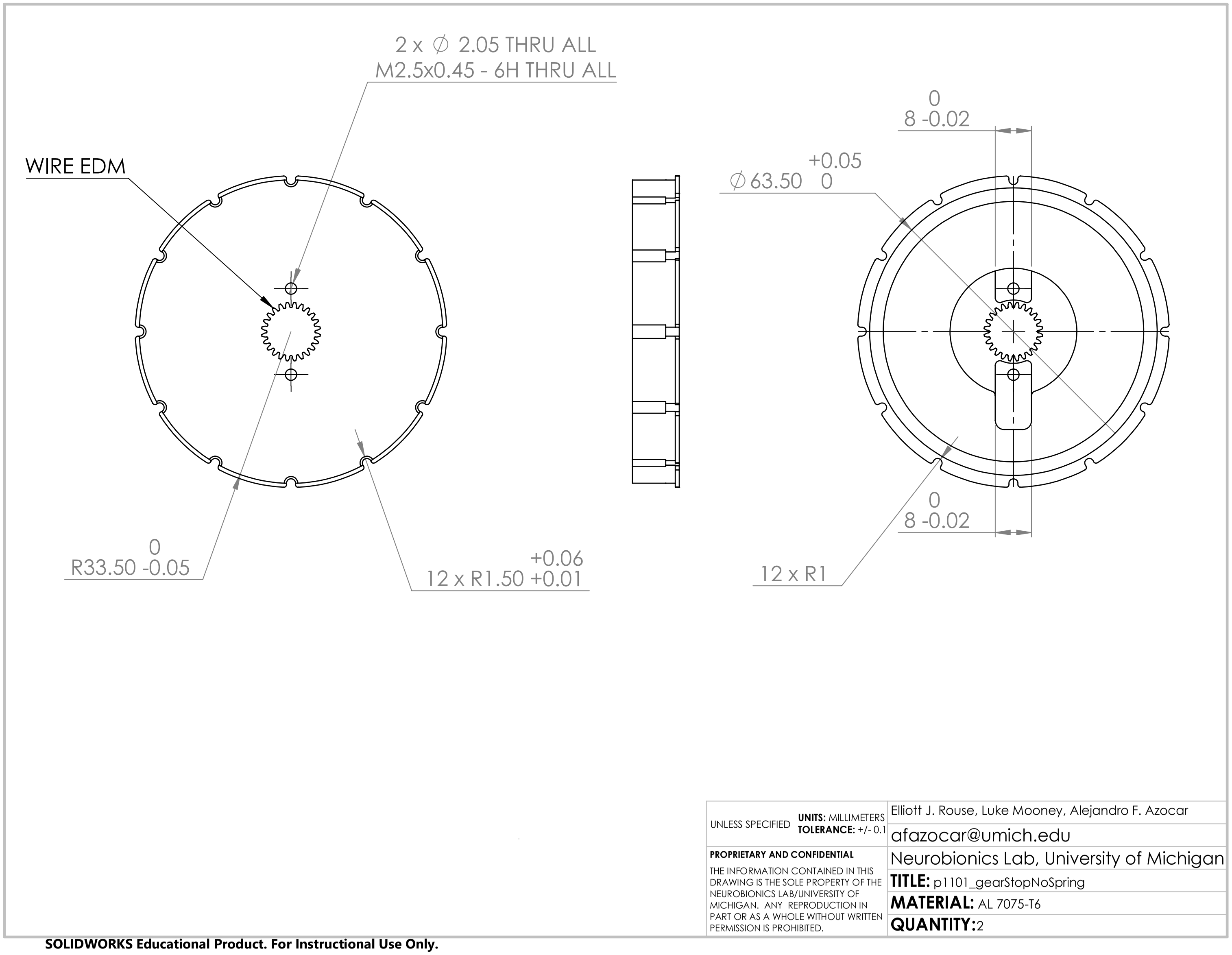

Figure A.36: OSL knee gear stop, non-SEA configuration.

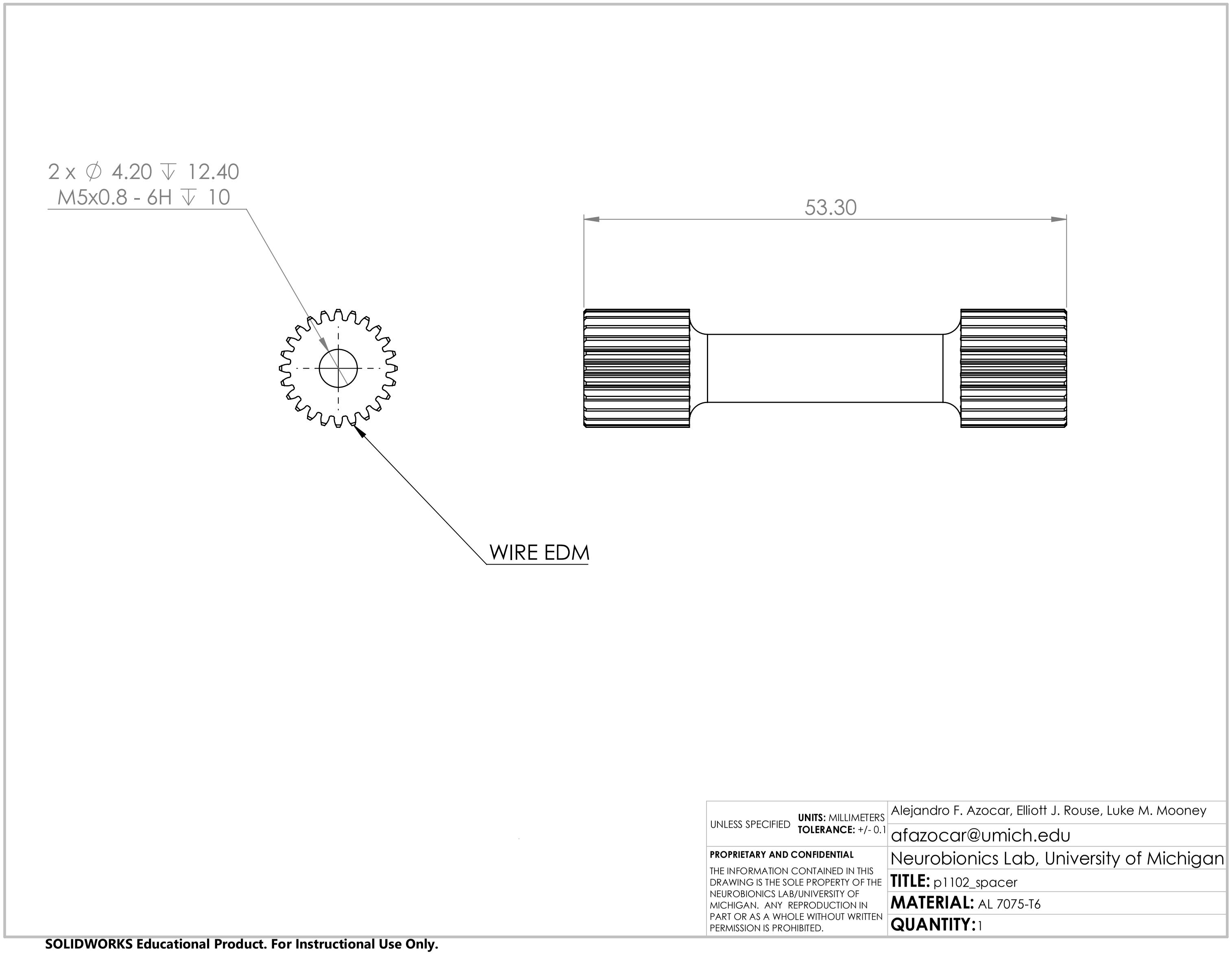

Figure A.37: OSL knee spacer, non-SEA configuration.

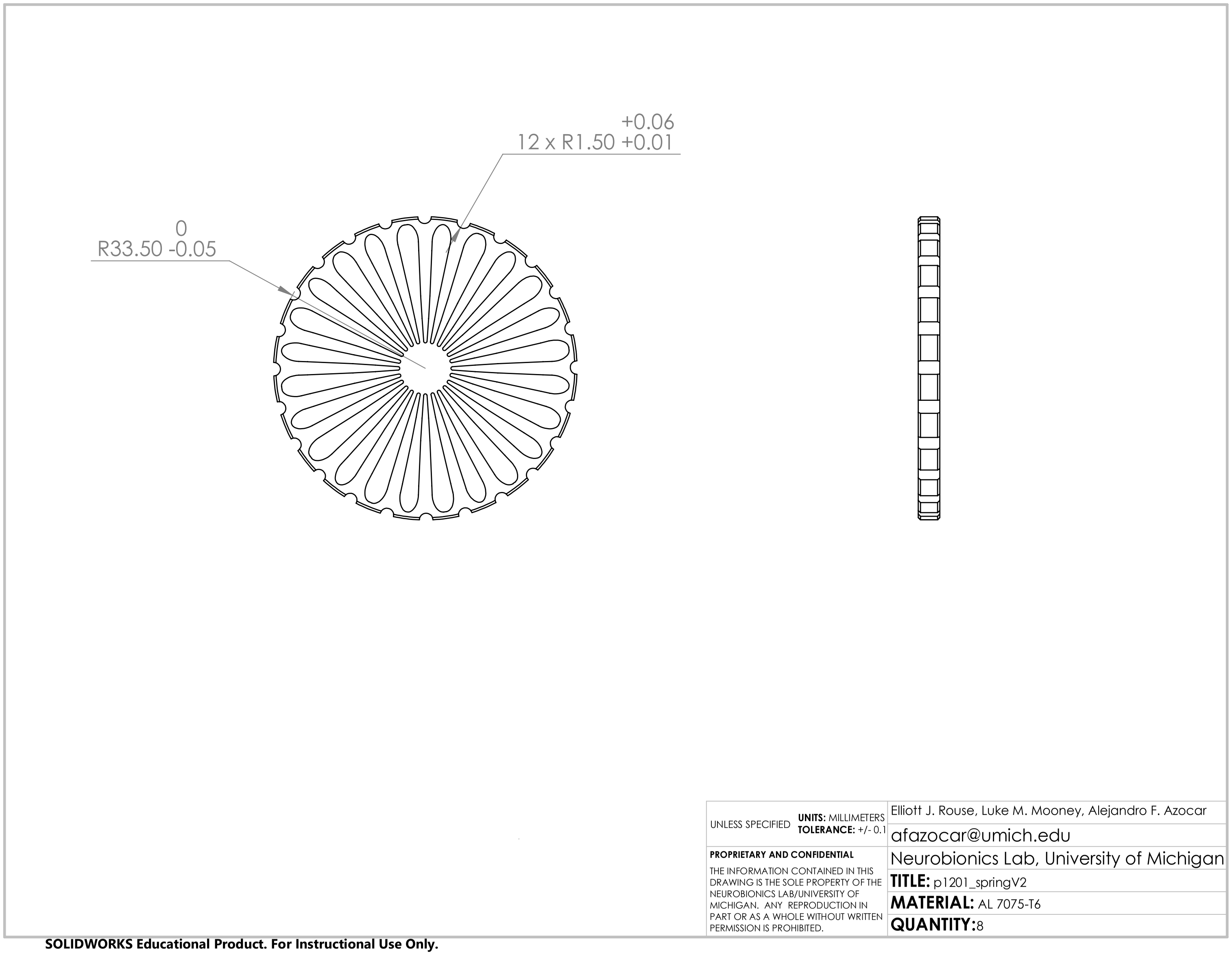

Figure A.38: OSL knee spring, symmetric.

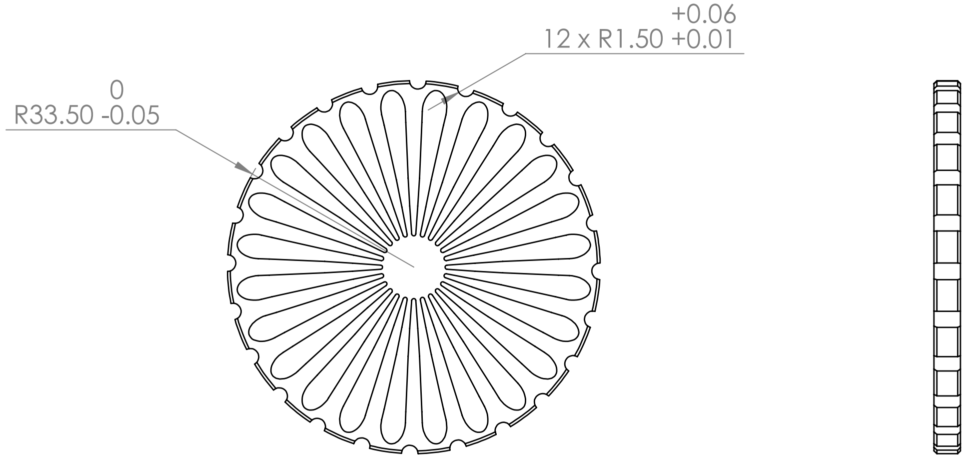

UNLESS SPECIFIED **UNITS:** MILLIMETERS **TOLERANCE:** +/- 0.1	Elliott J. Rouse, Luke M. Mooney, Alejandro F. Azocar afazocar@umich.edu
PROPRIETARY AND CONFIDENTIAL THE INFORMATION CONTAINED IN THIS DRAWING IS THE SOLE PROPERTY OF THE NEUROBIONICS LAB/UNIVERSITY OF MICHIGAN. ANY REPRODUCTION IN PART OR AS A WHOLE WITHOUT WRITTEN PERMISSION IS PROHIBITED.	Neurobionics Lab, University of Michigan **TITLE:** p1202_springV3 **MATERIAL:** AL 7075-T6 **QUANTITY:**8

Figure A.39: OSL knee spring, asymmetric.

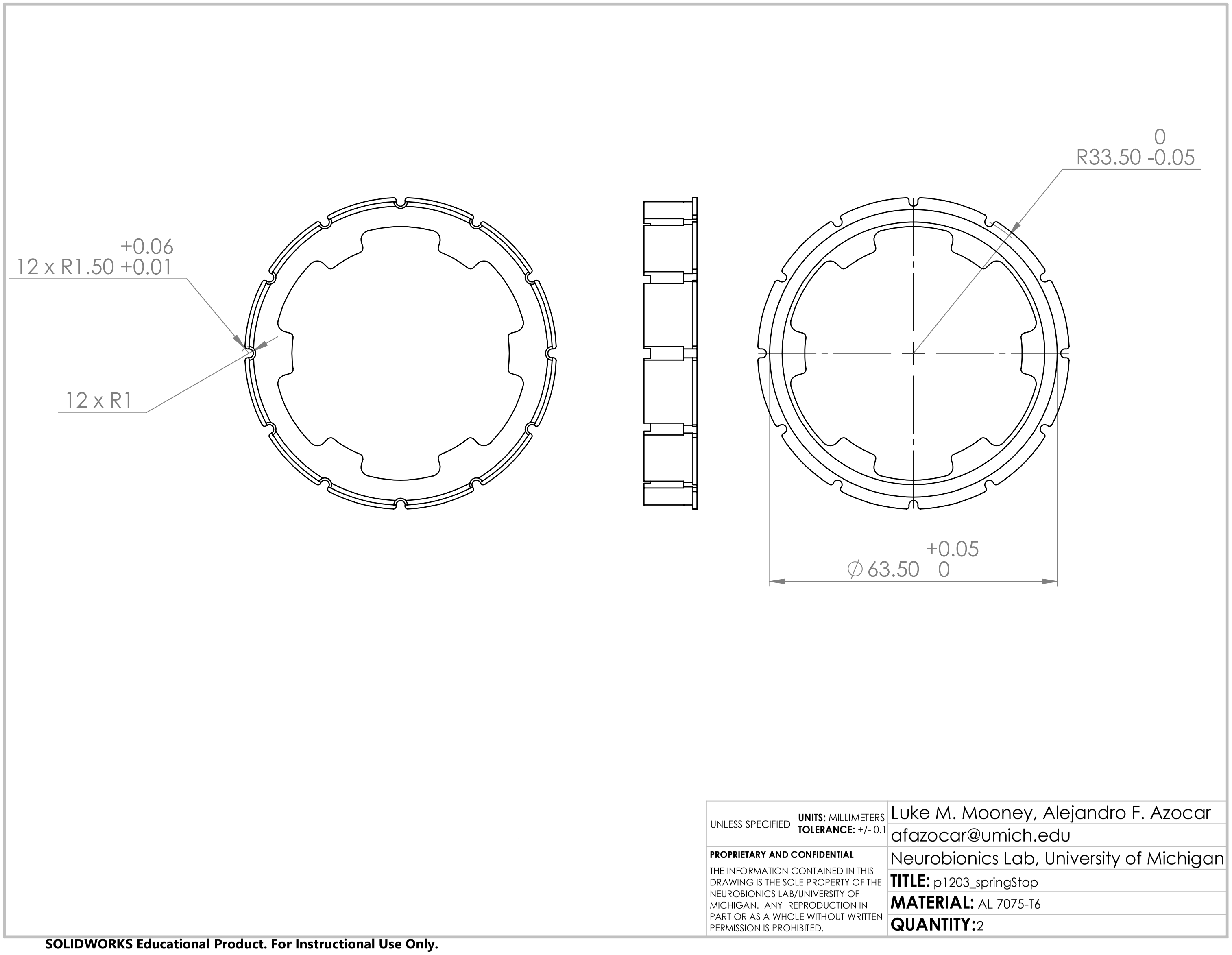

UNLESS SPECIFIED **UNITS:** MILLIMETERS **TOLERANCE:** +/- 0.1

Luke M. Mooney, Alejandro F. Azocar
afazocar@umich.edu
Neurobionics Lab, University of Michigan

PROPRIETARY AND CONFIDENTIAL

THE INFORMATION CONTAINED IN THIS DRAWING IS THE SOLE PROPERTY OF THE NEUROBIONICS LAB/UNIVERSITY OF MICHIGAN. ANY REPRODUCTION IN PART OR AS A WHOLE WITHOUT WRITTEN PERMISSION IS PROHIBITED.

TITLE: p1203_springStop
MATERIAL: AL 7075-T6
QUANTITY:2

Figure A.40: OSL knee spring stop.

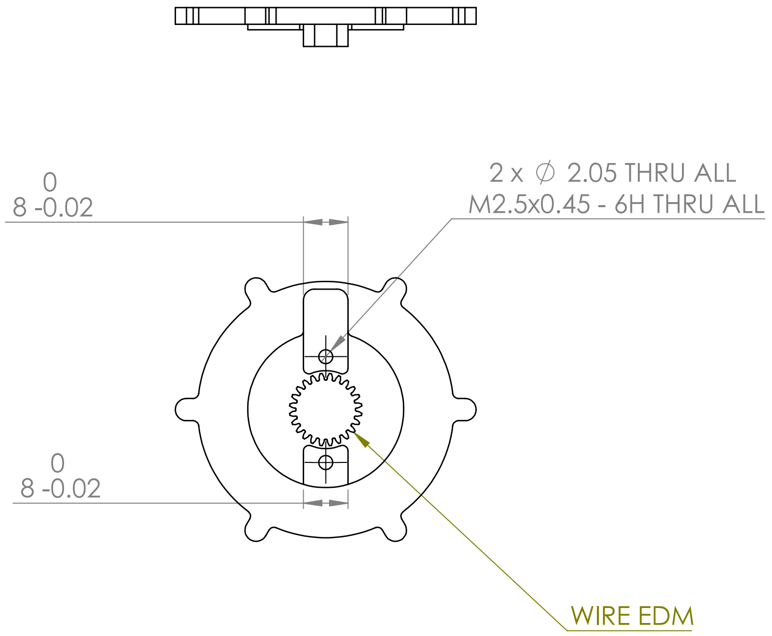

UNLESS SPECIFIED **UNITS:** MILLIMETERS **TOLERANCE:** +/- 0.1

PROPRIETARY AND CONFIDENTIAL

Elliott J. Rouse, Luke M. Mooney, Alejandro F. Azocar
afazocar@umich.edu
Neurobionics Lab, University of Michigan
TITLE: p1204_gearStopSpring
MATERIAL: AL 7075-T6
QUANTITY:2

Figure A.41: OSL knee gear stop, SEA configuration.

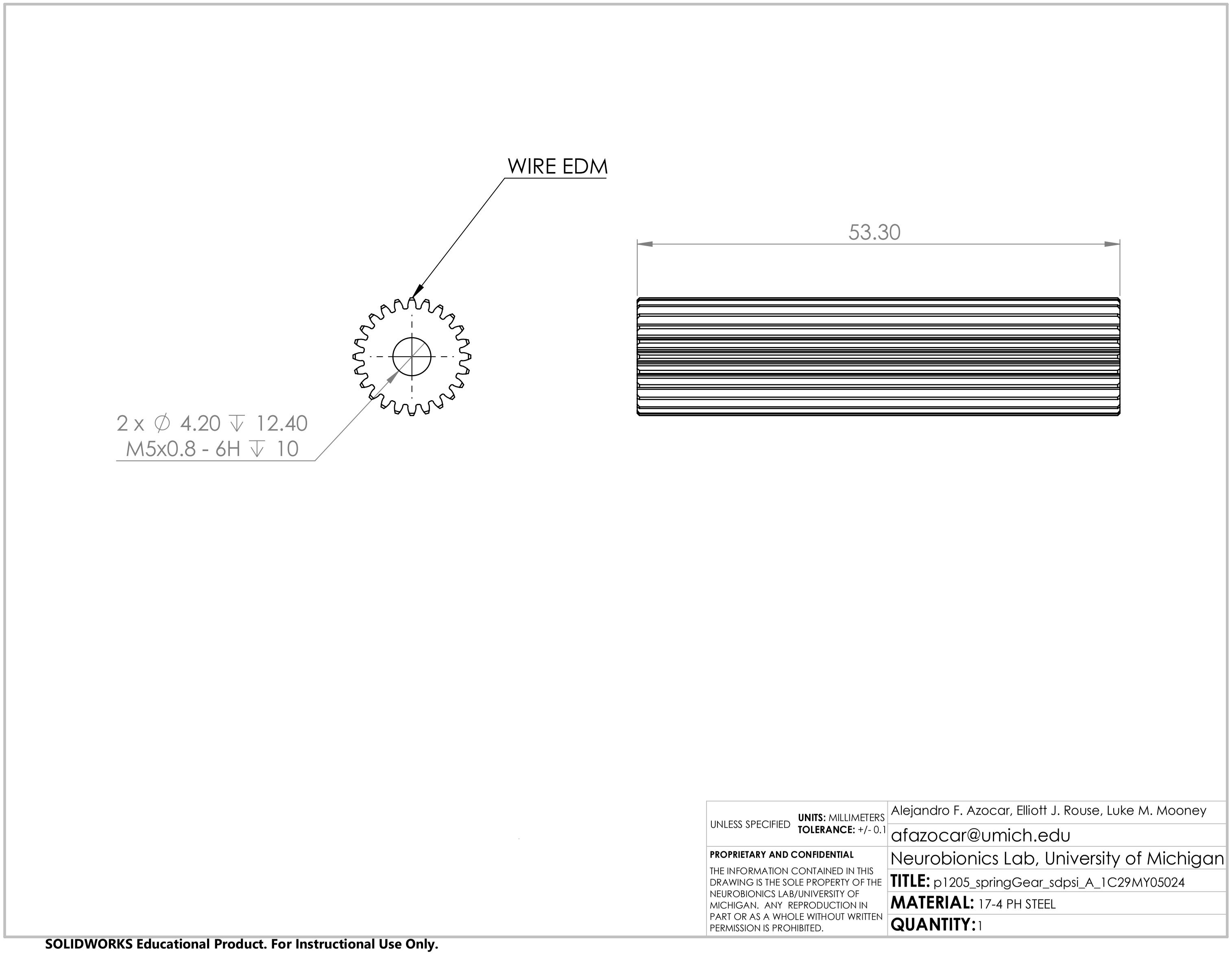

Figure A.42: OSL knee spring gear.

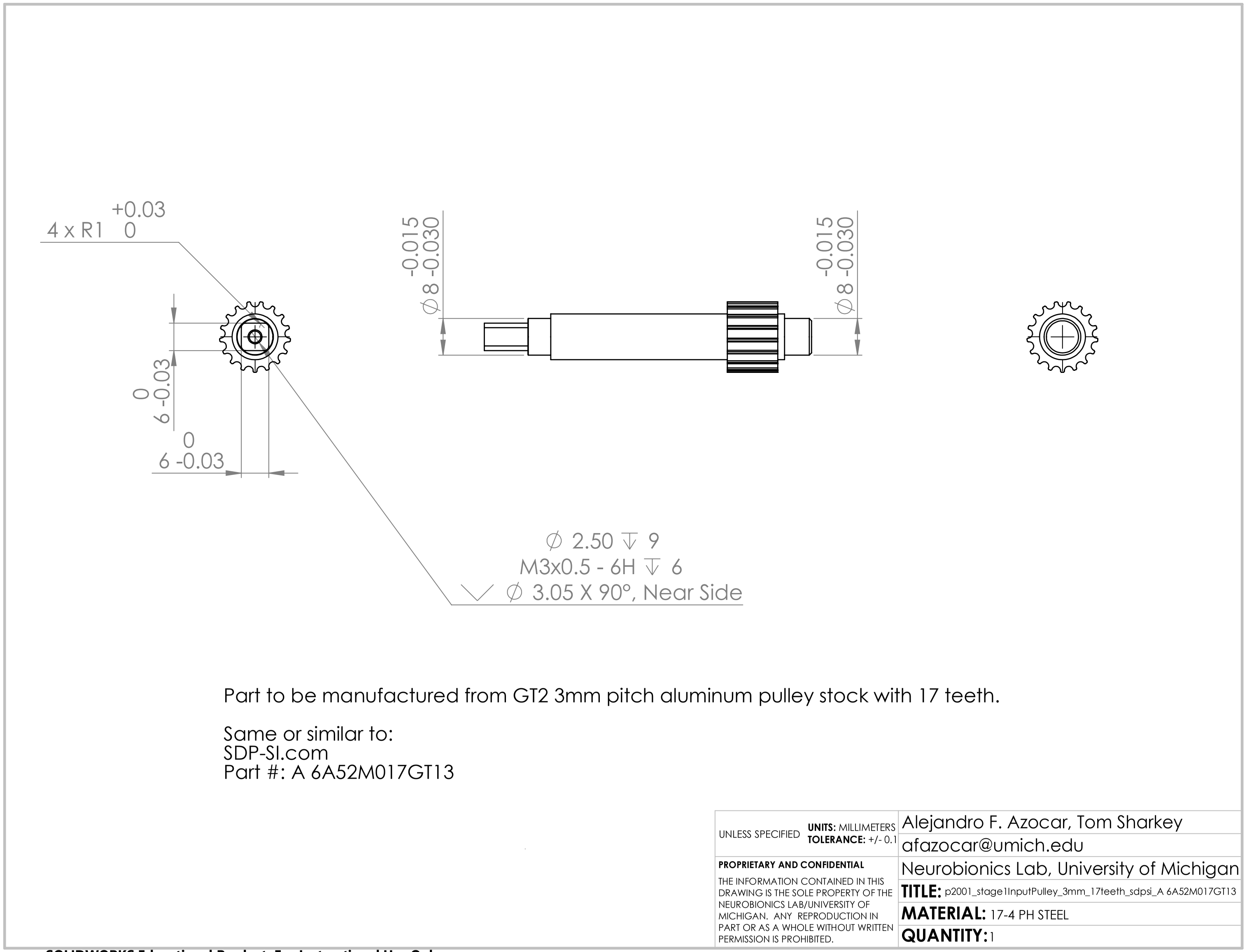

Part to be manufactured from GT2 3mm pitch aluminum pulley stock with 17 teeth.

Same or similar to:
SDP-SI.com
Part #: A 6A52M017GT13

UNLESS SPECIFIED **UNITS:** MILLIMETERS **TOLERANCE:** +/- 0.1	Alejandro F. Azocar, Tom Sharkey afazocar@umich.edu
PROPRIETARY AND CONFIDENTIAL THE INFORMATION CONTAINED IN THIS DRAWING IS THE SOLE PROPERTY OF THE NEUROBIONICS LAB/UNIVERSITY OF MICHIGAN. ANY REPRODUCTION IN PART OR AS A WHOLE WITHOUT WRITTEN PERMISSION IS PROHIBITED.	Neurobionics Lab, University of Michigan **TITLE:** p2001_stage1InputPulley_3mm_17teeth_sdpsi_A 6A52M017GT13 **MATERIAL:** 17-4 PH STEEL **QUANTITY:** 1

Figure A.43: OSL ankle stage 1 input pulley.

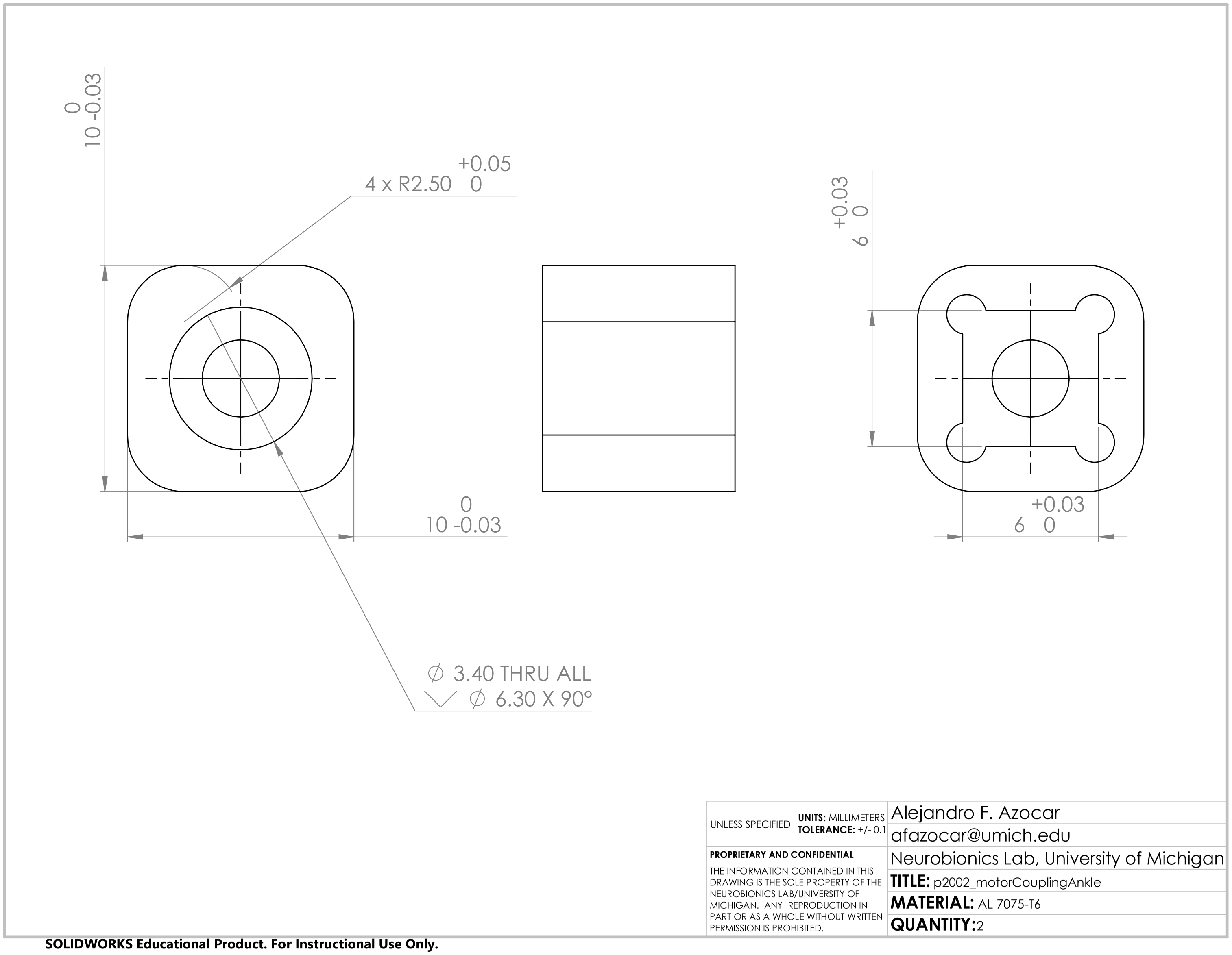

Figure A.44: OSL ankle motor coupling.

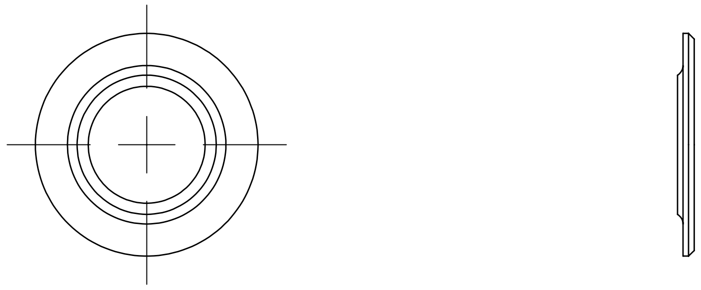

UNLESS SPECIFIED **UNITS:** MILLIMETERS **TOLERANCE:** +/- 0.1	Alejandro F. Azocar, Tom Sharkey afazocar@umich.edu
PROPRIETARY AND CONFIDENTIAL THE INFORMATION CONTAINED IN THIS DRAWING IS THE SOLE PROPERTY OF THE NEUROBIONICS LAB/UNIVERSITY OF MICHIGAN. ANY REPRODUCTION IN PART OR AS A WHOLE WITHOUT WRITTEN PERMISSION IS PROHIBITED.	Neurobionics Lab, University of Michigan **TITLE:** p2003_pulleyFlange_stage1InputSmall **MATERIAL:** ABS, black **QUANTITY:**2

Figure A.45: OSL ankle stage 1 input pulley flange, small.

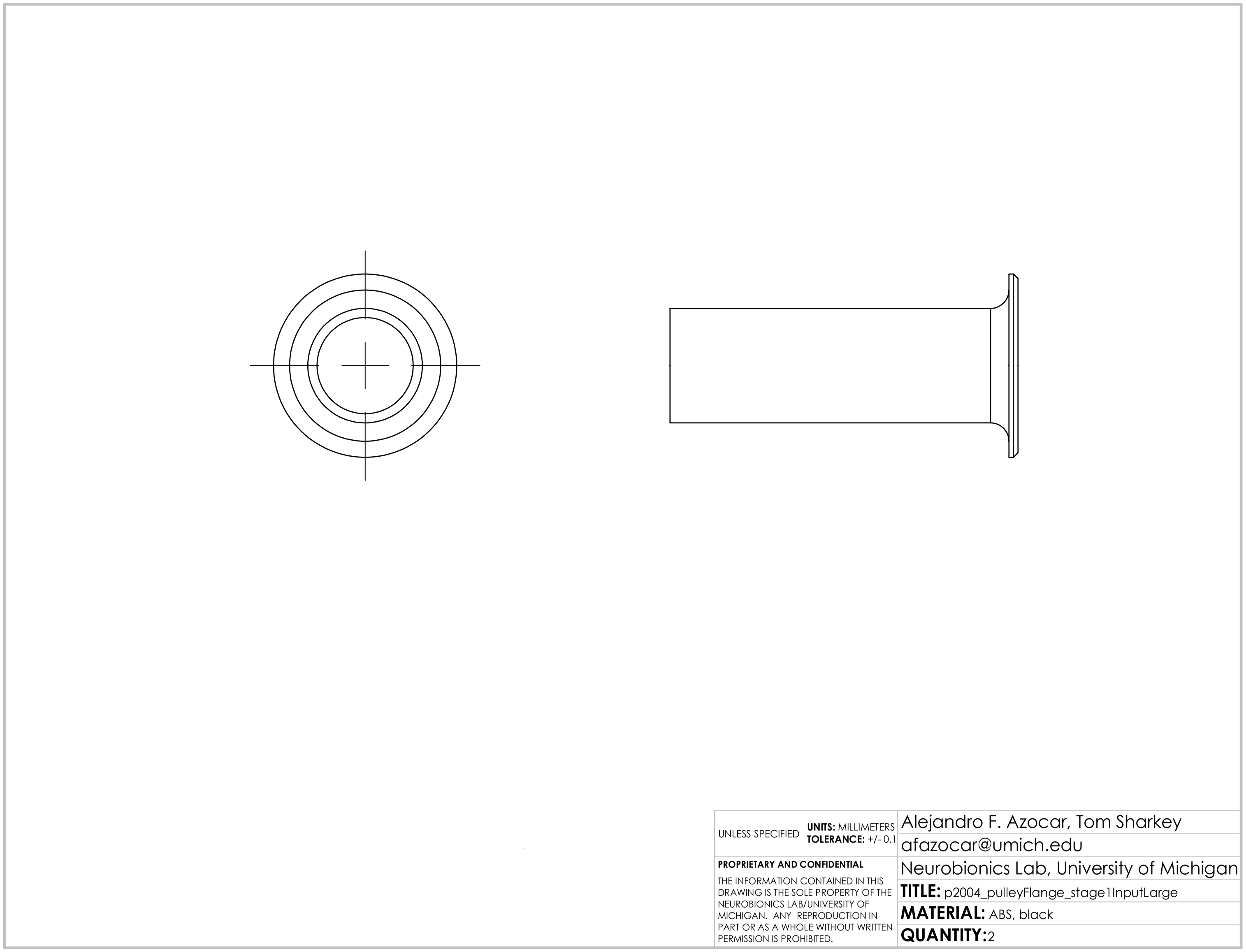

UNLESS SPECIFIED **UNITS:** MILLIMETERS **TOLERANCE:** +/- 0.1

PROPRIETARY AND CONFIDENTIAL

THE INFORMATION CONTAINED IN THIS DRAWING IS THE SOLE PROPERTY OF THE NEUROBIONICS LAB/UNIVERSITY OF MICHIGAN. ANY REPRODUCTION IN PART OR AS A WHOLE WITHOUT WRITTEN PERMISSION IS PROHIBITED.

Alejandro F. Azocar, Tom Sharkey
afazocar@umich.edu
Neurobionics Lab, University of Michigan
TITLE: p2004_pulleyFlange_stage1InputLarge
MATERIAL: ABS, black
QUANTITY:2

Figure A.46: OSL ankle stage 1 input pulley flange, large.

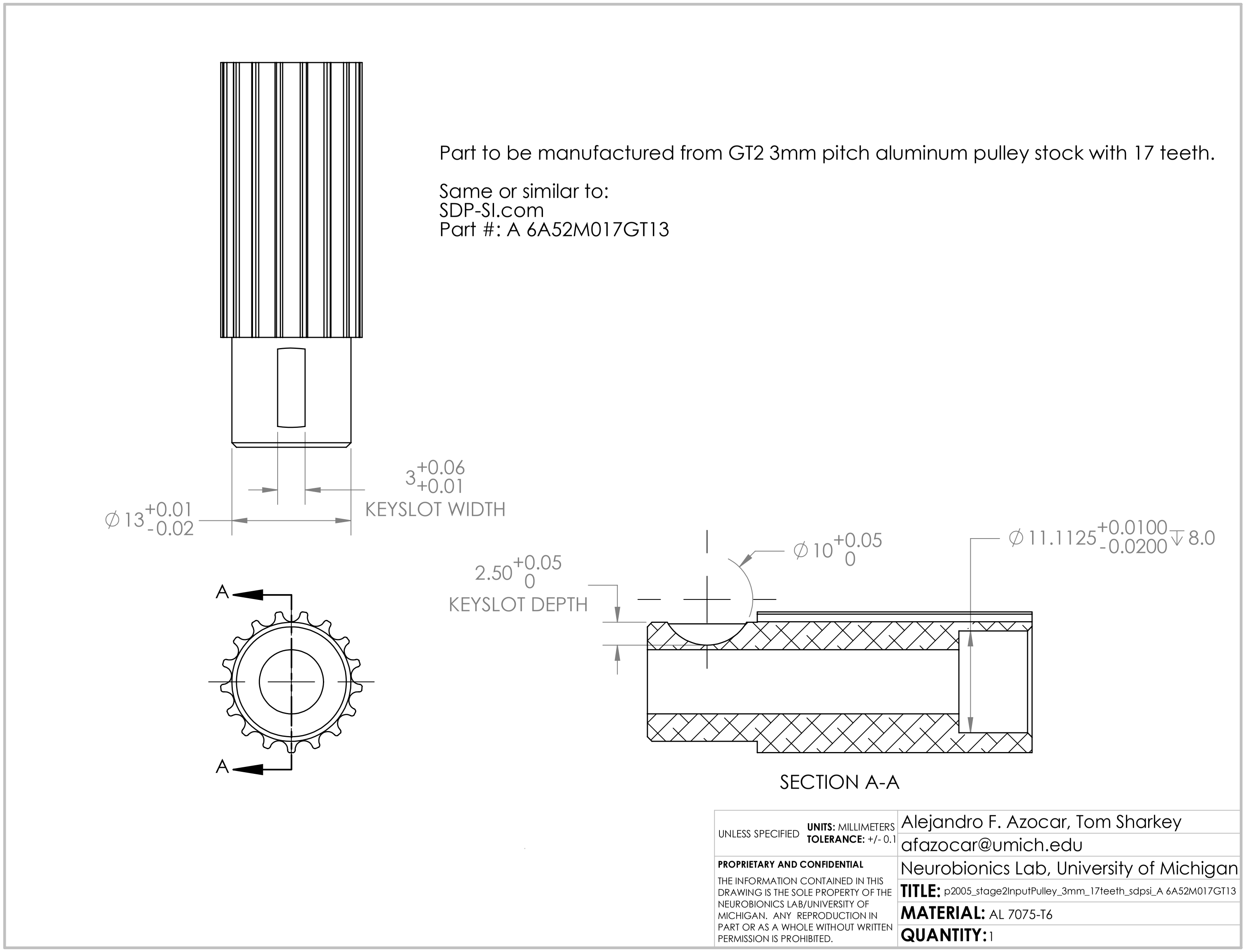

Part to be manufactured from GT2 3mm pitch aluminum pulley stock with 17 teeth.

Same or similar to:
SDP-SI.com
Part #: A 6A52M017GT13

UNLESS SPECIFIED **UNITS:** MILLIMETERS
TOLERANCE: +/- 0.1

Alejandro F. Azocar, Tom Sharkey
afazocar@umich.edu
Neurobionics Lab, University of Michigan

PROPRIETARY AND CONFIDENTIAL

THE INFORMATION CONTAINED IN THIS DRAWING IS THE SOLE PROPERTY OF THE NEUROBIONICS LAB/UNIVERSITY OF MICHIGAN. ANY REPRODUCTION IN PART OR AS A WHOLE WITHOUT WRITTEN PERMISSION IS PROHIBITED.

TITLE: p2005_stage2InputPulley_3mm_17teeth_sdpsi_A 6A52M017GT13
MATERIAL: AL 7075-T6
QUANTITY: 1

Figure A.47: OSL ankle stage 2 input pulley.

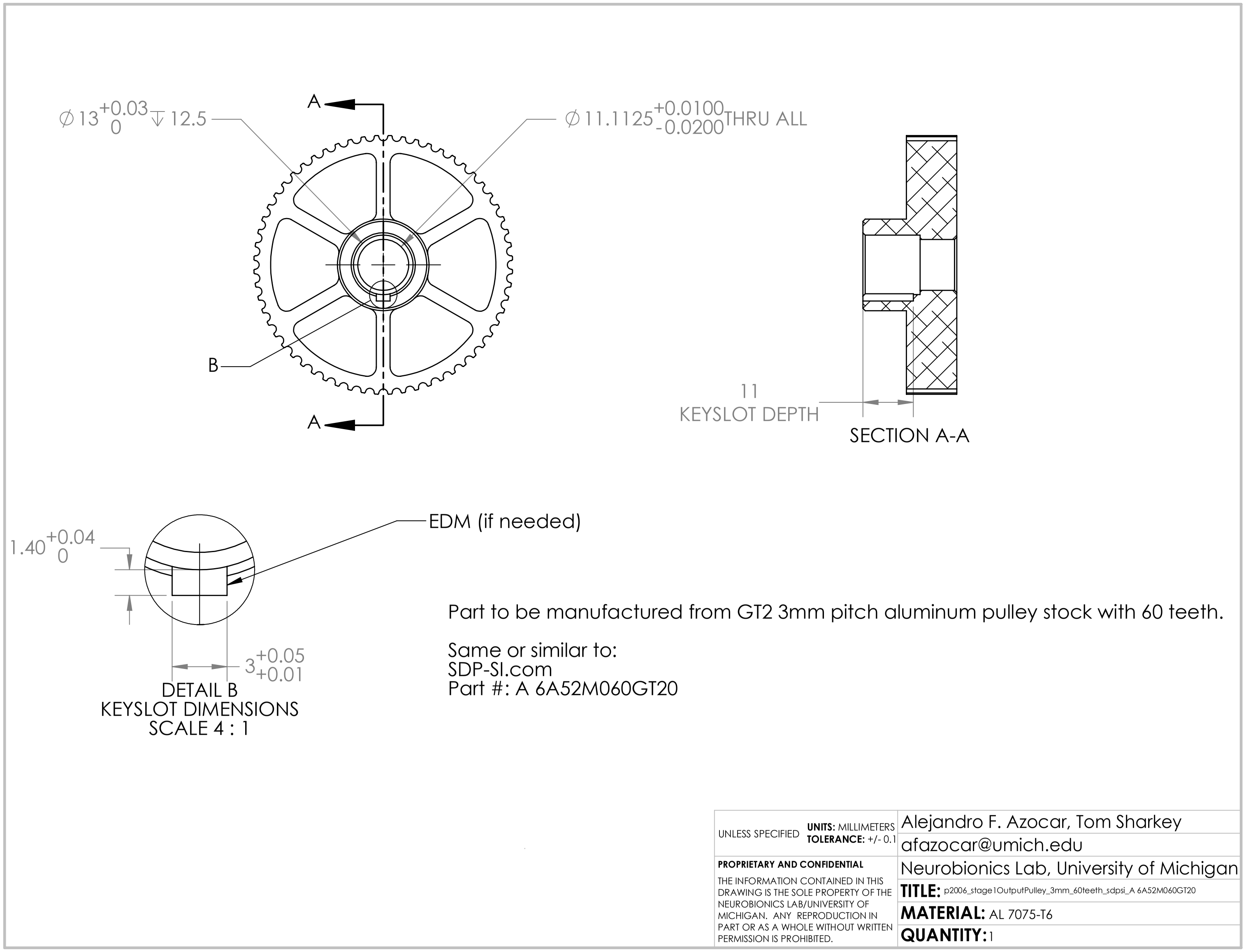

Part to be manufactured from GT2 3mm pitch aluminum pulley stock with 60 teeth.

Same or similar to:
SDP-SI.com
Part #: A 6A52M060GT20

UNLESS SPECIFIED **UNITS:** MILLIMETERS **TOLERANCE:** +/- 0.1

Alejandro F. Azocar, Tom Sharkey
afazocar@umich.edu
Neurobionics Lab, University of Michigan

PROPRIETARY AND CONFIDENTIAL

THE INFORMATION CONTAINED IN THIS DRAWING IS THE SOLE PROPERTY OF THE NEUROBIONICS LAB/UNIVERSITY OF MICHIGAN. ANY REPRODUCTION IN PART OR AS A WHOLE WITHOUT WRITTEN PERMISSION IS PROHIBITED.

TITLE: p2006_stage1OutputPulley_3mm_60teeth_sdpsi_A 6A52M060GT20
MATERIAL: AL 7075-T6
QUANTITY: 1

Figure A.48: OSL ankle stage 1 output pulley.

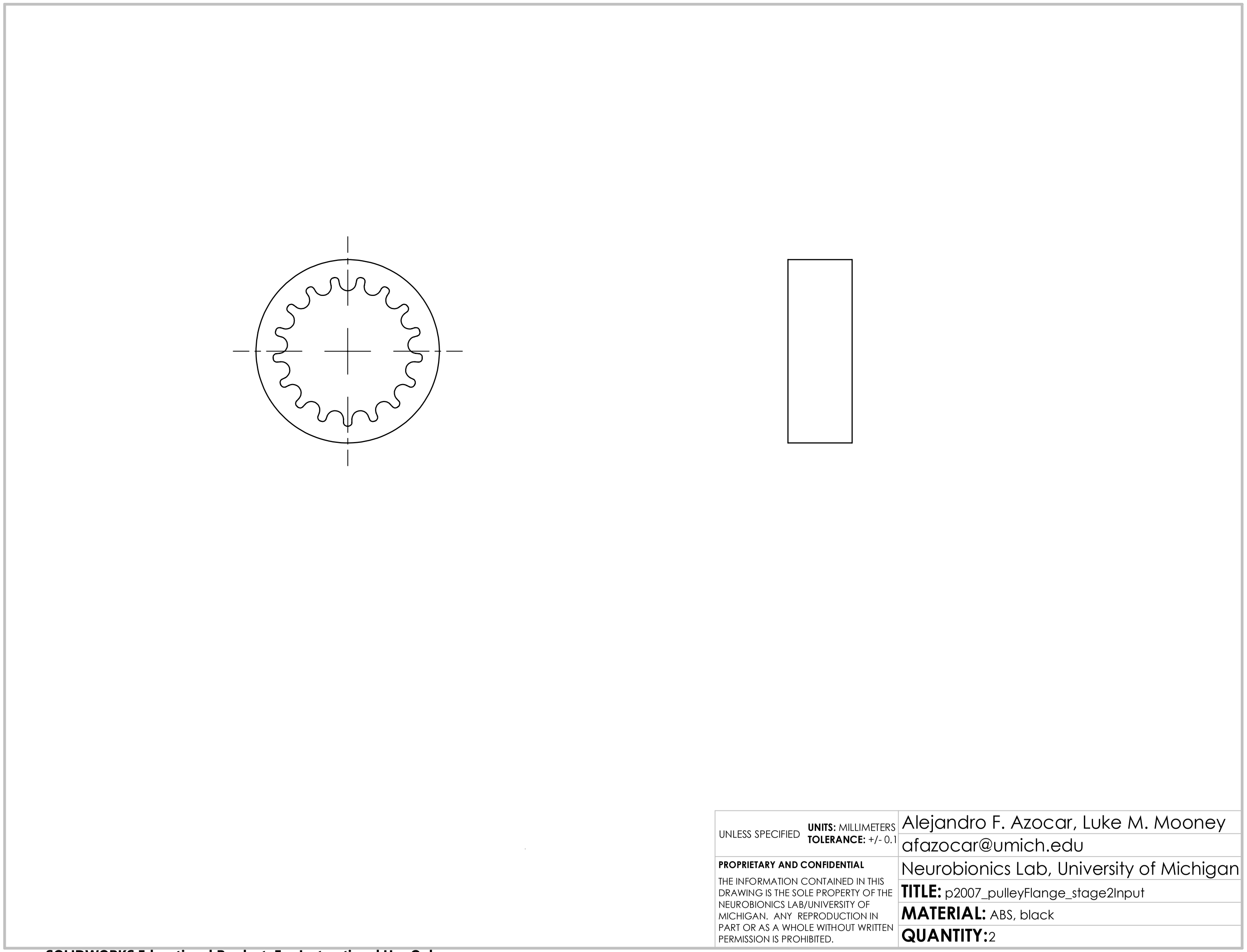

UNLESS SPECIFIED **UNITS:** MILLIMETERS **TOLERANCE:** +/- 0.1

Alejandro F. Azocar, Luke M. Mooney
afazocar@umich.edu
Neurobionics Lab, University of Michigan

PROPRIETARY AND CONFIDENTIAL

THE INFORMATION CONTAINED IN THIS DRAWING IS THE SOLE PROPERTY OF THE NEUROBIONICS LAB/UNIVERSITY OF MICHIGAN. ANY REPRODUCTION IN PART OR AS A WHOLE WITHOUT WRITTEN PERMISSION IS PROHIBITED.

TITLE: p2007_pulleyFlange_stage2Input
MATERIAL: ABS, black
QUANTITY:2

Figure A.49: OSL ankle stage 2 input pulley flange.

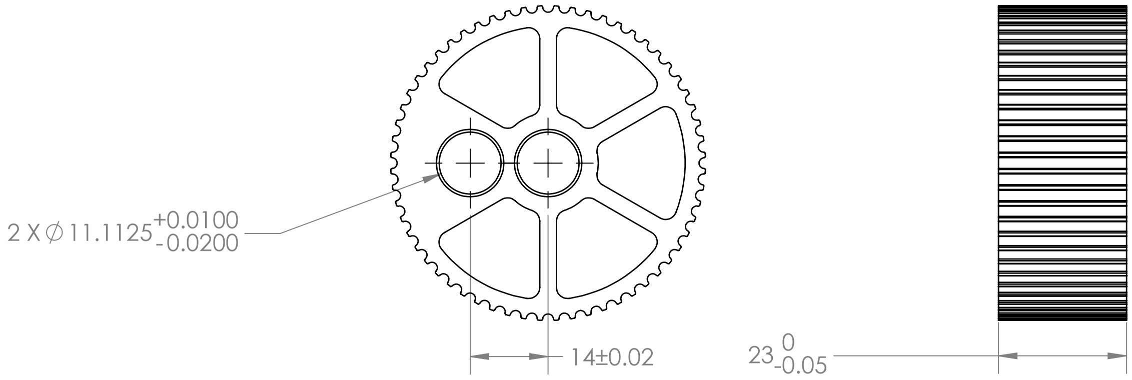

Part to be manufactured from GT2 3mm pitch aluminum pulley stock with 60 teeth.

Same or similar to:
SDP-SI.com
Part #: A 6A52M060GT20

UNLESS SPECIFIED **UNITS:** MILLIMETERS **TOLERANCE:** +/- 0.1	Alejandro F. Azocar, Tom Sharkey afazocar@umich.edu
PROPRIETARY AND CONFIDENTIAL THE INFORMATION CONTAINED IN THIS DRAWING IS THE SOLE PROPERTY OF THE NEUROBIONICS LAB/UNIVERSITY OF MICHIGAN. ANY REPRODUCTION IN PART OR AS A WHOLE WITHOUT WRITTEN PERMISSION IS PROHIBITED.	Neurobionics Lab, University of Michigan **TITLE:** p2008_stage2OutputPulley_3mm_60teeth_sdpsi_A 6A52M060GT20 **MATERIAL:** AL 7075-T6 **QUANTITY:** 1

Figure A.50: OSL ankle stage 2 output pulley.

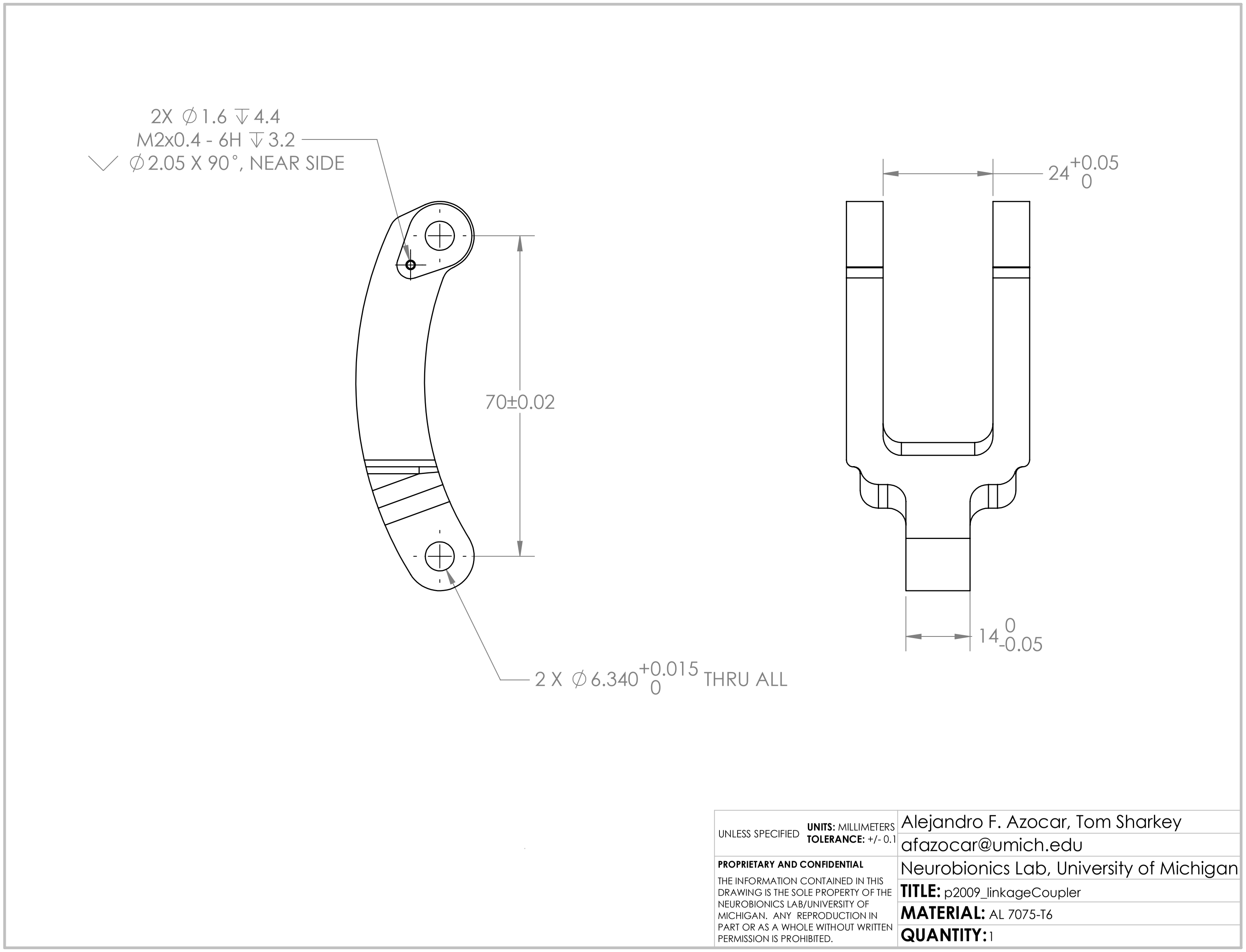

Figure A.51: OSL ankle linkage coupler.

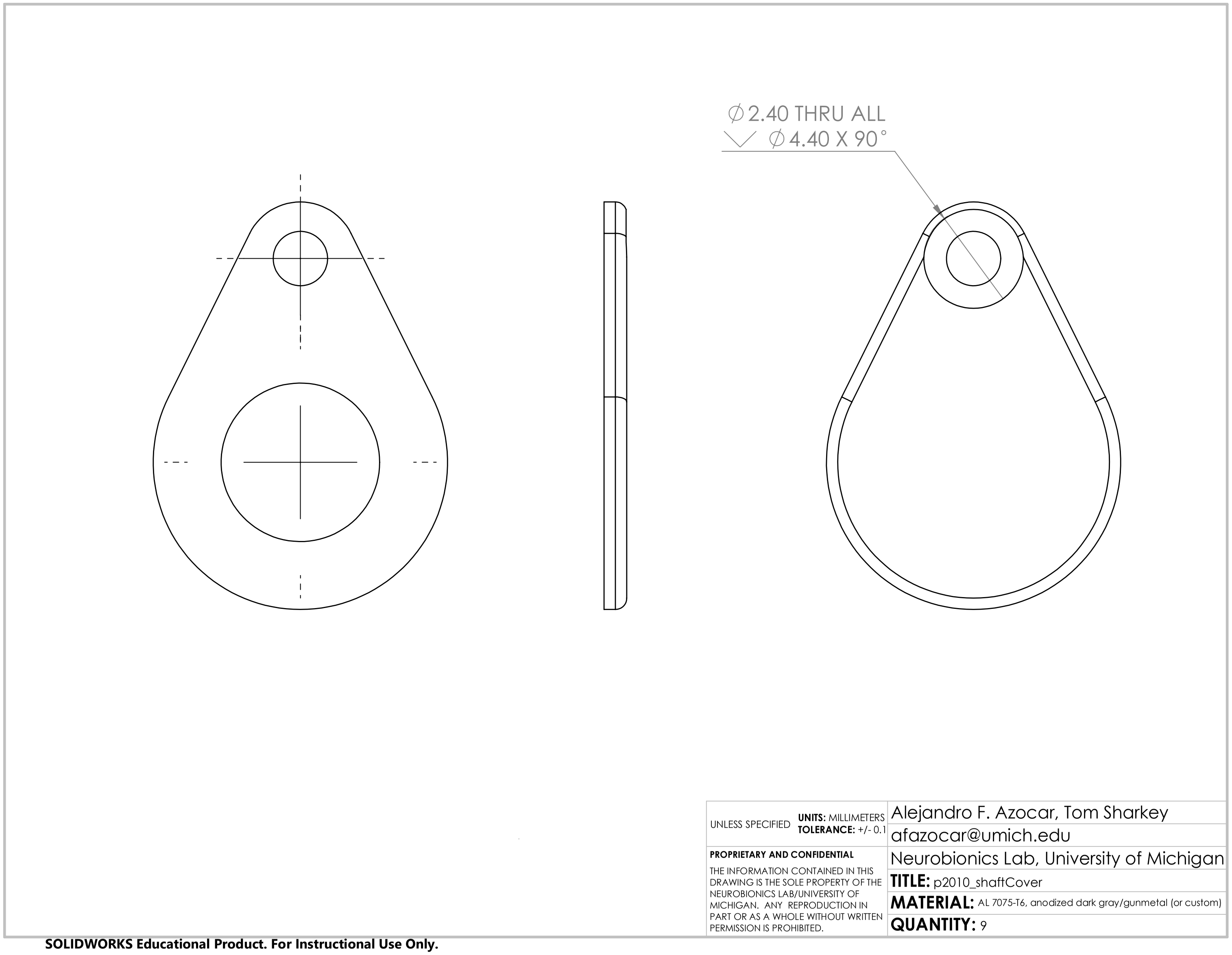

UNLESS SPECIFIED **UNITS:** MILLIMETERS **TOLERANCE:** +/- 0.1

Alejandro F. Azocar, Tom Sharkey

afazocar@umich.edu

Neurobionics Lab, University of Michigan

TITLE: p2010_shaftCover

MATERIAL: AL 7075-T6, anodized dark gray/gunmetal (or custom)

QUANTITY: 9

PROPRIETARY AND CONFIDENTIAL

THE INFORMATION CONTAINED IN THIS DRAWING IS THE SOLE PROPERTY OF THE NEUROBIONICS LAB/UNIVERSITY OF MICHIGAN. ANY REPRODUCTION IN PART OR AS A WHOLE WITHOUT WRITTEN PERMISSION IS PROHIBITED.

Figure A.52: OSL ankle shaft cover.

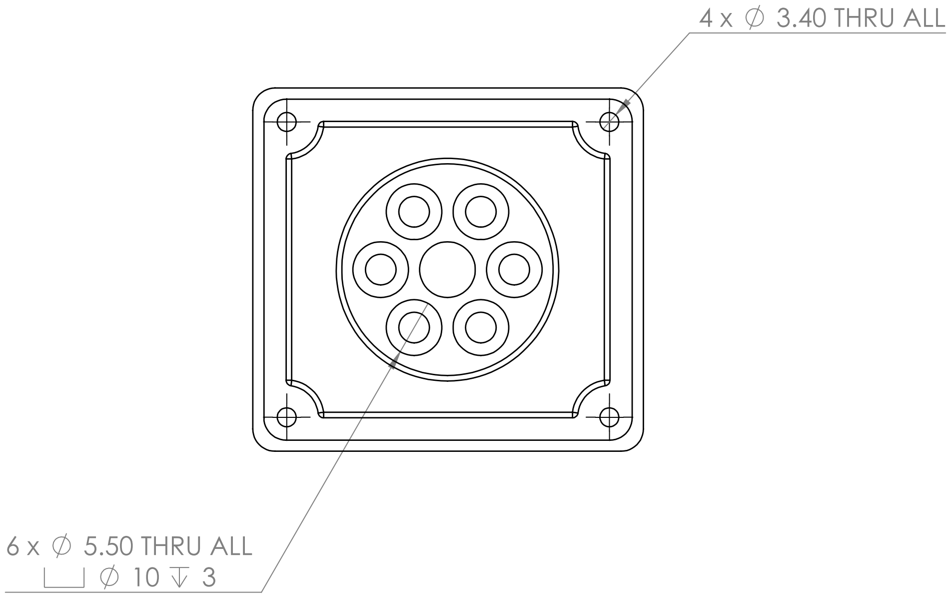

UNLESS SPECIFIED **UNITS:** MILLIMETERS **TOLERANCE:** +/- 0.1	Alejandro F. Azocar, Tom Sharkey afazocar@umich.edu
PROPRIETARY AND CONFIDENTIAL THE INFORMATION CONTAINED IN THIS DRAWING IS THE SOLE PROPERTY OF THE NEUROBIONICS LAB/UNIVERSITY OF MICHIGAN. ANY REPRODUCTION IN PART OR AS A WHOLE WITHOUT WRITTEN PERMISSION IS PROHIBITED.	Neurobionics Lab, University of Michigan **TITLE:** p2011_proxBase **MATERIAL:** AL 7075-T6, anodized black (or custom) **QUANTITY:** 1

Figure A.53: OSL ankle proximal base.

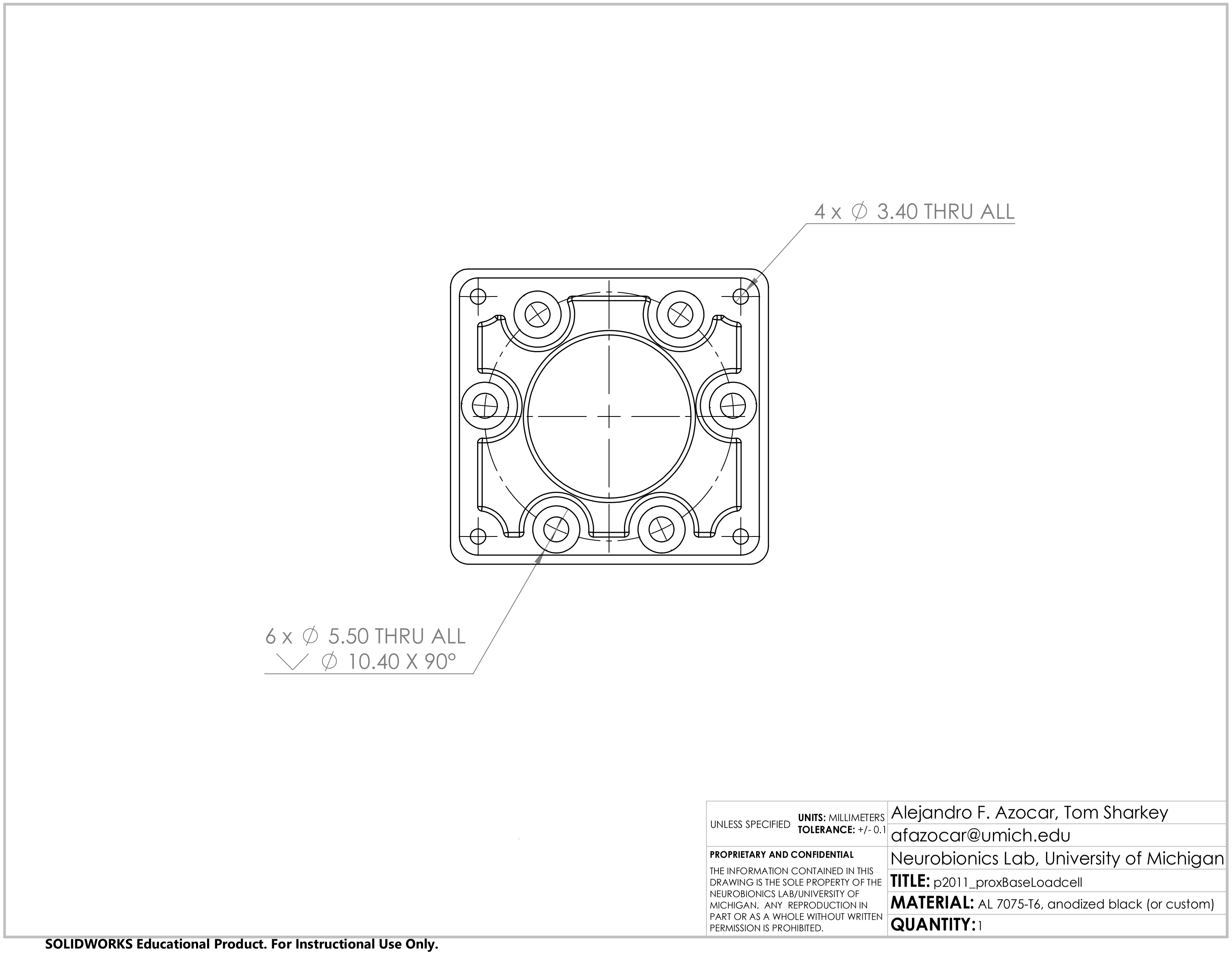

Figure A.54: OSL ankle proximal base, compatible with M3564F loadcell.

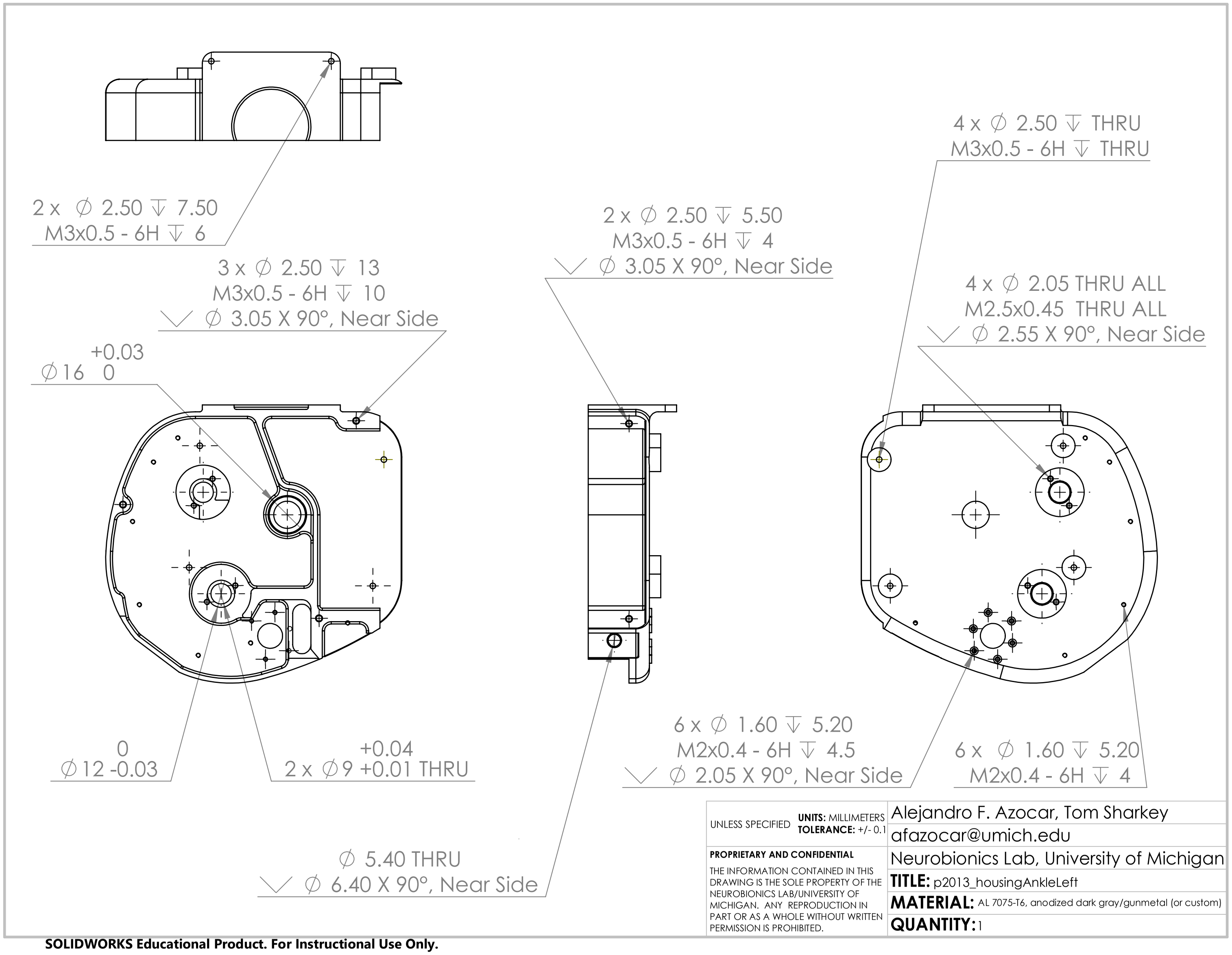

Figure A.55: OSL ankle housing, left.

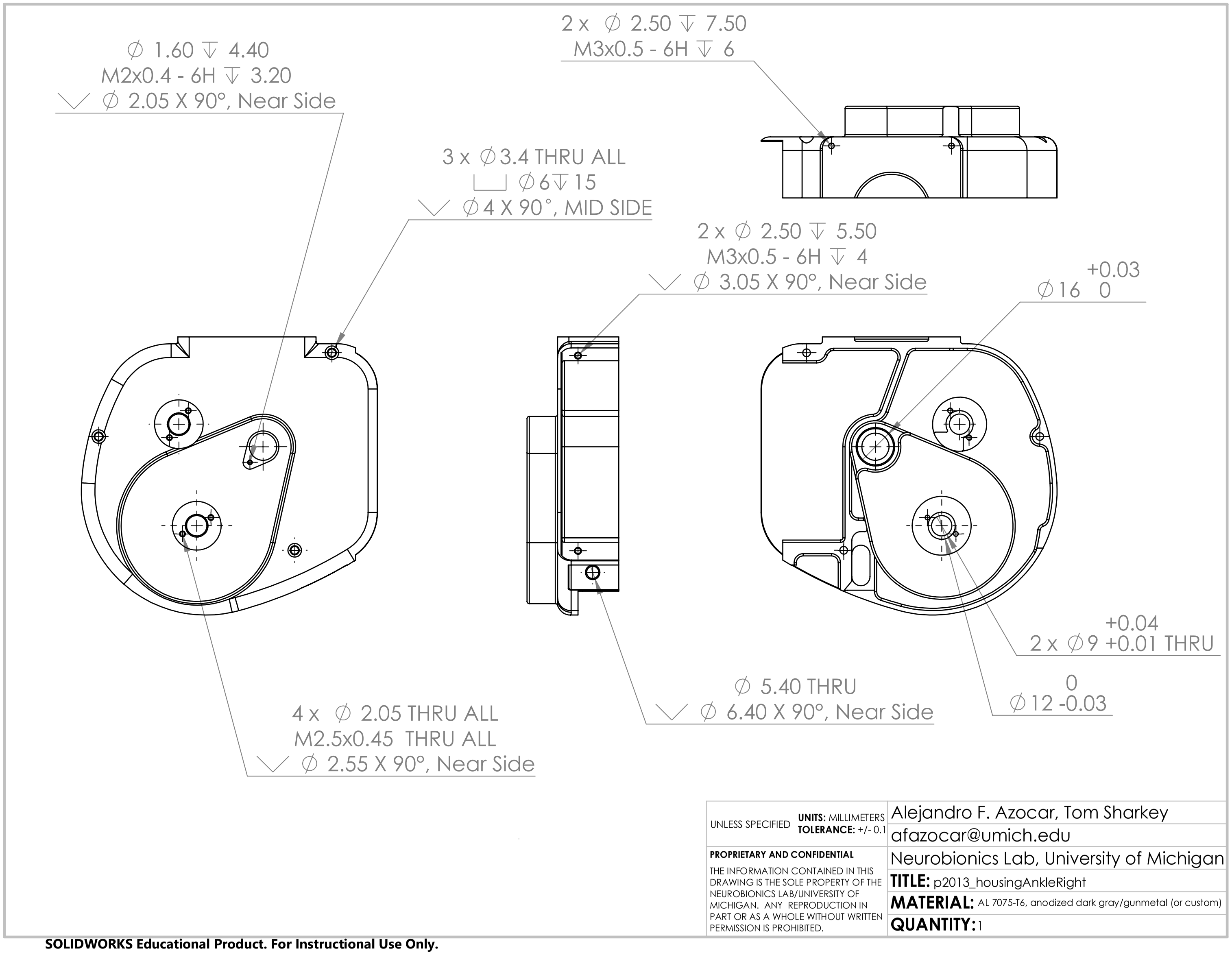

Figure A.56: OSL ankle housing, right.

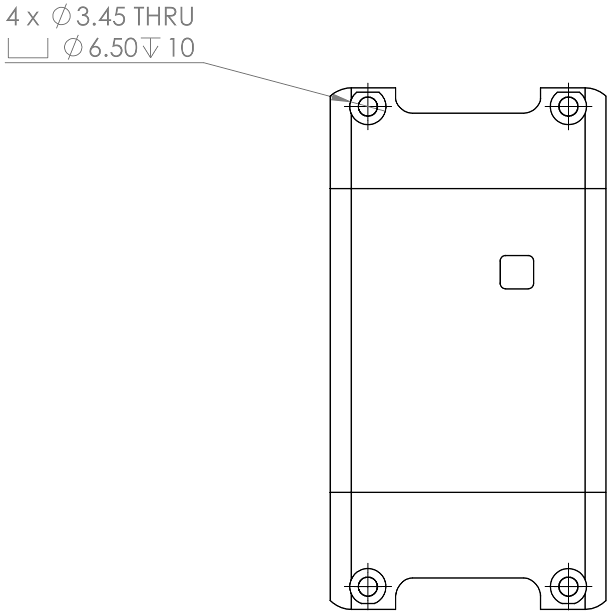

UNLESS SPECIFIED **UNITS:** MILLIMETERS **TOLERANCE:** +/- 0.1	Alejandro F. Azocar, Tom Sharkey afazocar@umich.edu
PROPRIETARY AND CONFIDENTIAL THE INFORMATION CONTAINED IN THIS DRAWING IS THE SOLE PROPERTY OF THE NEUROBIONICS LAB/UNIVERSITY OF MICHIGAN. ANY REPRODUCTION IN PART OR AS A WHOLE WITHOUT WRITTEN PERMISSION IS PROHIBITED.	Neurobionics Lab, University of Michigan **TITLE:** p2014_electronicsCoverAnkle **MATERIAL:** ABS, black **QUANTITY:** 1

Figure A.57: OSL ankle electronics cover.

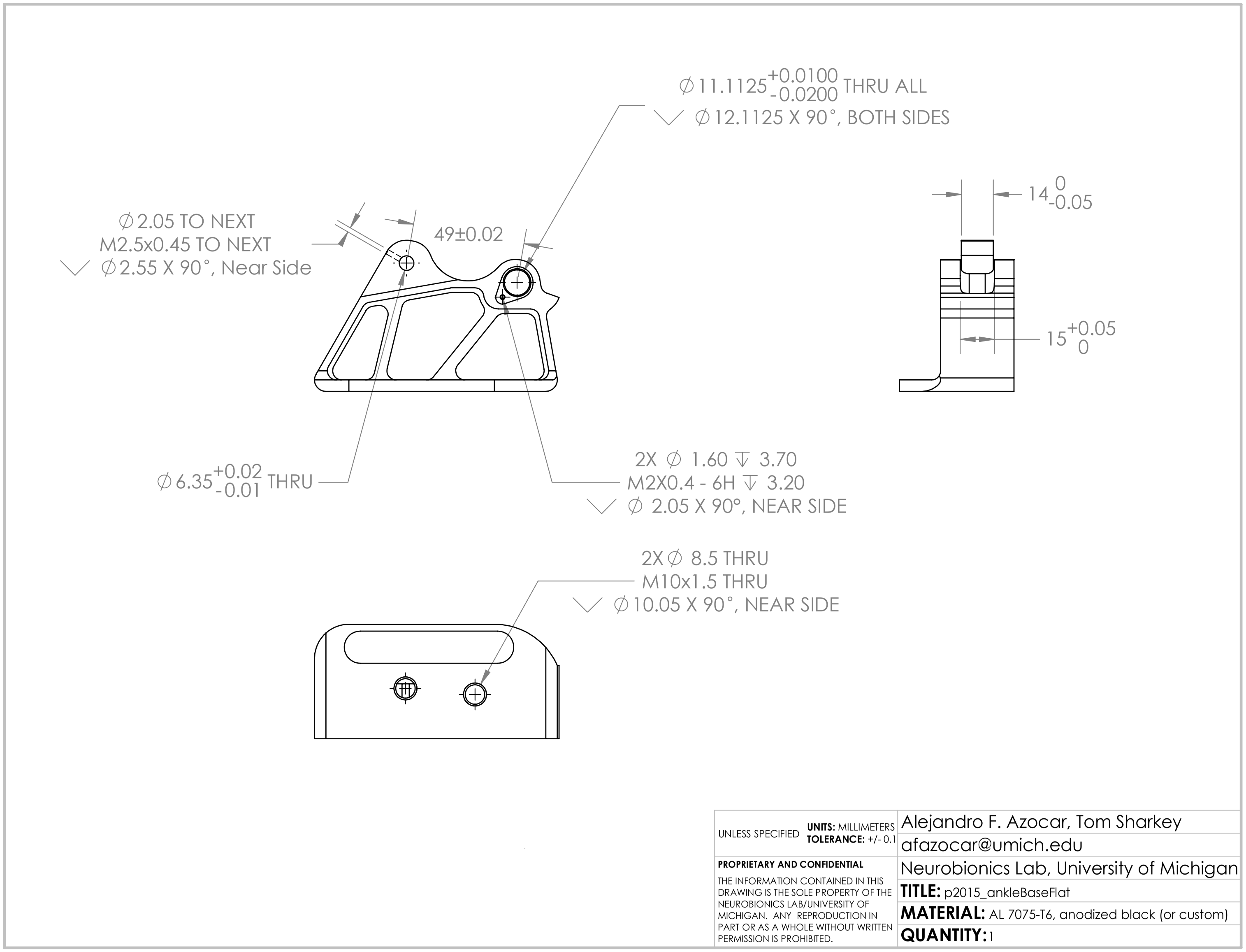

Figure A.58: OSL ankle base, flat foot configuration.

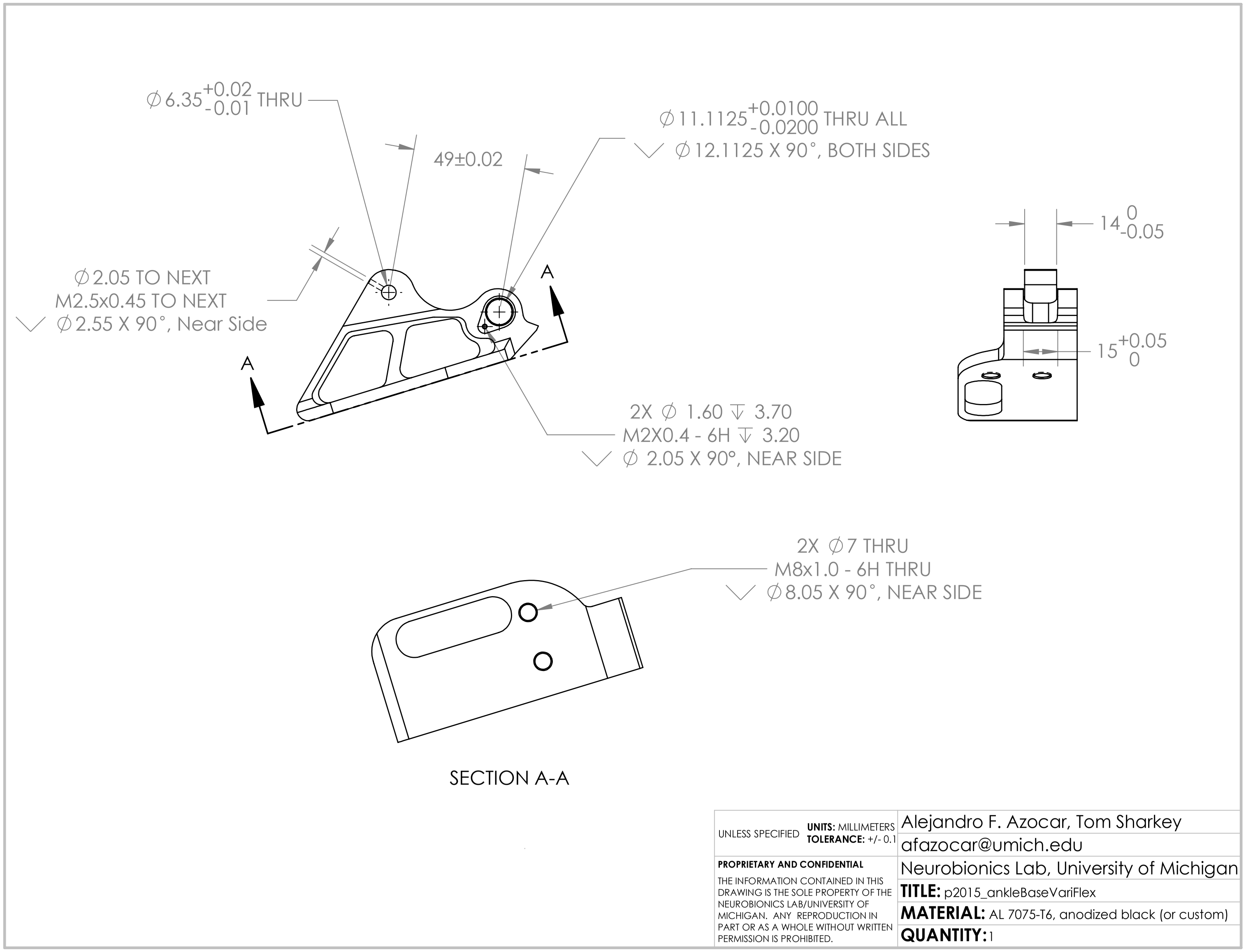

Figure A.59: OSL ankle base, VariFlex foot configuration.

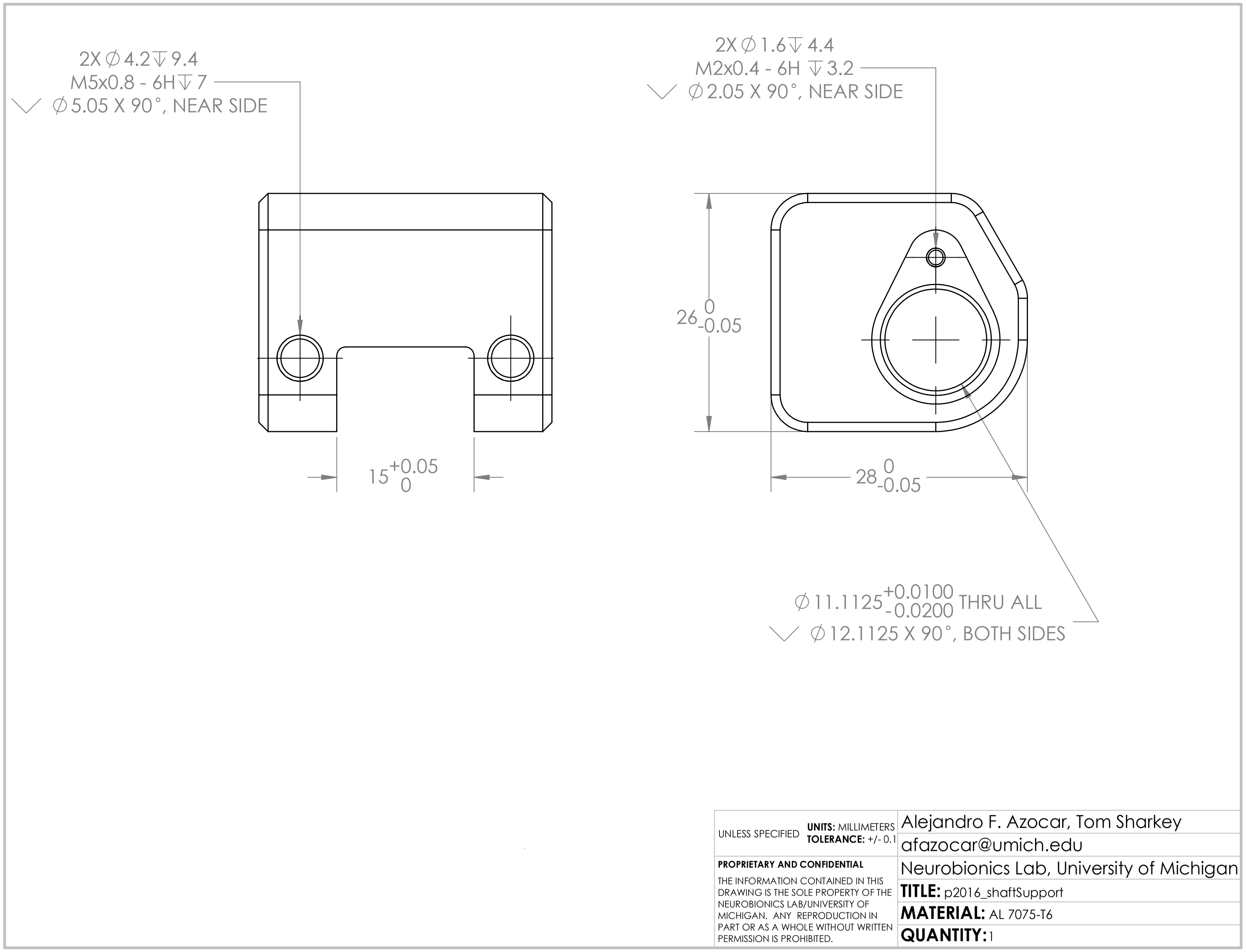

Figure A.60: OSL ankle shaft support.

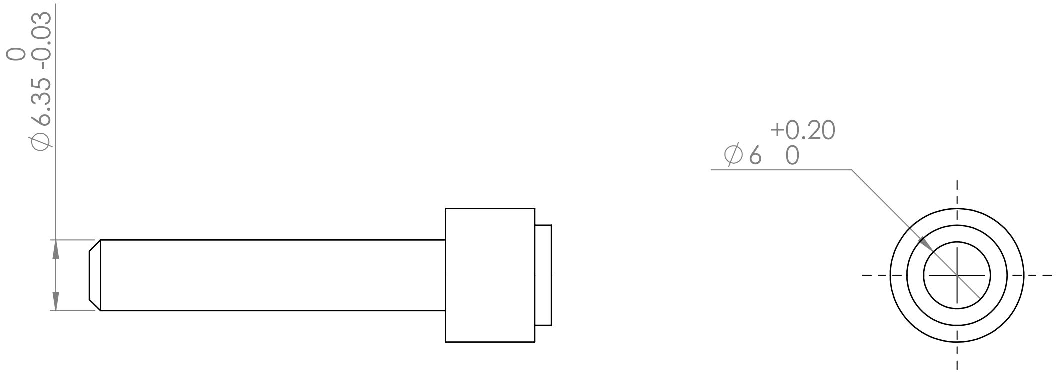

UNLESS SPECIFIED **UNITS:** MILLIMETERS **TOLERANCE:** +/- 0.1	Alejandro F. Azocar, Tom Sharkey afazocar@umich.edu
PROPRIETARY AND CONFIDENTIAL THE INFORMATION CONTAINED IN THIS DRAWING IS THE SOLE PROPERTY OF THE NEUROBIONICS LAB/UNIVERSITY OF MICHIGAN. ANY REPRODUCTION IN PART OR AS A WHOLE WITHOUT WRITTEN PERMISSION IS PROHIBITED.	Neurobionics Lab, University of Michigan **TITLE:** p2017_shaftAnkleJoint **MATERIAL:** AL 7075-T6 **QUANTITY:**2

Figure A.61: OSL ankle joint shaft.

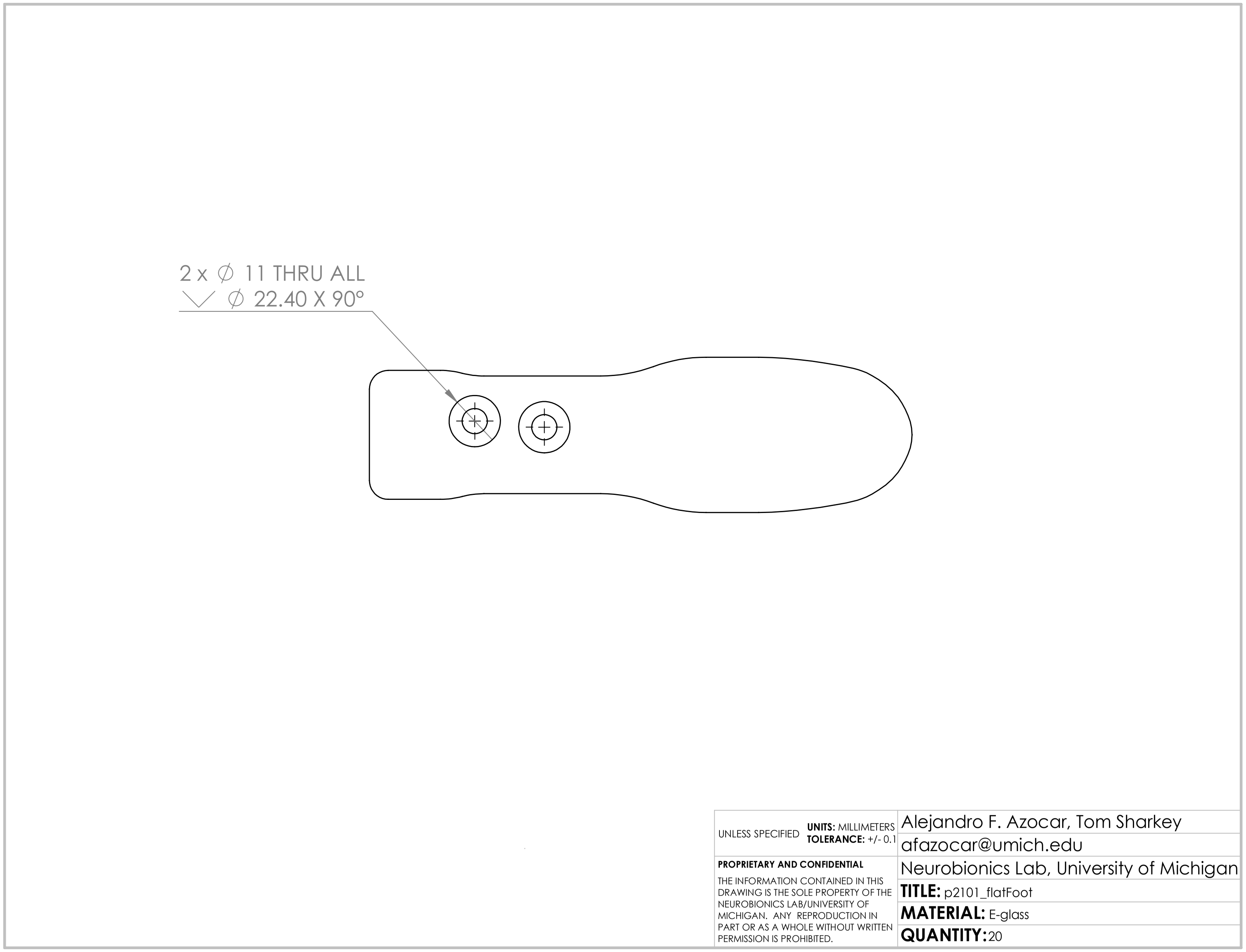

Figure A.62: OSL ankle flat foot.

Appendix B

Open-source Leg: Testing

This appendix contains highlights of the OSL, including: assembly, testing with an able-bodied adapter, and testing with patients—both in the Neurobionics Lab and the Shirley Ryan AbilityLab (courtesy of the Center for Bionic Medicine).

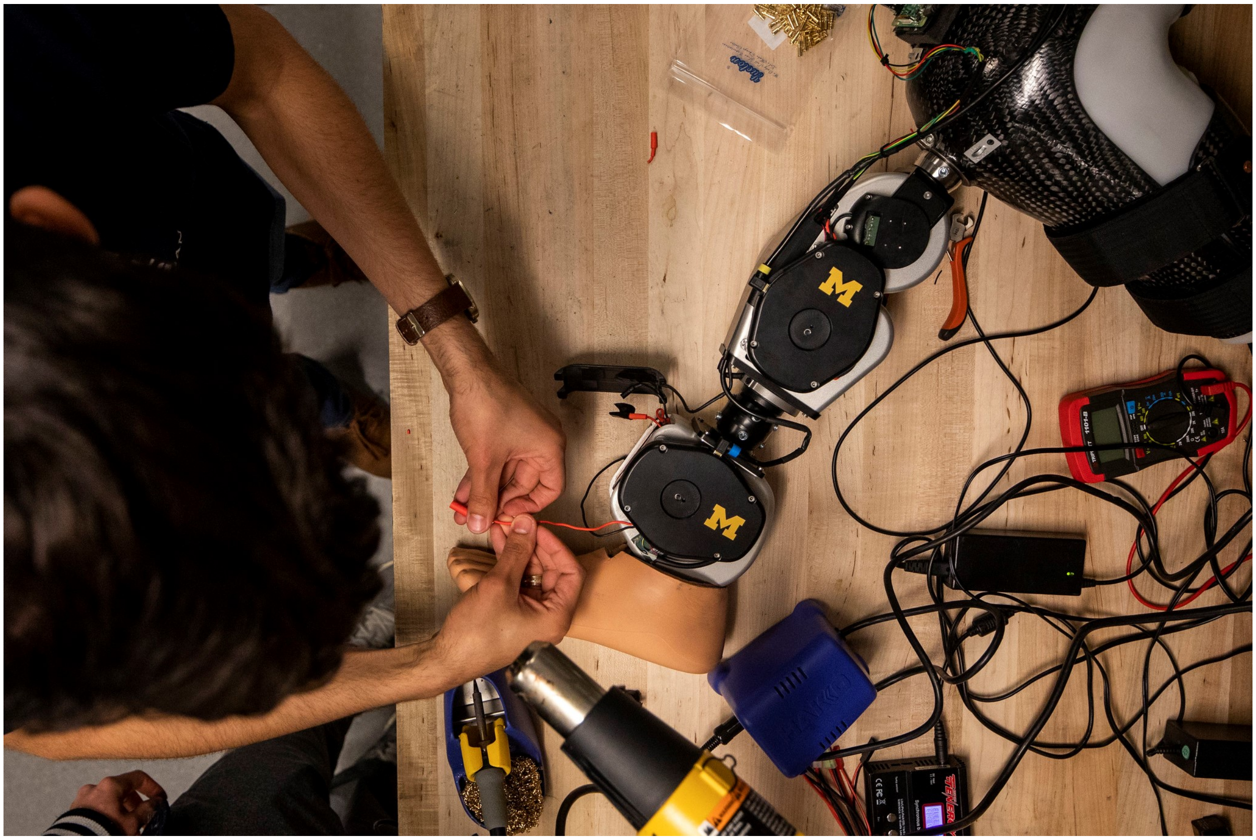

Figure B.1: Assembling the OSL.

Figure B.2: Walking with the OSL using an able-bodied adapter.

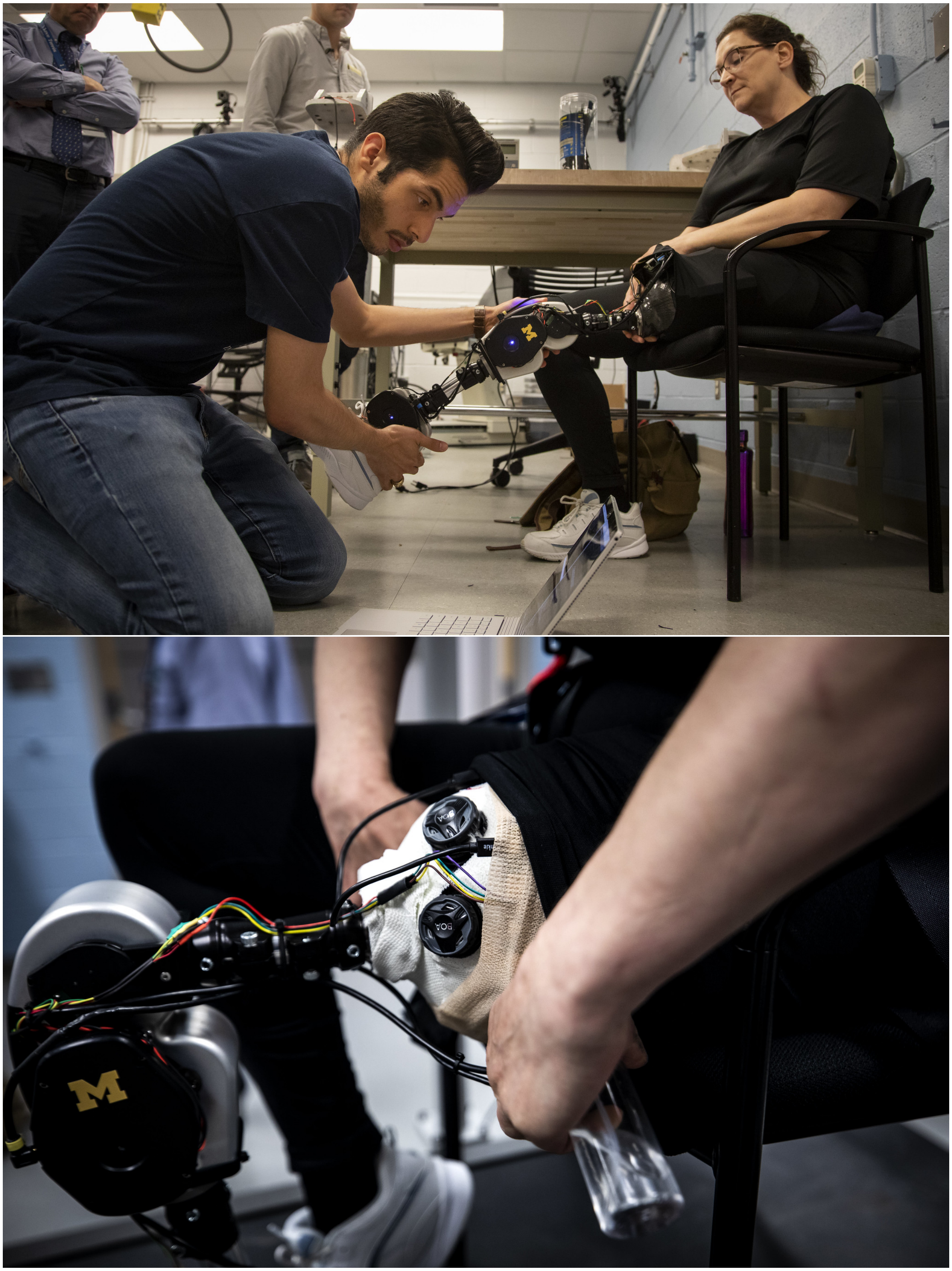

Figure B.3: Setting up the OSL with the Neurobionics Lab’s first patient.

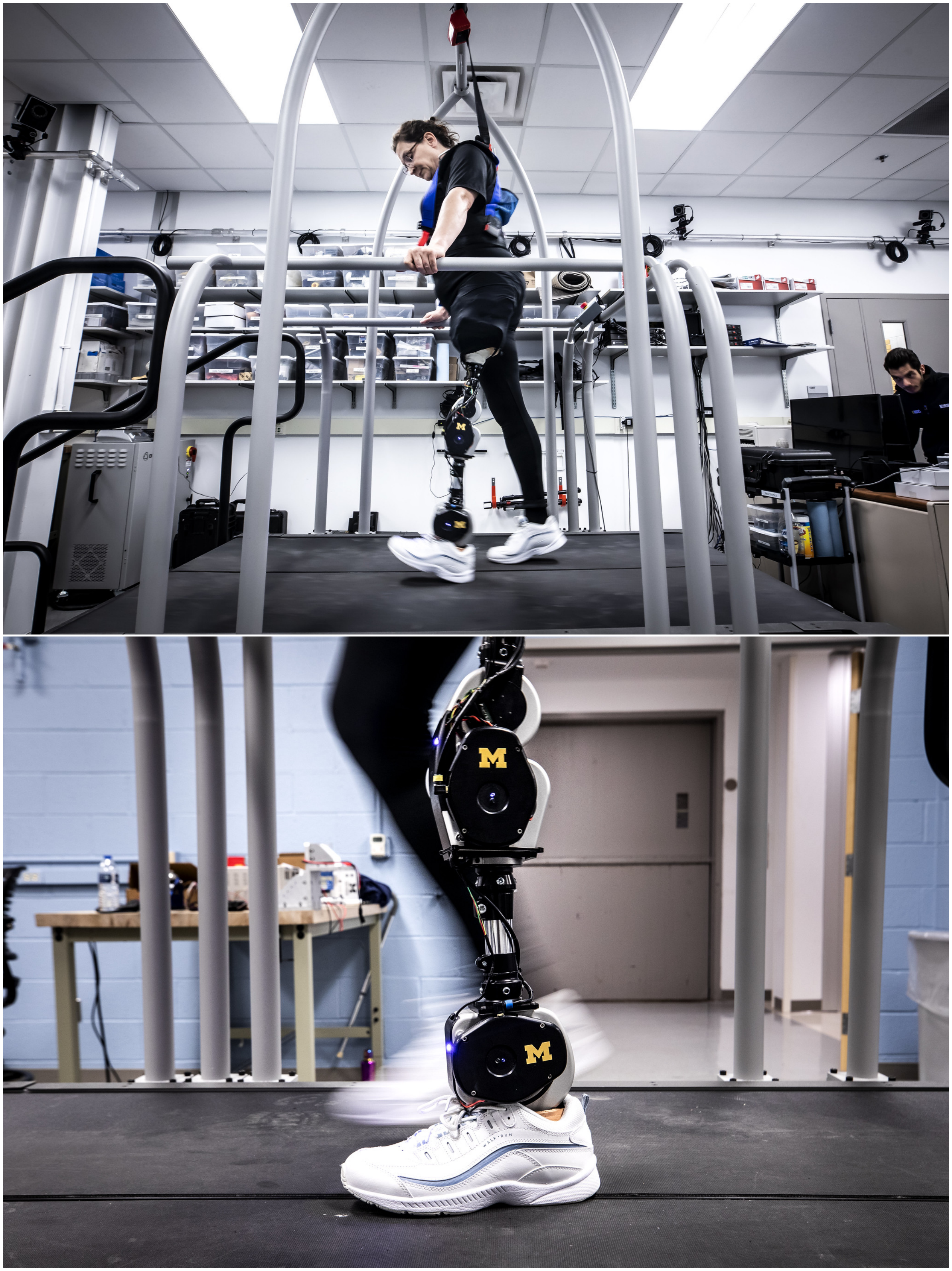

Figure B.4: Neurobionics Lab's first patient walking with the OSL.

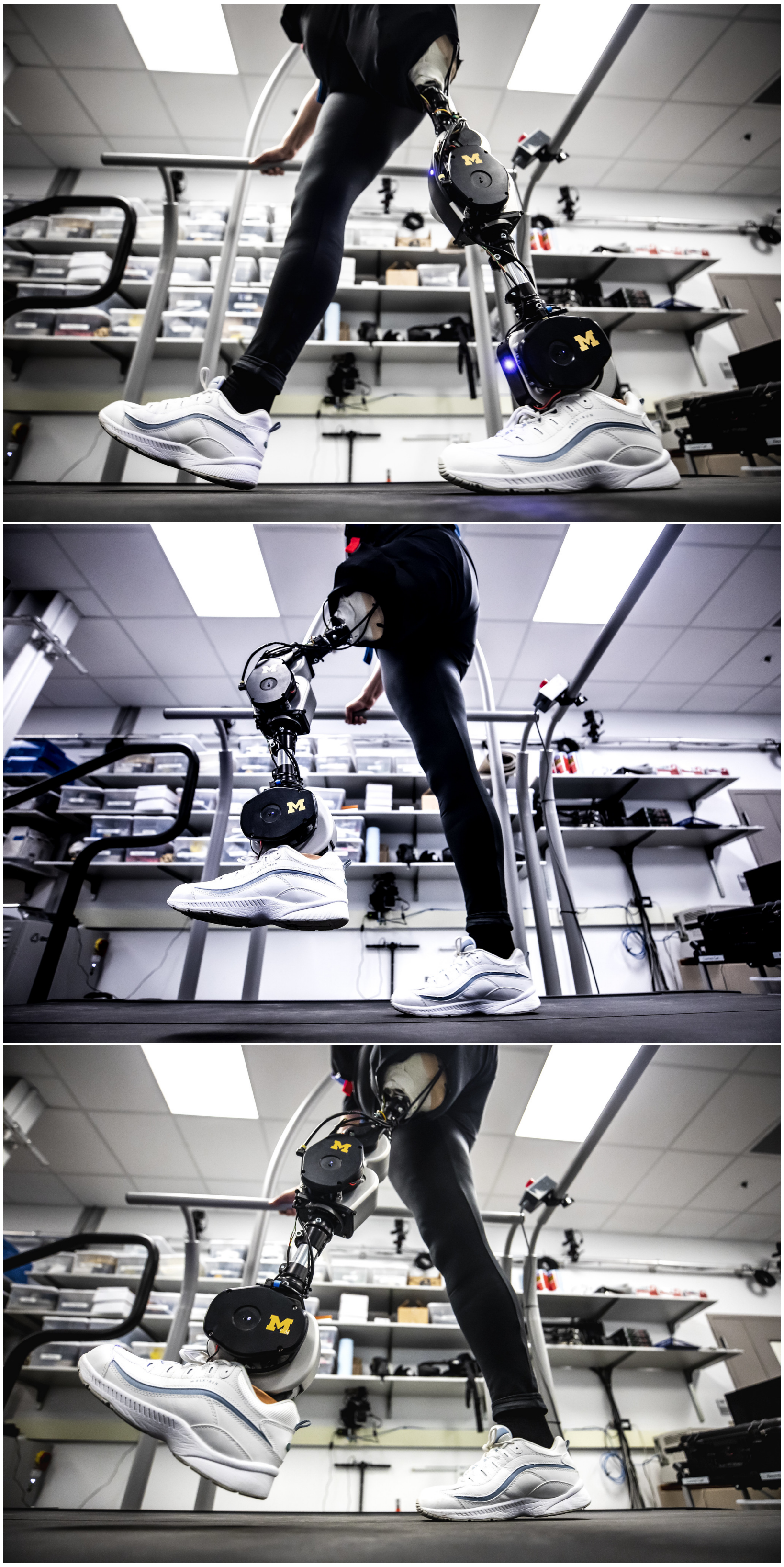

Figure B.5: Progressing through the gait cycle with the OSL.

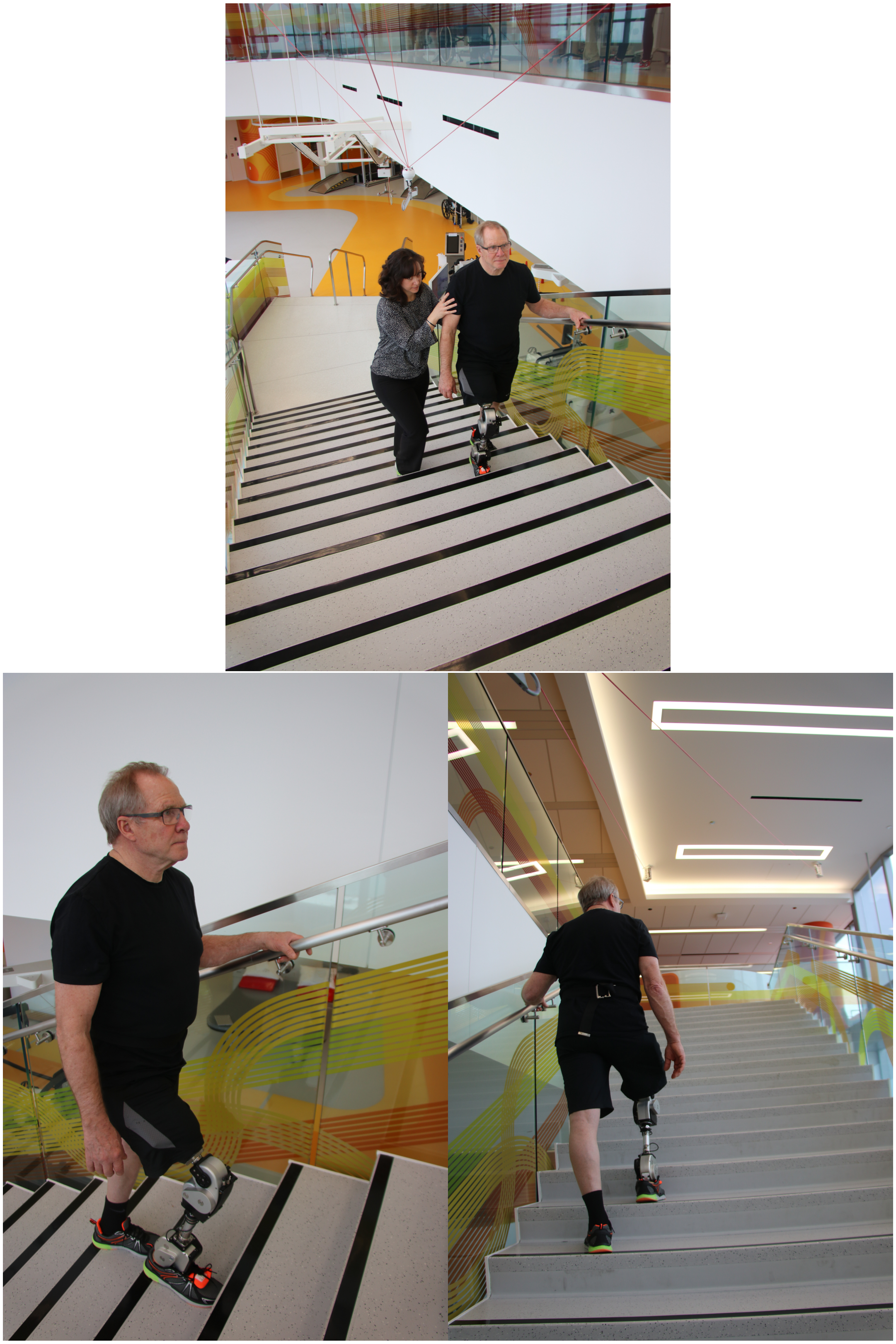

Figure B.6: Walking up stairs with the OSL at the Shirley Ryan AbilityLab.

Appendix C

A Tale of Four Cities

My Ph.D. journey started in 2015, in the Neurobionics Lab and the Center for Bionic Medicine at Northwestern University (Chicago, IL). In 2017, we moved the Neurobionics Lab to the University of Michigan (Ann Arbor, MI) and in 2019, I began a residency program at X (Mountain View, CA). In 2020, due to the COVID-19 pandemic, I returned home (Houston, TX) to finish out my Ph.D. I am grateful for all the incredible friends, coworkers, and mentors I have had over the last 5 years, all around the country.

Figure C.1: Center for Bionic Medicine, 2017.

Figure C.2: Neurobionics Lab, 2019.

Figure C.3: X Team, 2020.

Figure C.4: Azocar Lab, 2020.

Bibliography

[1] A. F. Azocar, L. M. Mooney, L. J. Hargrove, and E. J. Rouse, "Design and Characterization of an Open-source Robotic Leg Prosthesis," in *IEEE International Conference on Biomedical Robotics and Biomechatronics*, (Enschede), pp. 111–118, 2018.

[2] A. F. Azocar, L. M. Mooney, J. F. Duval, A. M. Simon, L. J. Hargrove, and E. J. Rouse, "Design and clinical implementation of an open-source bionic leg," *Nature biomedical engineering*, accepted, in press.

[3] A. F. Azocar and E. J. Rouse, "Stiffness Perception During Active Ankle and Knee Movement," *IEEE Transactions on Biomedical Engineering*, vol. 64, no. 12, pp. 2949–2956, 2017.

[4] A. F. Azocar, A. L. Shorter, and E. J. Rouse, "Perception of Mechanical Impedance During Active Ankle and Knee Movement," in *IEEE International Conference on Engineering in Medicine and Biology*, pp. 3044–3047, 2018.

[5] A. F. Azocar, A. L. Shorter, and E. J. Rouse, "Damping Perception During Active Ankle and Knee Movement," 2019.

[6] M. K. Shepherd, A. F. Azocar, M. J. Major, and E. J. Rouse, "The Difference Threshold of Ankle-Foot Prosthesis Stiffness for Persons with Transtibial Amputation," in *IEEE International Conference on Biomedical Robotics and Biomechatronics*, pp. 100–104, 2018.

[7] M. K. Shepherd, A. F. Azocar, M. J. Major, and E. J. Rouse, "Amputee Perception of Prosthetic Ankle Stiffness During Locomotion," *Journal of NeuroEngineering and Rehabilitation*, vol. 15, no. 99, 2018.

[8] K. Ziegler-Graham, E. J. MacKenzie, P. L. Ephraim, T. G. Travison, and R. Brookmeyer, "Estimating the Prevalence of Limb Loss in the United States: 2005 to 2050," *Archives of Physical Medicine and Rehabilitation*, vol. 89, no. 3, pp. 422–429, 2008.

[9] R. L. Waters, J. Perry, D. Antonelli, and H. Hislop, "Energy cost of walking of amputees: the influence of level of amputation.," *The Journal of bone and joint surgery. American volume*, vol. 58, no. 1, pp. 42–46, 1976.

[10] T. Schmalz, S. Blumentritt, and R. Jarasch, "Energy expenditure and biomechanical characteristics of lower limb amputee gait : The influence of prosthetic alignment and different prosthetic components," *Gait & Posture*, vol. 16, pp. 255–263, 2002.

[11] W. C. Miller, M. Speechley, and B. Deathe, “The prevalence and risk factors of falling and fear of falling among lower extremity amputees,” *Archives of Physical Medicine and Rehabilitation*, vol. 82, no. 8, pp. 1031–1037, 2001.

[12] R. Gailey, K. Allen, J. Castles, J. Kucharik, and M. Roeder, “Review of secondary physical conditions associated with lower-limb amputation and long-term prosthesis use.,” *Journal of rehabilitation research and development*, vol. 45, no. 1, pp. 15–29, 2008.

[13] C. D. Murray, “The Social Meanings of Prosthesis Use,” *Journal of Health Psychology*, vol. 10, no. 3, pp. 425–441, 2005.

[14] B. D. Rybarczyk, D. L. Nyenhuis, J. J. Nicholas, R. Schulz, R. J. Alioto, and C. Blair, “Social discomfort and depression in a sample of adults with leg amputations,” *Archives of Physical Medicine and Rehabilitation*, vol. 73, no. 12, pp. 1169–1173, 1992.

[15] R. Sinha, W. J. Van Den Heuvel, and P. Arokiasamy, “Factors affecting quality of life in lower limb amputees,” *Prosthetics and Orthotics International*, vol. 35, no. 1, pp. 90–96, 2011.

[16] D. A. Winter, *Biomechanics and Motor Control of Human Movement.* Hoboken, NJ: Wiley, 4th ed., 2009.

[17] G. Bovi, M. Rabuffetti, P. Mazzoleni, and M. Ferrarin, “A multiple-task gait analysis approach: kinematic, kinetic and EMG reference data for healthy young and adult subjects.,” *Gait & Posture*, vol. 33, no. 1, pp. 6–13, 2011.

[18] D. A. Winter and S. E. Sienko, “Biomechanics of below-knee amputee gait,” *Journal of Biomechanics*, vol. 21, no. 5, pp. 361–367, 1988.

[19] D. J. Lura, M. W. Wernke, S. L. Carey, J. T. Kahle, R. M. Miro, and M. J. Highsmith, “Crossover study of amputee stair ascent and descent biomechanics using Genium and C-Leg prostheses with comparison to non-amputee control,” *Gait & Posture*, vol. 58, no. July, pp. 103–107, 2017.

[20] H. Hobara, Y. Kobayashi, T. Nakamura, N. Yamasaki, K. Nakazawa, M. Akai, and T. Ogata, “Lower extremity joint kinematics of stair ascent in transfemoral amputees,” *Prosthetics and Orthotics International*, vol. 35, no. 4, pp. 467–472, 2011.

[21] U.S. Bureau of Labor Statistics, *Physical strength required for jobs in different occupations in 2016.* https://www.bls.gov/opub/ted/2017/physical-strength-required-for-jobs-in-different-occupations-in-2016.htm.

[22] U.S. Bureau of Labor Statistics, Civilian Labor Force Level [CLF16OV], retrieved from FRED, Federal Reserve Bank of St. Louis, *Civilian Labor Force Level.* https://fred.stlouisfed.org/series/CLF16OV.

[23] T. Bosch, J. Van Eck, K. Knitel, and M. de Looze, “The effects of a passive exoskeleton on muscle activity, discomfort and endurance time in forward bending work,” *Applied Ergonomics*, vol. 54, pp. 212–217, 2016.

[24] E. P. Lamers, A. J. Yang, and K. E. Zelik, “Feasibility of a Biomechanically-Assistive Garment to Reduce Low Back Loading During Leaning and Lifting,” *IEEE Transactions on Biomedical Engineering*, vol. 65, no. 8, pp. 1674–1680, 2018.

[25] K. Yamamoto, K. Hyodo, M. Ishii, and T. Matsuo, “Development of Power Assisting Suit for Assisting Nurse Labor,” *JSME International Journal*, vol. 45, no. 3, pp. 703–711, 2002.

[26] K. Naruse, S. Kawai, H. Yokoi, and Y. Kakazu, “Development of Wearable Exoskeleton Power Assist System for Lower Back Support,” in *IEEE/RSJ International Conference on Intelligent Robots and Systems*, pp. 3–8, 2003.

[27] H. Hara and Y. Sankai, “HAL equipped with passive mechanism,” in *IEEE/SICE International Symposium on System Integration (SII)*, pp. 1–6, IEEE, 2012.

[28] M. Wehner, D. Rempel, and H. Kazerooni, “Lower Extremity Exoskeleton Reduces Back Forces in Lifting,” in *ASME Dyn. Syst. Control*, pp. 1–8, 2009.

[29] P. Wretenberg and U. P. Arborelius, “Power and work produced in different leg muscle groups when rising from a chair,” *European Journal of Applied Physiology*, vol. 68, pp. 413–417, 1994.

[30] L. M. Mooney, E. J. Rouse, and H. M. Herr, “Autonomous exoskeleton reduces metabolic cost of human walking Autonomous exoskeleton reduces metabolic cost of human walking,” *Journal of NeuroEngineering and Rehabilitation*, vol. 11, no. 80, pp. 1–11, 2014.

[31] S. H. Collins, M. B. Wiggin, and G. S. Sawicki, “Reducing the energy cost of human walking using an unpowered exoskeleton,” *Nature*, vol. 522, no. 7555, pp. 212–215, 2015.

[32] U.S. Census Bureau, *2010 Census Briefs, Age and Sex Composition*. https://www.census.gov/programs-surveys/decennial-census/decade/decennial-publications.2010.html.

[33] F. C. Sup and M. Goldfarb, “Design of a Pneumatically Actuated Transfemoral Prosthesis,” in *ASME International Mechanical Engineering Congress and Exposition*, pp. 1–10, 2006.

[34] F. Sup, A. Bohara, and M. Goldfarb, “Design and Control of a Powered Transfemoral Prosthesis,” *The International Journal of Robotics Research*, vol. 27, no. 2, pp. 263–273, 2008.

[35] S. K. Au, P. Dilworth, and H. Herr, “An Ankle-Foot Emulation System for the Study of Human Walking Biomechanics,” in *IEEE International Conference on Robotics and Automation*, no. May, pp. 2939–2945, 2006.

[36] S. K. Au and H. M. Herr, “Powered ankle-foot prosthesis,” *IEEE Robotics and Automation Magazine*, vol. 15, no. 3, pp. 52–59, 2008.

[37] A. M. Huff, B. E. Lawson, and M. Goldfarb, “A Running Controller for a Powered Transfemoral Prosthesis,” in *IEEE Engineering in Medicine and Biology Conference*, pp. 4168–4171, IEEE, 2012.

[38] B. E. Lawson, J. Mitchell, D. Truex, A. Shultz, E. Ledoux, and M. Goldfarb, "A robotic leg prosthesis: Design, control, and implementation," *IEEE Robotics and Automation Magazine*, vol. 21, no. 4, pp. 70–81, 2014.

[39] A. H. Shultz, B. E. Lawson, and M. Goldfarb, "Walking on uneven terrain with a powered ankle prosthesis: A preliminary assessment," *Proceedings of the Annual International Conference of the IEEE Engineering in Medicine and Biology Society, EMBS*, vol. 2015-Novem, pp. 5299–5302, 2015.

[40] B. E. Lawson, B. Ruhe, A. Shultz, and M. Goldfarb, "A powered prosthetic intervention for bilateral transfemoral amputees," *IEEE Transactions on Biomedical Engineering*, vol. 62, no. 4, pp. 1042–1050, 2015.

[41] E. D. Ledoux and M. Goldfarb, "Control and Evaluation of a Powered Transfemoral Prosthesis for Stair Ascent," *IEEE Transactions on Neural Systems and Rehabilitation Engineering*, vol. 25, no. 7, pp. 917–924, 2017.

[42] B. E. Lawson, E. D. Ledoux, and M. Goldfarb, "A Robotic Lower Limb Prosthesis for Efficient Bicycling," *IEEE Transactions on Robotics*, vol. 33, no. 2, pp. 432–445, 2017.

[43] A. J. Young, T. A. Kuiken, and L. J. Hargrove, "Analysis of using EMG and mechanical sensors to enhance intent recognition in powered lower limb prostheses," *Journal of Neural Engineering*, vol. 11, no. 5, 2014.

[44] A. J. Young, A. M. Simon, and L. J. Hargrove, "A training method for locomotion mode prediction using powered lower limb prostheses," *IEEE Transactions on Neural Systems and Rehabilitation Engineering*, vol. 22, no. 3, pp. 671–677, 2014.

[45] A. M. Simon, K. A. Ingraham, N. P. Fey, S. B. Finucane, R. D. Lipschutz, A. J. Young, and L. J. Hargrove, "Configuring a powered knee and ankle prosthesis for transfemoral amputees within five specific ambulation modes," *PLoS ONE*, vol. 9, no. 6, 2014.

[46] L. J. Hargrove, A. J. Young, A. M. Simon, N. P. Fey, R. D. Lipschutz, S. B. Finucane, E. G. Halsne, K. A. Ingraham, and T. A. Kuiken, "Intuitive control of a powered prosthetic leg during ambulation: a randomized clinical trial.," *Journal of the American Medical Association*, vol. 313, no. 22, pp. 2244–52, 2015.

[47] S. K. Au, J. Weber, and H. M. Herr, "Powered ankle-foot prosthesis improves walking metabolic economy," *IEEE Transactions on Robotics*, vol. 25, no. 1, pp. 51–66, 2009.

[48] H. M. Herr and A. M. Grabowski, "Bionic ankle-foot prosthesis normalizes walking gait for persons with leg amputation.," *Proceedings. Biological sciences / The Royal Society*, vol. 279, no. 1728, pp. 457–64, 2012.

[49] M. E. Carney, *Design and Evaluation of a Reaction-Force Series Elastic Actuator Configurable as Biomimetic Powered Ankle and Knee Prostheses by*. PhD thesis, Massachusetts Institute of Technology, 2020.

[50] T. Elery, S. Rezazadeh, C. Nesler, and R. D. Gregg, "Design and Validation of a Powered Knee – Ankle Prosthesis With High-Torque, Low-Impedance Actuators," *IEEE Transactions on Robotics*, pp. 1–20, 2020.

[51] N. Thatte and H. Geyer, "Toward balance recovery with leg prostheses using neuromuscular model control," *IEEE Transactions on Biomedical Engineering*, vol. 63, no. 5, pp. 904–913, 2016.

[52] H. Zhao, J. Horn, J. Reher, V. Paredes, and A. D. Ames, "First steps toward translating robotic walking to prostheses: a nonlinear optimization based control approach," *Autonomous Robots*, vol. 41, no. 3, pp. 725–742, 2017.

[53] E. J. Rouse, L. M. Mooney, and H. M. Herr, "Clutchable series-elastic actuator: Implications for prosthetic knee design," *The International Journal of Robotics Research*, vol. 33, pp. 1611–1625, 2014.

[54] S. Pfeifer, A. Pagel, R. Riener, and H. Vallery, "Actuator with angle-dependent elasticity for biomimetic transfemoral prostheses," *IEEE/ASME Transactions on Mechatronics*, vol. 20, no. 3, pp. 1384–1394, 2015.

[55] A. Pagel, R. Ranzani, R. Riener, and H. Vallery, "Bio-Inspired Adaptive Control for Active Knee Exoprosthetics," *IEEE Transactions on Neural Systems and Rehabilitation Engineering*, vol. 25, no. 12, pp. 2355–2364, 2017.

[56] T. Lenzi, M. Cempini, L. J. Hargrove, and T. A. Kuiken, "Design, Development, and Testing of a Lightweight Hybrid Robotic Knee Prosthesis," *International Journal of Robotics Research*, vol. in press, 2018.

[57] M. Tran, L. Gabert, M. Cempini, and T. Lenzi, "A Lightweight, Efficient Fully Powered Knee Prosthesis With Actively Variable Transmission," *IEEE Robotics and Automation Letters*, vol. 4, no. 2, pp. 1186–1193, 2019.

[58] J. K. Hitt, T. G. Sugar, M. Holgate, and R. Bellman, "An Active Foot-Ankle Prosthesis With Biomechanical Energy Regeneration," *Journal of Medical Devices*, vol. 4, no. 1, p. 011003, 2010.

[59] P. Cherelle, V. Grosu, A. Matthys, B. Vanderborght, and D. Lefeber, "Design and validation of the ankle mimicking prosthetic (AMP-) Foot 2.0," *IEEE Transactions on Neural Systems and Rehabilitation Engineering*, vol. 22, no. 1, pp. 138–148, 2014.

[60] L. Gabert, S. Hood, M. Tran, M. Cempini, and T. Lenzi, "A Compact, Lightweight Robotic Ankle-Foot Prosthesis: Featuring a Powered Polycentric Design," *IEEE Robotics & Automation Magazine*, vol. 27, no. March, pp. 87–102, 2020.

[61] J. M. Caputo and S. H. Collins, "A universal ankle-foot prosthesis emulator for human locomotion experiments," *Journal of Biomechanical Engineering*, vol. 136, no. 3, p. 035002, 2014.

[62] J. M. Caputo and S. H. Collins, "Prosthetic ankle push-off work reduces metabolic rate but not collision work in non-amputee walking.," *Scientific Reports*, vol. 4, p. 7213, 2014.

[63] M. Kim and S. H. Collins, "Once-per-step control of ankle-foot prosthesis push-off work reduces effort associated with balance during walking.," *Journal of neuroengineering and rehabilitation*, vol. 12, no. 1, p. 43, 2015.

[64] M. Kim, T. Chen, T. Chen, and S. H. Collins, "An Ankle–Foot Prosthesis Emulator With Control of Plantarflexion and Inversion–Eversion Torque," *IEEE Transaction on Robotics*, vol. In Press, pp. 1–12, 2018.

[65] M. Kim, H. Lyness, T. Chen, and S. H. Collins, "The Effects of Prosthesis Inversion/Eversion Stiffness on Balance-Related Variability During Level Walking: A Pilot Study," *Journal of Biomechanical Engineering*, vol. 142, no. September, pp. 1–9, 2020.

[66] S. K. Au, J. Weber, and H. M. Herr, "Biomechanical Design of Powered Ankle-Foot Prosthesis," in *Proceedings of the IEEE 10th International Conference on Rehabilitation Robotics*, pp. 298–303, 2007.

[67] A. H. Shultz, B. E. Lawson, and M. Goldfarb, "Variable cadence walking and ground adaptive standing with a powered ankle prosthesis," *IEEE Transactions on Neural Systems and Rehabilitation Engineering*, vol. 24, no. 4, pp. 495–505, 2016.

[68] M. Cempini, L. J. Hargrove, and T. Lenzi, "Design, development, and bench-top testing of a powered polycentric ankle prosthesis," *IEEE International Conference on Intelligent Robots and Systems*, vol. 2017-Septe, pp. 1064–1069, 2017.

[69] M. R. Tucker, H. Bleuler, O. Lambercy, A. Pagel, R. Gassert, J. Olivier, V. Heike, R. Reiner, M. Bouri, and d. R. M. Jose, "Control Strategies for Active Lower Extremity Prosthetics and Orthotics : A Review," *Journal of NeuroEngineering and Rehabilitation*, no. January 2015, 2015.

[70] B. Hu, E. J. Rouse, and L. J. Hargrove, "Fusion of Bilateral Lower-Limb Neuromechanical Signals Improves Prediction of Locomotor Activities," *Frontiers in Robotics and AI*, vol. 5, no. June, pp. 1–16, 2018.

[71] L. J. Hargrove, A. M. Simon, A. J. Young, R. D. Lipschutz, S. B. Finucane, D. G. Smith, and T. A. Kuiken, "Robotic leg control with EMG decoding in an amputee with nerve transfers.," *The New England Journal of Medicine*, vol. 369, no. 13, pp. 1237–42, 2013.

[72] M. Liu, D. Wang, and H. H. Huang, "Development of an Environment-Aware Locomotion Mode Recognition System for Powered Lower Limb Prostheses," *IEEE Transactions on Neural Systems and Rehabilitation Engineering*, vol. 24, no. 4, pp. 434–443, 2016.

[73] B. Laschowski, W. Mcnally, A. Wong, and J. McPhee, "Preliminary Design of an Environment Recognition System for Controlling Robotic Lower-Limb Prostheses and Exoskeletons," in *IEEE International Conference on Rehabilitation Robotics*, pp. 868–873, IEEE, 2019.

[74] N. E. Krausz, T. Lenzi, and L. J. Hargrove, "Depth Sensing for Improved Control of Lower Limb Prostheses," *IEEE Transactions on Biomedical Engineering*, vol. 62, no. 11, pp. 2576–2587, 2015.

[75] Y. Massalin, M. Abdrakhmanova, and H. A. Varol, "User-Independent Intent Recognition for Lower Limb Prostheses Using Depth Sensing," *IEEE Transactions on Biomedical Engineering*, vol. 65, no. 8, pp. 1759–1770, 2018.

[76] H. A. Varol, F. Sup, and M. Goldfarb, "Multiclass Real-Time Intent Recognition of a Powered Lower Limb Prosthesis," *IEEE Transactions on Biomedical Engineering*, vol. 57, no. 3, pp. 542–551, 2010.

[77] A. J. Young and L. J. Hargrove, "A Classification Method for User-Independent Intent Recognition for Transfemoral Amputees Using Powered Lower Limb Prostheses," *IEEE Transactions on Neural Systems and Rehabilitation Engineering*, vol. 24, no. 2, pp. 217–225, 2016.

[78] H. Huang, F. Zhang, L. J. Hargrove, Z. Dou, D. R. Rogers, and K. B. Englehart, "Continuous Locomotion-Mode Identification for Prosthetic Legs Based on Neuromuscular– Mechanical Fusion," *IEEE Transactions on Biomedical Engineering*, vol. 58, no. 10, pp. 2867–2875, 2011.

[79] U. H. Lee, J. Bi, R. Patel, D. Fouhey, and E. Rouse, "Image Transformation and CNNs: A Strategy for Encoding Human Locomotor Intent for Autonomous Wearable Robots," *IEEE Robotics and Automation Letters*, vol. 5, no. 4, pp. 5440–5447, 2020.

[80] N. Hogan, "Impedance control: An approach to manipulation: Part I- Theory," *Journal of Dynamic Systems, Measurement, and Control*, vol. 107, no. March, pp. 304–313, 1985.

[81] H. Vallery, J. Veneman, E. Van Asseldonk, R. Ekkelenkamp, M. Buss, and H. Van Der Kooij, "Compliant actuation of rehabilitation robots," *IEEE Robotics and Automation Magazine*, vol. 15, no. September, pp. 60–69, 2008.

[82] E. Perreault, L. J. Hargrove, D. Ludvig, H. Lee, and J. Sensinger, "Considering Limb Impedance in the Design and Control of Prosthetic Devices," in *Neuro-Robotics: From Brain Machine Interfaces to Rehabilitation Robotics*, vol. 2, ch. 3, pp. 59–83, Springer, 2014.

[83] J. C. Dean and A. D. Kuo, "Elastic coupling of limb joints enables faster bipedal walking," *Journal of the Royal Society Interface*, vol. 6, no. 35, pp. 561–73, 2009.

[84] E. J. Rouse, L. J. Hargrove, E. J. Perreault, and T. A. Kuiken, "Estimation of human ankle impedance during the stance phase of walking," *IEEE Transactions on Neural Systems and Rehabilitation Engineering*, vol. 22, no. 4, pp. 870–878, 2014.

[85] D. Quintero, D. J. Villarreal, D. J. Lambert, S. Kapp, and R. D. Gregg, "Continuous-phase control of a powered knee–ankle prosthesis: Amputee experiments across speeds and inclines," *IEEE Transactions on Robotics*, vol. 34, no. 3, pp. 686–701, 2018.

[86] S. Kumar, A. Mohammadi, D. Quintero, S. Rezazadeh, N. Gans, and R. D. Gregg, "Extremum Seeking Control for Model-Free Auto-Tuning of Powered Prosthetic Legs," *IEEE Trans. Control Sys. Tech.*, pp. 1–16, 2019.

[87] S. Rezazadeh, D. Quintero, N. Divekar, E. Reznick, L. Gray, and R. D. Gregg, "A Phase Variable Approach for Improved Rhythmic and Non-Rhythmic Control of a Powered Knee-Ankle Prosthesis," *IEEE Access*, vol. 7, pp. 109840–109855, 2019.

[88] D. J. Villarreal, H. A. Poonawala, and R. D. Gregg, "A Robust Parameterization of Human Gait Patterns Across Phase-Shifting Perturbations," *IEEE Transactions on Neural Networks and Learning Systems*, vol. 25, no. 3, pp. 265–278, 2017.

[89] M. A. Holgate, T. G. Sugar, and A. W. Bohler, "A novel control algorithm for wearable robotics using phase plane invariants," *Proceedings - IEEE International Conference on Robotics and Automation*, pp. 3845–3850, 2009.

[90] H. Geyer and H. Herr, "A Muscle-Reflex Model That Encodes Principles of Legged Mechanics Produces Human Walking Dynamics and Muscle Activities," *IEEE Transactions on Neural Systems and Rehabilitation Engineering*, vol. 18, no. 3, pp. 263–273, 2010.

[91] M. F. Eilenberg, H. Geyer, and H. M. Herr, "Control of a powered ankle-foot prosthesis based on a neuromuscular model," *IEEE Transactions on Neural Systems and Rehabilitation Engineering*, vol. 18, no. 2, pp. 164–173, 2010.

[92] J. Zhang, P. Fiers, K. A. Witte, R. W. Jackson, K. L. Poggensee, C. G. Atkeson, and S. H. Collins, "Human-in-the-loop optimization of exoskeleton assistance during walking," *Science*, vol. 356, pp. 1280–1284, 2017.

[93] K. A. Witte, P. Fiers, A. L. Sheets-singer, and S. H. Collins, "Improving the energy economy of human running with powered and unpowered ankle exoskeleton assistance," *Science Robotics*, vol. 5, 2020.

[94] P. W. Franks, G. M. Bryan, R. Reyes, and S. H. Collins, "For an Exo to Be, as Good as Can Be, Help the Ankle ,the Knee, the Hip or All Three?," in *Dynamic Walking*, 2020.

[95] J. R. Koller, D. H. Gates, D. P. Ferris, and C. D. Remy, "'Body-in-the-Loop' Optimization of Assistive Robotic Devices: A Validation Study," in *Robotics: Science and Systems*, 2016.

[96] Y. Ding, M. Kim, S. Kuindersma, and C. J. Walsh, "Human-in-the-loop optimization of hip assistance with a soft exosuit during walking," *Science Robotics*, vol. 3, no. 15, p. eaar5438, 2018.

[97] G. McGimpsey and T. C. Bradford, *Limb Prosthetics Services and Devices, Critical Unmet Need: Market Analysis*. Bioengineering Institute Center for Neuroprosthetics, Worcester Polytechnic Institute.

[98] E. S. Gardinier, B. M. Kelly, J. Wensman, and D. H. Gates, "A controlled clinical trial of a clinically-tuned powered ankle prosthesis in people with transtibial amputation," *Clinical Rehabilitation*, p. 026921551772305, 2017.

[99] R. C. Browning, J. R. Modica, R. Kram, and A. Goswami, “The effects of adding mass to the legs on the energetics and biomechanics of walking,” *Medicine and Science in Sports and Exercise*, vol. 39, no. 3, pp. 515–525, 2007.

[100] G. A. Pratt and M. M. Williamson, “Series Elastic Actuators,” in *IEEE/RSJ International Conference on Intelligent Robots and Systems*, pp. 399–406, 1995.

[101] P. Malcolm, R. E. Quesada, J. M. Caputo, and S. H. Collins, “The influence of push-off timing in a robotic ankle-foot prosthesis on the energetics and mechanics of walking.,” *Journal of NeuroEngineering and Rehabilitation*, vol. 12, no. 1, p. 14, 2015.

[102] E. R. Esposito, K. M. Rodriguez, C. A. Ràbago, and J. M. Wilken, “Does unilateral transtibial amputation lead to greater metabolic demand during walking?,” *Journal of Rehabilitation Research & Development*, vol. 51, no. 8, pp. 1287–1296, 2014.

[103] Z. T. Harvey, B. K. Potter, J. Vandersea, and E. Wolf, “Prosthetic advances.,” *Journal of surgical orthopaedic advances*, vol. 21, no. 1, pp. 58–64, 2012.

[104] L. Nolan, A. Wit, K. Dudziñski, A. Lees, M. Lake, and M. Wychowañski, “Adjustments in gait symmetry with walking speed in trans-femoral and trans-tibial amputees,” *Gait and Posture*, vol. 17, no. 2, pp. 142–151, 2003.

[105] Q. Wang, K. Yuan, J. Zhu, and L. Wang, “Walk the walk: A lightweight active transtibial prosthesis,” *IEEE Robotics and Automation Magazine*, vol. 22, no. 4, pp. 80–89, 2015.

[106] P. Cherelle, G. Mathijssen, Q. Wang, B. Vanderborght, and D. Lefeber, “Advances in Propulsive Bionic Feet and Their Actuation Principles,” *Advances in Mechanical Engineering*, vol. 2014, pp. 1–21, 2014.

[107] M. Windrich, M. Grimmer, O. Christ, S. Rinderknecht, and P. Beckerle, “Active lower limb prosthetics: a systematic review of design issues and solutions,” *BioMedical Engineering OnLine*, vol. 15, no. S3, pp. 5–19, 2016.

[108] C. M. Lara-Barrios, A. Blanco-Ortega, C. H. Guzmán-Valdivia, and K. D. Bustamante Valles, “Literature review and current trends on transfemoral powered prosthetics,” *Advanced Robotics*, vol. 32, no. 2, pp. 51–62, 2018.

[109] S. A. Gard and D. S. Childress, “What Determines the Vertical Displacement of the Body during Normal Walking?,” *Journal of Prosthetics and Orthotics*, vol. 13, no. 3, pp. 64–67, 2001.

[110] A. D. Segal, M. S. Orendurff, G. K. Klute, M. L. McDowell, J. A. Pecoraro, J. Shofer, and J. M. Czerniecki, “Kinematic and kinetic comparisons of transfemoral amputee gait using c-leg and mauch sns prosthetic knees.,” *Journal of Rehabilitation Research & Development*, vol. 43, no. 7, 2006.

[111] V. L. Chiu, A. S. Voloshina, and S. H. Collins, “An ankle-foot prosthesis emulator capable of modulating center of pressure,” *IEEE Transactions on Biomedical Engineering*, vol. 67, no. 1, pp. 166–176, 2019.

[112] D. Quintero, D. J. Villarreal, and R. D. Gregg, "Preliminary Experiments with a Unified Controller for a Powered Knee-Ankle Prosthetic Leg Across Walking Speeds," *IEEE Int. Conf. on Intelligent Robots and Systems*, 2016.

[113] M. Liu, F. Zhang, P. Datseris, and H. Huang, "Improving Finite State Impedance Control of Active-Transfemoral Prosthesis Using Dempster-Shafer Based State Transition Rules," *Journal of Intelligent and Robotic Systems: Theory and Applications*, vol. 76, no. 3-4, pp. 461–474, 2014.

[114] H. Zhao, J. Horn, J. Reher, V. Paredes, and A. D. Ames, "Multicontact Locomotion on Transfemoral Prostheses via Hybrid System Models and Optimization-Based Control," *IEEE Transactions on Automation Science and Engineering*, vol. 13, no. 2, pp. 502–513, 2016.

[115] T. R. Clites, M. J. Carty, J. B. Ullauri, M. E. Carney, L. M. Mooney, J.-F. Duval, S. S. Srinivasan, and H. M. Herr, "Proprioception from a neurally controlled lower-extremity prosthesis," *Sci. Transl. Med*, vol. 10, no. 30, 2018.

[116] R. G. Budynas and J. K. Nisbett, *Shigley's Mechanical Engineering Design*. New York, NY: McGraw-Hill Education, 10 ed., 2015.

[117] S. Seok, A. Wang, M. Y. Chuah, D. J. Hyun, J. Lee, D. M. Otten, J. H. Lang, and S. Kim, "Design Principles for Energy-Efficient Legged Locomotion and Implementation on the MIT Cheetah Robot," *IEEE/ASME Transactions on Mechatronics*, vol. 20, no. 3, pp. 1117–1129, 2015.

[118] K. M. Lynch, N. Marchuk, and M. Elwin, *Embedded Computing and Mechatronics with the PIC32 Microcontroller*. Waltham, MA: Newnes, 1 ed., 2016.

[119] "Handbook of timing belts, pulleys, chains and sprockets.," tech. rep., Stock Drive Products/Sterling Instrument (SDP/SI).

[120] S. Kalouche, "Goat: A legged robot with 3d agility and virtual compliance," in *2017 IEEE/RSJ International Conference on Intelligent Robots and Systems (IROS)*, pp. 4110–4117, IEEE, 2017.

[121] G. Kenneally, A. De, and D. E. Koditschek, "Design Principles for a Family of Direct-Drive Legged Robots," *IEEE Robotics and Automation Letters*, vol. 1, no. 2, pp. 900–907, 2016.

[122] J. F. Duval and H. M. Herr, "FlexSEA: Flexible, Scalable Electronics Architecture for wearable robotic applications," *Proceedings of the IEEE RAS and EMBS International Conference on Biomedical Robotics and Biomechatronics*, pp. 1236–1241, 2016.

[123] J. F. Duval and H. M. Herr, "FlexSEA-Execute: Advanced motion controller for wearable robotic applications," *Proceedings of the IEEE RAS and EMBS International Conference on Biomedical Robotics and Biomechatronics*, pp. 1056–1061, 2016.

[124] U. H. Lee, C.-W. Pan, and E. J. Rouse, “Empirical Characterization of a High-performance Exterior-rotor Type Brushless DC Motor and Drive,” in *IEEE/RSJ International Conference on Intelligent Robots and Systems*, (Macau, China), pp. 8018–8025, 2019.

[125] L. Ljung, *System Identification: Theory for the User*. Upper Saddle River, NJ: Prentice Hall PTR, second ed ed., 1999.

[126] J. Braun, “Formulae Handbook,” tech. rep., Maxon Motor, Sachseln, 2012.

[127] F. Sup, H. A. Varol, and M. Goldfarb, “Upslope walking with a powered knee and ankle prosthesis: Initial results with an amputee subject,” *IEEE Transactions on Neural Systems and Rehabilitation Engineering*, vol. 19, no. 1, pp. 71–78, 2011.

[128] A. R. Tilley, *The Measure of Man and Woman: Human Factors in Design*. Watson-Guptill, 1993.

[129] A. Protopapadaki, W. I. Drechsler, M. C. Cramp, F. J. Coutts, and O. M. Scott, “Hip, knee, ankle kinematics and kinetics during stair ascent and descent in healthy young individuals,” *Clinical Biomechanics*, vol. 22, no. 2, pp. 203–210, 2007.

[130] T. Schmalz, S. Blumentritt, and B. Marx, “Biomechanical analysis of stair ambulation in lower limb amputees,” *Gait and Posture*, vol. 25, no. 2, pp. 267–278, 2007.

[131] J. M. Stepien, S. Cavenett, L. Taylor, and M. Crotty, “Activity Levels Among Lower-Limb Amputees: Self-Report Versus Step Activity Monitor,” *Archives of Physical Medicine and Rehabilitation*, vol. 88, no. 7, pp. 896–900, 2007.

[132] C. Tudor-Locke and D. Bassett, “How many steps/day are enough? Preliminary pedometer indicies for public health,” *Sports Medicine*, vol. 34, no. 1, pp. 1–8, 2004.

[133] A. S. McIntosh, K. T. Beatty, L. N. Dwan, and D. R. Vickers, “Gait dynamics on an inclined walkway,” *Journal of Biomechanics*, vol. 39, no. 13, pp. 2491–2502, 2006.

[134] A. L. Shorter and E. J. Rouse, “Mechanical Impedance of the Ankle during the Terminal Stance Phase of Walking,” *IEEE Transactions on Neural Systems and Rehabilitation Engineering*, vol. 26, no. 1, pp. 135–143, 2018.

[135] J. F. Veneman, R. Kruidhof, E. E. G. Hekman, R. Ekkelenkamp, E. H. F. Van Asseldonk, and H. Van Der Kooij, “Design and evaluation of the LOPES exoskeleton robot for interactive gait rehabilitation,” *IEEE Transactions on Neural Systems and Rehabilitation Engineering*, vol. 15, no. 1, pp. 379–386, 2007.

[136] H. K. Kwa, J. H. Noorden, M. Missel, T. Craig, J. E. Pratt, and P. D. Neuhaus, “Development of the IHMC mobility assist exoskeleton,” *Proceedings - IEEE International Conference on Robotics and Automation*, pp. 2556–2562, 2009.

[137] P. D. Neuhaus, J. H. Noorden, T. J. Craig, T. Torres, J. Kirschbaum, and J. E. Pratt, “Design and evaluation of Mina: A robotic orthosis for paraplegics,” *IEEE International Conference on Rehabilitation Robotics*, 2011.

[138] N. Karavas, A. Ajoudani, N. Tsagarakis, J. Saglia, A. Bicchi, and D. Caldwell, "Tele-Impedance based stiffness and motion augmentation for a knee exoskeleton device," *Proceedings - IEEE International Conference on Robotics and Automation*, pp. 2194–2200, 2013.

[139] R. Lu, Z. Li, C.-y. Su, and A. Xue, "Development and Learning Control of a Human Limb With a Rehabilitation Exoskeleton," *IEEE Transactions on Industrial Electronics*, vol. 61, no. 7, pp. 3776–3785, 2014.

[140] M. K. Shepherd and E. J. Rouse, "Design and Validation of a Torque-Controllable Knee Exoskeleton for Sit-to-Stand Assistance," *IEEE/ASME Transactions on Mechatronics*, vol. 22, no. 4, pp. 1695–1704, 2017.

[141] H. Zhu, J. Doan, C. Stence, G. Lv, T. Elery, and R. Gregg, "Design and Validation of a Torque Dense, Highly Backdrivable Powered Knee-Ankle Orthosis," in *IEEE International Conference on Robotics and Automation*, pp. 504–510, 2017.

[142] H. Zhu, C. Nesler, N. Divekar, M. T. Ahmad, and R. D. Gregg, "Design and Validation of a Partial-Assist Knee Orthosis with Compact , Backdrivable Actuation," in *IEEE International Conference on Rehabilitation Robotics*, pp. 917–924, IEEE, 2019.

[143] H. Lee and N. Hogan, "Time-varying ankle mechanical impedance during human locomotion," *IEEE Transactions on Neural Systems and Rehabilitation Engineering*, vol. 23, no. 5, pp. 755–764, 2015.

[144] H. Lee, E. J. Rouse, and H. I. Krebs, "Summary of human ankle mechanical impedance during walking," *IEEE Journal of Translational Engineering in Health and Medicine*, vol. 4, 2016.

[145] J. A. Blaya and H. M. Herr, "Adaptive control of a variable-impedance ankle-foot orthosis to assist drop-foot gait," *IEEE Transactions on Neural Systems and Rehabilitation Engineering*, vol. 12, no. 1, pp. 24–31, 2004.

[146] E. J. Rouse, R. D. Gregg, L. J. Hargrove, and J. W. Sensinger, "The difference between stiffness and quasi-stiffness in the context of biomechanical modeling," *IEEE Transactions on Biomedical Engineering*, vol. 60, no. 2, pp. 562–568, 2013.

[147] K. Shamaei, G. S. Sawicki, and A. M. Dollar, "Estimation of quasi-stiffness of the human knee in the stance phase of walking," *PLoS ONE*, vol. 8, no. 3, 2013.

[148] S. Pfeifer, R. Riener, and H. Vallery, "Knee stiffness estimation in physiological gait," *2014 36th Annual International Conference of the IEEE Engineering in Medicine and Biology Society, EMBC 2014*, no. vm, pp. 1607–1610, 2014.

[149] K. Shamaei, M. Cenciarini, A. A. Adams, K. N. Gregorczyk, J. M. Schiffman, and A. M. Dollar, "Biomechanical effects of stiffness in parallel with the knee joint during walking," *IEEE Transactions on Biomedical Engineering*, vol. 62, no. 10, pp. 2389–2401, 2015.

[150] G. Aguirre-Ollinger, J. E. Colgate, M. A. Peshkin, and A. Goswami, "Active-impedance control of a lower-limb assistive exoskeleton," *2007 IEEE 10th International Conference on Rehabilitation Robotics, ICORR'07*, pp. 188–195, 2007.

[151] B. Jardim and A. A. G. Siqueira, "Development of series elastic actuators for impedance control of an active ankle foot orthosis," *Proceedings of the 20th International Congress of Mechanical Engineering, COBEM*, vol. 2009, pp. 1–8, 2009.

[152] T. Nichols and J. Houk, "Improvement in linearity and regulation of stiffness that results from actions of stretch reflex.," *J Neurophysiol*, vol. 39, no. 1, pp. 119–142, 1976.

[153] E. J. Rouse, L. J. Hargrove, E. J. Perreault, M. A. Peshkin, and T. A. Kuiken, "Development of a mechatronic platform and validation of methods for estimating ankle stiffness during the stance phase of walking.," *Journal of biomechanical engineering*, vol. 135, no. 8, p. 81009, 2013.

[154] D. S. Barrett, A. G. Cobb, and G. Bentley, "Joint proprioception in normal, osteoarthritic and replaced knees.," *The Journal of bone and joint surgery. British volume*, vol. 73, no. 1, pp. 53–56, 1991.

[155] H. A. Quintero, R. J. Farris, and M. Goldfarb, "A method for the autonomous control of lower limb exoskeletons for persons with paraplegia," *Journal of Medical Devices*, vol. 6, no. 4, p. 041003, 2012.

[156] S. Jezernik, G. Colombo, T. Keller, H. Frueh, and M. Morari, "Robotic orthosis Lokomat: A rehabilitation and research tool," *Neuromodulation*, vol. 6, no. 2, pp. 108–115, 2003.

[157] K. A. Strausser and H. Kazerooni, "The development and testing of a human machine interface for a mobile medical exoskeleton," *2011 IEEE/RSJ International Conference on Intelligent Robots and Systems*, pp. 4911–4916, 2011.

[158] L. A. Jones and I. W. Hunter, "A perceptual analysis of viscosity," *Experimental Brain Research*, vol. 94, no. 2, pp. 343–351, 1993.

[159] L. A. Jones and I. W. Hunter, "A perceptual analysis of stiffness," *Experimental Brain Research*, vol. 79, no. 1, pp. 150–156, 1990.

[160] G. Gescheider, *Psychophysics: Method, Theory, and Application*. Hillsdale: Lawrence Erlbaum Associates, 2 ed., 1985.

[161] D. Ludvig and E. J. Perreault, "Task-relevant adaptation of musculoskeletal impedance during posture and movement," *Proceedings of the American Control Conference*, pp. 4784–4789, 2014.

[162] F. A. A. Kingdom and N. Prins, *Psychophysics: A Practical Introduction*. Elsevier, 1 ed., 2010.

[163] C. Kaernbach, "Simple adaptive testing with the weighted up-down method," *Perception & Psychophysics*, vol. 49, no. 3, pp. 227–229, 1991.

[164] H. Levitt, “Transformed up-down methods in psychoacoustics,” *The Journal of the Acoustical society of America*, vol. 49, no. 2, pp. 467–477, 1971.

[165] L.-Q. Zhang and W. Z. Rymer, “Reflex and Intrinsic Changes Induced by Fatigue of Human Elbow Extensor Muscles,” *Journal of Neurophysiology*, vol. 86, no. 3, pp. 1086–1094, 2001.

[166] L. A. Jones, I. Hunter, and S. Lafontaine, “Viscosity discrimination: A comparison of an adaptive two-alternative forced-choice and an adjustment procedure,” *Perception*, vol. 26, no. 12, pp. 1571–1578, 1997.

[167] N. Vuillerme and M. Boisgontier, “Muscle fatigue degrades force sense at the ankle joint,” *Gait and Posture*, vol. 28, no. 3, pp. 521–524, 2008.

[168] J. C. Craig, “Vibrotactile difference thresholds for intensity and the effect of a masking stimulus,” *Perception & Psychophysics*, vol. 15, no. 1, pp. 123–127, 1974.

[169] G. K. Essick, O. Franzen, and B. L. Whitsel, “Discrimination and Scaling of Velocity of Stimulus Motion across the Skin,” *Somatosensory & Motor Research*, vol. 6, no. 1, pp. 21–40, 1988.

[170] E. Francisco, V. Tannan, Z. Zhang, J. Holden, and M. Tommerdahl, “Vibrotactile amplitude discrimination capacity parallels magnitude changes in somatosensory cortex and follows Weber’s Law,” *Experimental brain research*, vol. 191, no. 1, pp. 49–56, 2008.

[171] W. M. Bergmann Tiest, A. C. L. Vrijling, and A. M. L. Kappers, “Haptic Perception of Viscosity,” in *International Conference on Human Haptic Sensing and Touch Enabled Computer Applications (EuroHaptics)*, pp. 29–34, 2010.

[172] N. Deshpande, D. M. Connelly, E. G. Culham, and P. A. Costigan, “Reliability and validity of ankle proprioceptive measures,” *Archives of Physical Medicine and Rehabilitation*, vol. 84, no. 6, pp. 883–889, 2003.

[173] M. E. Héroux and F. Tremblay, “Weight discrimination after anterior cruciate ligament injury: A pilot study,” *Archives of Physical Medicine and Rehabilitation*, vol. 86, no. 7, pp. 1362–1368, 2005.

[174] L. A. Jones and I. W. Hunter, “Influence of the mechanical properties of a manipulandum on human operator dynamics. I. Elastic stiffness,” *Biological Cybernetics*, pp. 299–307, 1990.

[175] L. A. Jones and I. W. Hunter, “Influence of the mechanical properties of a manipulandum on human operator dynamics. II. Viscosity,” *Biological Cybernetics*, pp. 295–303, 1993.

[176] D. J. J. Bregman, *The Optimal Ankle Foot Orthosis: The influence of mechanical properties of Ankle Foot Orthoses on the walking ability of patients with central neurological disorders*. PhD thesis, Vrije Universiteit Amsterdam, 2011.

[177] S. Feyzabadi, S. Straube, M. Folgheraiter, E. A. Kirchner, S. K. Kim, and J. C. Albiez, “Human force discrimination during active arm motion for force feedback design,” *IEEE Transactions on Haptics*, vol. 6, no. 3, pp. 309–319, 2013.

[178] M. Mulder, M. Mulder, M. M. van Paassen, and D. A. Abbink, “Haptic gas pedal feedback,” *Ergonomics*, vol. 51, no. 11, pp. 1710–1720, 2008.

[179] J. S. Mehling, J. E. Colgate, and M. A. Peshkin, “Increasing the impedance range of a haptic display by adding electrical damping,” *Proceedings - 1st Joint Eurohaptics Conference and Symposium on Haptic Interfaces for Virtual Environment and Teleoperator Systems; World Haptics Conference, WHC 2005*, pp. 257–262, 2005.

[180] R. Adams and B. Hannaford, “Stable haptic interaction with virtual environments,” *IEEE Transactions on Robotics and Automation*, vol. 15, no. 3, pp. 465–474, 1999.

[181] K. P. Blum, B. Lamotte D’Incamps, D. Zytnicki, and L. H. Ting, “Force encoding in muscle spindles during stretch of passive muscle,” *PLoS Computational Biology*, vol. 13, no. 9, pp. 1–24, 2017.

[182] M. O. Ernst and M. S. Banks, “Humans integrate visual and haptic information in a statistically optimal fashion,” *Nature*, vol. 415, no. January, pp. 429–433, 2002.

[183] W. M. Bergmann Tiest and A. M. L. Kappers, “Cues for haptic perception of compliance,” *IEEE Transactions on Haptics*, vol. 2, no. 4, pp. 189–199, 2009.

[184] F. J. Clark, K. W. Horch, S. M. Bach, and G. F. Larson, “Contributions of cutaneous and joint receptors to static knee-position sense in man.,” *Journal of neurophysiology*, vol. 42, no. 3, pp. 877–888, 1979.

[185] P. E. Roland and H. Ladegaard-Pedersen, “A quantitative analysis of sensations of tension and of kinesthesia in man,” *Brain*, pp. 671–692, 1977.